D Phil Thesis

Investigation of K_{2P} channel Permeation and Gating

submitted by

Linus Johann Conrad

Green Templeton College,
on the the 7th October 2019
(TT 2018/2019)



supervised by
Stephen Tucker and Liz Carpenter

D Phil Thesis

Investigation of K_{2P} channel Permeation and Gating

submitted by
Linus Johann Conrad
Green Templeton College
on the the 7th October 2019 (TT 2018/2019)

Abstract

The ability to conduct potassium ions (K^+) selectively in the abundant presence of other ion species is crucial to the function of K^+ channels. While the mechanism of ion selectivity has been an intensely studied and debated topic, the protein structure responsible for ion-selectivity has long been identified as the so called selectivity filter (SF). The SF also doubles as the principal regulatory element (gate) in many K^+ channels.

In this project several phenomena related to the permeation, selectivity and gating at the SF of two-pore-domain K^+ channels (K_{2P} channels) were investigated. Firstly, the effect of mutations at the intracellular entrance of the TASK3 (TWIK-related acid sensitive K^+ 3) channel SF were studied. Secondly, the mechanism of pharmacological activation of the TREK2 (TWIK related K^+ channel 2) SF gate was probed on a single molecule level. Channel activation was found to be conferred by a change to the electrostatic milieu at the SF entrance.

Following from this electrostatic mechanism the dependence of gating on salt concentration (ionic strength) was probed. Here an unusual property emerged: TREK channels close in the presence of high ionic strength.

Finally, evidence was found that TREK2 may change its ion-selectivity in the context of voltage-dependent gating. This result suggests that TREK2 may have a stimulating effect on cellular excitability, which is a novel and atypical property for a K^+ channel

Contents

1 Introduction **1**
- 1.1 Ionic gradients and membrane potentials . . . 2
- 1.2 The action potential: Key observations from the squid axon . 4
- 1.3 The K^+-leak . . . 12
- 1.4 The K2P channel subfamily . . . 14
- 1.5 Canonical tetrameric K^+ channels . . . 23
- 1.6 Structure and function of K2P channels . . . 41
- 1.7 Aims and Objectives . . . 55

2 Methods **57**
- 2.1 Heterologous expression . . . 57
- 2.2 Data acquisition, and analysis . . . 62
- 2.3 Establishing a single-channel model system . . . 66

3 Characterisation of TASK mutations **69**
- 3.1 Introduction . . . 69
- 3.2 Materials and Methods . . . 72
- 3.3 Results . . . 74
- 3.4 Discussion . . . 79

4 Activators of TREK2 on the microscopic Level **85**
- 4.1 Introduction . . . 85
- 4.2 Materials, Methods and Analysis . . . 92
- 4.3 Results . . . 92
- 4.4 Discussion . . . 97

5 Inhibition of TREK currents in high ionic strength **103**
- 5.1 Introduction . . . 103
- 5.2 Materials and Methods . . . 106
- 5.3 Results . . . 107
- 5.4 Discussion . . . 116

6 Loss of selectivity in TREK2 **123**
- 6.1 Introduction . . . 123
- 6.2 Methods . . . 125
- 6.3 Results . . . 128
- 6.4 Discussion . . . 144

7 General discussion **157**
7.1 Summary 157
7.2 K_{2P} channels in a general context 159
7.3 Gating, Permeation and Selectivity entwined 162
7.4 A gating scheme of TREK 164
7.5 Biophysical study of polymodal channels 167

Bibliography **175**

Publications **203**

Glossary

AA arachidonic acid.

AG activation gate.

AP action potential.

ATI alternative translation initiation.

ATP adenosine triphosphate.

BK big K^+ channel, Ca^{2+}- and voltage-dependent large conductance K^+ channel.

CC current-clamp.

CMV cytomegalovirus.

CNG-channel cyclic nucleotide gated channel.

CNS central nervous system.

DRG dorsal root ganglion.

EDTA ethylenediaminetetraacetic acid.

ER endoplasmatic reticulum.

FFA flufenamic acid.

GoF gain of function.

GSUK *Geobacter sulfurreducens* K^+ channel.

HBC helix bundle crossing.

HEK293 human embryonic kidney cell-line 293.

HRE halothane response element.

HSV-TK Herpes simplex virus thymidine kinase.

K_{ir} inwardly rectifying K^+ channel.

K_{2P} two pore domain K^+ channel.

K_{cv} Chlorella virus K^+ channel.

K_v voltage-gated K^+ channel.

K_{ATP} ATP-sensitive K^+ channel.

KcsA K^+ channel of streptomyces A.

LB Luria broth.

MD molecular dynamics.

MthK Methanothermobacter thermautotrophicus K^+ channel.

MTS methanethiosulfonate.

Na_v voltage-gated K^+ channel.

ORF open reading frame.

PAH Pulmonary arterial hypertension.

PCR polymerase chain reaction.

PD pore domain.

pFAW Firdaus Abd-Wahab's plasmid.

pfu *Pyrococcus furiosus*.

PIP Phosphatidylinositolphosphate.

PKA protein kinase A.

PKC protein kinace C.

QA^+ quaternary ammonium ion.

RMP resting membrane potential.

SDM site directed mutagenesis.

SF selectivity filter.

TALK TWIK-related alkaline pH-activated K^+ channel.

TASK TWIK-related acid-sensitive K^+ channel.

TEA tetraethylammonium.

THIK TWIK-related halothane inhibited K^+ channel.

TK thymidine kinase.

TPA tetrapentylammonium.

TRAAK TWIK-related arachidonic acid activated K^+ channel.

TREK TWIK-related K^+ channel.

TRESK TWIK-related spinal cord K^+ channel.

TWIK tandem pore domain weakly inward rectifying K^+ channel.

VC voltage-clamp.

VGCC voltage-gated cation channel.

VSD voltage sensing domain.

Chapter 1

Introduction

All forms of life exploit electrochemical processes at their membrane interfaces. From the synthesis of metabolites such as adenosine triphosphate (ATP) in the mitochondrial membrane to neuronal signalling underlying sensation and cognition, regulated membrane currents are key to cellular function.

Before the discovery of individual classes or even the concept of ion channels as we know it today, the permeability of biological model membranes was studied in great detail. The fundamentals of modern neuroscience as well as the biophysics and cell biology of bioelectricity and ion channels were established through the pioneering work on the squid giant axon membrane in the first half of the 20th century.

This culminated in the publication of the seminal work by Hodgkin and Huxley (1952) who introduced a framework for mathematically modelling membrane currents that is used to this day. Their work predicted properties of voltage gated K^+- and Na^+-channels with remarkable accuracy at a time in which the molecular identity and properties of the membrane, let alone ion channels was still controversial.

1.1 Ionic gradients and membrane potentials

The lipid membrane separates the cytoplasm from the extracellular space. Its hydrophobic core makes it impermeable to charged particles. Ions may pass it only in a tightly regulated fashion flowing through pathways formed by membrane proteins. Through the action of ionic pumps and at the expense of energy, concentration gradients of ions are established and charges unevenly distributed on either side of the membrane. This results in a potential difference between the two sides of the membrane (membrane potential, V_m). A summary of the resulting gradients can be found in table 1.1.

Imagine two solutions of KCl with different concentrations, separated by a membrane permeable only to K^+. K^+ will diffuse down its concentration gradient, leaving the negatively charged Cl^- behind. Two forces will then govern the flow of K^+ through the membrane: (1) the chemical driving force (concentration gradient), (2) electrical driving force (charge separation, voltage across the membrane). Their equilibrium is described by the Nernst equation (Nernst 1888). The potential at which there is no net flow scales with the logarithm of the concentration gradient. For an ion species X this

Table 1.1: *Ion concentrations of skeletal muscle* Concentrations given in mM, c_{ext} denotes concentration outside of the cell, c_{int} inside of the cell. Table reproduced from (Hille 2001e). Calculated with eq. 1.1 at 37 °C.

Ion	c_{ext}	c_{int}	$\frac{c_{ext}}{c_{int}}$	V_X mV
Na^+	145	12	12	+67
K^+	4	155	0.0026	−98
Ca^{2+}	1.5	0.0001	15 000	+129
Cl^-	123	4.2	29	−90

equilibrium potential V_X is calculated with the following relation:

$$V_X = \frac{RT}{z_X F} \ln\left(\frac{c_{ext}}{c_{int}}\right) \tag{1.1}$$

Where R is the gas constant, F Faraday's constant, T the absolute temperature, z_X the valence of the ion X in question and c_{ext} and c_{int} the internal (int) and external (ext) ion-concentrations of the cell.

A current through a semipermeable membrane will drive the voltage across it towards the equilibrium potential of its carrying ion. A membrane that is permeable to several ion species will show an intermediate potential that is dependent on the magnitude of the conductances of these ion species. For situations in which there is a mixture of ions and net flow (non-equilibrium) the Goldman-Hodkin-Katz equation (GHK, also constant field equation) applies. In the case of a mixture of conductances as well as asymmetric ionic conditions V_m can be calculated with the following equation established by Hodgkin and Katz (1949) derived from the Goldman current or flux equation (Goldman 1943).

$$V_m = \frac{RT}{F} \ln\left(\frac{P_{K^+}\left[K^+\right]_{ext} + P_{Na^+}\left[Na^+\right]_{ext} + P_{Cl^-}\left[Cl^-\right]_{int}}{P_{K^+}\left[K^+\right]_{int} + P_{Na^+}\left[Na^+\right]_{int} + P_{Cl^-}\left[Cl^-\right]_{ext}}\right) \tag{1.2}$$

The Goldman equation hinges on assumptions about the membrane and the membrane interface that inform the permeability coefficient P which is based on a model in which the ion partitions into the membrane. For an in depth derivation and discussion see Alvarez and Latorre (2017) or Hille (2001f).

These equations make a set of predictions on the rectification and properties of ionic currents in asymmetric salt solutions that are discussed and demonstrated in section 5.4 and fig. 5.4B.

In analogy to Ohm's law, the magnitude of a macroscopic ionic current is proportional to its *driving force*, that is the difference between the equilibrium potential and the membrane voltage V. The quantity g_X refers to the conductance of the membrane for that ion.

$$I_X = g_X(V - V_X) \tag{1.3}$$

1.2 The action potential: Key observations from the squid axon

With these concepts we can start to explain some of the classical observations made from the squid axon. Excitable cells such as neurons and muscle cells are defined by their ability to produce action potentials (AP). Action potentials are rapid voltage spikes produced in response to a depolarising stimulus, such as a current injected near the membrane. The squid axon is large enough that preparations can be impaled with glass electrodes to directly record the potential difference across the axon membrane. This allowed first recordings of the AP to be made and its key properties to be discovered. A stylised AP response of the giant squid membrane is shown in fig. 1.1.

The key features of the AP can be summarised as such (Hille 2001a):

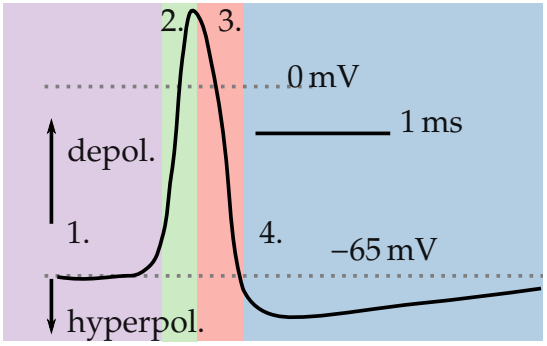


Figure 1.1: *Time course of the squid giant axon action potential* Retraced from Hodgkin and Katz (1949), assuming a −65 mV resting membrane potential. 1, purple-grey: resting membrane potential. 2, green: upstroke, depolarisation with 'overshoot'. 3, red: re-polarisation. 4, blue: after-hyperpolarisation.

1. the resting membrane potential (RMP) of excitable cells lies between −60 mV to −96 mV in physiological conditions and depolarises with increasing $[K^+]_{ext}$
2. action potentials are not produced in the absence of extracellular Na^+
3. the action potential exceeds 0 mV ('overshoots'), rate of depolarisation ('upstroke') and amplitude decrease when $[Na^+]_{ext}$ is lowered
4. repolarisation of the membrane is followed by an after-hyperpolarisation

1.2.1 Transient changes in permeability underlie the action potential

With the basics of the action potential outlined above we can now interpret the above in terms of g_{Na^+} and g_{K^+} and follow some of the conclusions of the Hodgkin Huxely model (Hodgkin and Huxley 1952). The action potential is brought about by transient changes in selective permeability for K^+ and Na^+.

At rest there is a large permeability for K^+ and the membrane potential lies close to V_{K^+}. A depolarisation by a current injection (or a receptor mediated current) is followed by a rapid upstroke of the potential. This is due to an increase in g_{Na^+} driving the potential towards V_{Na^+} and *positive* potentials

(overshoot). With a delay and slower rate of onset an increase in g_{K^+} begins to terminate the action potential and repolarises the membrane.

There follows a time in which no further potential can be elicited (refractory period) and V_m is hyperpolarised. Here the membranes ability to conduct sodium is reduced while g_{K^+} remains high.

We now know that this time-sequence of selective permeability changes is based on the action of different ion channels and their ability to regulate ion flow in response to changes to V_m.

1.2.2 Ion channels and gating

Ion channels are transmembrane proteins that allow the passage of ions across the membrane. The sequence of permeability changes of the whole membrane described in Hodgkin and Huxley (1952) is based on the ability of voltage-dependent K^+- and Na^+-channels to activate (*i.e.* open) in response to a change in V_m. This processes are called gating.

As demonstrated much later with the first high resolution recordings of single-channel currents (Hamill et al. 1981), channels in a membrane will always exist in a mixture of open, (conductive) and closed (non-conductive) states and interconvert between them. Stimuli such as voltage drive these changes and determine the ratio of open and closed channels, the open probability P_o.

For a macroscopic current the P_o can be defined as the fraction of the channels present that are open.

$$P_o = \frac{N_o}{N_o + N_c} \tag{1.4}$$

Here N describes is the number of channels and the subscripts denote their state.

Alternatively, for a single channel we can define P_o by the fraction of time spend in the open state (c_{open}) at equilibrium.

$$P_o = \frac{\sum_i c_{open}}{\sum_i c_{open} + \sum_j c_{closed}} \tag{1.5}$$

With a concept of ion-channels and gating in mind we can rewrite the g term of eq. 1.3. The total conductance is the number of channels N times their single-channel conductance γ scaled by their open probability P_o.

$$I_X = N_{total}\, \gamma\, P_o\, (V - V_X) \tag{1.6}$$

This equation, although reminiscent of Ohms law, will in practice almost never result in a linear relationship of driving force and current. Open probability and γ of a channel are non-linear functions of voltage, ion concentration temperature and a myriad of other variables.

Hodgkin and Huxely summarised the kinetics of g_{K^+} and g_{Na^+} into a set of non-linear expressions able to fully describe the current and voltage changes during the the AP.

The principal mechanism that regulates these currents on short time scales is change in the P_o of these ion channels. The relaxation to equilibrium of a current in response to a step change of a stimulus are a result of these gating events and their study using voltage clamp techniques is one of the key methods of studying ion channels to this day.

1.2.3 The molecular identities of g_X

Much later the main determinants of g_{K^+} and g_{Na^+} were identified as voltage-gated cation channels (VGCC) of the voltage-gated K^+ (K_v) and Na^+ (Na_v) channel families. For a review of these earlier efforts in cloning and identifying voltage gated ion channels see Yellen (2002) and Hille (2001h).

1.2.4 Activation and inactivation of voltage gated channels

Research on the AP of the squid axon showed that the activation process of g_{Na^+} terminates itself. The conductance decays in the presence of a sustained stimulus. This kind of gating behaviour is called inactivation. K_v- and Na_v-channels both inactivate by different mechanisms operating at different rates. The recovery from inactivation of Na_v-channels determines the refractory period. During this time the channels are predominantly closed and the proportion of channels available for activation is insufficient to generate an action potential. An example for such cyclic gating behaviour is given in the scheme of fig. 1.2.

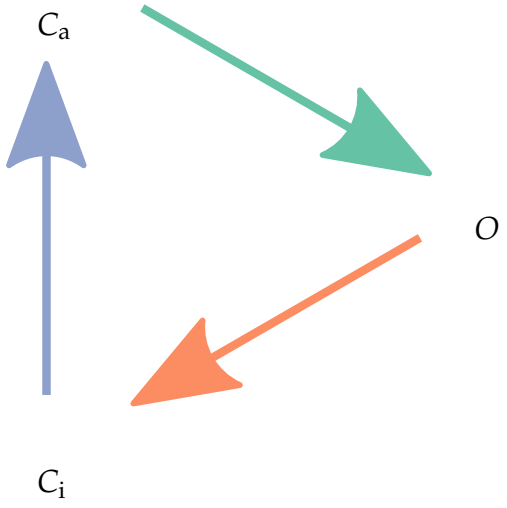


Figure 1.2: *A simple gating cycle* A simple scheme showing the changes that a voltage gated channel undergoes. The channel is in a resting conformation (C_a) and activates in response to voltage (activation, green arrow). From the activated state the channel undergoes inactivation (red arrow) into state C_i. The channel recovers from inactivation at hyperpolarised potentials (blue arrow).

1.2.5 Structural insights from the 'classical' era

A variety of information about the structure of a channel protein can be deduced from electrophysiological data alone. A cartoon model summarising the knowledge of channel structure available previous to the availability of structural data is shown in fig. 1.4. An early, however perhaps coincidental, insight was the modelling of g_{K^+} in the squid axon controlled by *4 gating particles* (Hodgkin and Huxley 1952). We now know that VGCC are tetrameric with 4 voltage sensing domains (VSD) per channel.

A long and narrow pore

Violations of the principle of independence, that means ions do not interact with each other while permeating (Hille 2001f), have been found as early as 1955 using radioactive tracer flux experiments (Hodgkin and Keynes 1955). From these 'long pore effects' it was concluded that K^+ diffuses single file through a long pore, with as many as 3 ions in a queue. A historical review of flux experiments can be found in Miller (1996), here, the interpretation of 'flux exponents' and their role in shedding light on the permeation mechanisms of VGCCs are discussed.

Another physical estimate of channel structure available from electrophysiological measurements is the radius of the pore. This can be established from permeability sequences in bi-ionic conditions. The radius of the narrowest point of the K^+-channel pre was estimated to be 3.3 Å by measurement of bi-ionic potentials (Hille 1973). This requires that K^+ sheds its hydration shell before entering this narrow section, the so called selectivity filter (SF, fig. 1.4).

Additional pre-structural evidence for multiple single-file binding sites in the K^+-channel pore came from Neyton and Miller (1988b) and Neyton and Miller (1988a). In these elegant single-channel studies the block by Ba^{2+}, which binds within the SF. Ba^{2+} competes with K^+ and also can being prevented to exit through adjacent K^+ occupied binding sites ('lock in') Careful quantification of these effects was used to used to establish the number and position of the K^+ binding sites. As a result occupancy of 4 ions per channel was proposed fig. 1.3.

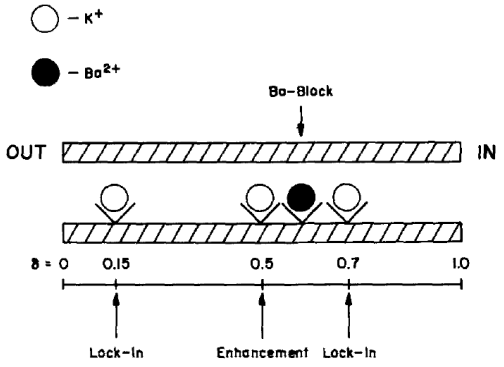


Figure 1.3: *Binding site model of Neyton and Miller* Cartoon model of the binding sites of the K^+ channel from Neyton and Miller (1988b). The scale shows the positions of the sites with respect to the electric field within the channel.

The gating charge

The Hodgkin-Huxley model predicted a movement of charged gating particles that move in response to a change in V_m. The movement of these charges trigger the gates of the voltage-gated channels to open. Such charge movement registers as a gating current precedes the onset of the ionic current. Due to their small relative size, gating currents can only be measured directly in the absence of ionic currents, often achieved by the presence of blockers or the absence of permeating ions (Armstrong and Bezanilla 1973). Gating currents represent the sum of all charges moved during the conformational change of the protein in response to a change to V_m.

An important concept in the analysis of gating currents is the gating charge per channel, that is the number of net elementary charges e_0 moved during the gating transition of one channel. A recent review of the history of the concept of gating currents and gating charge per channel and the methods of determining it has been written by Bezanilla (2018).

For K_v-channels, with most recent methods a value of 10-16 charges per channel can be measured depending on the K_v-channel under study and the measurement method (Noceti 1996; Ishida et al. 2015).

An alternative method to establish gating charge from direct measurements of gating currents, is to analyse the steepness of voltage gating. The distribution of different voltage dependent conformations at equilibrium and as a function of V_m is given by the Boltzmann equation below.

$$P_o\left(V_m\right) = \frac{1}{1 + \exp\left(\frac{w - z_g\, e_0\, V_m}{k_B T}\right)} \tag{1.7}$$

In the case of a strictly voltage gated channel this distribution should be closely related to to P_o. Approximations of P_o at different voltages can be gained from voltage step relaxation experiments by analysis of tail-currents. Fit of this relationships to the above equations yields estimates of z_g as gating charge movement per channel.

The cytoplasmic gate

The general idea that the channel pore can be occluded at the intracellular end had been established by Armstrong (1972). The tetraethylammonium cation (TEA) blocks ion permeation through K^+-channels when applied to either side of the membrane. The intracellular TEA binding site in K_v-channels may

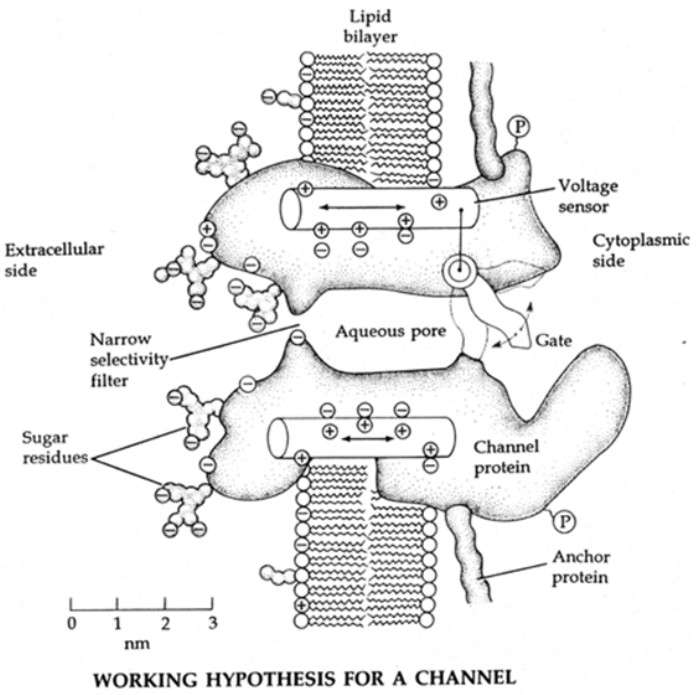


Figure 1.4: *Structural model of a K^+-channel pore* This represents the state of knowledge in the early 1990s, from (taken from Hille 2001h, fig 14). Before the structure of the channel was resolved key features such as the SF as well as the occluding inner gate had been established.

only be accessed when the channel is in its open state (Hille 2001b). When injected with TEA or other quarternary ammonium cations (QA^+), a squid axon membrane will still conduct K^+ on a depolarising step. This current will then decay after the channel has opened. This accessibility of the blocker to its binding site from the open conformation only demonstrated that the closed channel is occluded from the intracellular side (lower gate, fig. 1.4).

1.3 The K^+-leak

In addition to the VGCCs that propagate the action potential, further ionic conductances are required to establish the resting membrane potential, and also to depolarise the membrane to the threshold of Na_v activation that triggers an action potential. Examples of such conductances are inward rectifying K^+-channels (K_{ir}) that account for the strongly hyperpolarised

RMP of cardiac muscle cells and ligand-gated channels such as the nicotinic receptor that depolarise cells in response to neurotransmitter release.

Beyond the g_{K^+} and g_{Na^+} terms the Hodgkin-Huxley models contains an additional 'leak' conductance g_l of unknown ionic provenance. This membrane conductance was much smaller in size and showed no voltage dependence of interest. Due to their more subtle effects on excitability and mixed molecular identity, leak channels are more challenging to study. Thus these leak conductances originally received much less scholarly attention than voltage-gated conductances.

However, there has been a increase in research activity on the 'other' conductances, which has given us structural as well as functional insight into the many different ion channels that g_l consists of.

'Leak' is far from an accurate term for a current through ion-channels, as it suggest a faulty or uncontrolled flow, while such currents are always regulated or gated and often selective for a specific ions. Uncontrolled ion-flow is usually fatal for a cell as it dissipates ionic-gradients that are vital for function. Pore forming toxins or the membrane attack complex of the immune system produce large holes in the membrane that will kill cells by this mechanism.

Furthermore g_l should not be confused with passive membrane leaks which are recording artefacts and not biologically relevant. Passive leak occurs when the small currents flow through a less than perfect gigaseal or the holes in an impaled cell in two electrode voltage clamp. Worse still, is to conflate this with 'GHK-leaks', *i.e.* ion-channel currents that appear to obey the Goldman current equation (Duprat 1997).

Channels that comprise g_l may open in the absence of stimulus, have shallow or absent voltage activation and also do not inactivate. A large

number of Cl^-, K^+, Na^+ as well as non-selective channels are now known that fit this criteria. Because of this diversity it is more accurate to refer to these channels by their selectivity and regulatory profile rather than to categorise them as 'leak' or background channels.

K^+-selective channels with such properties are found in most tissues and K^+ channels of different families may fulfil this role, such as K_{ir} channels or K_v channels of the KCNKQ subfamily. The K_{2P} family of K^+-channels (two pore domain K^+ channels) contains 15 members, also form K^+-selective channels gated by diverse stimuli. Study of TASK (TWIK-related acid sensitive K^+ channel) and TREK (TWIK-related K^+ channel) form the focus of this thesis.

1.4 The K2P channel subfamily

The K_{2P} channels made their first appearance in the scientific literature with the description of a non-inactivating K^+ conductance inhibited by serotonin signalling found in *Aplysia* snail neurons (Klein and Kandel 1980). Alongside further descriptions of similar conductances in primary cell preparations (Kim 1992) the first K_{2P}-channel was cloned (Lesage et al. 1996) and termed TWIK (tandem pore domains in a weak inwardly rectifying K^+-channel).

A large group of channels including VGCCs and ionotropic glutamate receptors share an ancestral gene and have the same overall tetrameric architecture. To form a channel 4 pore domains (PD) consisting of 2 membrane spanning helixes assemble around a central pore axis (Derst and Karschin 1998). A tetrameric channel can be formed from 4 single pore domain containing protein chains (for example K_{ir}, fig. 1.5 left), 2 chains containing 2 PD (K_{2P}, fig. 1.5 right) or even all 4 PD in one chain (Na_v, not pictured).

The K_{2P}-channels can be divided into subfamilies, based on sequence homology. Furthermore K_{2P}-channels have been shown to have the ability to form heterodimers between members of the same family (TREK, TASK and THIK channels Rinné et al. 2015; Lengyel et al. 2016; Blin et al. 2014), as well as between subfamilies (Mi Hwang et al. 2014; Royal et al. 2019; Plant et al. 2012) However, some of the above studies are based on fusion proteins of K_{2P} dimers or GFP tagged channels, which is prone to give artefactual results by aggregation. The gold standard of evidence for heterodimerisation is normally demonstration of a channel with intermediate properties in a native preparation that is known to express both channel transcripts. This has been shown for TASK1/3 heterodimers in multiple tissues. Heterodimerisation greatly increases the diversity and possible number of unique K_{2P}-channels.

In the following section I will introduce all K_{2P}-channel subfamilies along with a short description of their unique biophysical properties and their physiological role:

TWIK family (TWIK 1,2,3) tandem pore domains in a weak inward rectifier K^+ channel. TWIK1 was the first K_{2P}-channel to be cloned (Lesage

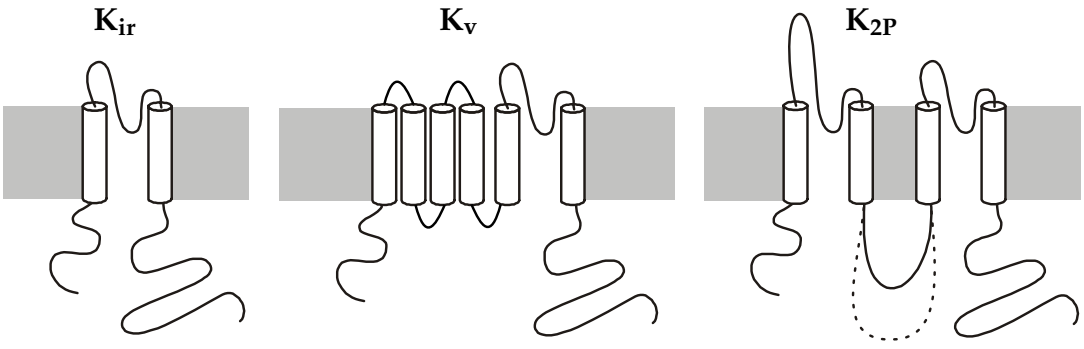


Figure 1.5: *Membrane topology of K^+-channel families* Membrane topology of K_{ir}, K_v and K_{2P}-channels. K_{ir}-channels are formed as a tetramer of 4 pore domains (PD, 1 pictured). K_v-channels comprise of an additional 4 transmembrane helix voltage sensing domain (VSD). K_{2P}-channels are formed as a dimer of protein chains with 2 linked PDs. The first transmembrane helix is elongated and forms a so called cap domain. The TRESK channel contains an extensive linker domain between the first and second PD (dotted line).

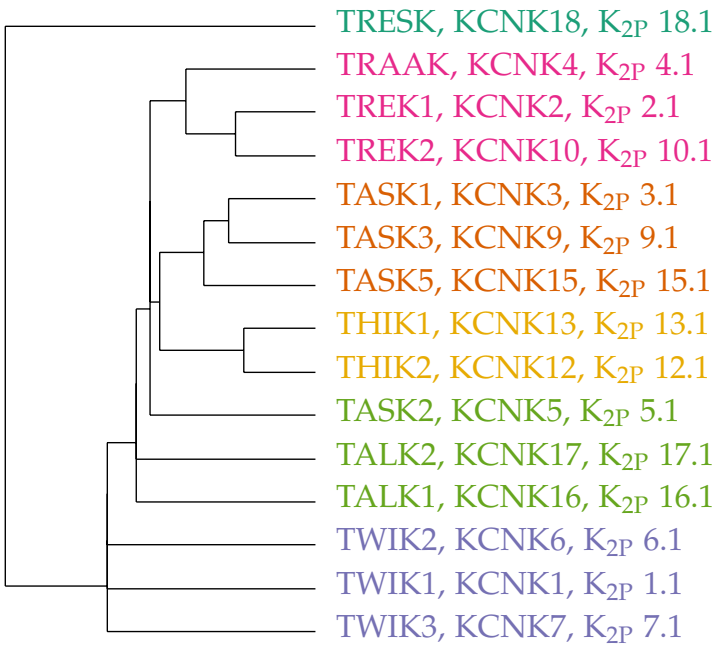


Figure 1.6: *Alignment tree of human K_{2P}* Alignments of all human K_{2P} protein sequences were aligned with the PSI-coffee algorithm (Chang et al. 2012). The tree is based on the BLOSUM score as implemented in JalView (Waterhouse et al. 2009).

et al. 1996). TWIK1 may an intracellular ion channel and its selectivity changes in response to exposure to low pH_{ext} (Feliciangeli et al. 2010; Ma et al. 2011b; Ma et al. 2012b). The physiological role of TWIK is not well known, it may contribute to abnormal depolarisation of cardiomyocytes in hypokalaemia (Ma et al. 2011a). TWIK2 is the only K_{2P}-channel that shows inactivation (Patel et al. 2000).

TASK family (TASK 1,3,5) Tandem pore domain acid sensitive K^+-channels. TASK channels are inhibited by extracellular acidification (Duprat 1997; Rajan et al. 2000). Several high affinity blockers have been developed for TASK channels (Streit et al. 2011; Flaherty et al. 2014). To date, currents of TASK5 have not yet been measured in heterologous expression systems (Ashmole et al. 2001). TASK channels are essential for high speed firing in cerebellar neurons (Brickley et al. 2007), network oscillations governing sleep (Pang et al. 2009), excitability of carotid body cells (Buckler 2015) as well as repolarisation of the heart (Limberg et al. 2011), also see section 1.4.1.

TALK family (TALK1,2, TASK2) TWIK related alkaline pH activated K^+ channel. TALK channel are activated by alkaline external pH (Reyes et al. 1998). TALK channels are constitutively active K^+ channels with important roles in epithelial cell function. They are involved in processes such as volume regulation of kidney epithelial cells (Barriere et al. 2003; Niemeyer et al. 2001) and secretion by enterocytes (Julio-Kalajzić et al. 2018).

Mechanosensitive K_{2P} (TREK1, TREK2, TRAAK) TWIK related K^+-channel and TWIK-related arachidonic acid-stimulated K^+-channel. TREK1 and TREK2 are stimulated by heat, intracellular protons and membrane tension (Patel 1998; Maingret et al. 1999). Extracellular protons activate TREK2 but inhibit TREK1 (Sandoz et al. 2009). TREK channels have a long C-terminal domain that is crucial to integration of these diverse stimuli (Bagriantsev et al. 2011; Bagriantsev et al. 2012). TREK channels are expressed in dorsal root ganglia (DRG) and regulate the excitability of sensory neurons (Alloui et al. 2006). In the central nervous system (CNS) deletion of TREK1 is associated with resistance to depression suggesting an involvement of the channel in perceptions of mood (Heurteaux et al. 2006), see also section 1.4.2.

TRESK family TWIK-related spinal cord K^+-channel. TRESK has a unique linker domain between the two PDs (fig. 1.5). This domain binds calmodulin and confers activation by intracellular Ca^{2+} (Czirják et al. 2004). TRESK is expressed in sensory neurons of dorsal root and trigeminal ganglia and involved in sensing various modes of painful stimuli. (Kang and Kim 2006).

THIK family (THIK1, THIK2) Tandem pore domain halothane inhibited K^+ channel. Contrary to other K_{2P} channels, THIK channels are inhibited

by volatile anaesthetics (Rajan et al. 2001). THIK2 is not functional in the plasma membrane and arrested in the endoplasmatic reticulum (ER) but may traffic to the membrane coassembled with THIK1 or by removal of its ER retention motif (Chatelain et al. 2013; Renigunta et al. 2014; Blin et al. 2014). THIK1 channels set the RMP of microglia and regulate their pattern of motility (Madry et al. 2018).

K_{2P} channels are expressed in almost every organ and tissue and coining a concise 'role' describing the function of all 15 channels is no longer possible or appropriate given the great increase to our knowledge into the diverse physiological processes they regulate. Instead I will give a brief introduction of TASK and TREK channel physiology (TASK1 and TREK2 in particular) that form the context of this pharmacological and biophysical project. The structure function and regulation of K_{2P} channels will be discussed in section 1.6 after giving an introduction to the general themes of K^+ channel biophysics in section 1.5

1.4.1 Physiology and pharmacology of TASK channels

TASK1 is found in the atria of human hearts where it is a major component of persistent outward current that shapes the repolarisation phase of the cardiac AP (Limberg et al. 2011). Knock-out models in mice showed cardiac phenotypes with a prolonged QT inverval (Decher et al. 2011), a common hallmark of many cardiac K^+ channelopathies (Bohnen et al. 2017). The bulk of the TASK current in human atrial cardiomyocytes appears to be carried by TASK1/3 heterodimers (Rinné et al. 2015). In knock-out models of TASK1

function is maintained by TASK3 homodimers in TASK3 co-expressing tissues (Aller 2005).

TASK channels are expressed in numerous neuronal cell types of the CNS for example in cerebellar granule neurons (Millar et al. 2000). They enable these neurons to fire at high frequencies due to their unique voltage-gating properties (Brickley et al. 2007). TASK3 is expressed in the developing brain (Zanzouri et al. 2006) and a loss of function mutation has been identified that confers the Birk-Barel syndrome, which includes mental retardation, facial deformities and abnormal hair growth among its symptoms (Barel et al. 2008). Interestingly TASK3 knock-out mice shown abnormalities in their sleeping patterns (Pang et al. 2009), this is likely controlled by TASK and TREK channels controlling the excitability in circuits of the thalamus that regulate wakefulness and sleep (Bista et al. 2015).

The specialised Type1 cells of the arterial oxygen sensing carotid body also express TASK channels. Their conductance keeps their membrane potentials hyperpolarised. Through the action of a yet undetermined oxygen sensor, TASK channels close to trigger neurotransmitter release. This feeds back information on blood pH and oxygen content to regulatory centres of the brain stem. (Buckler 2015). This oxygen sensing mechanism of the carotid body is essential for breathing regulation and TASK1 knock out mice show abnormalities in this function (Trapp et al. 2008).

TASK channels can be also found in the adrenal gland and similarly contribute to the secretion of adrenal hormones. Knock-out of TASK channels in the adrenal gland is associated with an aldosterone driven hypertension phenotype (Guagliardo et al. 2019; Davies et al. 2008).

In addition to these roles in hormone secreting and regulatory tissues TASK channels influence blood pressure directly in smooth muscle cells of

pulmonary arteries (Gurney et al. 2003). Decreased activity of K^+ channels depolarises vascular smooth muscle cells which results in increased tone and vasoconstriction (Boucherat et al. 2015). TASK1 contributes to setting the RMP of these cells and influences vascular tone of pulmonary arterties via this mechanism. Therefore, activation of TASK1 in pulmonary artery smooth muscle is a possible treatment strategy for pulmonary arterial hypertension (PAH), a fatal disease which is characterised by constriction and subsequent remodelling of pulmonary arteries.

Several mutations in TASK1 that result in loss-of-function are associated with hereditary forms of PAH (Ma et al. 2013). Functional defects in these mutated channels can be severe and irrecoverable (for example G106R, Cunningham et al. 2019).

Known blockers and activators of TASK channels

Due to their prominent role in cardiac and respiratory physiology, TASK channels are an attractive target to treat a number of related diseases. Among K_{2P} channels TASK channels are the only ones for which highly selective blockers are currently available. The compounds A1899 (Streit et al. 2011), ML365 (Zou et al. 2010) as well as BAY-1000493 and BAY-2341237 (Rödström et al. 2019) block TASK chanels with nanomolar affinity. Trials are underway to exploit TASK blockers to treat atrial fibrillation or sleep apnea (Rödström et al. 2019).

Various lower affinity blockers of TASK channels are also known, some of which deserve our attention for giving insights into structure and function of TASK channels through their mechanism of action. The cannabidoid anandimide blocks TASK (Maingret 2001) in a mechanism that involves the

halothane response element (HRE), a structure of the distal M4 helix (see also section 1.6.3, Veale et al. 2007a). Recently, bupivacaine has been shown to reduce the time dependent component of TASK channels by affecting TASK voltage gating (Rinné et al. 2019).

A modulator of K_{2P} channels and TASK3 in particular has already been put to prominent use in daily clinical practice. Halothane and other more contemporary volatile anaesthetics activate K_{2P} channels (Patel et al. 1999). This activatory effect is mediated by the HRE (Talley and Bayliss 2002). TASK3, like most K_{2P} channels can also be activated by flufenamic acid (FFA Veale et al. 2014b). FFA can rescue function of the G236R loss of function mutant of TASK3.

1.4.2 Physiology and pharmacology of TREK channels

TREK channels are expressed in a variety of the diverse sensory neuron types of the DRG. TREK currents are a major component of DRG neuron background current and contribute to regulating their excitability (Alloui et al. 2006). TREK channels are regulated by a variety of stimuli that may contribute to function in these sensory neurons. TREK channels respond to membrane stretch, extracellular and intracellular pH, temperature and PKA phosphorylation (see section 1.6.2 Patel 1998).

TREK1 and TREK2 are co-expressed in many tissues, particularly throughout the central nervous system (see below) but unique sites of TREK2 expression can be also found in the periphery such as in the kidney (Medhurst et al. 2001). Like TASK channels, TREK is also expressed in rat hearts (Kim 1992; Niu and Sachs 2003). Here it contributes to repolarisation controlled by

β-adrenergic stimulation (Bodnár et al. 2015). TREK1 contributes to setting the muscle tone of bladder (Lei et al. 2014).

In the CNS TREK channels control blood flow by controlling vascular smooth muscle tone (Blondeau et al. 2007). TREK channels are also expressed in astrocytes (Gnatenco et al. 2002) and brain vessel endothelium (Bittner et al. 2014). TREK1 knockout mice show a resistance to mood related phenotypes (Heurteaux et al. 2006) but the precise relation of such CNS pathologies to TREK expression in these diverse CNS tissues has not yet been clarified.

Known blockers and activators of TREK channels

The antidepressant fluoxetine and its derivative nor-fluoxetine block TREK channels (Kennard et al. 2005). The state dependence of block by these compounds was pivotal to annotate the crystal structures of TREK2 (see section 1.6.2, Dong et al. 2009; McClenaghan et al. 2016). Carvediol also blocks TREK in a state dependent manner (Kisselbach et al. 2014) suggestive of a similar mechanism (McClenaghan 2015).

TREK activators are candidates for novel analgesics; salient compounds and their putative mechanisms are introduced in chapter 4.

1.4.3 Gating and structure of K_{2P}

The structures of several K_{2P} channels have been solved with x-ray crystallography (Miller and Long 2012; Brohawn et al. 2012; Dong et al. 2015; Lolicato et al. 2017). Their structural properties will be dealt with in section 1.6.1.

K2P behaviour in classical blocker trapping experiments

TREK and TRAAK structures have been captured with varying degrees of splaying of their pore helices (Lolicato et al. 2014; Dong et al. 2015). There was no apparent physical obstruction of the ion conduction pathway in any of these structures. Although the pore is open, there is controversy about the annotation of these structures as conductive or non-conductive.

TREK1 channels remain accessible to intracellular TEA or other quaternary ammonium compounds (QA^+) while they are closed by an alkaline internal milieu (Piechotta et al. 2011). There is also no difference in accessibility between channels in a relaxed or stretched membrane (Aryal et al. 2017). TRESK has been shown to behave in a similar fashion with regard to its Ca^{2+}-dependent gating (Lengyel et al. 2018). Instead, these K_{2P} channels are thought to gate at the SF without a lower gate.

The SF is emerging as the principal gate in a number of other K^+ channels (Posson et al. 2013; Posson et al. 2015; Heer et al. 2017; Rauh et al. 2017). Gating via this mechanism is also thought to underlie the well researched inactivation processes in K_v channels (C-type inactivation, reviewed in Hoshi and Armstrong 2013). Therefore I will first introduce the general themes of the molecular biophysics of K^+ channel gating cycles as established in tetrameric K^+ channels (mainly KcsA) before expanding on multi-modal gating of K_{2P} channels.

1.5 Canonical tetrameric K^+ channels

The seminal publication by Doyle et al. (1998) of a structure of the bacterial K^+ channel KcsA marked a transition in the field of ion channel research and

was awarded with a Nobel prize for Roderick MacKinnon in 2003. With the structure of a K^+ channel at hand it was now possible to probe and directly test predictions of channel structure inferred from functional data such as pore radii (Hille 1973), as well as guide mutagenesis and drug discovery in functional experiments. The structure with its most important features is shown in fig. 1.7.

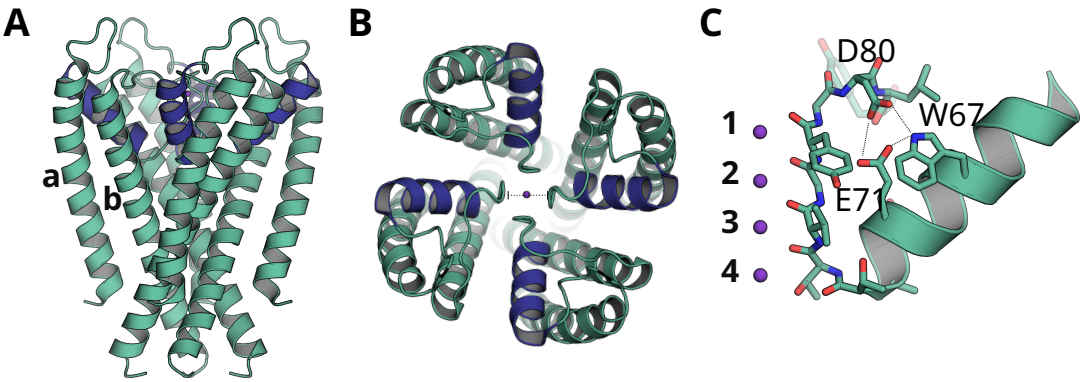


Figure 1.7: *Structure of KcsA* A: Lateral view of the KcsA channel. The 4 pore helices (dark blue) form a basket-like structure, which is supported by the inner (b) and outer (a) transmembrane helices. The structure is closed at the bottom by a crossing of the inner helices (helix-bundle-crossing). B: top view, the tetrameric channel shows four-fold symmetry around the pore-axis with a 3 Å radius. C: lateral view of the SF, 4 ions are bound along sites S1-4. Residues of the SF of one subunit (TTVGYGD sequence) as well as crucial residues of the inactivation network (section 1.5.3) are shown in stick representation.

1.5.1 Structure of a tetrameric K^+ channel

The 4 pore domains of a tetrameric channel assemble into a complex with fourfold symmetry (fig. 1.7B). The membrane spanning helices enclose the basket like pore helices and SF loops (fig. 1.7A), they cross the membrane obliquely and converge at their tip, the helix bundle crossing (HBC).

The selectivity filter region is 3Å wide. This is insufficient for the permeation of anything larger than K^+ stripped of of its hydration shell. These 'naked' K^+ can be found in single file within 4 binding sites formed by the

conserved sequence TTVGYGD, numbered S1 to 4 from the extracellular side (fig. 1.7C). The selectivity filter residues orient with their backbone carbonyl groups pointing into the permeation pathway. Their arrangement with 8 fold coordination by oxygen atoms mirrors the chemistry of K^+ coordination (Morais-Cabral et al. 2001) and hydration shells. The SF can be thought of as a water mimetic pore in which the carbonyl groups replace the hydration shell of K^+. The requirement for dehydration is an energetic barrier for the conduction of Na^+ and Li^+ ions that require larger energies to strip their hydration shells (Hille 2001c). This is one of the mechanisms of excluding Na^+ entry to maintain selective permeability (see section 1.5.4).

Additionally, the structure itself aids in cation conductance. The dipoles of the pore helices are arranged in such a way that they generate a negative electrostatic potential. This biases the cavity of the channel below the SF to be preferably occupied by cations, thus in addition to the selectivity filter itself the pore may contribute to selectivity and conduction (Roux 1999).

1.5.2 The gating cycle of KcsA

Following this breakthrough, detailed functional characterisation of KcsA followed. However, its low open probability and difficulty in reconstitution into model bilayers slowed progress. At last the Chris Miller's lab achieved to record single-channel currents of KcsA with conventional electrophysiological methods (Heginbotham et al. 1998; Heginbotham et al. 1999; LeMasurier et al. 2001). It was shown that functional hallmarks of eukaryotic K^+ channel function (such as permeability sequences, saturation behaviour) were conserved in KcsA.

In physiological conditions KcsA remains closed. Small KcsA currents can be can be recorded in pH <5.5 but P_o remains low (<10%). This riddle of low P_o was solved by Cordero-Morales et al. (2006). In non-stationary conditions (step changes in pH_{int}) KcsA responds with a current transient. Currents then inactivate to result in the low steady state P_o within few seconds. Spectroscopy and mutagenesis results supported that the HBC remains open while the current decays. Instead, the decline of P_o is determined by an inactivation process involving the selectivity filter.

Mutagenesis and further functional studies link KcsA inactivation gating with so called C-type inactivation in K_v channels. A careful and comprehensive characterisation of KcsA gating processes by Chakrapani et al. (2007a) followed. Inactivated (Zhou et al. 2001; Cuello et al. 2010a; Cuello et al. 2010b) and open conductive (Cuello et al. 2017) conformations of KcsA were crystallised and functionally annotated making KcsA one of the best mechanistically studied and understood ion channels. A cartoon summarising the gating cylce is shown in fig. 1.8.

Activation gating

Opening of the HBC is initiated by a proton binding event (fig. 1.8 step a). An intracellular histidine residue at the bundle crossing (H25) reduces pH sensing capability of KcsA and the coupling of pH to structural rearrangements as shown by NMR (Takeuchi et al. 2007). Functional studies, however, failed to assign a single pH sensing residue for activation gating (Posson et al. 2013) and a complex network of interactions may be involved.

Spectroscopy results suggested a movement of the intracellular helices resulting in the opening of the helix bundle crossing and an enlargement

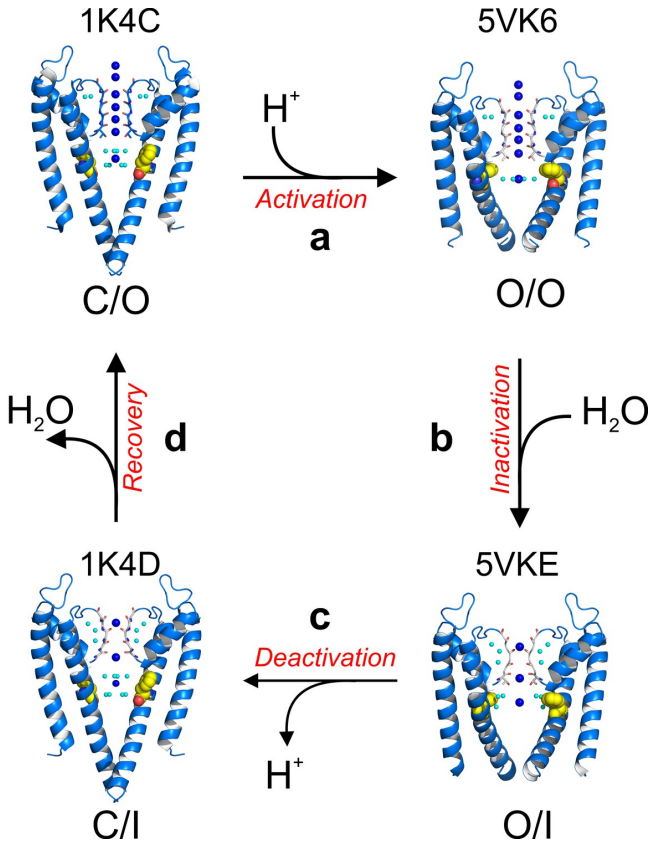


Figure 1.8: *Gating cycle of KcsA* Starting from top left: the HBC is closed and the SF primed for conduction (C/O), a proton binding event (a) then leads to a gradual opening the HBC (O/O). Clash of F103 (yellow) with T75 of the SF results in a propagating disturbation of the SF 'bowspring'. This results in a conformational change of the filter (b) that is pinched lost the S2 and 3 binding sites (O/I). In the absence of the stimulus the HBC returns to its resting position (c, C/I). The channel recovers to a functional SF structure (d, C/O), this process is weakly voltage dependent and requires exit of a water molecule embedded behind the inactivated SF. Taken from Cuello et al. (2017).

of the intracellular cavity of the channel (Perozo et al. 1998; Liu et al. 2001; Perozo et al. 1999). This behaviour is mirrored in a series of crystal structures resolved from identical trials (Cuello et al. 2010b) that captured the proposed changes to the cavity and the underlying motions of the pore lining helices. The bending of the inner membrane spanning helix (M2) that is required for the opening and closing of the HBC is enabled by a flexible region around a conserved glycine G104 ('glycine hinge'). The glycine hinge can be found in the inner helices of almost all K^+ channels including M4 and M2 of K_{2P} channels.

A recent study suggests that splaying of the HBC of KcsA is not sufficient to open the channel (Heer et al. 2017). A 1 Å dilation of the bottom of the selectivity filter is also required for conduction. This dilation is coupled to the movements of the outer transmembrane helices during activation gating. This

idea assigns only secondary importance to the HBC as a gate, rather Heer et al. suggest that in all K^+ channels movements in the pore lining helices couple to a SF gate but that the occlusion associated with this movements in channels with a HBC is an additional feature. Also, this suggests a closed SF structure (C/C) for the resting state with all binding sites intact (fig. 1.8a).

Inactivation gating

Residues that form part of an interaction network of pore helix and selectivity filter loop residues (TTVGYGD) and a water molecule wedged between these structures (Cuello et al. 2017) are crucial for the inactivation of KcsA. These are shown for a few key K^+ channels in the alignment of fig. 1.9A. Study of these sites was key for our understanding of inactivation in K^+ channels in general. Mutation of E71 to alanine in the SF supporting pore-helix results in slow and incomplete inactivation, whereas mutation of Y82 to alanine at the external mouth results in quick and near total closure following activation (Cordero-Morales et al. 2006).

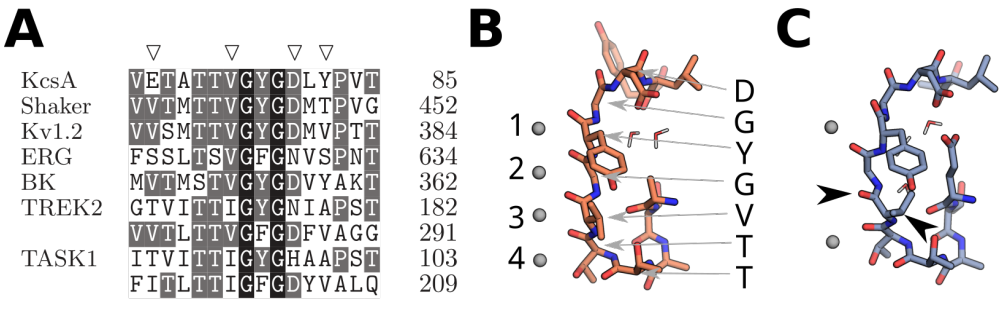


Figure 1.9: *Structural basis of KcsA inactivation* A: Sequence alignments of model K^+ channel and TREK2 and TASK1 selectivity filters (there is one SF sequence for each PD in K_{2P}). B: presumed open (5VK6, E71A mutation) and inactivated (5VKE, Y82A mutation) KcsA structures (C, Cuello et al. 2017). Movements of V76 and G77 shift the coordinating backbone carbonyl away from the pore axis and remove binding sites S2 and 3 (arrow).

Inactivation begins when the interaction network is perturbed through steric clashes of F103 of the inner pore helix (fig. 1.8) with T75 of the SF loop upon splaying of the HBC (Cuello et al. 2010a). This perturbation spreads throughput the SF and results in the loss of 2 consecutive binding sites (S2 and S3) and a pinch of the permeation pathway at G77 (fig. 1.9C).

The interaction supporting the SF (fig. 1.7 and fig. 1.9) is inherently unstable and prone to collapse when unrestrained by HBC opening. Strength and stability of this interaction network and therefore inactivation are tunable by mutagenesis (Cordero-Morales et al. 2007). This idea of a 'molecular bowstring' behind the SF has been translated to K_v (Pless et al. 2013) and K_{ir} (Dibb et al. 2003; Yang et al. 1997a) channels and may be a general feature of these channels.

Deactivation gating and repriming

The HBC of KcsA closes state in the presence of alkaline pH_{int} (fig. 1.8c). The inactivated state of the SF requires an additional water molecule for stabilisation (Cuello et al. 2017). Removal of this 'inactivation water' is obligatory for recovery from inactivation. Water access to the network behind the SF changes the speed of inactivation gating (Ostmeyer et al. 2013). The entranceway for water into the cavity behind the SF is narrowed by Y82. The Y82A mutation allows easy access of inactivation waters to the cavity behind the SF stabilising the pinched state and increasing the rate of inactivation (Cuello et al. 2017).

Additionally recovery from inactivation is favoured at depolarised voltages. This is the cause for the observed weak voltage-dependence of KcsA steady-state P_o. Inactivation may occur through at least two pathways, one involving

inactivation from the activated conducting channel, one from pre-open or deactivated states (Chakrapani et al. 2007a).

1.5.3 C-type inactivation and the filter gate

Some K_v channels inactivate with an inactivation particle located at their N-terminus. This particle occludes the permeation pathway following channel opening. This is called the 'ball and chain' mechanism or N-type inactivation.

However, in the absence of the N-terminus in truncated channel proteins a much slower inactivation process persists. This was called C-type inactivation, as it was thought to arise from the C-terminal end of the protein. C-type inactivation proceeds on a slower timescale than N-type inactivation which completes in few ms (Hoshi et al. 1991).

To not get confused (see below), I will use C-type inactivation as defined in Pau et al. (2017):

> "Herein, we adopt the following operational definition of C-type inactivation, which is based primarily on the original studies of Aldrich and colleagues (Hoshi et al. 1991; López-Barneo et al. 1993). C-type inactivation reflects a nonconducting state that occurs even in the absence of N-type inactivation, exhibits an apparent *dependence on activation gating*, is *allosterically influenced by the conformation of S6* [inner pore lining helices, M2 and M4 in K_{2P} channels] and primarily *involves changes in the extracellular part of the K^+-selective filter*. Because C-type inactivation is affected by many mutations around the selectivity filter itself and in S6 (Hoshi et al. 1991; López-Barneo et al. 1993; Yang et al. 1997b), it is

likely to be a common functional manifestation of multiple forms of the channel's overall structure"

An additional hallmark of C-type inactivation is that its rate is dependent on $[K^+]_{ext}$, with low K^+ concentrations favouring inactivation (Baukrowitz and Yellen 1995; Starkus et al. 1997). This fact is suggestive of the involvement of the extracellular mouth of the pore.

While the properties of C-type inactivation have been studied in great detail in K_v channels, especially so Shaker, few structures of K_v have been captured (Long 2005). Controversy about relating structures of 'pinched' KcsA channels (with little change to the extracellular mouth) to observed K_v inactivation therefore persist (Hoshi and Armstrong 2013), especially in relation to structures and inactivation processes captured in low or absent K^+_{ext} (defunct states, Zhou et al. 2001; Melishchuk et al. 1998; Loboda et al. 2001).

K_v channels may dilate and become permeable to Na^+ during inactivation in the absence of K^+ (Starkus et al. 1997; Kiss et al. 1999). Some Na^+ permeable 'dilated' states can recover selectivity through brief exposure to K^+ and depolarised potentials (Loboda et al. 2001). The dilated state is likely an intermediate in a transition from the inactivated to a defunct state.

Before being placed in the context of the gating cycle fig. 1.8, the pinched state of KcsA was captured in low K^+ concentration (Zhou and MacKinnon 2003). Therefore, it has been assumed that the pinched state is equivalent to the defunct state of K_v. However, slowly inactivating KcsA E71A channels do not enter the pinched state in the absence of K^+. Instead they adopt an alternative, conducting SF conformation with D80 rotated outward ('flipped'), and a reduced occupancy for K^+ in the S1 binding site. This structure has

been captured by separate groups in different conditions (Cheng et al. 2011; Cordero-Morales et al. 2006). MthK (*Methanothermobacter thermautotrophicus* K^+ channel) also does not pinch in the absence of K^+ (Ye et al. 2010). Therefore different K^+ channels behave may show distinct responses to being challenged by low $[K^+]_{ext}$ and structures captured in such conditions need not be equivalent.

The above definition holds for the structures and functional phenomena that were annotated as C-type inactivation in KcsA (as outlined in section 1.5.1). Convincingly, mutations that affect KcsA inactivation processes find their equivalent in Shaker and other K_v channels (Molina et al. 1997; López-Barneo et al. 1993; Perozo et al. 1993). K^+_{ext} too slows inactivation rates in KcsA (Chakrapani et al. 2007a).

With the recently completed full cycle of structures along the KcsA gating cycle (Cuello et al. 2017, fig. 1.8) and the open inactivated structure contained in it, there seems to be little reason to still assume that these structures represent functionally irrelevant K^+ depleted states. It could be shown that the inactivated structures captured through mutagenesis and cross-linking of the intracellular gate is equivalent in its SF conformation to the structure captured in low K^+ (Zhou et al. 2001).

In rationalising the differences and disagreements we need to remind ourselves that KcsA is only distantly related to mammalian K_v channels, while some hallmarks of the inactivation process are remarkably conserved, their precise structural basis may not. Alternatively, crystal structures may just have captured different intermediates of a similar process.

1.5.4 Selective permeability

Preventing Na^+ entry into the cell upon channel opening is one the principal requirements for a K^+ channel to fulfil its function. The K^+ channel paradoxically enables transport at rates close to the limit imposed by diffusion, while tightly excluding extracellular Na^+. This property is commonly referred to as ion selectivity in K^+ channels.

Preference or selectivity for transport of one ion species can be defined by different terms. We may say a binding site is selective if it binds one ion preferably in the presence of another in equilibrium (as determined with various methods, reviewed in, Lockless 2015). Selective binding may not translate to selective permeation though, as in the example of the Ba^{2+} or Na^+ ion, binding ions may permeate so slowly that they effectively block current through K^+ channels (Neyton and Miller 1988b; Nimigean and Miller 2002).

We can also define ion-selectivity as having the larger unitary conductance (rate of transport through the open channel) between some different tested ions, however, this might pose problems as integrity of ion channel structures may depend on occupancy of their physiologically permeant ion (see section 1.5.3) and yield aberrant results.

The most physiological relevant aspect of selectivity is the ability to transport only one ion-species in the presence of others. A measurable quantity of this property is the permeability ratio based on reversal potentials as defined by eq. 1.2. This equation, however assumes diffusion through the membrane of ions moving independent of each other (see section 1.2.5). Despite this simplification the GHK-voltage equation has an excellent track record of providing robust quantifications of selectivity (Alvarez and Latorre 2017).

Layers of selectivity

Several mechanisms and explanations for ion selectivity have been brought forward over time, few fit the complexities of the K^+ channel field entirely. Instead multiple ways of enabling selective transport and excluding other ions work together to bring about the seemingly paradoxically efficient selective transport of K^+ channels. I will briefly outline some of these *layers of selectivity* before summarising the presently emerging concept of kinetic selectivity which unites permeation, selectivity and gating by looking at the dynamics selectivity filter occupancy.

Molecular sieve A particle may not permeate a pore that has a smaller radius than itself. This truism does not explain how smaller ions may be excluded. This 'molecular sieve' idea was important to estimate lower bounds for the opening of several ion channels in the absence of structural information (for example Hille 1973).

Coordination, hydration and snug fit The size constraints of the SF (3.3 Å radius, Hille 1973) necessitate shedding of the hydration layer of the ion prior to entry. This penalises Na^+ permeability as the hydration energy ($-105\,\mathrm{kcal\,mol^{-1}}$) is larger than of the K^+ ion ($-85\,\mathrm{kcal\,mol^{-1}}$). The same is true for other small ions such as Li^+ ($-131\,\mathrm{kcal\,mol^{-1}}$ Hille 2001d).

Additionally the SF is uniquely fit to accept K^+. The size and spacing of the binding sites, as well as the number of carbonyl groups coordinating the ion match the preferred behaviour of K^+ in water (Zhou et al. 2001; Morais-Cabral et al. 2001). Na^+ ions however differ only slightly in their ionic radius (0.38 Å Hille 2001c) and may be accommodated into some K^+ channel SFs (Ye et al. 2010).

Electrostatics The cavity of the K^+ channel favours occupancy by monovalent cations by a concentration of negative charge (Roux 1999). Electrophysiologically this cavity ion binding site has been demonstrated to have a weak binding preference for K^+ over Na^+ (Neyton and Miller 1988b; Neyton and Miller 1988a).

Additionally the tight fit and coordination geometry has been proposed to rely on the precise electrostatic properties of the SF residues (Noskov et al. 2004).

Binding sites and occupancy Single sites may fail to distinguish between ions that have similar sizes but a series of precisely spaced sites is suitable to the task. An ion with a slightly larger radius may bind a single site, but its ionic radius may overlap with adjacent sites and make their filling less probable. Na^+ ions bind the SF at an alternative site between S4 and S3 ('B' sites, Thompson et al. 2009; Ye et al. 2010; Zhou et al. 2001). In order to maintain binding to multiple sites they must be occupied by ions that register *exactly* and do not overlap with adjacent sites. Ions of inappropriate size cause a 'register shift' that fails to maintain steady occupancy and conduction (Zhou and MacKinnon 2003), the channels are optimized to bind a *queue* of K^+ rather than one ion alone. Thus selectivity emerges out of the binding patterns of multiple ions and their correlated movements.

The interpretation of crystal structures with respect to ion occupancy may yield diverging results and has resulted in controversies surrounding the entwined selectivity and permeation mechanisms (see p. 36ff).

Non-selective conduction through SFs

The NaK channel from *Bacillus Cereus* contains a unique degenerate SF sequence that renders all but the innermost K^+ binding sites defunct (Shi et al. 2006). It conducts Na^+ and K^+ equally well.

Interestingly, all binding sites as well as selective permeability can be restored by mutating the channel to have all 4 binding sites (then so called NaK2K, Derebe et al. 2011b). This demonstrates the importance of the outer binding sites for selectivity and confirmed an additional role for the 'molecular bowstring' (Dibb et al. 2003) in maintaining a selective SF structure by stabilising these sites.

NaK channels as well as selective mutants show K^+-selectivity as measured by equilibrium binding (Liu and Lockless 2013). These results highlight that models of selectivity need to take our knowledge of channel structures and ion binding sites into account (Hille 2001g) and that a 'kinetic' view is necessary to explain selective permeability. The number of the sites alone cannot explain selectivity.

Controversies surrounding permeation

The permeation through the K^+ channel pore may occur at rates close to the diffusion limit, major energy barriers for conduction of ion may not exist for this 'frictionless' movement.

Hodgkin and Keynes found evidence for a long pore with flux coupling in K^+ channels of the squid axon. Ions cannot pass each other in a queue within a long pore. Here the idea of a Coulomb knock-on mechanism for conduction was first formulated. This mechanism involves the ions queued

in the pore. Entry of a further ion moves the queue onward by electrostatic repulsion, where each ion 'knocks' the next out of its position.

Indeed, electron densities from crystal structures of KcsA showed K^+ occupancy along 4 sites with equal amplitude Zhou et al. (2001). However, this represents a weighted average of all the molecules present in the crystal. A mechanistic interpretation of such data was brought forward by Morais-Cabral et al. (2001). 'Frictionless' K^+ permeation was proposed to occur by cycling through 2 different SF occupancy patterns—so called 1-3 and 2-4 with waters in the unoccupied binding sites (`K1 W2 K3 W4` (1-3)$\longleftrightarrow$ `W1 K2 W3 K4`(2-4)).

Molecular dynamics (MD) simulations were used to annotate filter structures and propose permeation mechanisms. In agreement with the cycling mechanism, Bernèche and Roux (2001) found frictionless permeation and water co-permeation.

An alternative incompatible mechanism was put forward by Kopfer et al. (2014). In this study MD simulations were used in a computational electrophysiology configuration which allows spontaneous K^+ permeation in the presence of strong simulated electric fields (200 mV). Permeation only occurred with occupancy of *all 4* sites and ions were observed to move by direct Coulombic knock-on without interleaved water molecules.

This model was then contested by Kratochvil et al. (2016). Infrared (IR) spectroscopy conducted on synthetic, labelled KcsA protein yielded spectra corresponding to a mixture of SF occupancy patterns and conformational states (Kratochvil et al. 2016). These data were interpreted to be incompatible with the occurrence of hard knock-on by correlation with spectra computed from MD simulations. A follow up study additionally found a discrepancy between SF pinched conformations of inactivated KcsA and KcsA in low K^+

concentration (Kratochvil et al. 2017), that was at odds with the available crystal structures (Cuello et al. 2017).

Recently, another comprehensive MD treatment (Kopec et al. 2018) has reproduced the findings of Kopfer et al. (2014) in a range of Na^+ and K^+ mixtures with selective and non-selective (NaK derived) channels. They find that conduction at appreciable rate occurs only with direct knock-on and that water co-permeation is associated with low conduction rates and loss of selective transport.

Selectivity here is thought to arise from a combination of the penalty of dehydrating Na^+preventing entry and the failure of Na^+ binding in the 2,3-B-site to effectively 'knock' ion queues forward.

Independent replication of anomalous diffraction experiments similar to that of Zhou and MacKinnon (2003) in NaK2K came to the opposite conclusion that the filter is occupied by 4 ions at the time in the presence of 100 mM KCl (Langan et al. 2018). Also, recent NMR data are inconsistent with any water occupancy in the SF of NaK2K (Öster et al. 2019).

A crystallographic study in disagreement with Kopec et al. (2018) demonstrated that 4 binding sites are not necessary for selective conduction and that, as expected, for the cycling model that occupancy of site 1 and 3 are coupled in favour of the 2 occupancy cycling model (Tilegenova et al. 2019).

The full gamut of spectroscopic, computational and functional methods available at present has been applied to the bacterial ion channels NaK and KcsA. The high quality data obtained from these studies leave too much room for interpretation to give a definitive answer to this detailed question about SF occupancy.

Permeation and the cavity

In addition to influencing the rate of permeation, the cavity may also contribute to selectivity . Commonly, the pore of K^+ channels is assumed to be equivalent to the intracellular bulk solution. The voltage drop and resistance for permeation has been attributed to the SF alone as calculated with a continuum electrostatic approach (Jiang et al. 2002). Such calculations assume average bulk properties for the surrounding protein its media and thus model charges in a simplified way (for a comparison of continuum electrostatics to other approaches see Miller 1999).

However, assessment of this 'voltage drop' comes to different conclusions. K^+ channels may have a wide range of single channel conductances (10 pS to 300 pS) despite having near identical SF filter sequences, consequently another part of the structure must contribute to the resistance of the pore. The intracellular vestibule size and charge is a major determinant of unitary conductance in BK (big K^+ channel) channels (Brelidze and Magleby 2005; Brelidze et al. 2003). This effect can be replicated in other K^+ channels (Nimigean and Allen 2011; Moscoso et al. 2012) and the cavity may contribute to as much as a third of the voltage drop in K_v channels that have a small conductance (Diaz-Franulic et al. 2015).

In good agreement, the innermost Ba^{2+} 'lock in' site of the K^+ channel (fig. 1.3) lies one third into the electric field as seen from the inside (Neyton and Miller 1988a). A crystal structure of Ba^{2+} in KcsA suggests that the Ba^{2+} binding site is S4, placing the lock-in site in the cavity (Jiang and MacKinnon 2000).

Interestingly the cavity has a weak preference for K^+ over Na^+ and an elevated local concentration for K^+ compared to bulk solution (Neyton and

Miller 1988b; Zhou and MacKinnon 2004). Also selectivity of the defective $K_{ir}3.2$ mutant S177W could be restored by mutation of pore lining residues (Bichet et al. 2006) demonstrating a role of the cavity in selectivity in some channels.

Structure and 'flickery' gating

C-type inactivation events at the SF are observed on a long timescale ($\sim$1 s Hoshi et al. 1991). KcsA E71A (imparied inactivation) as well as activated KcsA WT currents show signs of additional SF gating events on a short time scale in single channel recordings (Chakrapani et al. 2011) Similar behaviour can also be found in mutant K_{ATP} channels (ATP-sensitive K^+ channels, Proks et al. 2001). In KcsA several distinct *modes* of the behaviour within a burst are apparent while the activation gate is open (Chakrapani et al. 2007a). Accordingly, SF gating may occur at different timescales and a simple and direct relationship of timescale of gating and structure (eg. lower gates being fast, SF gates being slow) does not hold.

Several explanations for fast gating have been brought forward. Firstly, in MD simulations single carbonyl groups of the SF may rotate out of the pore axis for very short periods of time (Bernèche and Roux 2005). This is expected to briefly perturb the binding site. Carbonyl flip is too short lived to represent a measured gating event but was found to occur with increased frequency in low P_o modes of KcsA (Chakrapani et al. 2011), therefore it may represent an early intermediate of a SF gating event.

Secondly, short lived closures may be related to depletion of K^+ during conduction at high rates (Demo and Yellen 1992; Schroeder and Hansen 2007). This is expected to destabilise the SF and close the channel. Depletion

of the channel during conduction and closure could explain the observed K^+ concentration dependence of SF gating. More so, occupancy dependent phenomena link the controversies surrounding permeation to gating. As of now there is still no direct overlap of the the time-scales commonly accessible to electrophysiological methods (up to $\sim$7 µs, in ideal circumstances) and MD simulations ($\sim$0.1 µs to 1 µs) to directly address such short-lived events.

Structure and subconductances

Several K^+ channels may show openings with reduced amplitude, so called subconductances. In practice, such subconductance behaviours may be difficult to discern from 'modal' gating behaviour (chapter 4).

Mutations affecting the coupling of activation gate and SF as well as constructs designed to produce asymmetric movements of the 4 subunits of a K^+ channel produce subconductance behaviours (Chapman et al. 1997; Zheng and Sigworth 1997; Zheng and Sigworth 1998). Subconductances may therefore reflect partial splaying of the inner helices.

1.6 Structure and function of K2P channels

Before introducing the questions both raised and answered by the growing number of K_{2P} channel structures available to us now, I will briefly describe each structure before describing some of their features in detail.

1.6.1 Salient crystal structures of K_{2P}

The first structures of K_{2P} channels to be known were TWIK1 resolved by Miller and Long (2012) and TRAAK resolved by (Brohawn et al. 2012). A

higher resolution structure TRAAK of TRAAK stabilised by an anti-body fragment revealed an alternative arrangement of the Cap domain (see below) that was found in all following K_{2P} channel structures (Brohawn et al. 2013).

Subsequently, Lolicato et al. (2014) captured structures of TRAAK with gain-of function mutations and gave a description of the movements of the pore lining helixes in the intracellular half of the channel. At the same time an alternative interpretation for the same overall movements in the context of lipid and mechano-gating were brought forward by Brohawn et al. (2014b).

The structure of TREK2 was captured in 2 conformations (named 'UP' and 'DOWN') corresponding to similar rearrangements of the lower pore as in TRAAK (Dong et al. 2015). The interpretation of these two 'macrostates' resulted in some controversy which is dealt with in section 1.6.2.

Recently the structure of TASK1 was captured in a closed state in which an occluding lower gate can be found (Rödström et al. 2019). This is in contrast to the open-pore structures of mechanosensitive K_{2P} channels and a proposed generalised mechanism of gating without a lower gate in TREK (see section 1.4.3, Piechotta et al. 2011).

The structural features of K_{2P}

K_{2P} channels have several unique features that set them apart from other K^+ channels. On a structural level, these are mostly brought about by their membrane topology, in which there are 2 pore domains within one protein (see fig. 1.5) as well as the additional extracellular helices forming the cap domain.

The cap domain is formed by a unique arrangement of the dimeric channel. M1 and M2 do not lie adjacent to form one quadrant of the channel, instead

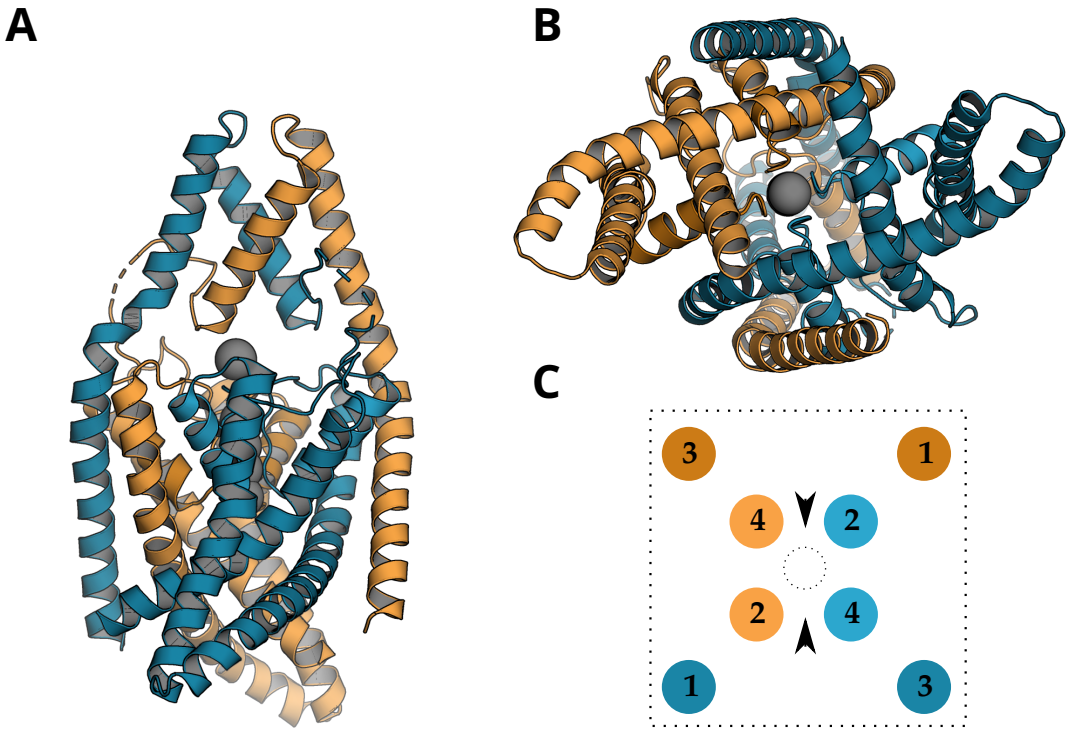


Figure 1.10: *Unique elements of K_{2P} structures* A: Side view of TRAAK with the domain swapped cap-structure (4I9W, Brohawn et al. 2013). The separate chains of the dimer are coloured orange and blue. The Cap helices span the pore axis like a roof. B: Bottom view of the channel, there is a symmetric arrangement with a rhomboid 'footprint'. C: Schematic of the arrangement of the membrane spanning helices around the pore axis. The M1 helix undergoes a domain swap. Localisation of the side portals (see section 1.6.2 is indicated by the arrows. Redrawn from Sepulveda et al. (2015), the pore helices were omitted.

the Cap helices between the two span over the extracellular pore mouth. M2 forms the pore lining on the opposite side to M1 in a domain swapped configuration (see fig. 1.10C).

In contrast to tetrameric channels that are fourfold symmetric (fig. 1.7B) the arrangement as shown in fig. 1.10B and C shows 2-fold symmetry. This is especially interesting for the SF itself, where the signature sequences of the two pore domains diverge (see fig. 1.9A).

1.6.2 Mechanosensitive K_{2P} channels

As their name suggests, mechanosensitive K_{2P} channels open in response to tension in the membrane. They also respond to a remarkable variety of additional stimuli all the while having only one SF gate. Accordingly, their structure is capable of translating diverse inputs into either stabilisation or destabilisation of the SF gate.

TREK channels will respond to changes in pH on either side of the membrane. Extracellular acidification activates TREK2 but inhibits TREK1 (Sandoz et al. 2009); intracellular acidification activates both TREK channels (Maingret et al. 1999). TREK channels have sensory capabilities and activate in response to membrane stretch (Patel 1998) and heat (Maingret 2000). Lipid second messengers (arachidonic acid (AA), PIP_2) likewise activate (Patel 1998; Chemin et al. 2005). Phosphorylation events mediated by PKA as well as PKC inhibit TREK channels (Bockenhauer et al. 2001; Kang et al. 2006). Finally, there is a strongly voltage-dependent open probability which is mediated by a sensitivity to electromotive force (Schewe et al. 2016).

A common theme that has emerged from the structure-function literature is that these stimuli can be loosely grouped into those that act on the SF gate directly, and others that stabilise it by allosteric action on the M4 helix.

Gating at the SF ('C-type gating')

The Gating of TREK and TASK channels in response to changes of pH_{ext} shares many of the hallmarks of C-type inactivation. Namely, homologous residues that form the 'molecular bowstring' of KcsA and K_v (see section 1.5.3) affect gating of K_{2P} as expected (Zilberberg et al. 2001). Also, protonable histidine residues (H87, H141, TREK1) participate in interactions with ho-

mologous residues critical for C-type inactivation of K_v and confer acid sensitivity (Cohen et al. 2008). Their inhibition by pH_{ext} is also reduced by $[K^+]_{ext}$ consistent with a stabilisation of a conductive structure by the permeating ion as in C-type inactivating K^+ channels (Cohen et al. 2008).

Ions such as Rb^+, Cs^+ activate K_{2P} channels (Schewe et al. 2016) analogous to KcsA, where these ions prevent entry into C-type inactivated pinched state (Tilegenova et al. 2017). Additionally, the voltage gating mechanism of K_{2P} channels is thought to rely on an event in which an ion-depleted SF is refilled in order to activate. This has obvious parallels to recovery from C-type inactivation which is also weakly voltage dependent in KcsA (Chakrapani et al. 2007b).

The only contradiction to the hallmarks of C-type inactivation as laid out in section 1.5.3 is that there is no obvious link to activation, ie. K_{2P} channels do not inactivate after stimulation. Rather, a C-type inactivation-related closed state is part of their activation and deactivation gating.

SF gating mediated by intracellular inputs

Intracellular acidification also activates TREK channels. This is mediated by a protonable residue E306 in the distal C-terminus of TREK1 (Honore 2002). The truncation of the C-terminus blunts the response of the channel to both pH_{int} and membrane stretch (Maingret et al. 1999), however, even truncated and reconstituted TREK proteins retain activity and some intrinsic mechanosensitivity (Berrier et al. 2013; Brohawn et al. 2014a). More detailed probing of C-terminal truncations and deletions revealed that the proximal C-terminus is critical for setting basal activity and mechanical and pH_{int} sensitivity (Kim et al. 2001). Phophorylation of C-terminal sites by PKA and

PKC (Bockenhauer et al. 2001; Kang et al. 2006) has profound inhibitory effects on gating. This suggests that regulation of P_o in TREK channels is mediated by this structural pathway.

Although there is no structural information on any of the intracellular domains to date, it seems likely that charged interfaces between the lipid membrane and amphiphatic helices of the C-terminal domain are crucial to relay these stimuli to the SF (Honore 2002; Chemin et al. 2005).

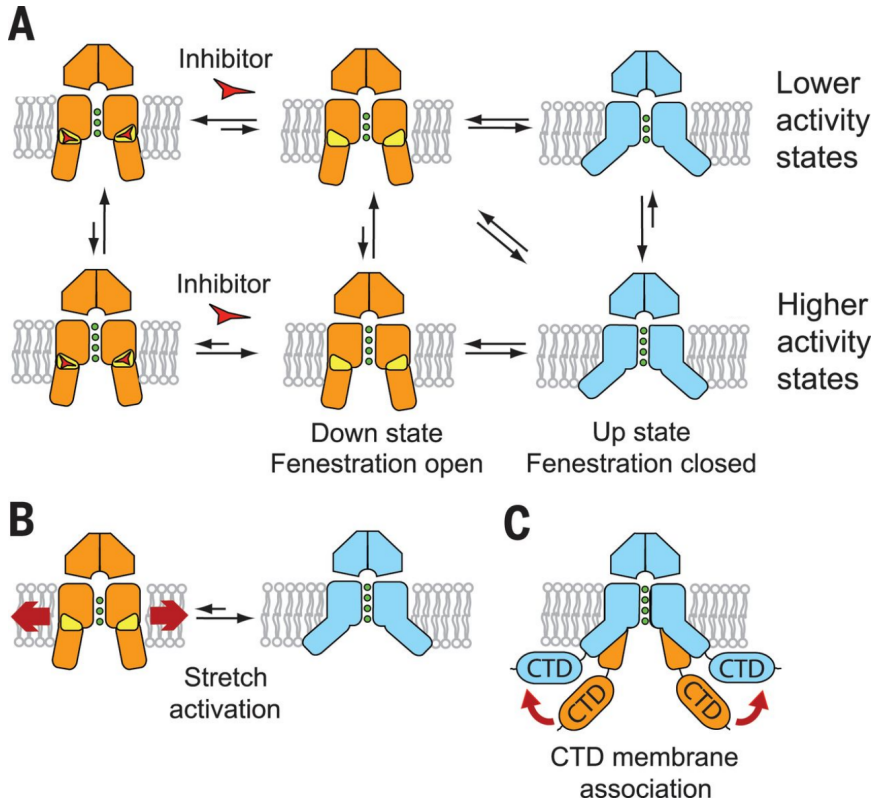


Figure 1.11: *The UP DOWN gating transition of mechanosensitive K_{2P} channels* A: Summary of the structures of TREK captured. The down state is able to bind the blocker norfluoxetine, its binding site is obliterated in UP structures. B: Mechanical stimulation promotes the UP state with an additional involvement of the regulatory C-terminal domain. Taken from Dong et al. (2015).

The UP-DOWN transition

A series of papers and crystal structures of mechanically gated K_{2P} channels sparked a debate about the motions of the pore lining helices that underlie gating by intracellular inputs (Brohawn et al. 2014b; Lolicato et al. 2014; Dong et al. 2015). TRAAK and TREK2 were captured with alternative conformations of the pore lining helices M4 and M2.

In the so-called DOWN structures the inner pore lining helices pass the membrane at a steep angle. Additionally there exists a lateral cleft ('side portals', see fig. 1.10) that is continuous with the plasma membrane.

The other ('UP') conformation has M4 packed closely to M2 sealing the side portal. In the original DOWN conformation a density below the filter, where the 'cavity ion' (Roux 1999) can commonly can be found, has been assigned to lipid entering from the side portal and competing with K^+ permeation. The 'DOWN' structures were therefore assigned non-conductive and mechanogating interpreted as pore block by lipids based on state-dependent access to the pore through the side portals (Brohawn et al. 2014b).

A cartoon representation of the structures and how they relate to gating according to the model of Dong et al. (2015) can be found in fig. 1.11

Similar inner helix motions of TRAAK structures with gain of function (GoF) mutations were interpreted in the opposite way (Lolicato et al. 2014). Here, these mutations that lie in the extracellular end of M4 or the M4 pore-helix interface resulted in structures sampling DOWN states. Because of the high open probability associated with these mutants (Bagriantsev et al. 2011) the DOWN state structures were interpreted as open conductive channels and the UP structure as closed and inactive.

Thirdly, 'DOWN' and 'UP' conformations were captured in TREK2 (Dong et al. 2015). Here the side portal of the 'DOWN' conformation was also found to be the binding site of the state-dependent blocker norfluoxetine (Kennard et al. 2005). From more detailed electrophysiological study of the drug binding in the presence of activating stimuli (McClenaghan et al. 2016) it emerged that activating stimuli such as membrane stretch and heat shift the channel towards 'UP' conformations. In agreement, MD simulations of TREK have demonstrated membrane stretch will trigger the 'UP' conformational change (Aryal et al. 2017; Brennecke and Groot 2018).

TREK1 (Lolicato et al. 2017) was captured in an 'UP' state with the activator ML335 bound. Here, the action of the drug and rearrangement of the network of interactions at the SF gate recapitulate the changes captured earlier with GoF mutations. This highlights the importance of the SF structure for interpreting the functional state of the channel (Lolicato et al. 2014).

Interestingly, the 'DOWN' to 'UP' conformational change can be gradual and involves bending of M2/M4 around the hinge glycine just like activation gating in KcsA or K_v channels. On the other hand, heat, mechanical gating and further stimuli associated with DOWN-UP movements show dependence on $[K^+]_{ext}$ indicative of a C-type inactivation like gate (Bagriantsev et al. 2011; Bagriantsev et al. 2012).

We can summarise these finding as follows: mechanically gated K_{2P} channels share the overall gating machinery with KcsA and other K^+ channels, however, their HBC is not an occluding gate (Piechotta et al. 2011). Gating stimuli sensed in the regulatory C-terminus are relayed to an 'UP' movement of M4. This movement is coupled to stabilisation of the SF gate through a network of contacts of the pore helix, SF loop and proximal M4 as demonstrated by the number of GoF mutations in this region (Bagriantsev et al. 2011). Thus

movement of the pore lining helices is not followed by inactivation as in KcsA (Cuello et al. 2010a) but coupling of this conformational change to the SF has a sustained activating effect ('inverse coupling', Ben-Abu et al. 2009).

N-terminal protein variants

TREK proteins may be produced in variants that diverge in their N-terminus. This is achieved by mRNA maturation processes (splicing) as well as alternative translation initiation. Alternative translation initiation is a process by which a start-codon may be skipped by the ribosome (leaky scanning) and translation starts from a subsequent start-codon/methionine in the sequence.

In the case of TREK2 there are 5 different variants that can be produced by these processes (see scheme fig. 1.12, Staudacher et al. 2011). There are 3 different copies of the first exon of the TREK2 encoding gene that contain the sequence of the proximal N-terminus resulting in 3 transcripts of isoforms named TREK2a-c. The second and third methionine residues (M60, M72) of the protein residues are encoded by the second exon and identical in all TREK2 isoforms. Fascinatingly, the coding sequence preceeding these methionines double as weak Kozak sequences (Staudacher et al. 2011). The composition of TREK2 proteins produced therefore depends on the relative strength of these additional Kozak sequences. All 5 of possible variants can co-assemble as dimers with subtly different biophysical properties (Staudacher et al. 2011; Blin et al. 2016).

A N-terminal truncation of TREK1 results in a variant (Δ56) with low activity and putatively poor K^+-selectivty (Thomas et al. 2008; Veale et al. 2014a). Also, the affinity of N-terminal truncation variants for state-dependent blockers such as norfluoxetine differs (Eckert et al. 2011; Kisselbach et al.

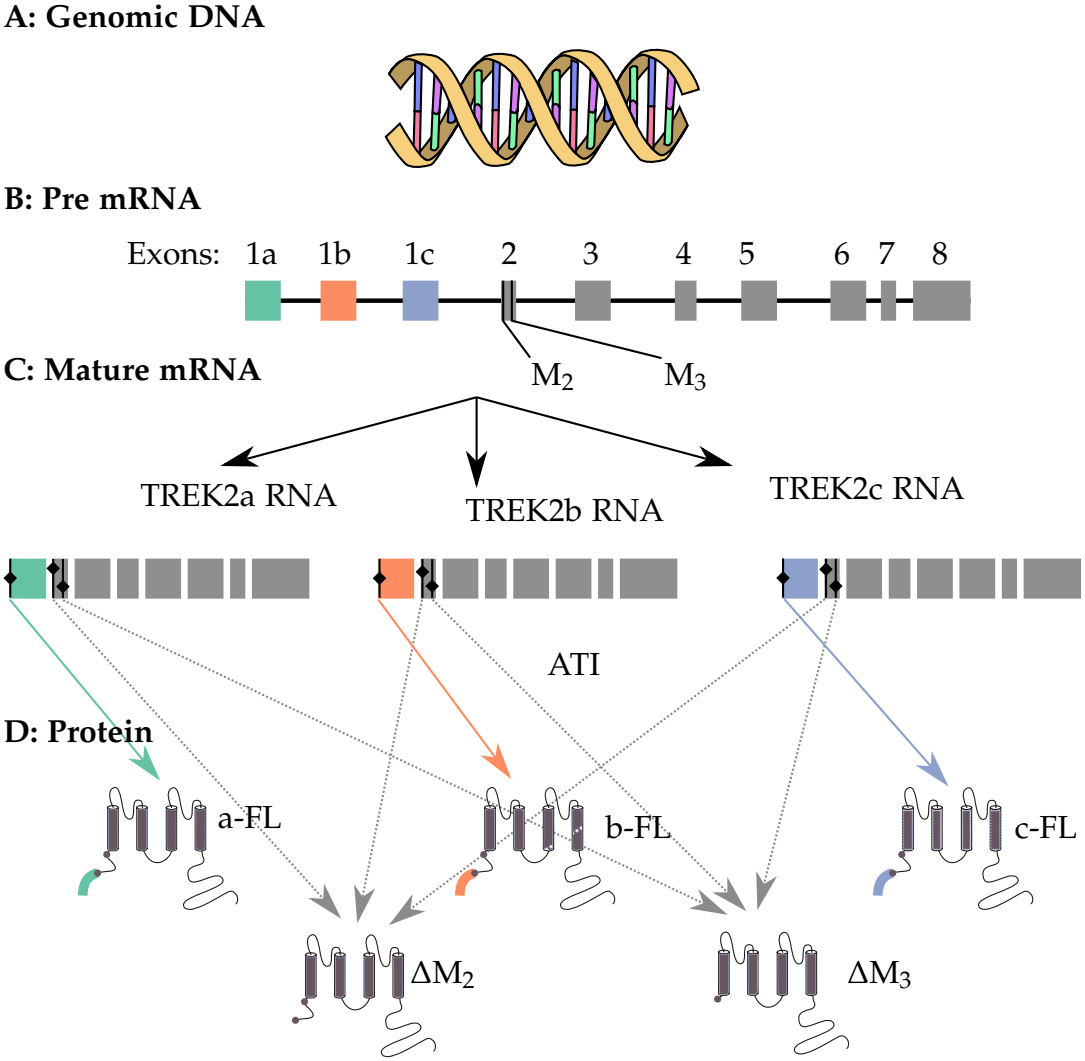


Figure 1.12: *ATI in TREK2* The TREK2 gene contains 10 different exons that are transcribed into 3 unique mRNAs differing in exon 1 coding for the distal N-terminus of the protein. Exon 2 contains two further ATG codons (M_2 and M_3) that can function as start codons. Accordingly translation of mature TREK2 mRNA can result in one of 3 protein chains, the full length ('FL') version being unique depending on the version of exon 1 spliced into the mRNA. Redrawn from Staudacher et al. (2011).

2014) suggesting a change to the status of the activation gate (see above) in these variants.

1.6.3 Structure and function in the TASK subfamily

TASK channels are known for their acid sensing capability, in addition to this their fast voltage-dependent gating is crucial for their function in cerebellar neurons (Brickley et al. 2007). A hallmark of TASK channel function (especially TASK1) is a strikingly low P_o (<1%, see for example, Renigunta et al. 2015).

SF gating

Acid sensitivity is conferred by protonation of histidine residue at the outer mouth of the SF (see fig. 1.9 Rajan et al. 2000; Duprat 1997) Consistent with a gating mechanism related to C-type inactivation closure by acidic pH_{ext} and voltage gating is in competition with the stabilising effect of raised $[K^+]_{ext}$ (Lopes 2000). This is the reason for the seemingly paradoxical increase of TASK outward currents that can be observed following increase of $[K^+]_{ext}$ (Lopes 2000).

Gating by G_q-signalling

TASK channels in are inhibited through G-protein-q coupled signalling cascades (for example, Millar et al. 2000; Talley et al. 2000). The precise mechanism and messenger involved remains controversial. There is evidence for closure by PIP_2 depletion (Chemin 2003), phosphorylation by PKC (Veale et al. 2007b) and binding of DAG (reviewed in, Mathie 2006). Activity of phospholipase C seems to be essential which suggests a role of PIP_2 in the process (Czirják et al. 2001; Schiekel et al. 2012). Indeed, PIP_2 has been shown to activate TASK channels consistent with an PIP_2 depletion mediated closure of the channel (Chemin 2003; Czirják et al. 2001).

The activation of TASK channels by inhalational anaesthetics such as halothane as well as inhibition by G_q-signalling depends on the presence of the so called HRE sequence (`243 VLRFMT 248`, TASK1) in the distal M4 (Talley and Bayliss 2002). Alternatively it has been suggested that TASK are blocked by DAG through a binding site at the proximal M4 which rationalises the dependence of Gq inhibition on presence of the HRE (Wilke et al. 2014).

The X-gate and 'HRE'

In addition to the the obvious role of the outer pore and the SF in gating evidence for an involvement of the intracellular parts of TASK has accumulated.

In addition to the importance of the HRE sequence in the action of both drugs and neurotransmitters (Talley and Bayliss 2002; Veale et al. 2007a), residues in the pore lining helices around the hinge glycines were found to confer gain of function and influence voltage-dependent gating of TASK3 (Ashmole et al. 2009).

Also residues in the pore lining residues that have been associated to a 'hydrophobic gate' (see section 1.6.5) in TWIK1 (Aryal et al. 2014a) confer gain of function in TASK channels (Ben Soussia et al. 2019). This site may also confer loss of function of TASK3 when mutated to arginine (Veale et al. 2014b).

These results will be discussed in chapter 3, within the context of the novel structure of TASK1 (Rödström et al. 2019) which demonstrated that the HRE and pore lining helices arrange to form an occluding gate ('X-gate').

1.6.4 Dynamic and altered selectivity in K_{2P}

Non-selective permeability has been reported for TREK, TASK and TWIK channels in a variety of contexts. Also, selectivity may change in response to a stimulus ('dynamic selectivity'). An in depth discussion of the evidence for non-selective permeability can be found in chapter 6.

Na^+ permeability in TREK1

The TREK1 ATI variant Δ56 and TREK1 I267T conduct Na^+ (Thomas et al. 2008; Decher et al. 2017). TREK alone or as a heterodimer with TWIK was found to be the carrier of glutamate efflux in astrocytes. (Woo et al. 2012; Woo et al. 2018; Mi Hwang et al. 2014) However, there is controversy about how glutamate is released by astrocytes with a role of further channels and transporters implied (Hamilton and Attwell 2010). There is also currently no way to explain transport of a large anion through the intact structure of a K^+ channel.

Na^+ permeability of TWIK

On prolonged exposure to acidic pH_{ext} TWIK1 undergoes a slow (5 min to 10 min) conformational change that results in a significant Na^+ permeability (Chatelain et al. 2012). TWIK1 shares the extracellular proton sensor of TASK channels (see above). Therefore this slow change was linked to a C-type inactivation-related conformational change (reviewed in Chen et al. 2014). Similar experiments seem to demonstrate a significant permeability of TASK to Na^+ in acidic external solutions (Ma et al. 2012a).

1.6.5 Hydrophobic gating

Another possible way of gating K_{2P} channels may be the phenomenon of hydrophobic gating. Hydrophobic gates are an emerging concept from biophysical chemistry and pore theory that have found an application in the ion channel field (Roth et al. 2008; Beckstein et al. 2004).

In a narrow and hydrophobic space such as an ion channel or a carbon tube (nano tube) electrostatics and surface effects on a nanoscale can lead to variety of counter-intuitive effects. Depending on diameter and hydrophobicity of such a cavity, the energetic penalty for occupancy of hydrophilic molecules can become so large that these areas de-wet. This means that water molecules will be absent or only sporadically present in these areas and either vacuum or low density of water (vapour) taking its place.

De-wetting presents an insurmountable obstacle for conduction as delivery of a charged ion through water is necessary. A channel structure with a hydrophobic gate may appear physically unobstructed but remains non-conductive. Therefore identification of hydrophobic gates can be a successful strategy for interpreting channel structures as conductive or non-conductive conformations (Rao et al. 2019; Klesse et al. 2019).

MD simulations have implied hydrophobic gates contributing to the closure of a growing number of ion channels (for example nicotinic receptors, Piezo, BK and many others, Beckstein and Sansom 2006; Zheng et al. 2019; Jia et al. 2018).

A hydrophobic barrier was also found to impair conductance through TWIK1 (Aryal et al. 2014a). A ring of hydrophobic residues in M4 that face the pore cavity provide a sufficiently narrow and hydrophobic milieu to exclude water. Exchange with more hydrophilic residues resulted in a

pronounced gain of function. TASK1 and TASK3 also have homologous hydrophobic residues that likewise affect function (Veale et al. 2014b).

1.7 Aims and Objectives

The SF has long thought to be the principal gate of K_{2P} channels and mechanisms of gating brought forward have largely focussed on this structure (Schewe et al. 2016; Piechotta et al. 2011). However, the evidence for involvement of the pore as well as electrostatics in K^+ channel permeation and gating has accumulated (for example Diaz-Franulic et al. 2015; Aryal et al. 2014b).

One initial aim of this project was to expand on the idea and mechanism brought forward by Schewe et al. (2016) of the permeating ion stabilising the SF gate. This mechanism has the potential to reconcile established concepts of K^+ channel gating such as C-type inactivation with more recent results concerning the pore and SF entrance, such as hydrophobic gating—occupancy and electrostatics of the pore being the common theme.

First, I characterised mutations related to the 'hydrophobic cuff' in TASK3. These results were later overshadowed by the discovery of a lower gate in TASK1, to which I also contributed (chapter 3, Rödström et al. 2019).

The ongoing interest of the lab in activation mechanisms of K_{2P} channels motivated the study of the activator BL1249 (chapter 4). Here the evidence for activation through electrostatic stabilisation of an ion in the cavity by action of the drug is discussed. This electrostatic mechanism was further studied through experiments in high $[K^+]_{int}$. However, it was found that in such conditions the channels will close by a novel mechanism controlled by

ionic strength, irrespective of the occupancy of the pore, which we would assume near full in these conditions (chapter 5).

Finally, more detailed assessments of inward currents of TREK revealed that the channel may undergo transient changes in selectivity during its voltage gating cycle (chapter 6).

Chapter 2

Methods

In the following sections I will outline the protocols for crucial preparatory procedures. Experimental details necessary for the understanding of particular results are given closer to the sections in which they are relevant in the method sections of individual chapters.

2.1 Heterologous expression

All ion channel genes used in this study encode human isoforms. A modified pc.DNA cloning vector (named pFAW after its creator Firdaus Abd-Wahab) was prepared with genes for the K_{2P} channels of interest. This vector contains the cyto-megalovirus (CMV) promotor for mammalian cell expression as well as the *Xenopus leavis* β-globulin gene for expression in oocytes. A modified vector based on the commercially availabe pRL-TK (Renilla luciferase, thymidine kinase promotor, Promega) was used for low membrane expression in mammalian cells. All channel open reading frames (ORF) were preceded by the Kozak sequence `GCCGCCACC`.

Table 2.1: *Gene codes, description of used constructs and their abbreviations*

Gene name	Uniprot Code	Mutation	Abbreviation	aka
KCNK10 Isoform A	P57789-1		TREK2a	Isoform 1
KCNK10 Isoform B	P57789-4		TREK2b	Isoform 3
KCNK10 Isoform C	P57789-3		TREK2c	Isoform 2
		ΔM72	TREK2ΔM_3	
		ΔM60, M72L	TREK2ΔM_2	
KCNK10 Isoform B		M60L, M72L	TREK2b FL	
KCNK2 Isoform C			TREK1c	
KCNK9	Q9NPC2-1		TASK3	
KCNK3	O14649-1		TASK1	

Constructs were cloned with polymerase chain reaction (PCR) and restriction-ligation. An overview of the parent constructs made for use in this study see table 2.1.

2.1.1 Ligation Cloning

To sub-clone channels from the oocyte expression vector pBF into the more versatile pTK and pFAW vectors or truncated constructs, a restriction-ligation cloning strategy was used. An amount 2.5 µg to 5 µg plasmid DNA was digested with the enzymes producing the desired sticky ends. Restriction enzyme were purchased from Promega and reactions mixed with the appropriate buffer concentrates of the manufacturer.

For truncations primers with the needed restriction sites, Kozak sequences and start/stop codons were designed. DNA fragments to be inserted were produced with polymerase chain reactions (PCRs) using the Pfu (*Pyrococcus furiosus*) polymerase (Promega). The thermo-cycling protocol for gene amplification can be found fig. 2.1, bottom. The DNA fragments were separated by size by agarose gel electrophoresis. Bands corresponding to either the digested backbone vector or the gene of interest were cut and purified from the gel with the Quia-ex gel extraction kit (Quiagen). The elution volume

was 30 µL, these eluates were mixed in a ratio of 1:4 (by volume) of backbone to insert and ligated overnight at 4 °C with T4 DNA-ligase (Promega). The full ligation reaction was transformed into the *Escherichia coli* strain DH5α (section 2.1.3).

2.1.2 Site directed mutagenesis protocol

Point mutations were introduced to the genes of interest using site-directed mutagenesis (SDM). Primers binding to the site of interest and including the desired codon change for the point mutation were used in a PCR reaction. The thermocycling protocol for these reactions is shown in fig. 2.1, top. Sufficiently low concentration of the template DNA proved to be the most important factor in determining outcome of SDM reactions, the exact pipetting scheme can be found in table 2.2. Following the amplification of the plasmid the template DNA was inactivated by DpnI (1 h incubation time at 37 °C).

The DNA was then cleaned using the QiaQuick spin-column kit (Quiagen) and eluted into 28 µL of water. The full eluate was then transformed into DH5α cells.

Table 2.2: *Pipetting scheme for SDM PCR* For a single 50 µL reaction. Dry primers were solved to 100 µM according to the manufacturers (Sigma) instructions. The primer mix contained 5 µM of each forward and reverse primer (mixed 1 +1 in 18 parts water from the solved primers). The Pfu ultra enzyme is engineered for higher precision than the polymerase used for standard gene amplifications (see above).

Reagent	Amount in µL	Description
10x Pfu ultra reaction buffer	5	
Primer Mix	3	see above
dNTP mix	1	10 mM stock, Promega
Pfu ultra enzyme	1	Agilent Technologies
Template DNA dilution	X	Must contain 10–20 ng plasmid DNA
Water	add to 50 total	

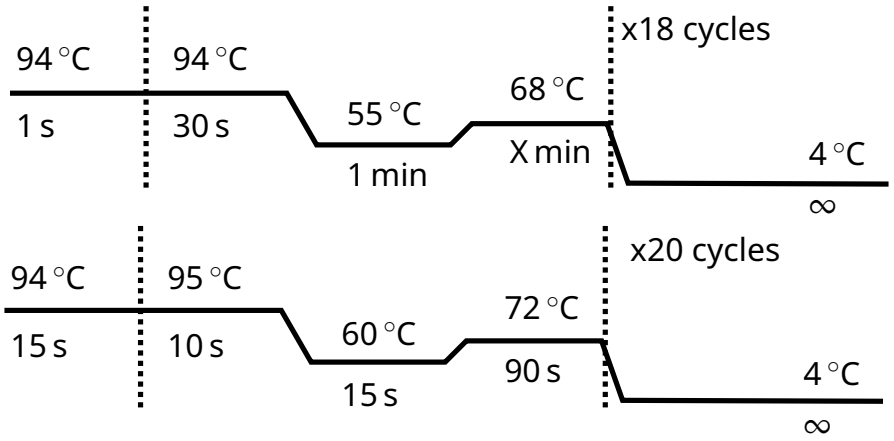


Figure 2.1: *Schematic of PCR cycle* Protocol of the PCR cycle used for site directed mutagenesis (top) and for producing inserts used in ligation cloning (bottom). The length of the elongation step is adjusted to the size of the amplicon, where x is its length in kilo bases.

2.1.3 Heat-shock transformation

Complete PCR or ligation reactions were mixed with 50 µL to 100 µL DH5α cells (Invitrogen) and incubated on ice for 20 min. The mixture was subjected to a heat shock for 45 s at 36 °C and spread immediately onto Luria-broth-agar (LB) plates containing 0.1 mg mL^{-1} Carbenicillin. Plates were incubated overnight (37 °C) or until visible colonies appeared and stored sealed from air at 4 °C.

2.1.4 Culture and DNA extraction

Overnight cultures of 4 mL to 5 mL LB were inoculated from an agar-plate using a pipette tip. DNA was extracted with the QiaPrep Spin Miniprep kit (Qiagen) following the manufacturer's protocol. Samples were eluated into 120 µL elution buffer. Clones were controlled for correct insertion of the point mutation by automated sequencing (samples processed by SourceBioscience, Oxford).

To produce larger amounts of plasmid for transient transfection, cultures of 20 mL to 100 mL were processed with the PureYield Plasmid Midiprep system (Promega).

2.1.5 Expression in Oocytes

In vitro transcription

The pFAW vector will produce transcripts that include the 3′ and 5′ untranslated regions of the *Xenopus* β–globin gene which increases expression (Krieg and Melton 1984). The vector was linearised by restriction digest and used as the template in an *in vitro* transcription reaction (AmpliCap-Max™ T7 High Yield Message Maker Kit, CamBio).

The transcription reactions were cleaned using the Quiagen RNAeasy mini kit. Quality and concentration of the mRNA produced was controlled by UV-spectroscopy (nanodrop) and gel-electrophoresis.

Oocyte preparation

Ovaries were removed from an euthanised *Xenopus* toad and dissociated by enzymatic digestion. The defolliculation buffer contained in mM: HEPES 10, $NaHCO_3$ 2.4, $MgSO_4$ 1.68, NaCl 88, KCl 1 . and 2 mg l^{-1} collagenase (Class II collagenase, Merck). Digestion lasted 1 h to 2 h at 21 °C with gentle shaking. The separated oocytes were then manually defolliculated with sharpened forceps. The oocytes were stored at 17 °C in Barth's solution (in mM): HEPES 10, $CaCl_2$ 0.41, $NaHCO_3$ 0.24, $Ca(NO_3)_2$ 0.47, $MgSO_4$ 1.6, NaCl 88, KCl 1.

Injected oocytes were kept in a modified Barth's solution with 80 mM KCl (isomolar substitution for NaCl). This was found to increase the viability

of cells expressing active K^+ channels, presumably by reducing the energy expended by Na^+/K^+-ATPases.

2.1.6 Expression in mammalian cells

HEK293 cells were purchased from Public Health England (European collection of authenticated cell cultures catalogue number 85120602) and cultured according to their guidelines (*Fundamental Techniques in Cell Culture* 2016).

For patch-clamping, cells were seeded into 35 mm dishes covered with 6 mm diameter glass coverslips that were coated with poly-lysine (Sigma). Transient transfections with the lipofectamine method were done using the FuGene reagent (Promega).

Currents were measured 18 h to 24 h post transfection. For the exact protocol and the rationale behind transfection conditions see section 2.3.2 and table 2.3.

Coverslips were treated in a 1:5000 dilution of cd8 dynabeads (Invitrogen) in PBS for 1 min to 3 min and washed by dunking them into a reservoir of the bath solution before being transferred to the recording chamber. Cells with at least 2 attached beads were considered successfully transfected and deemed suitable for recording.

2.2 Data acquisition, and analysis

An Axopatch200B amplifier (Molecular devices) was used for all patch clamp recordings shown. Giga-seals were formed using borosilicate pipettes of 2 MΩ to 4 MΩ (4 MΩ to 6 MΩ for single channels). The fast pipette capacitative

transient was compensated. Patches were excised by a fast upward motion of the pipette.

Solutions were exchanged with a gravity fed perfusion system (fig. 2.2 and section 2.3.1). Composition of the buffers used varied with the purpose of the experiment and are given in each chapter individually,

2.2.1 Acquisition and filtering

A sampled time series signal can be accurately re-constructed if the sampling rate is at least double of the highest frequency component present in the signal (Nyquist 1928). This threshold is called Nyquist rate. In practice, the highest frequency component in the signal is determined by the cut-off frequency of the lowpass filter used.

In this study, single-channel recordings were acquired at 50 kHz and filtered with the built-in 10 kHz 8-pole Bessel filter of the amplifier, macroscopic currents were sampled with 20 kHz and filtered at 2 kHz.

2.2.2 Semi-automatic data processing

All electrophysiological data was acquired with the WinEDR and WinWCP programmes (John Dempster, University of Strathclyde Glasgow). The resulting files (.wcp) were recorded in such a way to allow automated processing. This was achieved by using filenames that contained the relevant experimental metadata. The raw .wcp files were exported as text or .mat files and imported and processed in R. The analysis scripts were set up to process a batch of such files in a directory and write a summary analysis to a file. The summaries for each recording could then be collated and further processed.

2.2.3 Data visualisation

Wherever feasible all individual points (lines) of a dataset were plotted to give a unabridged impression of spread present in the data. Summary statistics are given and plotted as mean ± SEM unless otherwise stated.

In some cases plotting of all datapoints proved unsatisfactory or not well readable, in this case box and whisker plots were used to visualise the distribution of the data.

The summary statistics used for the box and whisker plot are as follows:

Box: 25th, 50th (median) and 75th percentile (1st, 2nd and 3rd quartiles)

Whisker: The whisker extends to the largest (or smallest for the lower whisker) datum within the interval from the end of the box (25th or 75th percentile) ± 1.5 times inter-quartile-range (difference between the 75th and 25th percentile)

Outliers All points outside of the interval delimited by the whiskers are considered outliers and plotted individually

2.2.4 Analysis of voltage step protocols

Rates of TREK2 activation are variable in excised patch (fig. 6.9). To analyse relaxation kinetics time course data were fit with single or double exponentials. However, these models did not yield satisfactory fits for all individual measurements within a dataset. The resulting variable and correlated parameter estimates could not be interpreted to a meaningful end.

Instead, apparent half times for completion of a relaxation were measured. For every sweep a threshold value at half the amplitude of the time dependent current was defined.

$$I_{\text{thresh}} = \frac{I_{steady} + I_{\text{inst}}}{2} \tag{2.1}$$

Where I_{steady} and I_{inst} are amplitudes measured at steady state and immediately after the voltage jump.

For every point of the time series the absolute difference to the threshold δ was calculated to find the timepoint at which the threshold is crossed. The calculation of δ is given by eq. 2.2, where $I(t)$ is the current time series, and I_{thresh} is the half-maximal current as determined by eq. 2.1.

$$\delta = |I(t) - I_{\text{thresh}}| \tag{2.2}$$

The value of $t_{1/2}$ was read from the δ time-series by returning the time after the voltage-jump jump t at which δ was smallest. The current time series was filtered with a Sawitzky-Golay filter to calculate the threshold crossing. This served to minimise influence of higher frequency noise values of $t_{1/2}$.

Analysis of IV-curves

Isochronal IV-curves such as shown in chapter 6 were constructed by measuring the average current in a 1 ms window at different timepoints after the voltage jump. IV-curves generated from step-protocols are sampled at discrete voltages. To quantify the reversal potential (V_{rev}) of the current and extrapolation is needed. This was done by means of a polynomial fit. From each IV-curve a points in ± 30 mV interval around the smallest current value were fitted with a polynomial of second order. The y-intercept of this fitted curve was extracted and used as an estimate for the reversal potential.

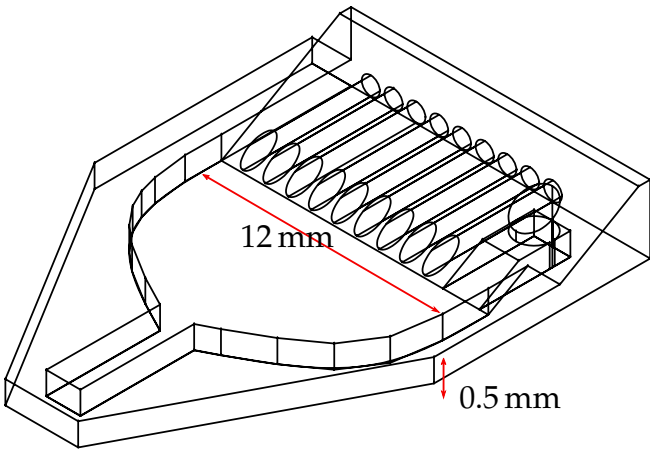


Figure 2.2: *Drawing of the low-volume perfusion chamber* The port on the right side accepts 1.5 mm outer diameter (OD) tubing to be used as agar bridge. The 9 ports for perfusion were fitted with 0.6 mm OD PTFE tubing (Sigma).

2.3 Establishing a single-channel model system

Single-channel recording is a technique that allows capturing quantitative functional data of individual molecules with unmatched time-resolution. It comes with a trade-off though, data-collection is challenging and the analysis time-consuming and complex. For this project a dedicated single-channel recording set-up was built. The following section describes adaptations made to the recording set-up as well as the model system to achieve low-noise single-channel recordings of TREK2.

2.3.1 Low fluid-level perfusion system

The main source of stray noise are fluid films inside the pipette or wetting the pipette shaft. These noise sources were reduced by: (a) coating the pipette tip with Sylguard (Sigma), (b) minimising the fluid level inside the pipette (c) and maintaining a low fluid level in the recording chamber.

In order to achieve such a low fluid level, a recording chamber was designed and 3D printed from nylon resin (fig. 2.2). The chamber has a port to connect an agar filled tube as reference electrode.

With all these precautions noise levels of <200 fA rms noise at a 5 kHz bandwidth could be achieved.

2.3.2 Low membrane expression of channels

Another challenge for single-channel recordings is achieving a level of protein expression in the cells that results in one and only one channel in the pipette with reasonable success rate. However, transient transfection methods allow little control over expression levels. This is a known problem especially in the K^+ channel field, where membrane currents from excised patches may vary from unitary currents to several nA in the same preparation (Trapani and Korn 2003). Inducible stably expression cell-lines may perform better, yet this approach is not suited for studying mutations, as the time-consuming generation of a new line would be required for every new mutant of interest.

The widely used pcDNA vectors for transient expression use the cytomegalovirus promotor to drive the gene of interest. The pFAW vector also contains this promotor. Control of the gene by the CMV promotor results in strong overexpression, which is wanted for applications such as protein purification or other biochemical assays.

The dynamics of transcript levels and membrane expression in HEK293 cells transfected with a viral promotor are hard to predict. Low-levels of plasmid are sufficient for overexpression, as long as there is a 'filler' DNA present to aid transfection complex formation (Rajendra et al. 2012). This suggest that few copies of the plasmid per cell are sufficient to overexpress a gene.

In an otherwise identical expression system the CMV promotor has been shown to produce higher and more sustained expression levels than any other

Table 2.3: *Scheme for setting up co-transfections* For preparations intended for macroscopic recordings 500 ng of channel plasmid were used. To prevent false positively marked cells, cd8 DNA was always half the amount of channel DNA. This is for transfection of a 35 mm dish.

Vector	Formula	amount used
Channel-construct	x	100 ng to 300 ng
pcDNA3.1 CD-8	$0.5x$	
pFAW	$2000 - 1.5x$	

viral promotors (Damdindorj et al. 2014). The herpes simplex thymidine kinase promotor (HSV-TK) however produces low constitutive expression.

In the absence of any available HSV-TK cloning vectors we modified the pRL-TK vector available from Promega. This vector is designed for gene expression assays and contains a *Renilla* luciferase driven by the HSV-TK promotor. The modification allowed the replacement of the luciferase gene with TREK2 inserts with an additional restriction site.

For measuring single channels, a small amount of pTK vector was co-transfected with pcDNA3.1-cd8 as a marker and a large excess of empty pFAW. The small basal expression provided by the HSV-TK promotor and putative competition with the CMV promotors present resulted in little membrane expression and an acceptable success rate for single channel recording. The pipetting scheme for 1 35 mm dish is given in table 2.3.

Chapter 3

Characterisation of TASK mutations

3.1 Introduction

Hydrophilic substitution mutations within the inner pore in proximity to the selectivity filter appear to increase activity in K_{2P} channels and many other K^+ channels. One particular site confers robust gain of function and can be found exactly 5 residues C-terminal to the glycine hinge (fig. 3.1). This site has recently been termed TM2.6, based on its position in transmembrane helix 2 and relative to the hinge (Ben Soussia et al. 2019). These GoF mutations were exploited to study currents of otherwise silent members of the family



Figure 3.1: *Alignment of the pore lining helices of K^+ channels* The hinge glycine and the TM2.6/hydrophobic cuff position are marked with triangles.

such as THIK and TWIK channels (Chatelain et al. 2012; Chatelain et al. 2013; Renigunta et al. 2014).

A mechanism for gain of function of this mutation in TWIK1 (L146N) was proposed by Aryal et al. (2014a). This involves partial de-wetting of the region around TM2.6 (also named 'hydrophobic cuff') preventing conduction. However, these molecular dynamics simulations suggested that de-wetting occurs on a nano-second time scale. Although an attractive idea supported by research on carbon nanotubes and pore theory (Beckstein et al. 2004; Roth et al. 2008), there seems to be little way to confirm or expand on the occurrence of de-wetting on this time-scale with electrophysiological experiments.

The TM2.6 position and residues in its proximity have been mutated and studied in detail in other K^+ channels. In MthK mutation of A88 to a panel of residues revealed a complex effect on both open-probability, activation by Ca^{2+} and single-channel conductance (Shi et al. 2011). This effects were dependent on the size and hydrophobicity of the substituted residue: Large and hydrophobic residues (V, F) result in reduced conductance and P_o, the opposite is the case for hydrophilic or charged residues (D, N). This demonstrated a combined effect of the mutation on activation gating and permeation.

Residue F103 of KcsA is the key residue that transmits the coupling of the activation gate to the SF (Cuello et al. 2010a). This is 4 residues from the hinge site (TM2.5), likewise directly adjacent to the 'hydrophobic cuff'.

The structure of a K^+ channel of *Geobacter sulfurreducens* (thus named GSUK) was resolved with a mutated 'hydrophobic cuff' site. It was shown that the angle of the (homologous) M2 helix in the mutant channel (L97D) diverges at the glycine hinge suggesting a similarity to activation gating (Kong et al. 2012). The open probability, conductance and sensitivity to

inhibitory stimuli were also affected as seen in similar experiments with MthK.

Due to the dimeric architecture of K_{2P} channels there are 2 unique inner helices with a corresponding residue in each (TM2.6 L122 and TM4.6 G236 in TASK3, see alignment in fig. 3.1). In TASK3, mutations of TM4.6 have been studied. The point mutation G236R in TASK3 is a rare genetic variant that clinically manifests as a combination of facial deformities with neurodevelopmental symptoms (Birk-Barel syndrome, Barel et al. 2008). Current through poorly-functional TASK3 G236R can be recovered by addition of activators such as flufenamic acid (FFA, Veale et al. 2014b). TASK G236R also is inward rectifying (it conducts more inward than outward current) and this cannot be reversed by action of FFA.

Similarly, equivalent mutations in the *Drosophila* K_{2P} channel KCNK0 results in a constitutively active channel that poorly responds to inhibitory stimuli, while the single-channel conductance is unaffected (Ben-Abu et al. 2009). The proximity of this residue and other GoF mutants to the glycine hinge was interpreted as a link to activation gating (Ben-Abu et al. 2009; Ashmole et al. 2009)

The effects of the 'hydrophobic cuff' mutations in TWIK1 are difficult to interpret, as wild-type (WT) channels are not only poorly conductive but also may not behave like a K^+-selective channel in all circumstances (Nemetian-Ardestani et al. 2019; Chatelain et al. 2012). This complicates the interpretation of mutagenesis data when compared to a WT control. The initial aim of the project was therefore to characterise a putative 'hydrophobic cuff' site in a fully functional K_{2P} channel subfamily. To achieve this, the TM2.6 site in TASK3 (L122) was mutated to a panel of residues chosen to sample different

size, hydrophobicity and charge (A, S, D, N, V) and examined in two electrode voltage clamp (TEVC).

During the latter stages of this project 3 important studies further developed our knowledge of TM2.6-related gain of function. Firstly, Ben Soussia et al. (2019) demonstrated a gain of function through substitution of TM2.6 to D or N in all mammalian K_{2P} channels. The use of these mutations for generation of genetic models of GoF *in vivo* was also demonstrated for number of homologous *C. elegans* K_{2P} channels.

Secondly, our colleagues solved a crystal structure of TASK1 Rödström et al. (2019). Functional validation experiments of the construct they used for crystallisation were contributed through this project.

Thirdly, Al-Moubarak et al. (2019) revealed a size-dependent loss- or gain of function (similar to the pattern in MthK) in TM2.6 and TM4.6 mutations of TREK1. In this study it was again confirmed that loss of function through TM2.6 mutations can be reversed by activators or additional mutations. Furthermore, cross-linking with MTS-reagents (methanethiosulfonate) revealed that movements of the inner helices are involved in the activating action of FFA.

Our ideas about TASK1 function and the role of the TM2.6 residue were dramatically influenced by this newly available data.

3.2 Materials and Methods

Oocytes were injected with 0.1 ng of WT or mutant TASK3 mRNAs and incubated for 72 h at 18 °C and then another 24 h at 4 °C for TEVC experiments. For the TASK1 experiments 1 ng of RNA was injected with a 48 h incubation period.

TEVC experiments were performed with a Warner oocyte-clamp (OC-725-C). Data was digitalised with an Digidata1400A interface (Molecular Devices). Experimental control and recording was done with the WinWCP software (John Dempster). Data was aquired with a sampling rate of 2 kHz and a low pass cut-off frequency of 0.5 kHz. Voltage-ramp protocols were used to measure IV-responses. The ramps lasted for 0.5 s with ranges of −120 mV to 50 mV for low $[K^+]_{ext}$ and −100 mV to 100 mV for high $[K^+]_{ext}$ conditions. In each experimental condition 10 ramps were recorded, usually the first few contained anomalies, presumably to do with voltage dependent gating of endogenous currents (see also chapter 6). The last 5 sweeps of such a series were averaged and used for further analysis.

Experimental solutions for TEVC ('ND96 buffer') contained (in mM): 10 HEPES, 1.8 $CaCl_2$, 2 $MgCl_2$, 96 NaCl, 2 KCl, adjusted to the desired pH at room temperature with the hydroxide of the dominant cation. For solutions with pH 5.5 HEPES was swapped for MES. For experiments in 96 mM K^+ NaCl was exchanged for KCl.

The current response to pH_{ext} in fig. 3.5 was normalised to the value at pH 8.2 and fitted to the following equation (Reeve and Turner 2013).

$$\frac{I}{I_{\mathrm{pH}\,8.2}} = \frac{1}{1 + \exp\left(\frac{\mathrm{pK}_a - \mathrm{pH}}{n}\right)} \tag{3.1}$$

With pH representing the pH of the external solution, n representing a Hill coefficient and pK_a presenting the concentration of half maximal inhibition by protons (IC_{50}) expressed as pH value.

All data shown in the figures are given as mean ± standard error of the mean (SEM). Wherever applicable, all individual data points representing a measurement of a single oocyte are shown. Quantities such as overall

current, fractional block and rectification coefficient were tested for statistical significance using a one-way ANOVA (analysis of variance) and Tukey's honest significant difference test (Tukey's HSD). The estimated difference in these values to the WT mean and their p-values are given in table 3.1 at the end of the results section.

3.3 Results

Residue L122 of TASK3 was mutated to different residues (A,S,D,N,V) and function was tested by TEVC. Measurements were made in 3 conditions, with a physiological K^+ gradient at pH 7.4 and 5.5 and in symmetrical K^+ gradient (96 mM $[K^+]_{ext}$). These were chosen to assess function of H^+_{ext} sensitive gating of TASK3 and to check for abnormal rectification properties.

In physiological conditions no striking effects of the mutations on overall current levels could be seen. An outwardly rectifying *IV*-curve, typical for TASK3 in physiological K^+ gradient, could be seen for all mutants, except TASK3 L122D that shows diminished currents at higher voltages (fig. 3.2,

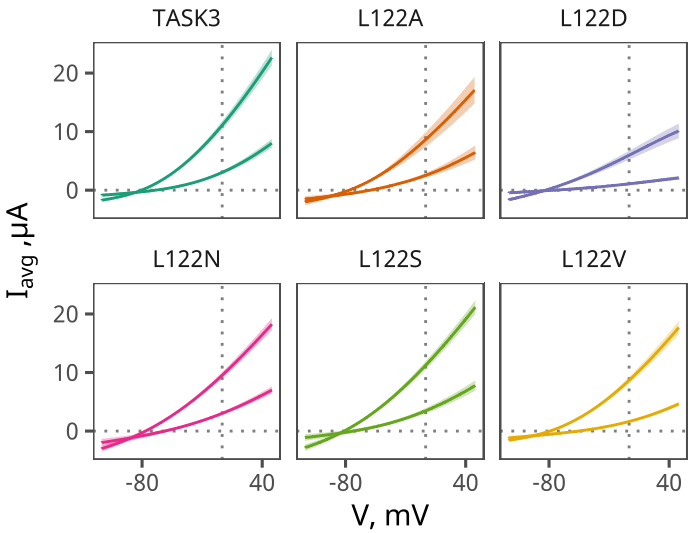


Figure 3.2: *TEVC IV-curves of 'hydrophobic cuff' mutants of TASK3* Currents were recorded with 2 mM $[K^+]_{ext}$ in pH 7.4 (larger currents), and pH 5.5 (smaller currents). Shaded areas represent SEM. Recordings were made in 3 different batches of oocytes, with at least 6 replicates per group and batch, n >16 oocytes for each treatment.

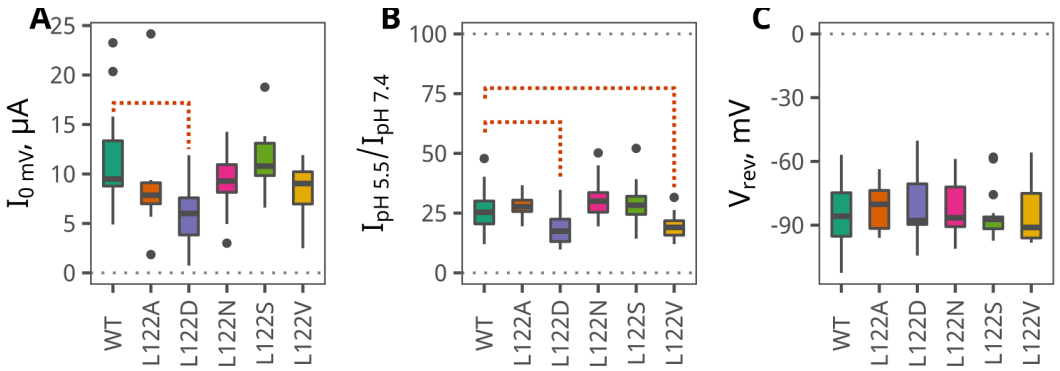


Figure 3.3: *Properties of the IV-curves in 2 mM K^+_{ext}* A: Magnitude of outward current at 0 mV of the 'hydrophobic cuff' mutants. B: Residual current of TASK3 at pH 5.5. TASK3 L122D and L122V are more sensitive to a pH of 5.5. C: Reversal potential of the *IV*-curves at pH 7.3. Statistically significant comparisons to the WT are marked with brackets. See table 3.1 for the exact p-values. A summary of how the box and whisker plots were generated can be found in section 2.2.3.

table 3.1). Sensitivity to external acidification was slightly increased in TASK3 L122D and L122V (fig. 3.3B, table 3.1). The reversal potential of the TASK3 WT *IV*-curves in 2 mM $[K^+]_{ext}$ was -85.5 ± 2.3 mV (mean $\pm$ SEM, no significant difference to the mutants, table 3.1). A summary of the reversal potentials measured is shown in fig. 3.3C. This is consistent with unimpaired K^+ selectivity of all mutants.

The tests in a symmetrical K^+ gradient showed Ohmic *IV*-curves in the L122S, A and N mutants. L122V and A as well as the wild type retained an outwardly rectifying behaviour. TASK3 L122D again stood out with an inwardly rectifying behaviour (fig. 3.4A).

Comparison of the ratio between currents at equivalent driving force of opposite sign (fig. 3.4B) show that the hydrophilic mutants have little preference for either current direction. Rectification in the WT was variable between batches of oocytes, however, ratios of 2:1 or more favouring outward currents were observed, such prominent rectification was never seen in the mutant channels.

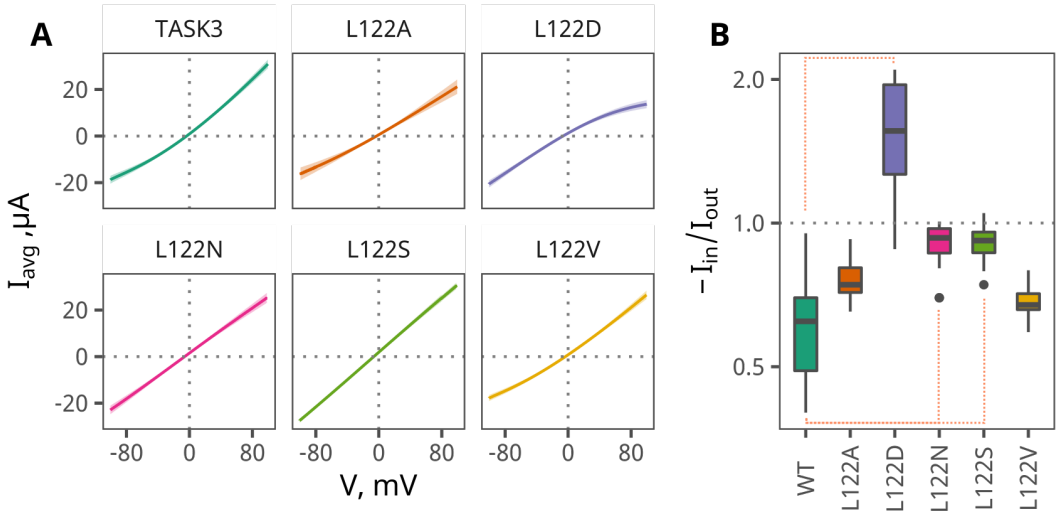


Figure 3.4: *Whole-cell currents in high K^+* A: IV-curves in symmetrical K^+ solutions (96 mM $[K^+]_{ext}$). Changing residue L122 to a smaller or hydrophilic residue results in an open-rectifying behaviour. The TASK3 wild-type maintains outward rectification under these conditions. The L122D mutation shows a saturating behaviour with increased voltage. Recordings were made in 3 different batches of oocytes, with at least 6 replicates per group and batch, n > 14 oocytes. B : Ratio of the inward and outward currents ('rectification coefficient') calculated from the data shown in A, y-axis is on a log scale. See table 3.1 for p-values of compared rectification coefficients.

Due to the absence of a GoF in terms of an increase in current, which was the initially proposed object of study, the project was terminated at this point. Instead, priorities shifted towards obtaining data to support ongoing structural studies of TASK1. This is described in the next section.

3.3.1 Functional validation of a crystallisation construct of TASK1

A thorough understanding of the relationship between structure and function is ideally based on an original structure of the protein of interest. Based upon previous experience with TREK1 and TREK2, the C-terminal domain of the protein was deleted in the trial construct. This aids crystallisation. Trials by our colleagues resulted in successful crystallisation of a TASK1 construct

WT vs	estimate	adj.p.value
Current at 0 mV, 2 mM K^+_{ext}		
TASK3 L122A	-2.4396128	0.2061235
TASK3 L122D	-5.0796478	**0.0000515**
TASK3 L122N	-1.5386646	0.5531296
TASK3 L122S	0.1478502	0.9999909
TASK3 L122V	-2.4073882	0.1806805
Reversal Potential in 2 mM K^+_{ext}		
TASK3 L122A	3.8800933	0.9254735
TASK3 L122D	3.6808632	0.9342457
TASK3 L122N	3.8024094	0.8790500
TASK3 L122S	0.1659455	1.0000000
TASK3 L122V	0.5581622	0.9999905
Fractional block at pH 5.5_{ext}		
TASK3 L122A	0.0233394	0.8992595
TASK3 L122D	-0.0762052	**0.0083142**
TASK3 L122N	0.0456649	0.1722570
TASK3 L122S	0.0352047	0.5657085
TASK3 L122V	-0.0659212	**0.0291434**
Rectification coefficient in 96 mM K^+_{ext}		
TASK3 L122A	0.1527340	0.1248858
TASK3 L122D	0.9626060	**0.0000000**
TASK3 L122N	0.2991190	**0.0000184**
TASK3 L122S	0.3006294	**0.0000253**
TASK3 L122V	0.0748918	0.7739354

Table 3.1: *Statistical analysis* Differences of parameter measured in mutant channels to the mean of TASK3 WT and their p-value. All values were calulated by one-way ANOVA and Tukey's HSD test. Significant comparisons are highlighted in bold.

truncated at position 259 (TASK1Δ259–394, hereafter named ΔC). To ensure the functional activity of this truncated construct, it was expressed in oocytes, and currents were examined in TEVC. Responses of TASK1 to changes in extracellular pH were recorded to assess whether this physiologically relevant stimulus still affects the truncated channel as expected.

Basal currents of TASK1ΔC were increased relative to the WT from $6.0 \pm 7.0\,\mu A$ to $17.2 \pm 1.7\,\mu A$ (mean ± SEM of the pooled baseline data of the experiments in fig. 3.5, n =14 each). Currents of both constructs were reliably blocked by

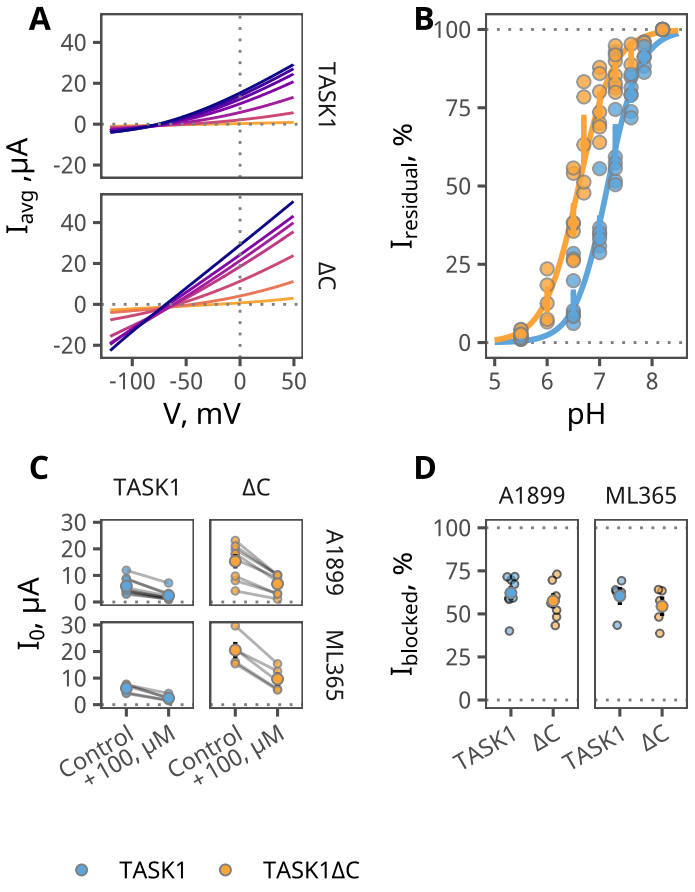


Figure 3.5: *Validation of TASK1ΔC* A: Whole cell currents recorded from ooocytes at pH values from 5.5 (yellow) to 8.2 (purple), 2 mM $[K^+]_{ext}$. Number of cells: TASK1 7, TASK1ΔC 8. B: Normalised currents (to amplitude at pH 8.2). Solid coloured line show the result of a logistic fit. fits were restrained to include 1 and 0 as their extreme values eq. 3.1. C: Blocked current after application of 100 nM blocker solution to the outside of the oocyte.

extracellular acidification. The truncated channel appears to be slightly more sensitive to closure by protons: The pH response is shifted from 7.20±0.05 to 6.65±0.05 (pK_a value of the fit of eq. 3.1, ±95% confidence interval of the estimate fig. 3.5 B).

High-affinity blockers (A1899 and ML365, Streit et al. 2011; Zou et al. 2010) were tested to probe normal function of the channel pore in which they are thought to bind. Importantly, there was no apparent change in block by 100 nM of the compounds added to the external solution (see fig. 3.5C). This suggests that the structure of the inner pore of the ΔC construct remains similar to the structure of the WT.

3.4 Discussion

The recently resolved structure of TASK1 allows us to directly visualise the position of TM2.6 residues. This information is vital to inform the interpretation of the mutagenesis data. Therefore I will briefly introduce the features of the structure before addressing the functional data at hand in section 3.4.3.

3.4.1 The X-gate

A cartoon of the structure including the TM2.6 site is shown in fig. 3.6. TASK1 has been captured in a closed state. Closure is achieved by the M4 helices crossing back over the pore axis and occluding it. This novel arrangement has been called an 'X-gate' and is stabilised by interaction of the HRE with M2 and the N-terminal end of M1 ('latch', fig. 3.6).

3.4.2 TASK1 crystallisation

The data at hand confirm that TASK1ΔC is a fully functional K^+ channel and maintains its hallmark sensitivity to pH_{ext} (albeit with a shifted response). The increase in current amplitude while retaining other properties can be explained by a trafficking effect. TASK1 surface expression is determined by the interplay of an ER retention motif and auxiliary proteins such as 13-3-3 (reviewed in Kilisch et al. 2015). The truncation at E259 removes this ER retention signal and this is expected to enhance surface expression and by extension overall current.

Both truncated and WT channel retain their sensitivity to TASK1 specific blockers. This suggests that the conformation of the inner pore in which

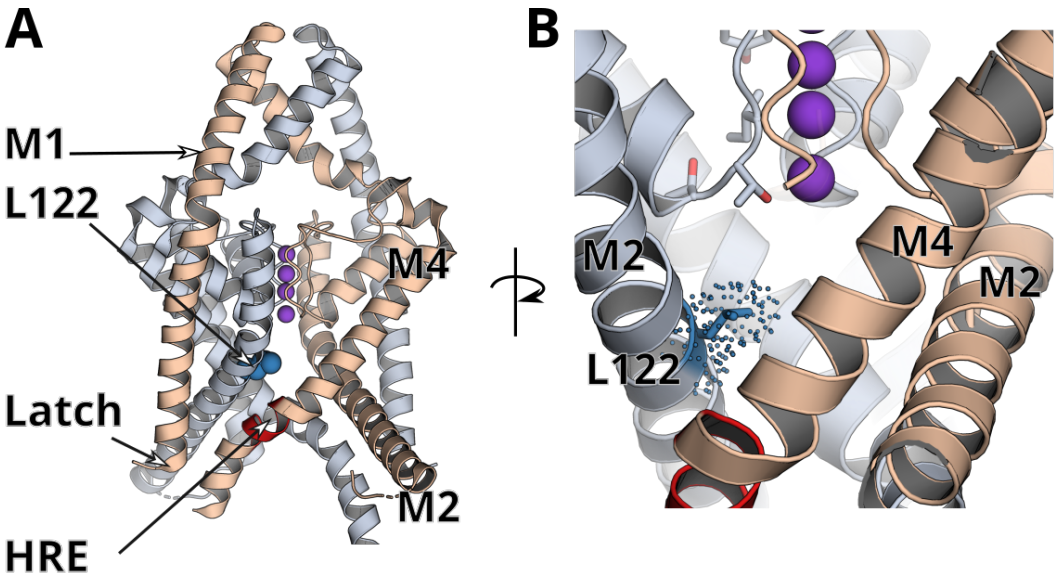


Figure 3.6: *Structure of TASK1 with a closed X-gate* Chain A and B of the dimer are coloured in pale blue and red. A: lateral view of the channel. The bottom of structure is occluded by M4 crossing the pore axis and closing it. This closure is mediated by a kinked traverse section of M4 corresponding to the HRE sequence, contacts with M2 of chain B as well as contacts with the proximal part of M1 ('latch') M3 and pore helix of chain A have been removed to allow a view into the channel. L122 is shown as spheres (dark blue). B: View into the pore, rotated around the pore axis relative to A. The side chain of L122 (shown with dots) points directly into the cavity below the selectivity filter and does not contribute to the interactions of the HRE with M2 that stabilises closure.

these are suspected to bind remains unchanged (Ramírez et al. 2017) and that this construct is suitable for structural analysis.

3.4.3 The TM2.6 site

The TEVC data collected here fail to demonstrate the lack of sensitivity to closure (by pH_{ext}) and overall increase in amplitude that is typical of similar mutations of TM4.6 (Veale et al. 2014b) as well as the robust increase in amplitude seen for L122 mutations by Ben Soussia et al. (2019).

However, significant differences can be found to other more subtle properties such as rectification in high K^+_{ext}. The reduced rectification observed with hydrophilic and small side-chain residue (L122A, S and N) is consistent

with a stabilisation of the gate at negative potentials or inward driving forces which promote closing of most K_{2P} channels (Schewe et al. 2016).

We do not know why the L122N mutation did not show the increased amplitude as found in the near identical experiment of Ben Soussia et al. (2019). However, TASK3 has a relatively high basal open probability (compared to TASK1). Consequently, the effect size for the GoF mutants of the two channels is different (larger for TASK1), with a less than 3-fold change for TASK3, which is among the smallest effects in the screen of all K_{2P} channels (Ben Soussia et al. 2019). In general, TEVC should be sensitive enough to determine such smaller differences. Indeed, a power calculation with the population estimates of this dataset concludes that about 1.4 fold changes should be detectable with the commonly accepted values of 0.05 and 0.8 for significance level and power using a t-test.

Curiously, TASK1 L122D shows an anomalous inward rectification behaviour, reminiscent of voltage-dependent Mg^{2+} or polyamine block in K_{ir} channels. This effect it likely to underlie the reduced amplitude of outward current through TASK3 L122D (fig. 3.3A). A similar pore charge substitution mutation in *Shaker* confers block by Mg^{2+} and inward rectification (Moscoso et al. 2012). Rectifying and saturating IV-curves of TM2.6 mutation were also observed in THIK2 I158D (Chatelain et al. 2013).

Interestingly, the TM2.5 site is crucial for Mg^{2+} block and and a determinant of the rectification properties of K_{ir} channels (Lu and MacKinnon 1994). Strong rectifiers (eg $K_{ir}2.1$) have a negative charged residue in this position (D), while weak inward rectifying channels harbour a neutral residue (N, $K_{ir}1.1$). Given that of all tested mutations only the negative charge of TASK3 L122D conferred this effect, it seems likely that this negative charge enables block by intracellular divalent cations.

The charge- and size-dependent effect of TM2.6 mutations can be found in nearly all K^+ channels in which it has been investigated. A detailed mechanistic assessment of such mutations (in MthK, Shi et al. 2011) suggested an effect of the mutation on stability of the gate and coupling to the activation gate. This is based on the residue-size dependent effect on the mutant channels' response to Ca^{2+} and the involvement of TM2.6 in packing against the adjacent subunit's inner helix.

A very recent study (Al-Moubarak et al. 2019) found the same size-dependent pattern for mutations of TREK1 and could also directly relate the current enhancement by FFA to movements of the inner helices with an MTS crosslinking experiment.

While we have no structural information of the open state of TASK1, it is tempting to speculate that the interaction of M2 and M4 needs to be broken in order for the X-gate to open and that based on the phenotype of TM4.6 mutants (see below) G236 and L122 are crucial for coupling the gates movement to conformational changes at the SF.

In K_{2P} channels, the TM4.6 site mutations confer a gain of function with a resistance to inhibitory stimuli that is consistent to such a coupling effect. While TM2.6 points directly into the cavity and the ion conduction pathway (fig. 3.6B), a strong direct effect of mutations at this position on unitary conductance of mechanosensitive K_{2P} channels has not been observed (Ben Soussia et al. 2019). In agreement with this idea, currents through the defective G236R mutant in TASK3 (TM4.6) can be rescued by other known GoF mutations and activators. Possibly conduction through G236R is preserved and it is mostly a closure of the lower gate (alleviated by the above interventions) that results in loss of function.

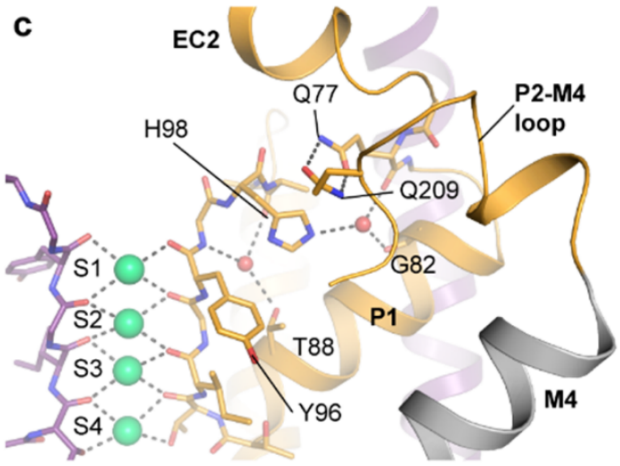


Figure 3.7: *The molecular bowstring in TASK1* View of the interaction at the extracellular end of TASK1. In other K^+ channel this region defines selectivity and gating. Protonation of H98 is likely to be a crucial event in TASK1 closure through extracellular acidification. Taken from Rödström et al. (2019), figS2c.

Bulky substitution mutants (G236F) were in particular resistant to closure by muscarine mediated inhibition. Such inhibition depends on the presence of the HRE (Talley and Bayliss 2002) which we now know constitutes the X-gate of TASK channels.

A dominance of a lower-gate or coupling effect also explains the lack of effect TM2.6 mutations on external pH gating observed here. In TASK channels the 'molecular bowstring' of the outer SF is formed of a sensing histidine residue (Rajan et al. 2000, see fig. 3.7). Closure by protons is likely to be mediated by directly affecting the SF, not the lower gate. How the X-gate influences the SF gate and how this coupling is exactly realised is a central question for the understanding of TASK function. Based on mutagenesis (Veale et al. 2014b; Ashmole et al. 2009; Al-Moubarak et al. 2019) and precedent from bacterial K^+ channels (Cuello et al. 2010a) the TM4.5 and 6 positions are likely to be central in this process.

Furthermore, it has since been demonstrated that the unusually low permeability of TWIK to K^+ can be attributed to its unusual SF properties (Nemetian-Ardestani et al. 2019). This gives secondary importance to an additional effect of the 'hydrophobic barrier' (Aryal et al. 2014a).

Conclusions

The striking effects of TM2.6 mutations in K^+ channels seem to be based on a combination of several different mechanisms:

a: Contribution to a subunit interface The second membrane spanning helix of K^+ channels undergoes conformational changes during activation gating. This includes the packing of these helices of two subunits against each other by hydrophobic contacts. This is conferred by the TM2.6 residue and its vicinity.

b: Contribution to a coupling event Coupling of the TM2 movements to the filter gate of KcsA occurs by a steric clash at position TM2.5 with the second threonine residue of the SF sequence (Cuello et al. 2010a). The size-dependent effect of such coupling phenotypes in MthK, TREK1 and TASK3 mutations (Shi et al. 2011; Veale et al. 2014b; Al-Moubarak et al. 2019) hints to such a steric clashing event of this residue as well.

c: Contribution to pore electrostatics The TM2.6 residue points into the pore and contributes to its lining at a crucial point: the cavity in which K^+ is stripped of its hydrating waters. The electrostatics within the cavity is likely to be crucial for the stabilisation of K^+ in the pore and conduction (Roux 1999). A putative intracellular blocking event observed in TASK3 L122D is consistent with this. The contribution and interaction of pore electrostatics with regard to both conduction and gating can be exploited by activators of mechanosensitive K_{2P} channels. This forms the basis of the following chapter.

Chapter 4

Activators of TREK2 on the microscopic Level

4.1 Introduction

Due to their involvement in nociception K_{2P} channels and TREK channels in particular have attracted attention as putative target structures for the development of novel analgesics (Mathie and Veale 2015; Alloui et al. 2006).

TREK channel openers are predicted to hyperpolarise the resting membrane potential and therefore to dampen excitability of nociceptive sensory neurons. This would result in decreased sensitivity to painful stimuli.

The compound BL1249 was discovered by its effect on bladder smooth muscle (mediated by TREK1 and possibly BK channels, Tertyshnikova et al. 2005). The molecular structure of the drug is shown in fig. 4.1. Beyond K_{2P} channels, BL1249 activates a number of K^+ channels such as BK and hERG (Schewe et al. 2019). Nevertheless, BL1249 is an attractive lead compound to

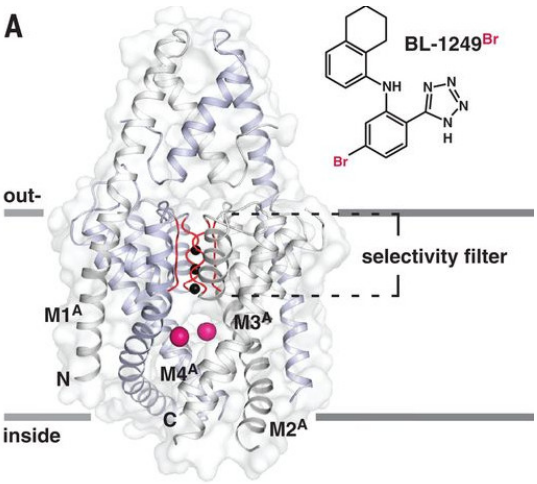


Figure 4.1: *Binding of BL1249* Cartoon depiction of the anomalous density peaks corresponding to a brominated BL1249 bound to TREK2. Additional pharmacological and computational assessment of the binding site was consistent with BL1249 binding in the cavity and being exposed to the channel conduction pathway. Taken from Schewe et al. (2019).

develop more selective drugs and attempts were made to study and improve this undesirable property (Pope et al. 2018; Iwaki et al. 2019).

TREK channel activating caffeate compounds have analgesic effects *in vivo* (Vivier et al. 2017) and the development of specific TREK activators has gained some traction with several candidate compounds emerging out of parallel drug screenings such as ML335 (Lolicato et al. 2017) and GI-530159 (Loucif et al. 2018).

4.1.1 Known mechanisms of TREK activators

Activators of TREK channels must act via its common SF gate (Bagriantsev et al. 2011; Bagriantsev et al. 2012; Piechotta et al. 2011). Recent structural and functional studies have revealed the binding sites of ML335 behind the selectivity filter loop (in TREK1, see fig. 4.2, Lolicato et al. 2017) whereas BL1249 binds in a cavity adjacent to the intracellular SF entrance (TREK2 fig. 4.1, Schewe et al. 2019).

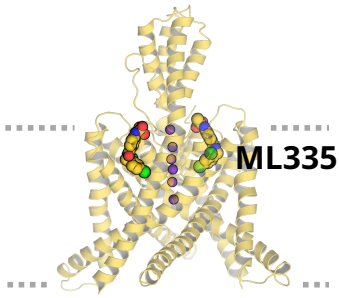


Figure 4.2: *Binding of ML335* Cartoon depiction of the structure of TREK1 with ML335 bound (6CQ8). ML335 (spheres) binds behind the selectivity filter.

BL1249 is a modulator of pore electrostatics

The data presented here alongside further data presented in that study were interpreted as evidence for a general mechanism of stabilising K^+ channel SF gates by increasing occupancy of the S4 binding site (Schewe et al. 2019).

The drug was found to bind below the SF by a combination of crystallographic, computational and electrophysiological methods. MD simulations showed, that conduction as well as occupancy of the cavity K^+ binding site would be increased by the presence of BL1249 (Schewe et al. 2019).

BL1249 achieves this effect by introducing partial negative charges to the 'nanocavity' area below the selectivity filter. The protonable tetrazole ring of BL1249 is predicted to enter the conduction pathway and contribute to stabilisation of K^+ below the SF (Schewe et al. 2019).

Pore electrostatics are a major contributor to K^+ channel conduction and selectivity (Nimigean et al. 2003; Roux 1999). High conductance of K^+ is aided by electrostatically attracting cations to the channel entrance ('electrostatic funnelling', Brelidze et al. 2003). Accordingly, a funnelling mechanism was hypothesised to account for the action of BL1249 on both conduction and gating via increased occupancy of the S4 site (Schewe et al. 2019).

ML335 stabilises the C-type gate

The K_{2P} channel SF gate shares the overall architecture with channels such as KcsA and K_v channels that undergo C-type inactivation (as introduced in section 1.5.3). The gating of TREK1 channels by stimuli such as external pH share properties of C-type inactivation such as sensitivity to $[K^+]_{ext}$ (see also section 1.6.2, Cohen and Schulten 2004).

The upper part of M4 of TREK1 also carries several sites of gain of function mutations (Bagriantsev et al. 2011) and interfaces with the pore helix and SF structures in a way that stabilises the SF gate.

Binding of ML335 behind the selectivity filter stabilises these interfaces similarly to GoF mutations in the same region (G124I, Lolicato et al. 2014). This is likely to prevent collapse into a yet undetermined C-type inactivated conformation.

4.1.2 Structural determinants of TREK2 conductance

A hallmark of TREK channel gating is bursting behaviour with short flickery openings. In fact, the discovery of a channel identifiable by these properties pre-dates the cloning of TREK channels (Kim 1992).

The single channel IV-curve of TREK2 channels is strongly inward rectifying. Different subconductances have been observed in expression systems (Bang et al. 2000; Kang et al. 2007) as well as in reconstituted membrane systems (Peter Proks, unpublished data).

Some of the different conductances of TREK2 could later be attributed to different TREK2 proteins. There are 5 different possible TREK2 protein chains that can be produced by a combination of RNA splicing as well as ATI (see section 1.6.2 and fig. 1.12). The occurance of small conductance TREK2 could

be attributed to the ATI variant starting at the first methionine (M_1, TREK2b-FL) whereas the variants produced by starting from M_2 and M_3 conduct bigger unitary currents (Simkin et al. 2008). Some 'subconductances' observed previously thus stemmed from a mixture of multiple different TREK2 proteins with different conductances present in a single patch, however, recordings from cells transfected with TREK2ΔM_3 still have at least 2 different open levels (Simkin et al. 2008).

4.1.3 'Fast' gating

Measured differences in open-channel current (the amplitude of a channel opening) do not necessarily reflect a real change in conduction through the channel. As an example, the open channel IV-curve of BK channels (in certain conditions) and chlorella virus K^+ channels (K_{cv}) paradoxically develop a negative slope at high positive potentials (Rauh et al. 2017; Geng et al. 2013; Schroeder et al. 2013). This is due to the properties of low-pass filters that are used to record single-channel data.

Low-pass filters distort the signal of higher frequencies and ion-channels may gate at high-frequencies beyond the filter cut-off ('fast gating'). This results in short channel-openings that appear distorted in a filtered recording.

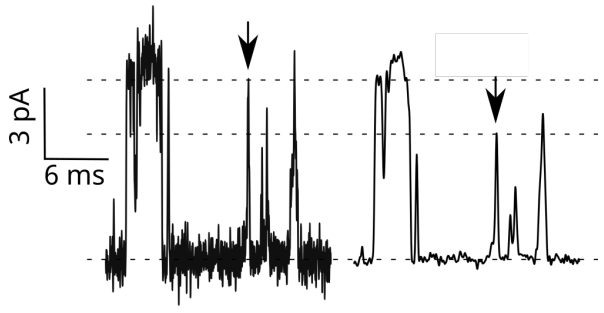


Figure 4.3: *Example for distortion by low-pass filters* Openings of TREK2 with two different low-pass filters. Left, signal filtered with the 10 kHz Bessel filter of the Axopatch 200B and after additional filtering with a Gauss-filter (2 kHz, 0.6 kHz effective bandwidth). The arrows and dotted lines show the reduction of amplitude of a short channel opening.

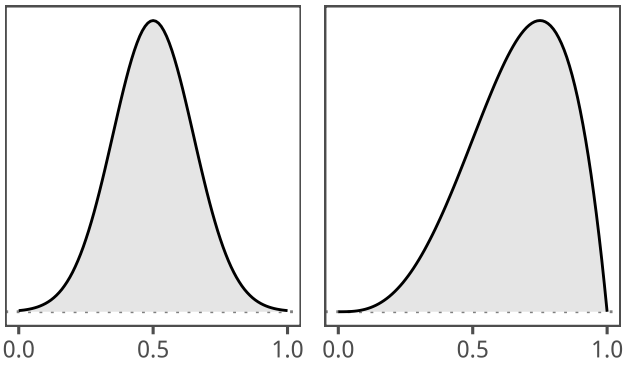


Figure 4.4: *Distribution shapes of amplitude histograms* Example of the probWability density functions underlying amplitude histograms. Left: normal or Gaussian distribution with mean 0.5 and standard deviation of 0.15. Right: β-distribution with shape parameters $\alpha = 4$ and $\beta = 2$.

These distortions result in a peaked shape, with reduced amplitude (fig. 4.3, arrows).

Amplitude histograms of such distorted signals may have a characteristically skewed shape. In this case, the shape of the open state peak can be described by the beta-distribution (example plotted in fig. 4.4 right, Fitzhugh 1983) instead of a Gaussian-distribution (fig. 4.4 right) for well resolved openings. A fit of the beta-distribution allows the rate constants of the underlying fast gating process to be inferred in the case of filtering by a simple 1 pole filter. Consequently, the shape parameters α and β then correspond to opening and closing rate constants. This method was first been deployed by Yellen (1984) to measure the rates of Na^+ block of the BK channel.

Examples of beta-functions with different values for their shape parameters corresponding to the case of fast or slow gating are shown in fig. 4.5.

Estimates of the open-channel current from visibly skewed amplitude histograms (apparent current, I_{app}) underestimate the true rate of transport through the open channel (I_{true}) because the peak of the beta-distribution is shifted towards a smaller amplitude (see fig. 4.5B and C). However, analysis of the histograms combined with kinetic modelling of the fast gating to fit the beta-distribution shape can yield even more information from single channel recordings, including estimates of I_{true} (reviewed in Schroeder 2015).

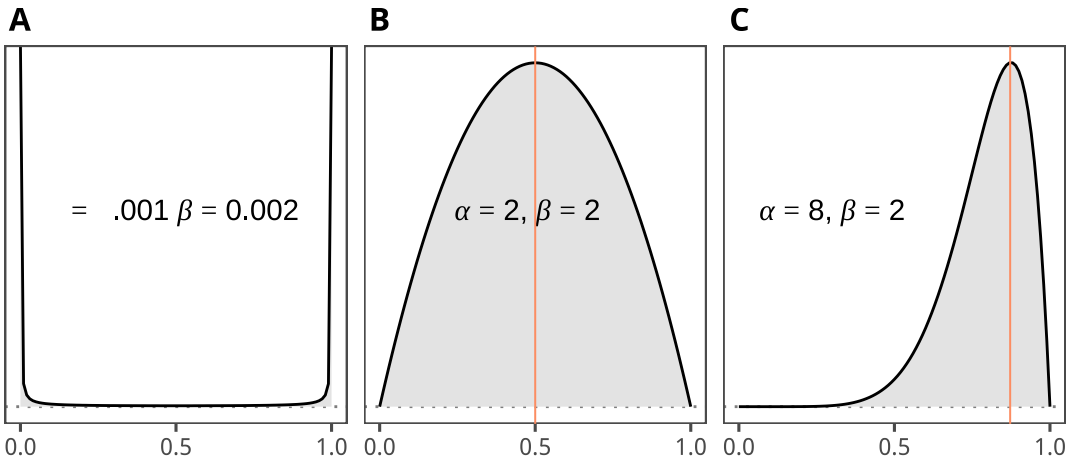


Figure 4.5: *Example scenarios of fast gating* The beta function represents the distribution of a filtered signal that assumes a value of either 0 (closed) or 1 (open). The shape parameters α and β represent the closing and opening rates. A: The rate constants are slow, only values of 0 and 1 are sampled, B: rate constants are large (fast) and symmetric, a broad 'smeared' peak at 0.5 can be seen C: asymmetric rate constants. Do note that in all cases with fast rate constants the peak (indicated by the red vertical lines) lies between 0 and 1 and I_{true} (1) is underestimated.

An increase in I_{app} may be therefore be observed as a result of a change in fast gating. If an otherwise short lived open state is stabilised this may result in longer, less distorted openings and I_{app} will lie closer to I_{true}. Different fast gating regimes may result in distinct values of I_{app} and can appear as subconductance levels in amplitude histograms although the underlying I_{true} is unchanged (Läuger 2009). This poses a challenge to interpreting I_{app} values in the context of activation mechanisms in which we might expect an elongation of opening times.

Work from our colleagues (Schewe et al. 2019) suggested that the position in which BL1249 binds may have a direct effect on single-channel conductance (γ). To test an effect of BL1249 on conduction as predicted by MD simulations described by Schewe et al. (2019), I measured open-channel currents of TREK2ΔM$_3$ activated by ML335 and BL1249.

4.2 Materials, Methods and Analysis

Single-channel currents from HEK293 cells expressing TREK2ΔM3 were recorded with the patch-clamp technique in the inside-out configuration. The symmetrical solutions used contained (in mM: 116 KCl, 5 Tris (pH 7.2), 2 K_2 EDTA (ethylenediaminetetraacetic acid).

Responses to 1 s pulses to a range of voltages from −100 mV to 100 mV were used to obtain an all-point amplitude histogram at each step. Open-channel amplitudes were determined by finding the local maxima of a log-scale smoothed density estimate of the data using the findPeaks function implemented in the pracma R package (Borchers 2018). Correct estimation of the amplitudes was checked by hand and corrected if necessary by reading the amplitude from histograms displayed using WinEDR software (Dempster).

Following the initial recording, activators BL1249 or ML335 were applied in concentrations close to their respective EC_{50} values (3 and 10 μM). The largest occurring opening levels in a stretch of recording were then analysed.

4.3 Results

In order to probe the effect of BL1249 on conductance, open-channel IV-curves of TREK2ΔM_3 were determined from single channel recordings. The results are summarised in table 4.1.

Behaviour of TREK2ΔM_3

TREK2ΔM_3 is reported to have at least two subconductance states (Simkin et al. 2008). In my recordings channel behaviour was often more variable, with subconductances as well as modal behaviour of the channels. Even within

Table 4.1: *Summary statistics of single channel conductances* Mean amplitudes (in pA), conductances (pS, I_{open} divided by V) and indicated summary statistics. This data set represents paired measurements in which after recording conductance at baseline (Control) either ML335 or BL1249 were applied. The rectification coefficient was calculated as $\left|\frac{I_{inward}}{I_{outward}}\right|$.

Condition	V	n	I_{open}	Min. γ	γ	Max. γ	Rect.
Control	-100	11	−29.24	255	292 ± 8	352	1.64
	100	9	17.80	123	178 ± 9	212	—
3 μM BL1249	-100	6	−35.21	306	352 ± 16	408	1.64
	100	5	21.40	176	214 ± 17	273	—
10 μM ML335	-100	5	−29.42	285	294 ± 5	309	1.43
	100	4	20.56	161	206 ± 16	229	—

identical conditions in the absence of activating stimuli, channels exhibited show variable behaviours within bursts, different P_o and conductance (see fig. 4.6).

The additional smaller conductances do not seem to cluster with the published 180 and 220 pS conductance states of TREK2ΔM$_3$ and there is no

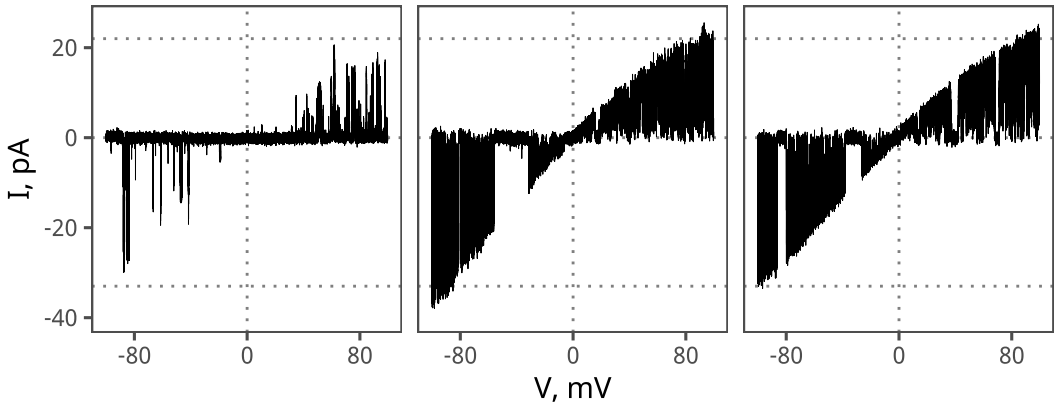


Figure 4.6: *Variability in TREK single-channel behaviour* Traces of single-channel recorded with a voltage-ramp protocol (−100 mV to 100 mV, 0.4 s). The examples shown are from 3 separate patches and were chosen to give an idea of the open-channel IV-curve (openings at a wide range of potentials). There may be low P_o with short flickery openings (left). High P_o with bursts of a poorly defined amplitude in the outward direction (middle) or bursts with a slightly reduced amplitude (right). Horizontal lines were drawn at −33 pA and 22 pA which represent amplitudes consistent with the large conductance of TREK2ΔM$_3$ at −100 mV and 100 mV respectively.

obvious pattern to their occurrence. This was particularly prominent in the outward direction.

Conductance in baseline conditions varied between 120 pS to 210 pS in the outward direction (see table 4.1). IV-curves show inward rectification with inward currents being 1.6 times larger than outward currents at 100 mV.

Due to this variability and unpredictable behaviour the data seemed unsuitable for rigorous kinetic analysis of gating and P_o. Therefore I limited analysis to open-channel IV-curves and further focused on within-patch comparisons to account for the variability across patches.

The conductance of activated TREK2ΔM_3

Example of such pairwise comparison for raw single traces are shown in fig. 4.7. Application of either activator resulted in dramatic increases of P_o. This is the expected principal effect of both of these activating drugs. Additionally, with any mode or conductance levels present an increase of single-channel conductance was observed with application of BL1249. In contrast, application of ML335 did not increase the single-channel conductance except in one patch.

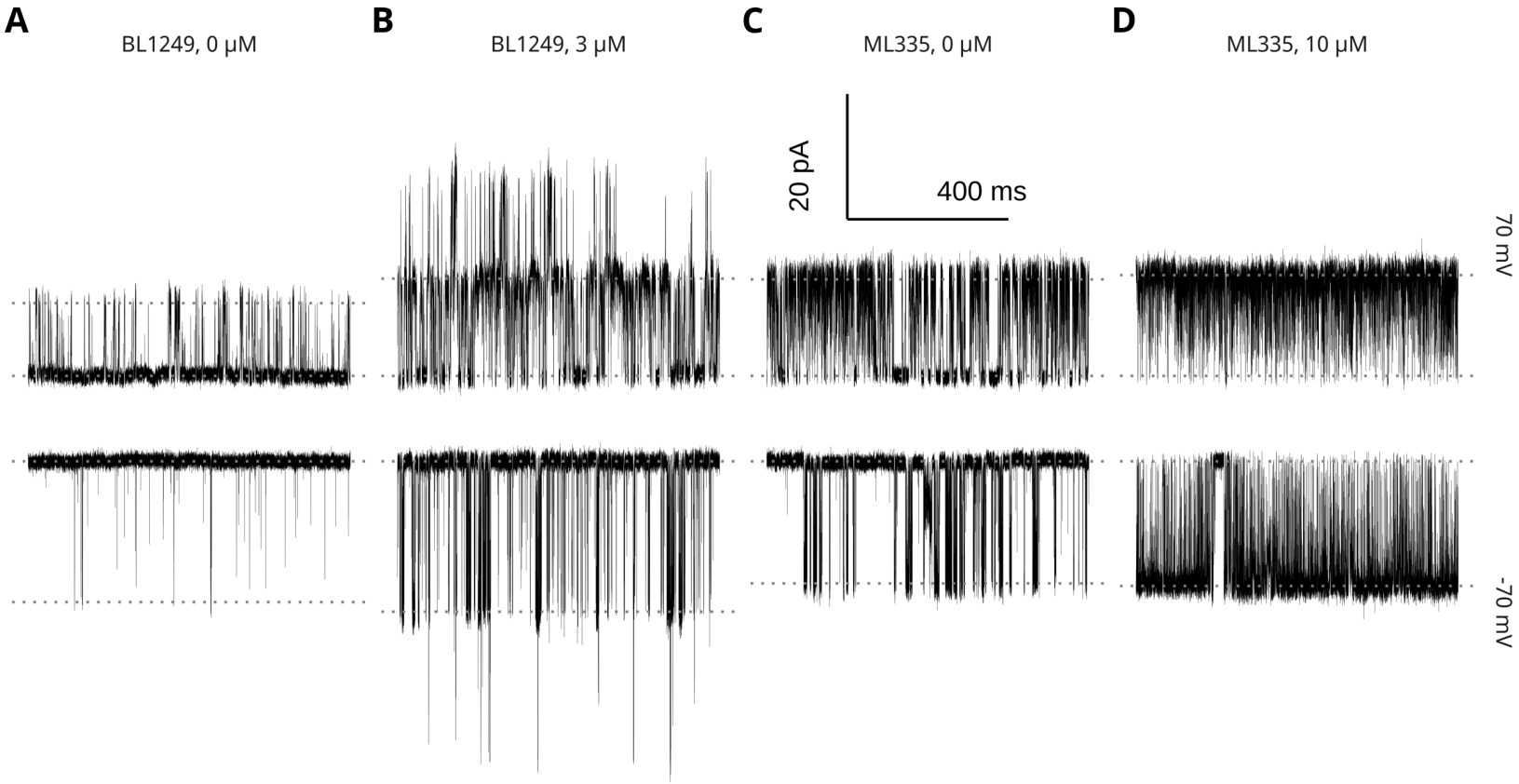


Figure 4.7: *Example traces of pharmacologically stimulated TREK2* Time course with channel openings of TREK2ΔM_3 at $\pm 70\,\mathrm{mV}$. Traces were measured in two different patches. There is an increase of conductance within the same patch for BL1249, and not for ML335. The open channel amplitude varied within patches and subconductances are visible. Traces in column A and C represent identical conditions in separate patches.

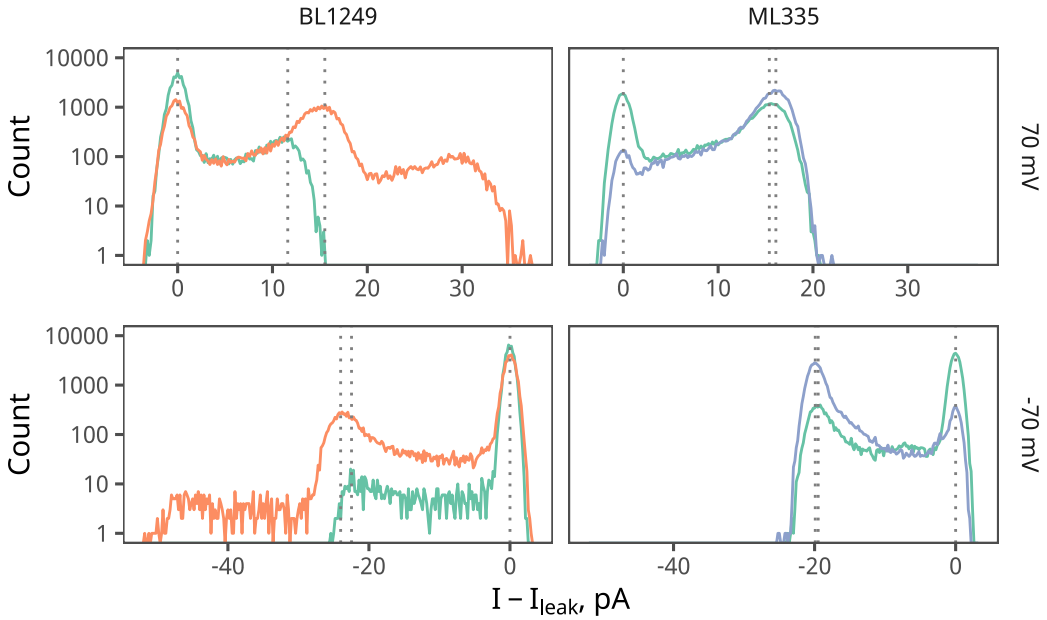


Figure 4.8: *Amplitude Histograms of stimulated TREK2ΔM$_3$ currents* All-point histograms of 0.95 s of recording for each condition. Do note that all open-state peaks show a broadened, skewed shape indicating fast gating and filter distortion.

Corresponding amplitude histograms are shown in fig. 4.8. Here we can see visibly skewed distributions in all conditions tested (at a 10 kHz bandwidth, fig. 4.8). This demonstrates that gating at rates exceeding the cutoff frequency occurs in all circumstances.

Open channel *IV*-curves of all recordings and paired amplitudes are plotted in fig. 4.9. While variability is high and the effect subtle (∼20% increase), appreciable increases of conductance occur only with BL1249, most prominently at large negative potentials (fig. 4.9A inset) in which subtle changes to conductance will be more readily apparent due to the size of the currents (33 pA to 40 pA).

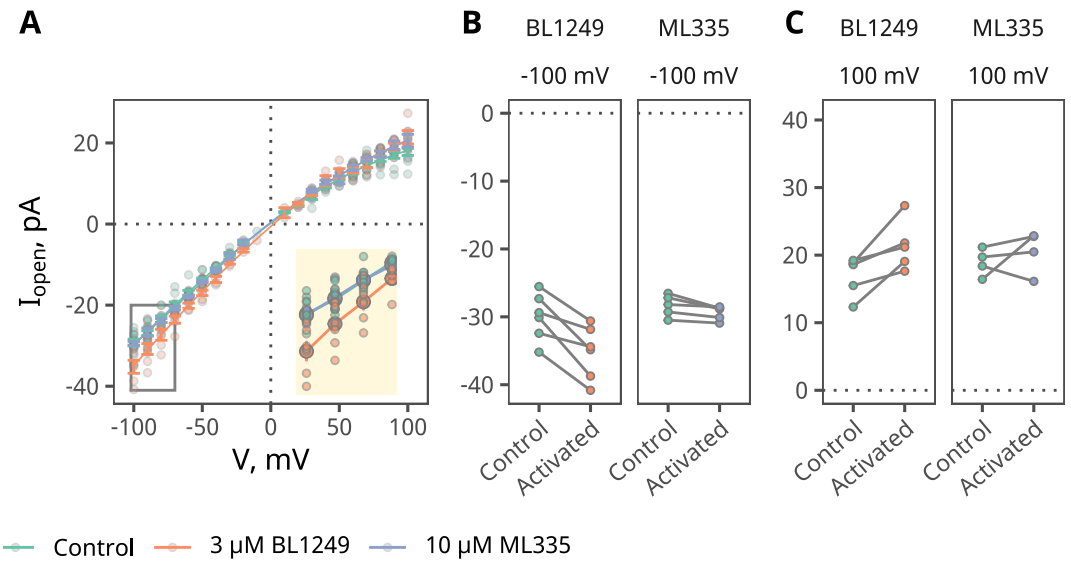


Figure 4.9: *Activators of TREK2 and conductance* A: Open channel IV-curves of TREK2delM3 with and without 3 µM BL1249 and 10 µM ML335. Inset: Enlargement of the inward currents at large negative potentials, here the signal-to noise ratio is most favourable to discerning the effect of BL1249. B, C: Amplitudes at ±100 mV, values determined on same patch are connected with a line.

4.4 Discussion

The application of BL1249 was followed by a 20 % apparent increase of γ while no change was seen for ML335. Similar increases have been observed for BL1249 with reconstituted TREK2 channels (Michael Clausen, unpublished data) and TREK1 in oocyte patches (Schewe et al. 2019).

According to eq. 1.6 we would expect at most a 20 % increase of membrane current by the effects on γ alone, if P_o was unaffected. This is by far exceeded in macroscopic current recordings of TREK2 activation by BL1249. Therefore increase of P_o is the expected main effect of the activator. Also, due to the large, near diffusion limited unitary conductance of TREK2 there is only little headroom for an increase. Larger relative increases in conductance have

been reported for TREK1, which has a smaller single-channel conductance (Schewe et al. 2019). While the observed increase in γ is interesting from a mechanistic point of view (see below), this effect will only make a small contribution to the robust activation that can be observed with application the drug. However, the effect on conduction could be a larger contributor in other K^+ channels, especially those with small single-channel conductances.

Inspection of the amplitude histograms with skewed distribution shapes tells us that fast gating processes occur in TREK2ΔM_3 and that all obtained values of the open channel current might be underestimations of I_{true}.

It is entirely plausible that channel activators (as well as activating stimuli) would increase the lifetime of channel openings. This would increase the observed I_{app} while I_{true} may remain the same. Therefore we must be careful to attribute the *observed* increase of open-channel current with application of BL1249 to an increased γ. No matter what it signifies mechanistically (see below), this observed increase seems to be specific to activation by BL1249. Other activating stimuli of TREK channels such as stretch (Clausen et al. 2017), phosphorylation (Bockenhauer et al. 2001) and ML335 do not increase observed open channel current. Gain of function mutations that introduce negative charges into the pore also do not show dramatic increases to γ in mechanosensitive K_{2P} channels (Ben Soussia et al. 2019).

The SF region of K^+ channels is highly conserved and is thought to represent the only resistance ('voltage drop') in the permeation pathway (Jiang et al. 2002). However, K_{2P} (as well as other K^+ channel) unitary conductances vary between 20 pS to 220 pS (THIK and TREK2ΔM_3 respectively Kang et al. 2014; Simkin et al. 2008). This difference can only be accounted for by additional resistance to permeation present in some K^+ channels. Such differences can be found in the inner pore where point mutations introducing negative

charges to the cavity have been shown to increase single-channel conductance (Brelidze et al. 2003; Nimigean et al. 2003; Moscoso et al. 2012; Shi et al. 2011).

The BK channel has 8 charged residues at its intracellular entrance, that are crucial for its large single-channel conductance. These residues are reported to exert their effect not by changing the geometry of the permeation pathway (by a conformational change) but through electrostatics alone. The local concentration of K^+ at the channel mouth is increased by the attraction of negative charges and because γ is concentration dependent this will result in larger conductances compared to channel without such a charged ring. TREK2 contains 4 of these 8 negative charges in the homologous positions and this is likely contributing to its large single-channel conductance.

The binding site of BL1249 is immediately below the entrance to the SF. Molecular docking results suggest that the partially negatively charged tetrazole moiety of the drug points toward the conduction pathway (Schewe et al. 2019). In contrast, ML335 binds behind the selectivity filter and stabilises interactions of filter loop and pore helix that are implied in C-type inactivation gating of K_v channels and KcsA and the related gating process of TREK channels (Cohen and Schulten 2004; Lolicato et al. 2017). Binding of ML335 is not accompanied by a conformational change of the SF or its binding sites that would imply an effect on conduction (Lolicato et al. 2017).

A likely explanation for the data is therefore that BL1249 increases γ via local increase in K^+ concentration mediated by electrostatic funnelling at the SF entrance.

Several alternative scenarios would also explain this observed increase, some involving fast gating:

a: Binding of BL1249 stabilises a pre-existing high subconductance state

b: Binding of BL1249 increases open times and causes an increase of I_{app}

Whereby others are assuming a genuine increase of conductance:

c: BL1249 binding causes a conformational change, likely in the intracellular pore region. This results in larger single-channel conductance.

d: BL1249 is membrane permeable therefore it may partition into the membrane thereby acting like a charged lipid. Charged lipids can change the surface charge of the membrane and likewise may be increasing K^+ supply at the channel mouth (as considered in Park et al. 2003).

These possibilities are now addressed in turn.

Scenario a, Binding of BL1249 stabilises a pre-existing high subconductance state At present, we do not know whether the known subconductances of TREK2 reflect different gating modes resulting in distinct values of I_{app} or reflect different conformations with distinct I_{true}. Increase of the open-channel current was observed with any mode or sub conductance present. In some patches the open-channel current exceeded the currents expected based on the large TREK2ΔM_3 conductance (Simkin et al. 2008, see table 4.1 max. values). Therefore it seems unlikely that BL1249 changes preference for a large subconductance state.

Scenario b, Binding of BL1249 increases open times and causes an increase of I_{app} Given the variability and rectification of the open-channel IV-curves as well as the beta-distribution shapes encountered in amplitude histograms a contribution of fast gating to the observed increase of γ seems likely. Also, activation by BL1249 does not seem to increase open-time long enough to resolve I_{true}, in this case we would expect to see the measured values converge to I_{true} after stimulation and variability to decrease. Open-

channel currents determined from both activated and baseline recordings however showed large variability and beta-distributed amplitudes.

This scenario is also compatible with an electrostatic mechanism. 'Fast gating' of the BK channel SF is thought to occur through emptying and re-filling of the SF (Schroeder and Hansen 2007; Demo and Yellen 1992). K^+ depletion and refilling is also suggested to underlie K_{2P} channel voltage-dependent gating (Schewe et al. 2016). Local K^+ concentration would therefore be predicted to affect these processes favouring a stable and conductive SF and long opening times.

Scenario c, BL1249 binding causes a conformational change in the channel, this results in a higher conductance For the reason described above scenario c is difficult to test. We know from the shape of the distributions that we do not resolve I_{true}. Explicit treatment to whether a measured increase of I_{app} reflects an increase of I_{true} requires extensive analysis of stable single-channel recordings that can be described by a concise kinetic scheme (Schroeder 2015). This was unfortunately not the case for our data.

Scenario d, BL1249 partitions into the membrane thereby acting like a charged lipid BL1249 readily crosses membranes, its binding site is on intracellular side of the channel but it can achieve its activating effect in whole-cell patch clamp of mammalian cells as well as in *Xenopus* oocytes. The lipophilic molecule must therefore be able to be dissolved in the membrane, likely in a protonated state. Speculatively, the deprotonated drug would orient with the negatively charged tetrazole ring facing the aqueous phase, just like a lipid headgroup.

Scenario d. is very similar to the proposed electrostatic funneling mechanism. In this case an effect of conductance might be mediated by a non-specific effect of the drug in the membrane while the effect on P_o to be mostly mediated by the drug in its binding site. Such possibilities are also not mutually exclusive. Anionic lipid headgroups such as PIP_2 are known to activate TREK (Chemin et al. 2005). Manipulating membrane surface charge by action of lipids also has a profound effect on voltage-gating of K_v channels (Hite et al. 2014; Börjesson et al. 2010) and can be mimicked by drugs that insert into the membrane (Silverå Ejneby et al. 2018).

Conclusions

Apparent increase of γ by an activator is an interesting biophysical phenomenon and has rarely been observed. To my knowledge the only examples are $P2X_4$ receptors, where γ is increased through activation by the drug Ivermectin (Priel and Silberberg 2004) and TRPV channels where activation by lysophosphatidic acid confers the effect (Canul-Sánchez et al. 2018).

With application of BL1249 an increase to the open-channel current was observed. In the context of further evidence (Schewe et al. 2019) this suggests that activation of BL1249 occurs via a distinct mechanism that affects either conduction or fast gating. To test this hypothesis further, tests of the K^+-dependence of this putative electrostatic mechanism were conducted and the results are discussed in the next chapter.

Both increasing the lifetime of a flickery state or an increase in I_{true} are consistent with a mechanism of activation by BL1249 that involves electrostatics and K^+ occupancy. This mechanism is collectively supported by the structural, MD and binding competition data shown in Schewe et al. (2019).

Chapter 5

Inhibition of TREK currents in high ionic strength

5.1 Introduction

Voltage gating of K_{2P} channels is an important hallmark of their function and enables them to specifically shape the action potential firing patterns of the neuronal cells in which they are expressed (Brickley et al. 2007; MacKenzie et al. 2015).

The most prominent and well studied voltage regulated proteins are voltage gated K^+ and Na^+ channels (Na_v, K_v). These proteins sense the transmembrane electric field through the action of a voltage sensing domain (VSD). VSDs comprise 4 membrane spanning helices (S1-4). S4 contains positively charged residues that move along a series of positions ('clicks') in a groove formed from S1-3. This upward movement is coupled to the activation gate of the tetrameric channel and opens it. For K_v channels this movement corresponds to gating charge movement of 10-13 e_0 per channel (Noceti 1996;

Ishida et al. 2015, for *shaker and $K_v1.2$*) for the net conformational change and the resulting voltage activation curves have a sharp transition.

K_{2P} channels are also voltage gated but do not contain a VSD. This voltage sensitivity is therefore intrinsic to the pore domains. Voltage-dependent gating processes (both voltage activation and inactivation) with shallow transition curves and $\leq 2\,e_0$ gating charge estimates have been observed in a number of K^+ channels which lack VSDs such as KcsA (Chakrapani et al. 2007a), MthK (Thomson and Rothberg 2010), K_{cv} (Rauh et al. 2017; Santos et al. 2008) and K_{ir} (Choe et al. 2001).

A striking similarity between these phenomena is their dependence on the permeating ion. In some cases this could be traced back to the selectivity filter directly (Rauh et al. 2017; Rauh et al. 2018; Posson et al. 2012). Some of the above mechanisms resemble C-type inactivation by virtue of their dependence on $[K^+]_{ext}$ (Thomson and Rothberg 2010). In the case of KcsA, the recovery from inactivation is a voltage-dependent step (Chakrapani et al. 2007a).

With the exception of TASK channels (Rödström et al. 2019) K_{2P} channels are thought to gate exclusively at the SF (Piechotta et al. 2011), a property likely shared with other K^+ channels such as the BK channel (Wilkens and Aldrich 2006) and MthK (Posson et al. 2012; Posson et al. 2015). A principal role of the SF accessory to other gates has also been proposed in K_{ATP} channels (Proks et al. 2003). The KcsA activation gate, to which we owe the structural description of the bundle crossing gate (Doyle et al. 1998), has recently been assigned a merely auxiliary role in opening the SF gate (Heer et al. 2017).

In the case of K_{2P} channels, a recent study has made use of Rb^+ as a permeating ion to study the intrinsic voltage gating mechanism (Schewe et al.

2016). In that study it was shown that rather than sensing transmembrane voltage directly, K_{2P} channels sense the electromotive force of the permeating ion. This proposed mechanism of 'flux gating' involves opening of the channel through binding of the permeating ion to a depleted S4 binding site and is reminiscent of the voltage gating mechanism of ClC Cl^- channels where opening is coupled to the permeating ion's movement (Pusch et al. 1995; Chen 1996).

The gating charge of K_{2P} channels was estimated to be $\sim 2.2\, e_0$ and was interpreted as the ion moving into the focused electric field within the selectivity filter (Schewe et al. 2016). This region is theorised to comprise most, if not all of the 'voltage drop' across the membrane (Jiang et al. 2002). The prerequisite of this 'flux gating' mechanism in K_{2P} channels is that there are empty K^+ binding sites in the selectivity filter available for filling. However, the occupancy pattern of the SF binding sites at rest and during conduction still remain controversial (Kopfer et al. 2014; Kopec et al. 2018; Kratochvil et al. 2016; Kratochvil et al. 2017; Tilegenova et al. 2019). Selective conduction at high rates has been theorised to be only possible with simultaneous occupancy of all SF binding sites (Kopfer et al. 2014; Kopec et al. 2018).

The hard knock-on permeant ion mechanism was used to help explain the activating effect of the drug BL1249 (see chapter 4). Stabilisation of K^+ in the cavity by drug binding is thought to act on several different K^+ channels which lack a lower gate and thus gate primarily at the SF (Schewe et al. 2019).

The following series of experiments in high $[K^+]_{int}$ were initially designed to probe and extend these ideas. Surprisingly, I observed a reduction in overall TREK2 currents under these conditions that could be traced back to impaired gating in high ionic strength.

5.2 Materials and Methods

HEK293 cells were measured 24 h after transfection with plasmid DNA of TREK2ΔM_3 or TREK1c and TREK2b M60L, M72L (TREK2b-FL, fig. 1.12 Simkin et al. 2008; Staudacher et al. 2011). All measurements were recorded using with patch-clamp in the inside-out configuration. Pipette solutions contained (mM): 5 Tris, 2 K_2EDTA, 116 KCl. Internal test solutions contained 5 Tris, 2 K_2EDTA, 116 KCl (120 K^+ total) and an additional amount of chloride salt (KCl or NMDG-Cl) to make a total salt concentration of 250, 500 or 1000 mM. Tris-HCl was chosen over HEPES as a buffer system to minimise errors in K^+ concentration incurred by adding large amounts of KOH.

Voltage-clamp protocols were offset according to the expected Nernst and liquid junction potentials in each test solution. In this way a range of −100 mV to 100 mV net driving force for K^+ was sampled in each condition. Junction potentials were calculated with pClamp which implements calculations and ionic mobilities described in Ng and Barry (1995) and Barry and Lynch (1991).

As expected for K^+ channels in overexpression systems (Trapani and Korn 2003), current amplitudes in excised patches varied greatly. To compare IV-curve shapes irrespective of total current, amplitudes were normalised to the value at 70 mV in the symmetric 120 mM KCl solution eq. 5.1 (see fig. 5.1A).

$$I_{\text{norm}} = \frac{I}{I_{70\,\text{mV}}} \tag{5.1}$$

Macroscopic currents were aquired with 20 kHz sampling rate and low-pass filtered with a 2 kHz lowpass filter. Single-channel recordings were acquired at 50 kHz and filtered with 10 kHz.

Single-channel amplitude were determined as outlined in section 4.2. Driving forces were calculated with the Nernst equation assuming a room temperature of 22 °C (using eq. 1.1).

Open-channel IV-curves were fit with a 3rd order polynomial (eq. 5.2) using linear regression in R.

$$f(x) = a_1\,x + a_2\,x^2 + a_3\,x^3 + c \tag{5.2}$$

The model has no mechanistic meaning and was chosen for its ease of implementation, fitting and calculation of the slope (derivative) as an estimate of conductance.

Saturation curves of unitary conduction γ and $[K^+]_{int}$ were fit with a Michaelis-Menten model of the formula:

$$\gamma = \frac{\gamma_{max} \cdot [K^+]}{[K^+] + K_m} \tag{5.3}$$

All concentration values in these studies are given as salt concentrations and have not been corrected for activity.

Values of $t_{1/2}$ shown in fig. 5.6 were measured by the procedure outlined in section 2.2.4. Fold activation with voltage was calculated by dividing the steady state current following a voltage jump by the instantaneous current.

5.3 Results

5.3.1 Increased ionic strength reduces TREK2 currents

To test putative K^+-dependent gating at the inner channel mouth (Schewe et al. 2016) TREK2 currents were recorded in increased internal KCl concen-

tration. Application of hyperosmolar KCl solutions was followed by a drop in overall currents (shown in fig. 5.1A).

To control for a non-specific effect due to the increase in ionic strength, the experiment was repeated using NMDG-Cl of equivalent concentration. This also resulted in near full reduction of the current over the tested concentration range. It is worth noting that the response of outward currents to increasing NMDG-Cl concentration is steeper and monotonous compared to a more graded response in KCl, this is most prominent in TREK1 (see fig. 5.1C). Both the tested TREK2b-FL mutant and TREK1c WT followed this pattern,

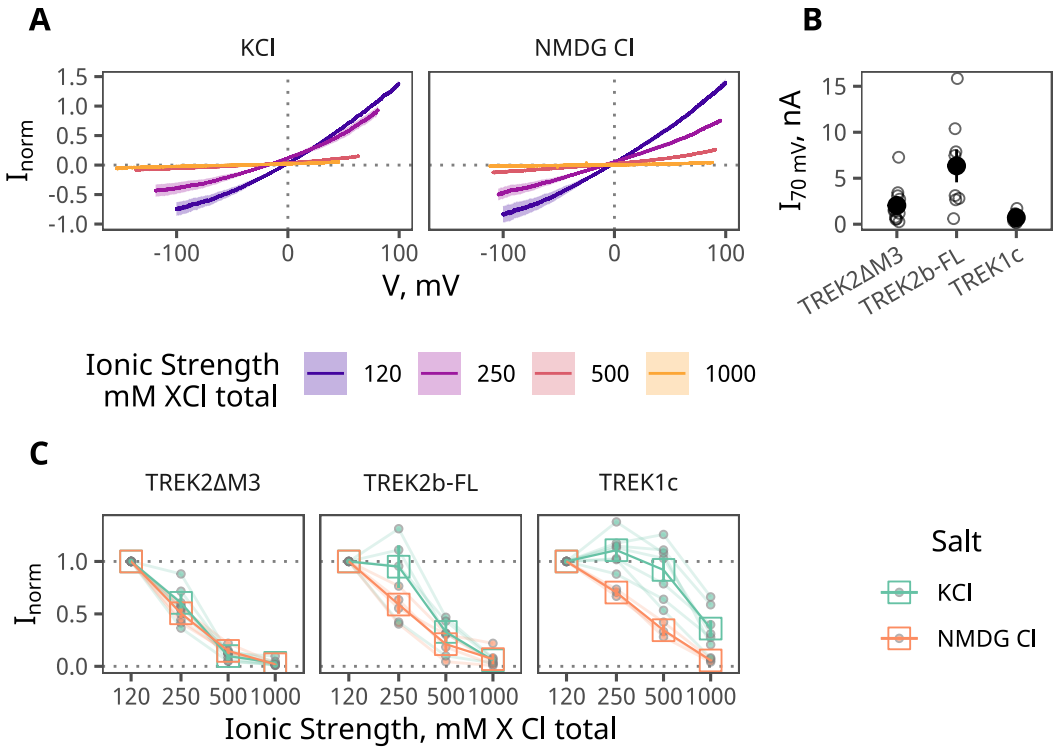


Figure 5.1: *TREK2ΔM$_3$ IV-curves in high internal ionic strength* A: Average normalised IV-curves of TREK2ΔM$_3$ in varying ionic strength. Shaded area represents SEM, n > 4 for detailed number of patches in each condition see table 5.1 B: Absolute current values at 70 mV for the baseline condition (120 mM KCl $_{int}$) for each patch. The full length TREK2b-FL mutant shows larger currents in excised patches than TREK1c or the truncated construct. C: Normalised current, corrected for K^+ driving force. There was considerable variability in the response between different constructs and between replicates. n > 3, see table 5.1. Faint lines and filled circles represent responses of individual patches.

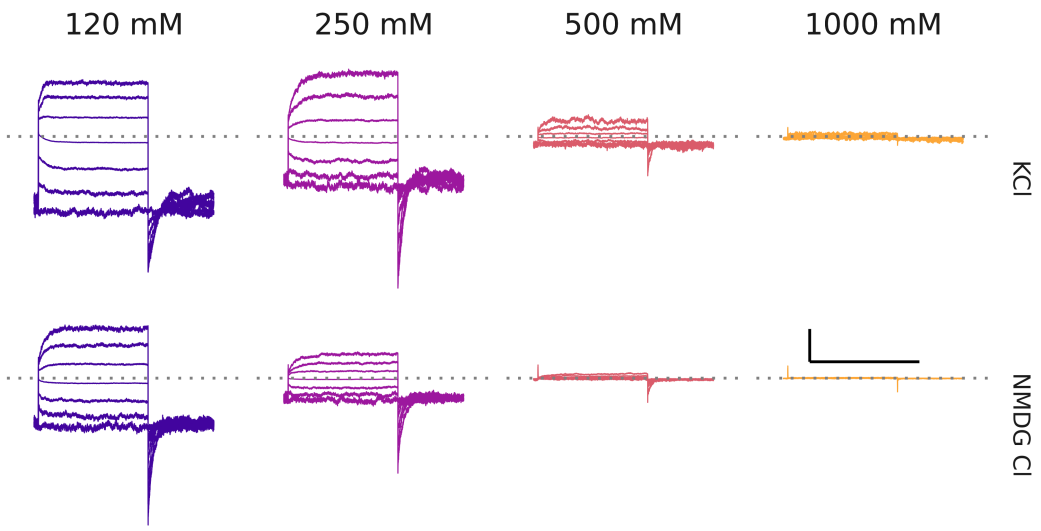


Figure 5.2: *Voltage step responses of TREK2ΔM$_3$ in different Ionic Strength* Voltage steps were run from a holding voltage of −120 mV driving force to test voltages of −120 mV to 120 mV in 10 mV increments. Tail currents were recorded on stepping back to −120 mV. Scalebars represent 0.5 s and 2 nA.

albeit with variations in the extent of the reduction (fig. 5.1C). TREK2ΔM$_3$ responded most prominently to an approximate doubling (2.08 fold change) of ionic strength with residual currents of 61±7% for KCl and 51±3% in NMDG-Cl (mean and SEM, $n = 6$ and 5 respectively).

In addition to the ramp protocols described above, voltage step responses were recorded for all conditions from holding voltages equivalent to −100 mV driving force for K^+. Typical current families are shown in fig. 5.2.

5.3.2 Single channel currents reveal saturating conduction

Some of the currents in elevated ionic strength were sufficiently small to observe individual channel openings (fig. 5.3). Although a formal analysis of P_o is not feasible due to the large and unknown number of channels present in the patches, these traces demonstrate a strong reduction of P_o and an increased occupancy of long-lived closed states.

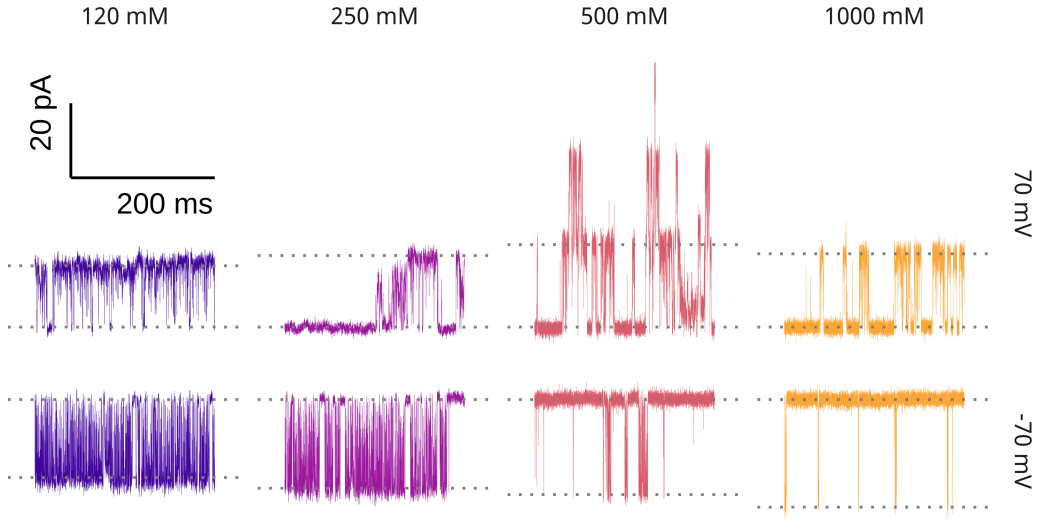


Figure 5.3: *Single-channel traces in high internal Ionic Strength* Example time-courses of low P_o TREK2ΔM$_3$ currents in high $[K^+]_{int}$. Outward (top row) and inward (bottom row) single channel currents at a net driving force of ±70 mV in 120 mM to 1000 mM KCl. Different subconductances and flickers are apparent. Scale shows 20 pA and 200 ms. Fitted amplitudes for the closed and open state are shown as grey lines, the leak current was subtracted

The open-channel IV-curves extracted from these residual currents are shown in fig. 5.4A. Unitary current increases with the amount of available K^+, the opposite was seen in the case of macroscopic currents.

The dependence of membrane current on the concentration of permeating ions can be modelled by the Goldman current equation. Figure 5.4B illustrates rectification behaviour as calculated by the Goldman current equation (eq. 5.4) for the asymmetric gradients used in this study.

$$I = \frac{Pz^2F^2}{RT}V_m\frac{c_{\text{int}}\cdot\exp\left(\frac{zF\,V_m}{RT}\right)-c_{\text{ext}}}{\exp\left(\frac{zF\,V_m}{RT}\right)} \tag{5.4}$$

The Goldman equation, which also underlies eq. 1.2, describes the membrane current density (I) dependent on membrane voltage (V_m), temperature (T) and the gradient of the permeating ion c_{ext} and c_{int}. F, R represent

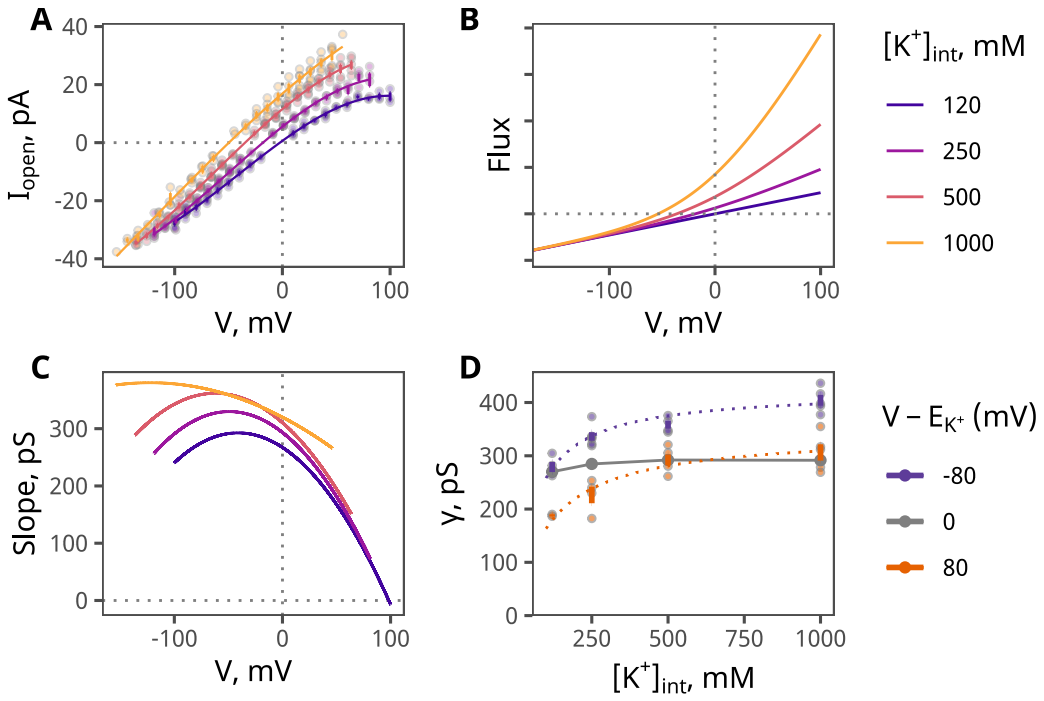


Figure 5.4: *Single-channel IV-curves in high internal Ionic Strength* A: Amplitudes were extracted from short stretches of recordings (0.95 s) at voltages ranging from ±100 mV either side of the calculated reversal potential in the given K+ gradient. Data collected at high ionic strength (>500 mM) represent opening events recorded from residual activity of patches conducting large currents in baseline condition (large amount of channels). Lines represent a third order polynomial fit. Number of patches for each reconstructed curve is atleast 4 whereas the number of replicates at a given voltage can be less, if the amplitude could not be determined due to lack of openings. See table 5.1 for all n numbers. B: Current-density-V relation calculated with eq. 5.4 for the K^+ gradients in the experiment. The magnitude of the calculated flux is arbitrary. Compare and contrast with B. C: Slope conductance depending on voltage, derivative of the polynomial fits shown in B. D: Measures of unitary conductance plotted against the internal potassium concentration. Amplitudes were divided by the calculated driving force for potassium. The slope at the point of current reversal ($V = V_{K^+}$, y-axis intercept of the fit in A) was taken from the fits shown in C. A Michaelis-Menten curve was fit to the data (dotted lines).

the Faraday and gas constant and P and z the permeability coefficient (see chapter 1) and charge of the ion.

The equation predicts a monotonous increase of conductance for increased concentrations of the permeating ion. However, a plot of different estimates of conductance against the available $K^+{}_{int}$ reveals a saturating behaviour (fig. 5.4D). When fit with a Michaelis-Menten model these yield values of 343±40 pS maximum conductance with a half maximal concentration of

110±59.8 mM for internal K^+ (values for 80 mV, 95% confidence interval of fit estimates). This is in good agreement with similar measurements done for the BK channel (Blatz 1984) although care should be taken with interpreting the K_m value here as the estimate lies outside of the range of the K^+ concentrations sampled and more accurate values can be obtained in symmetrical $[K^+]$.

Saturating behaviour that diverges from predictions made from the GHK current equation is typical for K^+ channels and a hallmark of their multi-ion permeation mechanism (Blatz 1984; LeMasurier et al. 2001; Heginbotham and MacKinnon 1993).

5.3.3 Control for non-specific effects of anions or osmotic pressure

Alongside an increase in ionic strength on the inside, the conditions used in the previous experiments introduce an osmotic pressure gradient and a resultant increase in membrane tension. This is of concern in channels that are also gated by membrane stretch, such as TREK2.

Changes in ionic strength may also influence further physical properties of membranes such as stiffness that are suitable to influence gating of a lipid and tension gated channel (Suchyna et al. 2009). Additionally all experiments were done in solutions containing chloride as the only anion. To rule out these possible confounds I measured currents in conditions designed to control for Cl^- concentration and high osmolarity.

TREK2ΔM_3 currents were reduced by raising the ionic strength by a factor of $\sim$2. Therefore, further controls were conducted in this condition to minim-

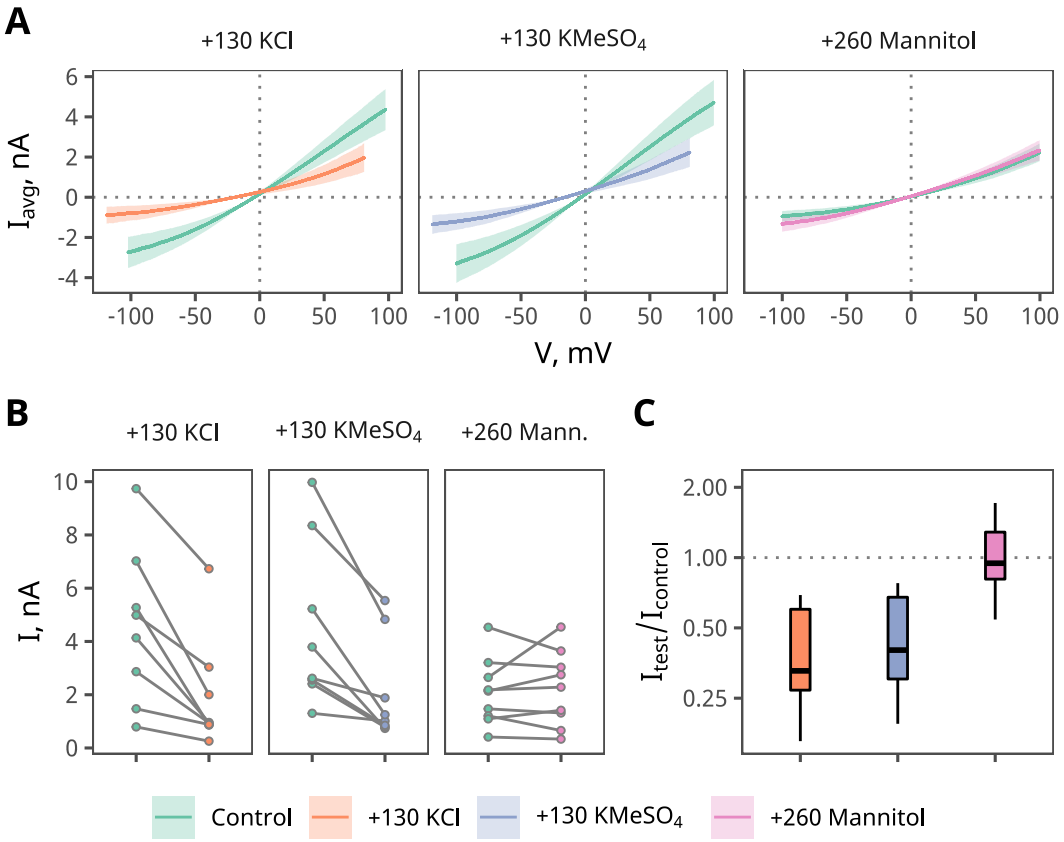


Figure 5.5: *Control for osmolarity* A: Mean *IV*-curves in excised patches. Shaded areas represent ± SEM. One test solution was applied to every patch, then it was discarded (this is the reason why there are separate control curves for every condition, n >8 paired recordings). B: Currents at 95 mV driving force. C: Relative current change. The mannitol test solution has no appreciable effect on current.

ise interference due to molecular crowding, viscosity of the solution (Brelidze and Magleby 2005) and osmotic gradients.

The following solutions were applied to patches kept in 120 mM KCl solution (control), a. 250 mM KCl (as previously) b. 120 mM KCl, 130 mM $KMeSO_4$ (same ionic strength, different anion) c. 120 mM KCl, 260 mM Mannitol (same osmotic strength, no change in ionic strength).

All solutions were prepared in 10 mM Tris-HCl buffer adjusted to pH 7.2. To minimise effects on patch properties in these conditions that might have

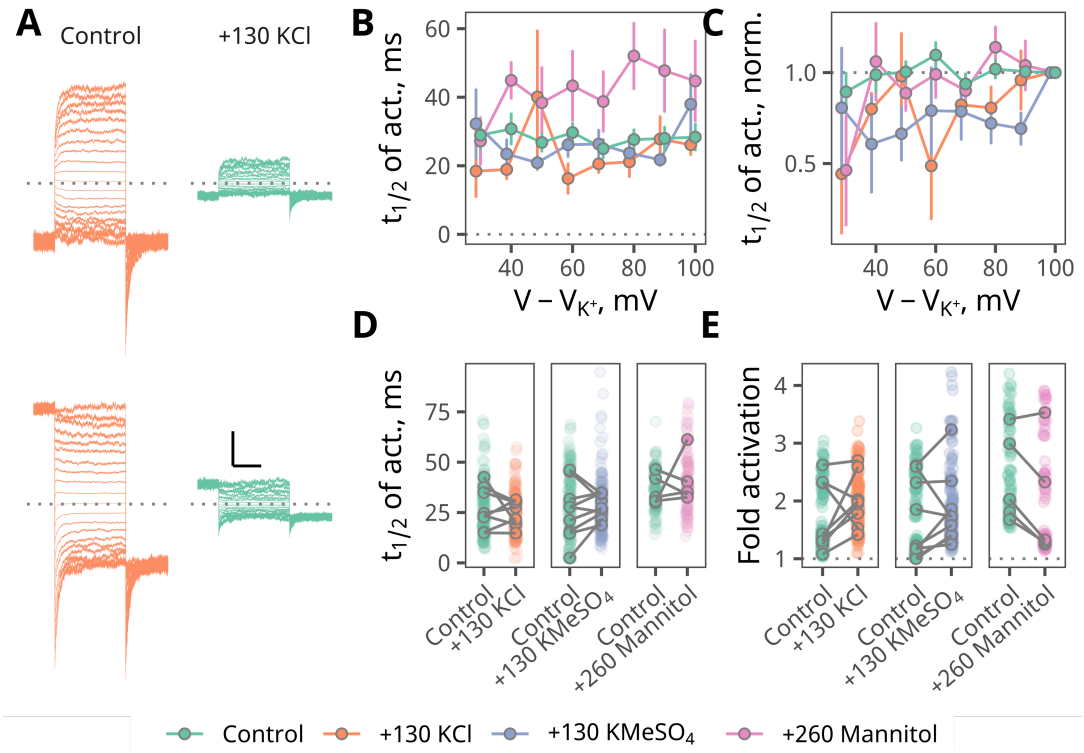


Figure 5.6: *Voltage dependent relaxations rates in TREK* A: Example current families recorded with a deactivating pre-pulse (–100 mV, top) or an activating pre-pulse (100 mV, bottom), scale-bar represents 0.2 s and 2 nA. This is a paired recording showing current after application of a high ionic-strength solution in the same patch. B: Activation $t_{1/2}$ values for different test voltages C: Data of B normalised to the activation rate at 100 mV, there is little appreciable voltage dependence of the activation rate. D: Activation rate at 100 mV for the pre-pulse of the data shown in A bottom. 20 sweeps were recorded (faint dots) for each patch (average, big dots). Measurements for the same patch before and after application are connected with a line. E: Fold activation of the pre pulses.

occurred in longer measurements or with repeated application patches were discarded after recording ramps and step protocols in the test-solution.

Current size and relative reduction with the test solution were quite variable, however every patch tested showed reduced current in response to application of more concentrated salt solutions to the intracellular side (see fig. 5.5B). By contrast, application of the mannitol solution failed to elicit a consistent reduction of the current.

To further analyse the effect of high salt concentrations, I analysed voltage-dependent gating using a step-protocol with a hyperpolarised, deactivating

pre-pulse (−100 mV) and a protocol with a depolarised, activating pre-pulse (100 mV). Relaxation rates and fold activation of this time-course data varied greatly and the data at hand do not allow detection of a discernible voltage-dependence or striking difference between conditions in these parameters (fig. 5.6).

High ionic strength may weaken salt bridges that are essential for the integrity of protein structures. K^+ channels are especially sensitive to $[K^+]_{ext}$ and can collapse into dilated or irreversibly defunct states (Loboda et al. 2001). This occurs in low internal K^+ concentration and can be dampened by favouring outward conduction, however the opposite is found in the conditions tested here.

To test for a putative irrecoverable loss of channel function in high ionic strength, application of control (fig. 5.7, blue) and 250 mM KCl solutions (fig. 5.7, red) was alternated. This resulted in reversible reduction and recovery of currents. 'Washout' and 'block' completed as fast as the bath

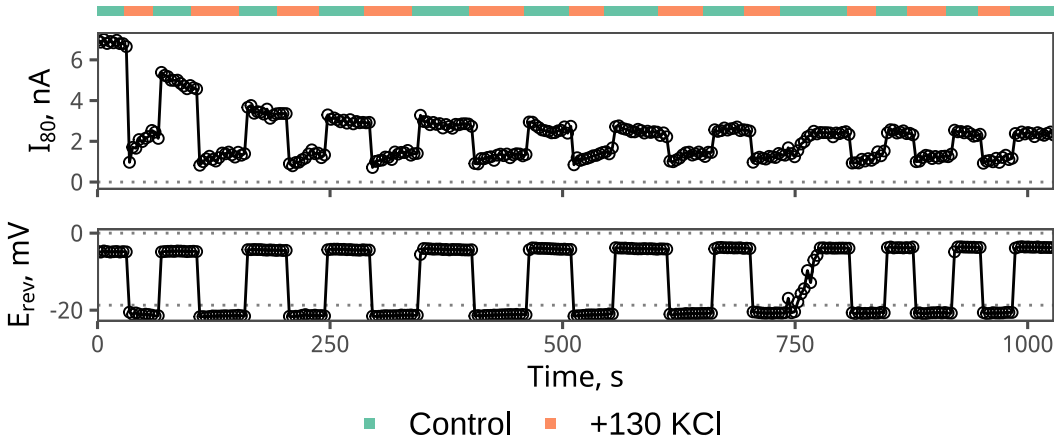


Figure 5.7: *Current reduction is fast and reversible* Time course data of repeated application of 250 mM KCl solution to an inside out patch. 1 example shown of 3 measurements. Voltage ramps from −100 mV to 100 mV were continually applied to an inside out patch. Full solution exchange was usually achieved in the course of 1 ramp (1.5 s) as shown by the expected change in reversal potential. Channel activity decreased spontaneously over the course of the measurement and then stabilised (rundown).

perfusion for long measurements and many changing cycles (>10 min and >10 solution changes, fig. 5.7). The reduction in current therefore does not appear to be the result of an irreversible collapse of the protein structure.

5.4 Discussion

Here we show that TREK currents are reduced by the application of solutions with supra-physiological ionic strength to the intracellular side. This was surprising as increased availability of permeable ions would normally be expected to *increase* conduction (Goldman 1943), especially so in the outward direction (fig. 5.4B). Indeed, the bi-phasic response of outward currents to increased concentration of permeable KCl but not NMDG-CL of TREK1c and the ATI variant construct TREK2b-FL supports that current increases with modestly elevated $[K^+]_{int}$ (fig. 5.1C).

However, IV-curves of unitary current better reflect permeation and are less confounded by gating than macroscopic IV-curves. The recordings shown in fig. 5.3 also demonstrate that conduction in different K^+ concentrations indeed behave as predicted.

When studying permeation through K^+ channels we expect to observe correlates their multi-ion pore and permeation mechanism, such as saturation of conductance in increased concentrations of permeating ions (Blatz 1984; Heginbotham and MacKinnon 1993; LeMasurier et al. 2001).

The single-channel IV-curve of TREK2 in symmetrical solutions is inwardly rectifying (Bang et al. 2000; Clausen et al. 2017, see also chapter 4)). Inward rectification of single-channel IV-curves is partially relieved with raised $[K^+]_{int}$ but persists in conditions in which substantial *outward* rectification is predicted by the Goldman equation (fig. 5.4 B and C).

Saturating behaviour occured in TREK2ΔM_3 with maximum conductance values of 300 pS to 400 pS typical for K^+ channels with large conductance such as BK (Blatz 1984).

The IV-curves shown in fig. 5.4A show a combination of intrinsic rectification, saturation and Goldman behaviour, while falling short in producing the prominent outward rectification as predicted (fig. 5.4 B). With this canonical behaviour at the level of conduction through a single channel, the reduction of macroscopic currents must be due to a decreased open probability.

Patches that conducted currents up to several nano ampere showed little residual P_o in 500 mM to 1000 mM KCl in the internal solutions. Openings were brief and separated by long closures. Stretches of 10 ms to 100 ms without openings could be observed in patches that contained hundreds of channels thus indicating low residual P_o ($<<1\%$) in these conditions.

Although the channel responds similarly to KCl and NMDG-Cl, we cannot rule out that the reduction in current is due to block by arresting K^+ or another cation in a low affinity inner binding site rather than a nonspecific effect of ionic strength on the channel.

Ions like Ba^{2+} and Na^+ block the selectivity filter by binding in its sites (S4 for Ba^{2+}, and a 'B' site for Na^+, Neyton and Miller 1988b; Neyton and Miller 1988a; Nimigean and Miller 2002; Thompson et al. 2009; Jiang and MacKinnon 2000). These binding sites are within the electric field and consequently block is voltage-dependent. Such 'blocking' ions will eventually permeate the channel: their action is not by stopping conduction but slowing it to near standstill. High positive voltages facilitate blocker unbinding on the other side of the membrane (causing it to permeate) in a process known as 'punch through'.

$NMDG^+$ is too large (7.3 Å mean diameter, Villarroel et al. 1995) to enter the canonical selectivity filter structure of K^+channels (3 Å diameter Doyle et al. 1998) and cannot block the channel by being arrested in the filter like Ba^{2+} or Na^+. Over the (relatively mild) sampled range of voltages, no signs of voltage-dependent block or 'punch through' in either steady state IV-curves or voltage-step responses (figs. 5.2 and 5.6) were observed. However, these effects might not be seen unless larger positive voltages are applied.

TREK2 channels are gated by voltage as well as membrane tension. We fully expect that currents should be perturbed by changes in surface charge at the membrane as elicited by a change in ionic strength. In particular the C-terminus of the channel is thought to form an intracellular protein-membrane interface and contains charged amino acids. This interface has been implicated in gating of TREK1 by membrane tension (Chemin et al. 2005).

The (proximal) C-terminus is also crucial in relaying gating stimuli such as membrane tension, phosphorylation (Bockenhauer et al. 2001) and internal pH (Honore 2002) to the selectivity filter gate of TREK channels and the same charged interfaces may be involved in propagating these signals.

The N-terminus of TREK channels has a profound influence on the biophysical properties of the channel, including selectivity and conduction, which rationalises the difference of TREK2b-FL and TREK2ΔM_3 in response to high ionic strength (Simkin et al. 2008; Veale et al. 2014a; Thomas et al. 2008). However, the available crystal structures of mechanosensitive K_{2P} channels (TRAAK, TREK2, TREK1 Brohawn et al. 2012; Dong et al. 2015; Lolicato et al. 2017) do not contain structural information of the large intracellular domain comprised of both N- and C-termini which were truncated to aid crystallisation.

Raising the intracellular salt concentration will globally weaken polar interactions such as salt bridges by decreasing the range of electrostatic interactions. This may have dramatic irreversible effects on the structure causing current reduction. However, the speed of onset and reversibility of the observed effects suggest that the channel structure remains intact (fig. 5.7).

Elevated internal ionic strength is a transient event in cell volume regulation, and some channels (VRAC/LRRC8) and transporters involved in these processes respond to changes in a range of up to 200 mM intracellular salt concentration (Strange et al. 2019). Except for TREK2ΔM_3 little response over this range was seen with the tested constructs. The cell-free measuring techniques here are not suited to imply a physiological role of TREK ionic strength sensitivity. This is more likely a side effect of the sensitivity to ionic strength of the charged protein and membrane interfaces involved in gating by internal pH and membrane tension (Chemin et al. 2005).

The decline in P_o in salt concentrations in a range from 120 mM to 250 mM (fig. 5.1C) is a possible source of variation. Recording buffers are commonly prepared with HEPES and a set amount of KCl adjusted with *additional* hydroxide. HEPES acid has two protonable moieties only one of which is mostly deprotonated in physiological pH. The second has a pKa of 7.48 at room temperature; at pH 7.2 we expect protonated and deprotonated form in a ratio of roughly 2:1. Thus for HEPES titration we add roughly 1.3 mmol KOH per mol HEPES. For an 'internal' solution further KOH may be required to neutralise other acids present such as chelating agents. This will result in varying ionic strength (>10-15mM) that may be sufficient to reduce P_o of TREK channels. Using K^+ or Na^+ salts of these components instead of their free acids is therefore recommended for a better control of ionic strength.

Additionally, in structural biology techniques, high salt concentrations may be used to aid protein crystallisation. This poses challenges to interpreting the functional states of K^+ channel SF structures. The available K_{2P} channel structures by Dong et al.; Miller and Long; Lolicato et al. and others were captured in 0.15 M to 0.2 M KCl. This is outside of the range in which we expect a strong bias for the closed state facilitated by higher ionic strength.

Mechanistically, the most prudent interpretation of the data seems that weakening electrostatic interactions in the presence of high salt concentration on the inside favours a closed conformation with a long lifetime. The characteristic response of different TREK proteins in cell-free patches suggests that the channel can intrinsically 'sense' the ionic strength of the intracellular medium.

The stabilised conformation is likely to have a SF filled with K^+, as it occurs in a concentration of K^+ in which conduction (a crude proxy for ion occupancy) has mostly saturated (see fig. 5.4 D). High conduction rates through K^+ channels are thought to only arise in full occupancy (Morais-Cabral et al. 2001; Kopfer et al. 2014, irrespective of the controversy of whether full occupancy corresponds to 2 or 4 ions in the SF). Additionally, considering the measured equilibrium binding affinity of the KcsA SF (Lockless et al. 2007) it seems unlikely that the SF would be devoid of K^+ in such high concentrations of KCl.

Potassium channels are not in general functionally impaired in high internal ionic strength and currents have been recorded in comparable strong K^+ gradients for BK, *Shaker* and $K_{ir}2.1$ (Blatz 1984; Starkus et al. 1995; Lopatin and Nichols 1996). Instead, high occupancy of the channel brought about by increase of $[K^+]$ on either side is associated with resistance to closure by

inactivation and higher channel activity (Ogielska and Aldrich 1999) as well as preventing collapse of the pore (Loboda et al. 2001, in *Shaker*).

In addition to the depleted resting conformation suggested in Schewe et al. (2016) a closed K^+ filled conformation may also exist in TREK channels and that is what I presume to underlie the reduced P_o in large internal K^+ concentrations ($[K^+]_{int} > 500\,mM$).

The experiments described here were designed to probe and extend upon the 'flux' gating mechanism proposed in Schewe et al. (2016). We would expect such a K^+-dependent activation mechanism to positively scale with increasing K^+ concentration, for example by a K^+-dependent activation rate. Little change in measures of voltage-dependent gating with change in $[K^+]_{int}$ was seen in within-patch comparisons. However, variability was high and the dataset at hand might not be sufficient to reliably observe small effects.

In addition to the K^+-dependent step being a fast event beyond the time resolution of the patch-clamp technique (Schewe et al. 2016), direct study of the K^+-dependent gating of TREK channels is complicated by the non-specific effect of ionic strength on gating. The reduced P_o of TREK2 in elevated ionic strength needs to taken into account in the design of biophysical experiments assessing TREK structure and function.

Table 5.1: *n-numbers for the experiment of fig. 5.4 A and fig. 5.1*

EK	120	250	500	1000
-100	4	6	4	1
-90	4	6	4	2
-80	3	6	4	5
-70	3	6	4	2
-60	3	6	5	4
-50	3	6	5	4
-40	3	6	6	2
-30	3	6	6	4
-20	3	5	6	3
-10	NA	2	3	3
10	4	4	3	2
20	4	5	6	3
30	3	5	6	4
40	4	4	6	5
50	3	4	5	4
60	3	3	6	4
70	3	5	5	5
80	2	4	5	5
90	3	4	5	5
100	3	4	5	5
110	NA	NA	NA	1

channel	filler.Ion	IonS	n
TREK1 WT	K	120	7
TREK1 WT	K	250	7
TREK1 WT	K	500	7
TREK1 WT	K	1000	7
TREK1 WT	NMDG	120	3
TREK1 WT	NMDG	250	3
TREK1 WT	NMDG	500	3
TREK1 WT	NMDG	1000	3
TREK2b FL	K	120	4
TREK2b FL	K	250	4
TREK2b FL	K	500	4
TREK2b FL	K	1000	4
TREK2b FL	NMDG	120	4
TREK2b FL	NMDG	250	4
TREK2b FL	NMDG	500	4
TREK2b FL	NMDG	1000	4
TREK2delM3	K	120	9
TREK2delM3	K	250	6
TREK2delM3	K	500	6
TREK2delM3	K	1000	6
TREK2delM3	NMDG	120	5
TREK2delM3	NMDG	250	5
TREK2delM3	NMDG	500	5
TREK2delM3	NMDG	1000	4

Chapter 6

Loss of selectivity in TREK2

6.1 Introduction

Selective permeability is one of the hallmarks of K^+channel function and breaking it has serious consequences for the maintenance of electrochemical gradients. Mutations to that effect may cause overexcitability of cells or even cell death as demonstrated by the weaver mutation of $K_{ir}3.2$ (Patil et al. 1995).

In addition to P_o and channel density (see eq. 1.6) the selectivity of some K^+channels is another factor that has been proposed to be regulated in order to control membrane current. This process is called dynamic selectivity. K^+channels may allow passage of Na^+ in some conditions when undergoing C-type inactivation (section 1.5.3). In general these and other SF gating events are associated with a reduced K^+-affinity in the outer pore (Ogielska and Aldrich 1999; Cheng et al. 2011).

Some K_{2P} channels are thought to have regulated selectivity properties. For example, TWIK becomes permeable to Na^+ in the presence of low pH_{ext}. The kinetics of this change and its residence time in acidic intracellular

compartments during trafficking is thought to be important for its function (Chatelain et al. 2012). TASK channels have been suggested to change their selectivity through the same pH_{ext}-dependent process (Ma et al. 2012a) involving the outer pore histidine residue of these channels (see fig. 3.1).

The ATI (section 1.6.2) variant TREK1ΔM56 (Thomas et al. 2008) as well as a disease associated loss of function mutation I267T of TREK1 (Decher et al. 2017) have also been reported to exhibit reduced K^+-selectivity. Furthermore, TREK1 conducts Na^+ in the absence of K^+ when its C-type gate is closed in low external pH (Bagriantsev et al. 2011). However, this is a general property of C-type inactivation in K_v channels (Kiss et al. 1999; Ogielska and Aldrich 1999; Starkus et al. 1997) and suggests a similarity between pH_{ext}-dependent gating of K_{2P} channels and C-type inactivation.

TREK1/TWIK1 heterodimers have also been reported to form a channel that is able to pass glutamate in astrocytes (Mi Hwang et al. 2014; Woo et al. 2012). However, the proposed ability to transport glutamate is inconsistent with any known K_{2P} or other K^+ channel structures and no structural interpretation of this phenomenon has yet been advanced.

6.1.1 Importance of the extracellular milieu

Excised patch currents of TREK in biophysical studies are commonly recorded in high $[K^+]_{ext}$ (Piechotta et al. 2011; Schewe et al. 2016). This allows passage of fairly large inward tail currents suitable for analysis (Schewe et al. 2016). However, composition of the external ionic milieu can be crucial for channel function, especially with regard to the stability of the SF gate (see above). Additionally, high $[K^+]_{ext}$ solutions or isomolar substitution of ionic components of the extracellular solution may mask otherwise occurring

competition between Na^+ and K^+ at the outer SF binding site (Lopatin and Nichols 1996; Ishihara 2018).

I made the initial observation that TREK2 currents in a physiological K^+-gradient showed unexpectedly large inward tail currents that seemed to be inconsistent with permeation of K^+ alone (fig. 6.1). This preliminary observation formed the basis for the following systematic assessment of non-selective permeation through TREK2 during voltage-dependent activation.

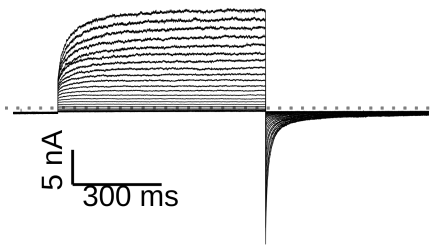


Figure 6.1: *Example of a large inward current* Example current family of TREK2 in a physiologial K^+-gradient (5 mM $[K^+]_{ext}$). Holding potential during the tail current relaxation is −120 mV. The currents are too large to be conceivably carried by just K^+, which has an electromotive force of just ∼40 mV in this condition. This is one of the example traces that are again shown in fig. 6.9.

6.2 Methods

6.2.1 HEK patch electrophysiology

Macroscopic TREK2 currents were recorded from inside-out patches of HEK-cells as described in chapter 5.

The pipette solution (external) contained (in mM): 140 NaCl, LiCl or NMDG-Cl; 5 KCl; 1.2 $MgCl_2$; 1.8 $CaCl_2$ and 10 Tris/TrisHCl buffered to pH 7.3. These are labelled '5K^+, 140Li^+', '5K^+, 140Na^+' and '5K^+, 140NMDG^+' in figure legends. The bath (internal) contained (in mM): 98 KCl, 40 KF, 2 K_2EDTA, 14 Mannitol and 10 Tris/TrisHCl buffered to pH 7.2.

The following voltage clamp protocol to test for a loss of selectivity and to probe different aspects of gating, the sequence of the step protocols is illustrated in fig. 6.2.

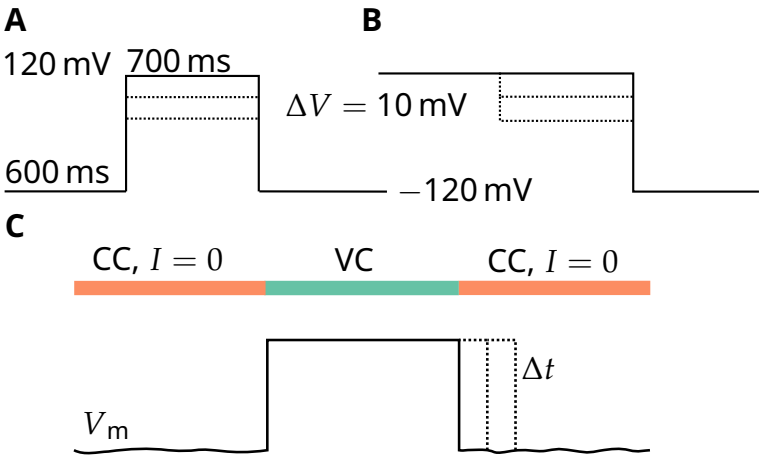


Figure 6.2: *Scheme of the VC protocols used* A: Protocol with a deactivating −120 mV pre-pulse. During the test-pulse activation gating is probed. B: Protocol with an activating 120 mV pre-pulse. During the test-pulse the channels deactivate. C: Scheme of a protocol to assess repolarisation of V_m in oocytes Cells are kept in current-clamp (CC) without injecting current. Then a test voltage-pulse (in voltage-clamp, VC) of varying length is applied. After the test pulse repolarisation is monitored in CC as before.

a. ramp protocol, from −120 mV to 120 mV with a slope of 200 mV s^{-1}

b. voltage steps from −120 mV to 120 mV after a deactivating pre-pulse (−120 mV, fig. 6.2A)

c. voltage steps from −120 mV to 120 mV after an activating pre-pulse (120 mV, fig. 6.2B)

After recording these 3 protocols, 1 mM TPA (tetrapentylammonium) was applied to the bath solution and the ramp measurement repeated. We expect near total block for this large concentration of TPA. This served to control for passive leak current.

As previously observed (fig. 5.6), TREK2 currents in excised patches are heterogeneous with large variability in the shape of the relaxation time courses and current amplitude. Estimates for $t_{1/2}$ for all different relaxations occuring during the protocols as well as the reversal potential were extracted from the raw-data by the procedures described in section 2.2.4. Values of

$t_{1/2}$ originating from time dependent currents $\leq$150 pA were found to be dominated by gating fluctuations and were removed from the analysis.

All potentials shown are corrected by a measured junction potential in the solution combination used.

Permeability ratios for an ion X ($\frac{P_{X^+}}{P_{K^+}}$) determined from V_{rev} (see fig. 6.15) were calculated by rearranging eq. 1.2 to the following expression:

$$\frac{P_{X^+}}{P_{K^+}} = \frac{[K^+]_{int} \cdot \exp(\frac{V_m F}{RT}) - [K^+]_{ext}}{[X^+]_{ext}} \tag{6.1}$$

Where V_m denotes the membrane potential, T is the absolute temperature and F and R represent the Faraday and gas constants. Do note that the above equation assumes strict selectivity for monovalent cations here, which might not be the case. The solutions used also include F^- (internal) and divalent cations (external) unaccounted for here.

6.2.2 TEVC experiments

Oocytes were prepared and injected as described in chapter 3. For TREK2b-FL 1 ng cRNA was injected and recordings were made 48 h post injection. Injection of water served as a control. Currents were recorded using ramp protocols as well as step-protocols with deactivating and activating pre-pulses. In addition, a Δt protocol with changes to clamping mode was devised to assess the resting membrane potential and the repolarisation of oocytes following a depolarising voltage-step (fig. 6.2C).

6.3 Results

6.3.1 Dynamic selectivity in excised patches

Initial assessment by ramp protocols

IV-curves from the ramp protocol can be seen in fig. 6.3A. Currents recorded in the presence of NMDG were smaller (0.5 ± 0.1 nA) vs 1.6 ± 0.3 nA in control conditions (Na^+ solution, mean and SEM). Block with TPA resulted in near complete current inhibition.

Reversal potentials extracted from these *IV*-curves and the TPA block are summarised in fig. 6.3B and C. In the presence of Na^+ or Li^+ V_{rev} was

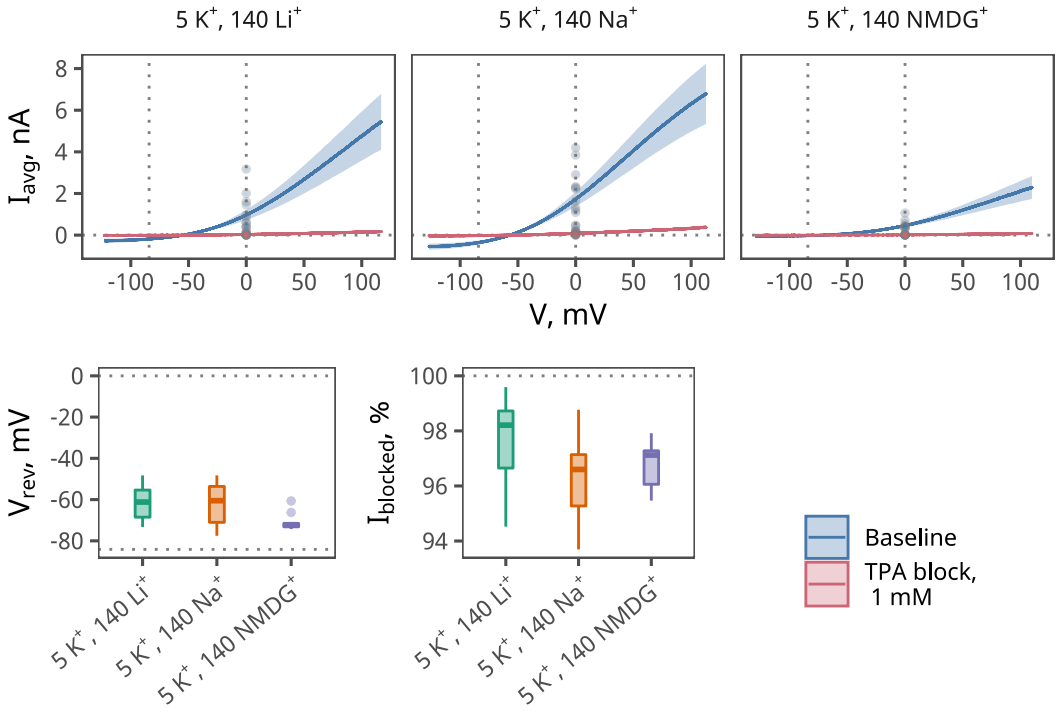


Figure 6.3: *IV-curves of TREK2 in varying external ionic conditions* A: *IV*-curves of TREK2 in 5 mM $[K^+]_{ext}$and 140 mM of a test-cation. n in each conditions is $\geq$10. B: Boxplots of V_{rev} in different pipette solutions. C: Boxplots of the blocked current with application of TPA.

-63 ± 3 mV and -62 ± 2 mV respectively, whereas V_{rev} was more hyperpolarised with $NMDG^+$ as the external ion (-71 ± 1 mV).

Control for passive membrane leak

A confound of interpreting reversal potentials is that passive leak currents might contaminate the measured ionic current. Here, we see large currents (1.12 ± 0.18 nA) that are blocked to 0.05 ± 0.01 nA (current at 0 mV, pooled from all recorded conditions). This suggests that most of the current can be blocked and is therefore carried by ion channels.

In the case of passive membrane leak the magnitude of V_{rev} would be underestimated (see eq. 1.2). The residual currents present a sum of passive membrane leak and ionic currents. Block by TPA varied (fig. 6.3C) and residual currents could be substantial in individual recordings.

To ascertain that contamination by passive leak was minimal, V_{rev} was compared before and after block. In cells with substantial leak currents we can expect a depolarised V_{rev} dominated by leak. However, we record such depolarised potentials only in cells with near complete TPA block and little residual current, whereas recordings with large residual current still have a

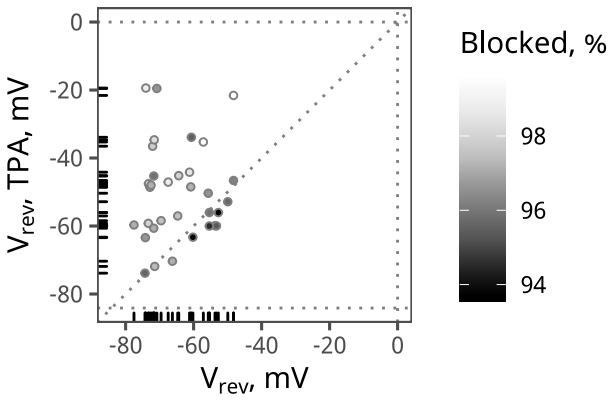


Figure 6.4: *Scatter of TPA block and V_{rev} (quality control)* Patches with significant passive membrane leak would show incomplete block (darker) and a depolarised potential (points diverging from the indicated diagonal) in the presence of TPA. However, most patches with imperfect block, have an unchanged V_{rev}, meaning the residual current is dominantly of channel origin, not passive leak.

hyperpolarised V_{rev}. This can be seen in the scatterplot in fig. 6.4. Therefore, it can be concluded that the values retrieved here do not match the expected value of V_{rev} in the case of selective permeation (−84 mV) and that this is not due to a technical issue.

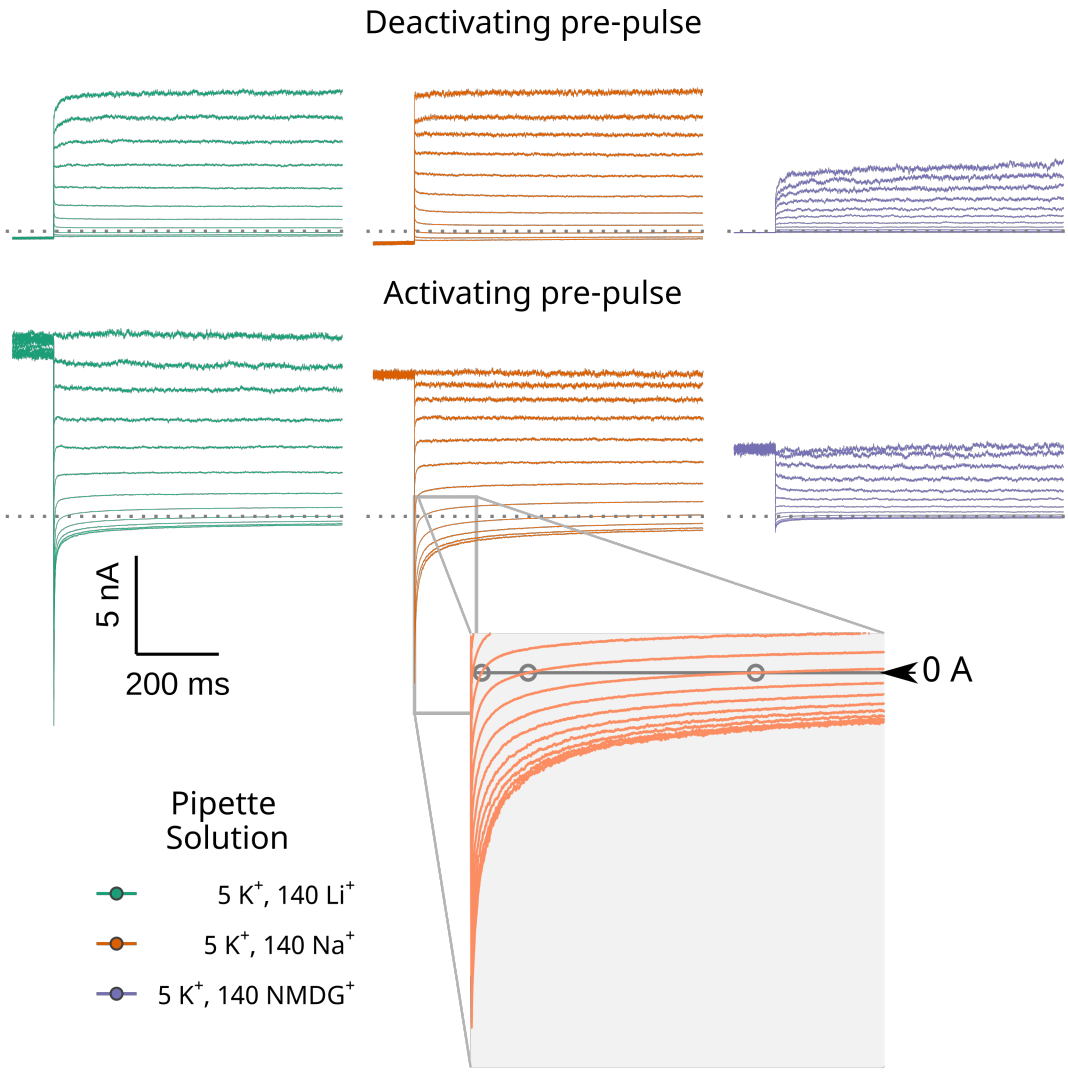


Figure 6.5: *Time courses of test-pulse relaxations* Example time courses of test-pulse relaxations with −120 mV pre-pulse (top) or 120 mV pre-pulse in all three external solutions tested. The inset shows a change of current direction during deactivation gating (circled).

Dynamic selectivity during deactivation

The recorded step-protocols (fig. 6.2A and B) enable us to assess putatively dynamic selectivity during voltage-activation. The fact that such a changes in selectivity indeed occur can directly be appreciated from the raw example current families plotted in fig. 6.5.

During the de-activation relaxation following a 120 mV pre-pulse large inward currents can again be observed (bottom row). At intermediate potentials these inward currents can be seen to change direction during the test pulse (inset). As the potential is fixed this change of direction can only occur by a change to the driving force, *i.e.* a change in the ion species that carries the current (see eq. 1.6).

Quantification of the selectivity change

We can demonstrate the inward currents and selectivity change by extracting current measurements at different fixed time-points during the relaxation and plotting them against the test-pulse voltage (isochronal IV-curves). A

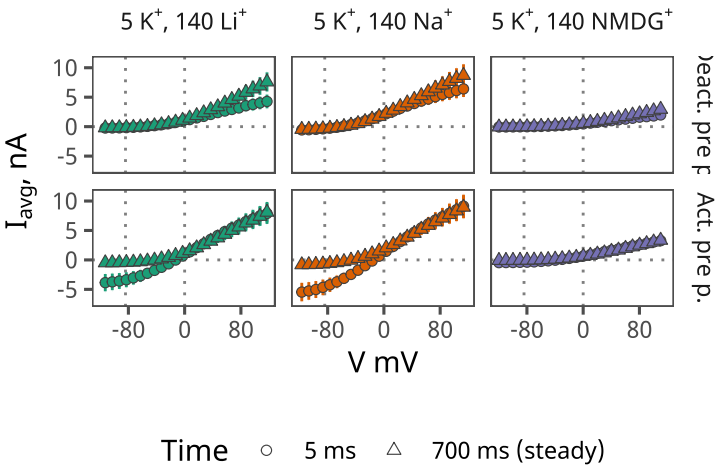


Figure 6.6: *Isochronal IV-curves of TREK2 with external cations* AverageIV-curves of the two step-protocols with −120 mV pre-pulse (top) or 120 mV pre-pulse. Current measurements were taken 5 ms after onset of the test-pulse, or at the end of the test pulse (700 ms, steady state current). Substantial inward current can be seen in Na^+ or Li^+ containing external solutions.

summary of the instantaneous and steady state IV-curves of all conditions and protocols is shown in fig. 6.6.

A 5 ms interval after the pulse was chosen as a measure of 'instantaneous' current here to rule out any contribution of capacitative transients to the measured value. Large inward currents could be seen and reversal of the pre-activated currents is shifted towards 0 mV, whereas the reversal of IV-curves with a deactivating pre-pulse remain unchanged. As for the ramp protocols, overall current (especially inward current) is reduced in the $NMDG^+$ containing external solution.

V_{rev} values extrapolated from these curves are plotted in fig. 6.7. Depolarised potentials of -43 ± 5 mV (Na^+) and -46 ± 5 mV (Li^+) could be estimated from the 5 ms isochronal IV-curve of the pre-activation protocols, a more hyperpolarised V_{rev} was observed in the presence of $NMDG^+$ (-58 ± 4 mV) consistent with the smaller inward currents seen in this condition.

This simple analysis suggests that selectivity of voltage-activated TREK2 is different from selectivity at rest. This unexpected and unusual property implies that TREK2 can also act as an excitatory conductance. However, the extant biophysical literature as well as *in vivo* studies firmly establish TREK as

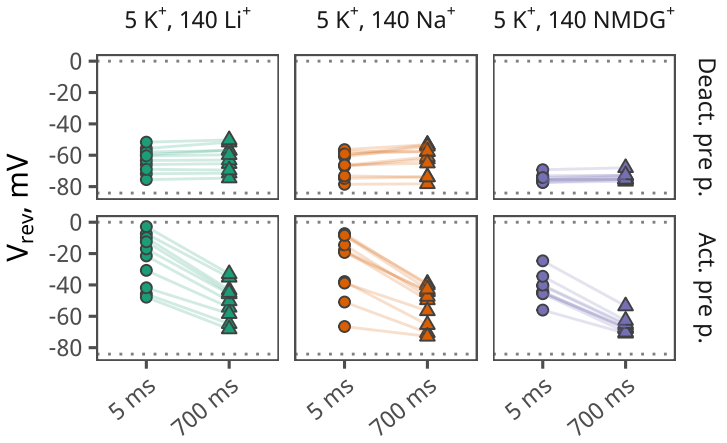


Figure 6.7: *Reversal potentials of instantaneous and steady state currents* Extrapolated potential of the IV-curves shown in fig. 6.6. Every point represents one patch, observations from the same patch are connected with lines.

a K^+ conductance and more evidence in support this novel result is required. In the following sections I will expand the analysis of the time-dependent change to selectivity as well as provide control experiments.

Time-dependence of the selectivity change

This analysis can be expanded to include isochronal IV-curves all along the test-pulse time course. The IV-curves generated by this approach are plotted in fig. 6.8A (for the Na^+ example measurement of fig. 6.5). Also, to demonstrate the accuracy of the extrapolation method, the extracted V_{rev} values are plotted alongside the IV-curve as vertical lines.

The extrapolated V_{rev} is plotted against the time-point of measurement in fig. 6.8B. With the deactivating pre pulse we can see that V_{rev} at steady

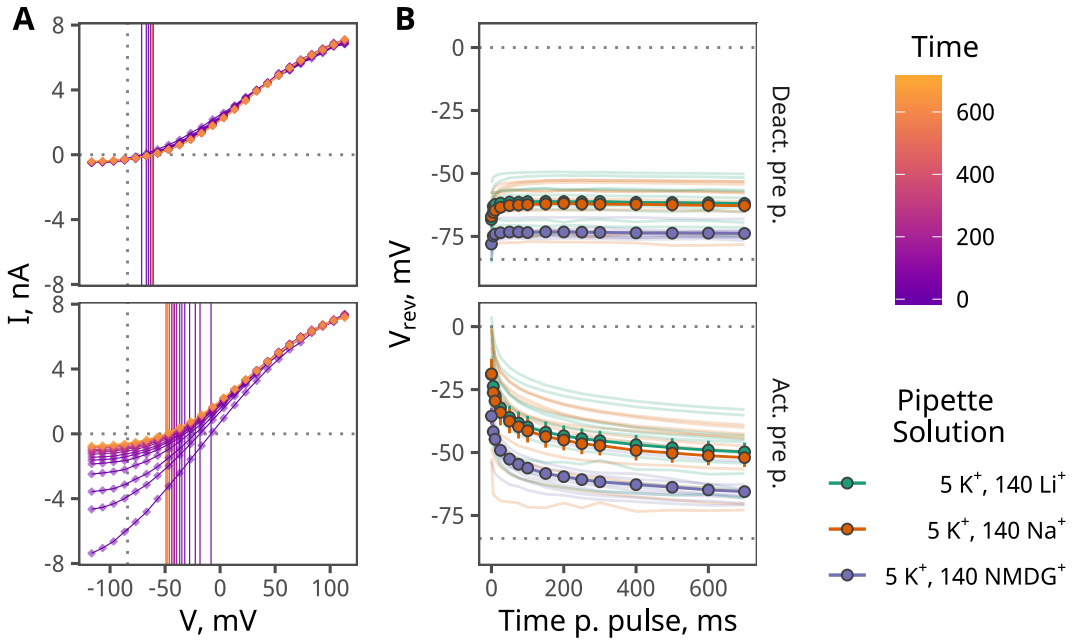


Figure 6.8: *Example of the extrapolation process and time-course of the shift in V_{rev}* A: Isochronal IV-curves of the example current family shown in fig. 6.5 (Na^+ pipette solution). Curves corresponding to 1 ms to 700 ms (steady) after the test-pulse are shown. V_{rev} is plotted as solid vertical lines. B: V_{rev} of isochronal IV-curves, time of the measurement on the x-axis. Faint lines are observations of single patches, averages and SEM are shown as filled points.

state is slightly more depolarised than at the start of the pulse. In contrast, with an activating pre-pulse, values of up to 0 mV can be observed indicating near total loss of selectivity. During deactivation gating this depolarised V_{rev} returns close to the value determined at steady-state. This demonstrates a transient and reversible loss of selectivity during voltage-dependent gating on a time-scale of 0.6 s.

Rate of the relaxations

As already demonstrated for a different dataset (fig. 5.6), variability of the voltage-dependent relaxations of TREK2 in excised patches can be considerable. The range of activation gating behaviours encountered included square-shaped responses with little to no time dependent current component,

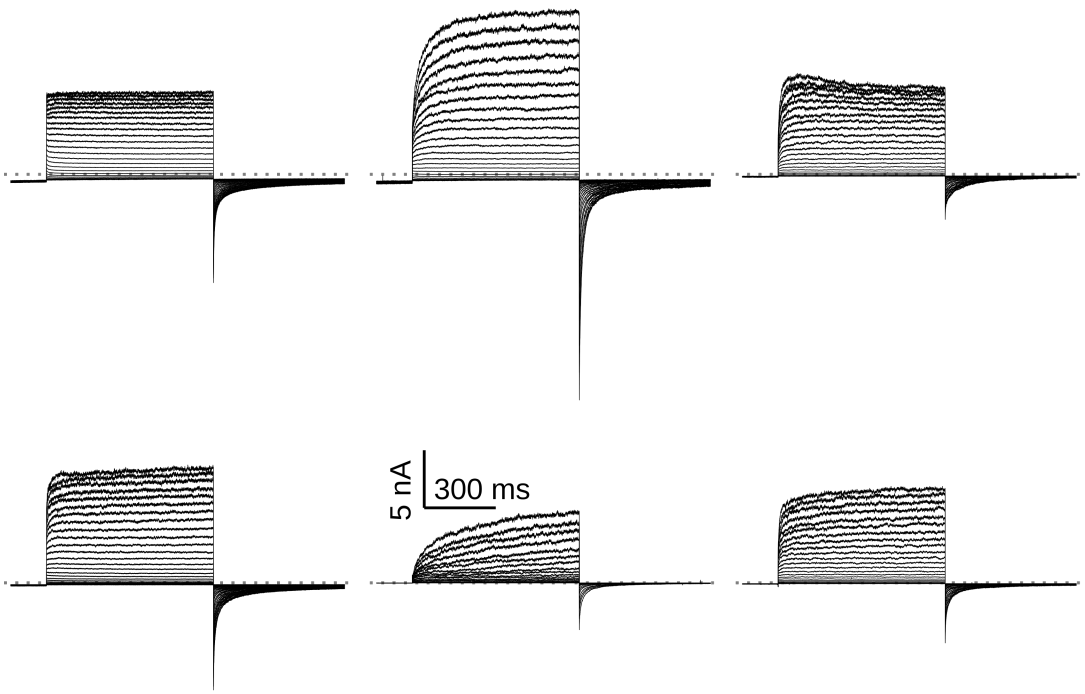


Figure 6.9: *Variability of kinetics* Example of current families recorded with the deactivating pre-pulse protocol in identical conditions (TREK2b-FL, Na^+ Pipette solution). Large tail current relaxations may also occur without prominently apparent activation (top left panel).

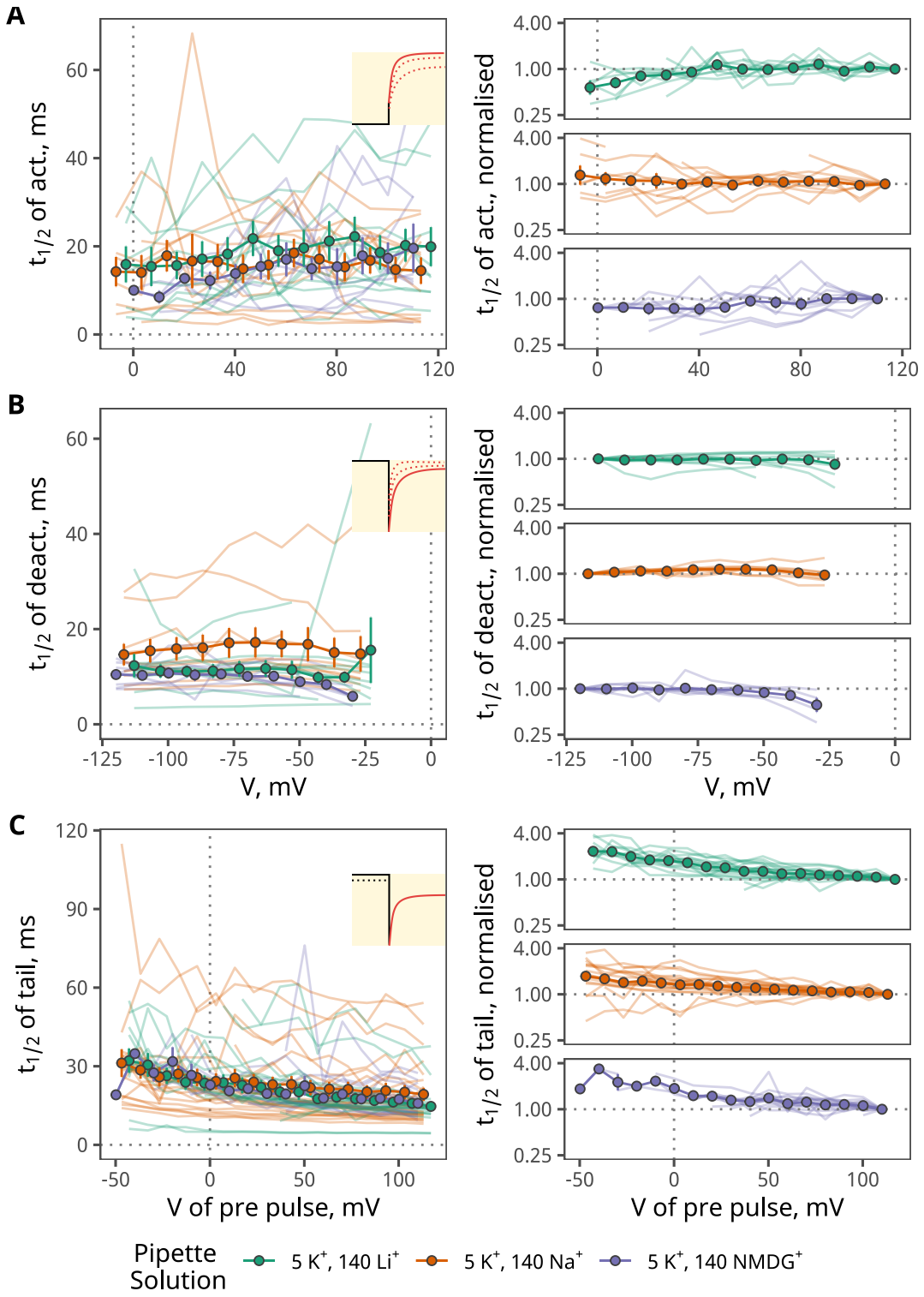


Figure 6.10: *Relaxation rates of the time-course data* A: Values of $t_{1/2}$ of the activation relaxation dependent on test voltage. B: Values of $t_{1/2}$ of the deactivation relaxation dependent on test voltage. C: Values of $t_{1/2}$ of the deactivation relaxation dependent on the preceding pulse, half-life of the tail current relaxation doubled over the tested range when corrected for patch to patch variability.

slowly activating, as well as bi-phasic weakly inactivating time-courses (see example traces fig. 6.9). Given this variability it was difficult to fit a concise and meaningful gating model to this dataset and extract estimates of the relaxation rates underlying the process. Instead, I opted for a 'no-model-in-mind' approach and extracted values for the half-life of all relaxations present in the protocols.

Values of $t_{1/2}$ for activation (test pulse of −120 mV pre-pulse protocol), deactivation (120 mV pre-pulse protocol) and the tail current at −120 mV (determined twice in every patch, pooled from both protocols) are shown in fig. 6.10.

As can be seen in fig. 6.10 left column, there is little detectable differences between the mean $t_{1/2}$ estimates in different conditions for any gating relaxation tested. To account the variability between patches $t_{1/2}$ estimates were normalised to the value at the most extreme voltage (-110 for deactivation, 120 mV for activation, fig. 6.10 right column). Activation and deactivation gating following a pre-conditioning pulse was unchanged over the tested voltage range (deactivation normalised value 0.98 ± 0.05 at −30 mV, activation 1.07 ± 0.15 at 30 mV, $n \geq 21$ after removal of small currents, pooled from all external solutions). Whereas the relaxation of the tail currents (at a

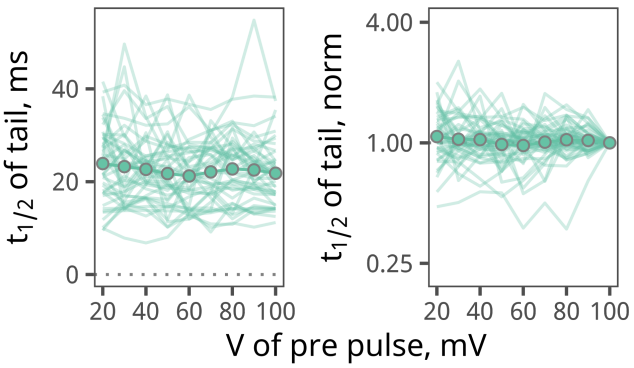


Figure 6.11: *Tail current relaxations in high* $[K^+]_{ext}$ Equivalent analysis of the voltage dependence of the tail relaxation in the control dataset (120 mM KCl, symmetrical, TREK2ΔM_3 construct) of the previous chapter. The tail relaxation rate does not seem to scale with voltage here.

fixed potential of −120 mV) seemed to be faster when the previous activating voltage was large (2.03 ± 0.20 normalised rate at −30 mV pre-pulse pooled from $n = 16$ patches after removal of small time dependent currents).

In the previous chapter, similar experiments and step-protocols were used with a high $[K^+]_{ext}$ solution without additional ions present (fig. 5.6). This data-set was re-analysed with regard to the estimate of $t_{1/2}$ of the tail-current relaxation and the data is plotted in fig. 6.11. Here no such dependence is visible.

Control for TREK2 isoforms

The variants of TREK channels produced by ATI (fig. 1.12) may have different biophysical properties (Simkin et al. 2008; Veale et al. 2014a; Kisselbach et al. 2014), especially so with regard to selectivity (TREK1, Thomas et al. 2008). In order to control for the possible influence of N-terminal truncation, the experiment was repeated with TREK2ΔM_3 to test whether this short N-terminal form shares the previously observed behaviour of conducting large inward currents. Na^+ was used as the external ion for this experiment.

A summary of the results with instantaneous and steady state IV-curves and V_{rev} along the relaxation is plotted in fig. 6.12. The same overall behaviour of TREK2ΔM_3 could be observed, with inward currents and shifts in V_{rev} occurring just like with the TREK2b-FL construct.

6.3.2 Control for recording configuration

Previous measurements of TREK2 showed near perfect selectivity for K^+ in intact cells (Staudacher et al. 2011; Simkin et al. 2008; Bang et al. 2000). These tests were usually conducted in intact cells using either whole-cell

patch clamp or TEVC. Whereas the experiments shown in this study were all recorded in inside-out configuration. Experiments with the described step-protocols were therefore repeated and IV-curves after activating and deactivating pre-pulses were recorded from whole oocytes (TEVC). This served to test whether the unusual selectivity properties seen in TREK2 currents are specific to the inside-out configuration.

Summary of the whole-cell currents in response to voltage-steps with activating and deactivating pre-pulses are shown in fig. 6.13. Here, no inward currents of comparable magnitude to the previous experiments were observed. Currents were small at potentials $>-50\,\mathrm{mV}$ and the reversal potentials were depolarised relative to the expected reversal potential of $\sim 98\,\mathrm{mV}$ (water, $-42.2 \pm 2.0\,\mathrm{mV}$, TREK2b-FL $-78.5 \pm 1.2\,\mathrm{mV}$, n > 12). This suggests that TREK acts here like a voltage-gated channel with little P_o at negative potentials.

Comparison with water injected cells thus suggests that around the reversal potential the overall current was dominated by an endogenous inward current.

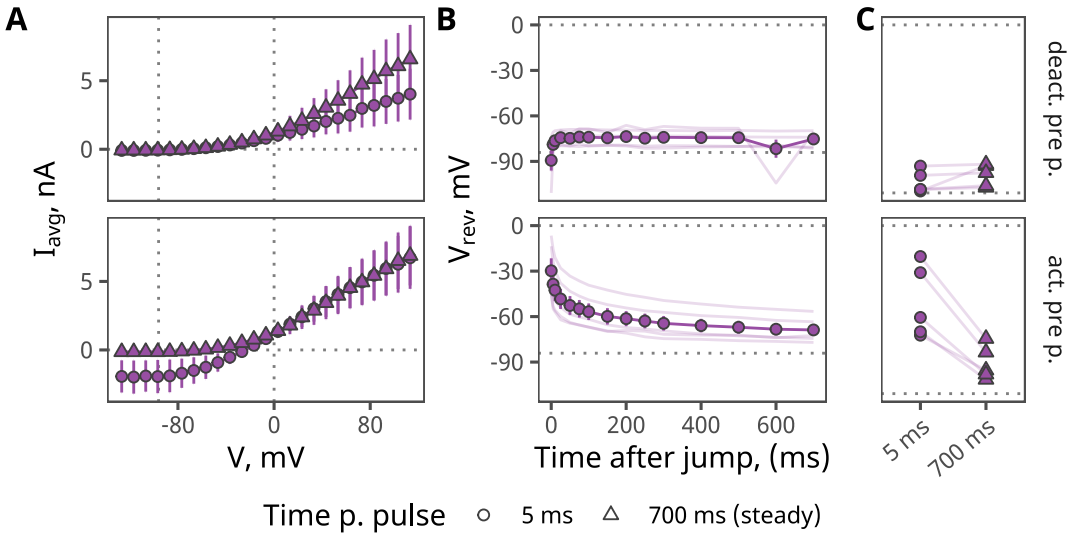


Figure 6.12: *Transient breakdown of selectivity is not specific to full length TREK2* The previous experiment as before using the TREK2ΔM$_3$ construct, Na^+ pipette solution. Inward currents and shifts of V_{rev} during deactivation gating can be observed in TREK2ΔM$_3$ too, n=5.

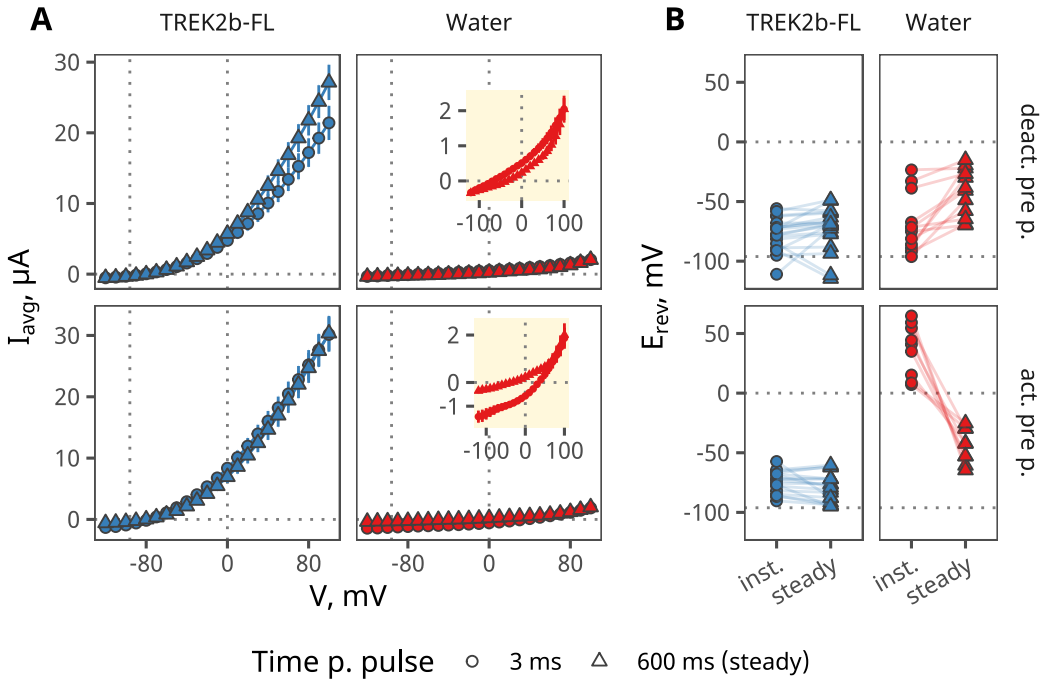


Figure 6.13: *TREK2 currents in intact oocytes* A: *IV*-curves of TREK2b-FL and water injected oocytes. The previously observed prominent inward currents are absent. However an up to 1 µA inward current is present in the water injected cells. This current must therefore be conferred by a prominent endogenous current (inset), not the action of TREK2. B: Reversal potentials of instantaneous and steady-state current. The 0 mV as well as the expected Nernst potential for K^+ assuming an $[K^+]_{int}$ of120 mM (Weber 1999) are shown as dotted lines in all panels.

This was more extreme following an activating pre-pulse (fig. 6.13 insets). Here a -1.44 ± 0.26 µA current (instantaneous current at −120 mV) can be observed. This current reverses at positive potentials (37 ± 7 mV, n =9).

There was no additional inward current in the same conditions in TREK2b-FL injected oocytes (-1.32 ± 0.16 µA), indicating that the channel was completely shut by a fast deactivation process or that there was little driving force for TREK current at −120 mV (as expected for K^+-selectivity). With absent inward currents there is no indication for a similar change of selectivity, this is also supported by the measured V_{rev} (fig. 6.13B).

In addition to the step-protocols a combined voltage- and current-clamp protocol was designed to measure dynamic changes in selectivity. Recording

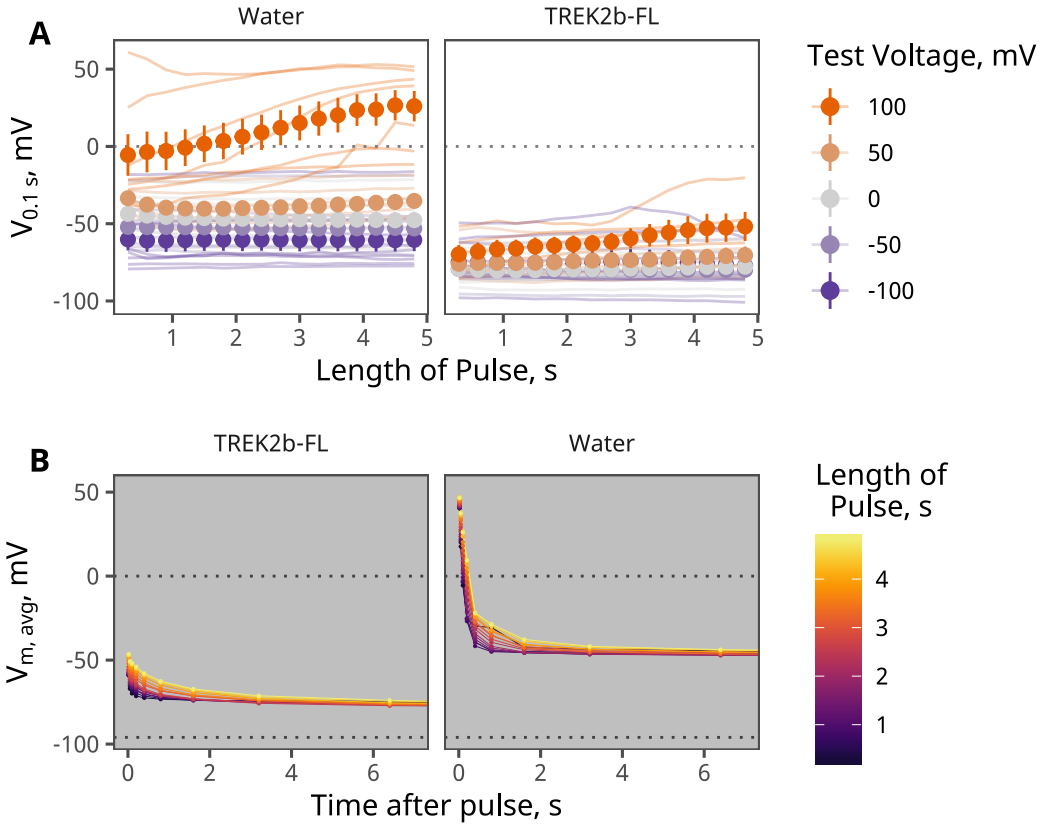


Figure 6.14: *An endogenous current depolarises oocytes* A: V_m following a voltage pulse of varying length and amplitude. The endogenous current is slow to activate and reaches its full effect after seconds of sustained depolarisation, n > 5 oocytes. B: Average time courses of the repolarisation following a 100 mV pulse. In oocytes the depolarisation conferred by the native Sodium current may persist for more than 8 s. This is a confound for all voltage-protocols that use sustained depolarisations of more than 0 mV.

from intact cells we can measure V_m directly and instantaneously in CC mode without the need to estimate it from IV-curves. Repolarisation of the oocyte was recorded following voltage test pulses (−100 mV to 100 mV) of varying lengths. Summary of V_m following the pulse and time course of the repolarisation are summarised in fig. 6.14A and B respectively.

Analysis of this Δt protocol recordings also reveals the action of an endogenous conductance. In both water and TREK2 injected cells, sustained depolarisation of V_m can be seen following test pulses of >0 mV. The endogenous conductance is slow to activate, a saturation of its depolarising effect

was only reached by 5 s pulses at 100 mV. Deactivation of this conductance was likewise slow, full repolarisation to resting V_m could take as long as 6 s.

Consistent with the fast deactivation and near complete lack of activity at negative potentials observed in the step protocol measurements (fig. 6.13), TREK2 expression was not sufficient to set resting V_m to the K^+ reversal potential and a slow re-polarisation corresponding to the deactivation of the endogenous current could be observed (fig. 6.14B).

6.3.3 Control for PKA phosphorylation state

The behaviour of TREK2 in excised patches was dominated by slow activation and deactivation kinetics. There were substantial currents at hyperpolarised potentials.

This was accompanied by transient changes to selectivity upon voltage activation. In intact cells, faster voltage-dependent relaxations and little channel activity at rest were observed. Similar distinguishable behaviours of TREK1 were classed into a 'voltage-gated' and a 'leak-mode' by Bockenhauer et al. (2001) and Sandoz et al. (2006). These modes could be switched through phosphorylation of a PKA sensitive site in the C-terminus (S348) or phosphorylation mimicking point mutations. Phosphorylation or the S348D mutation confers a low P_o voltage-dependent mode, whereas de-phosphorylation or the S348A mutation resulted in a 'leak' channel with uniform P_o at all membrane potentials (Bockenhauer et al. 2001).

As de-phosphorylation might occur after excising membrane patches, I suspected that variability of voltage gating in the previous dataset might be due to mixtures of phosphorylated and dephosphorylated TREK2 channels present in excised patches. Since PKA phosphorylation regulates voltage

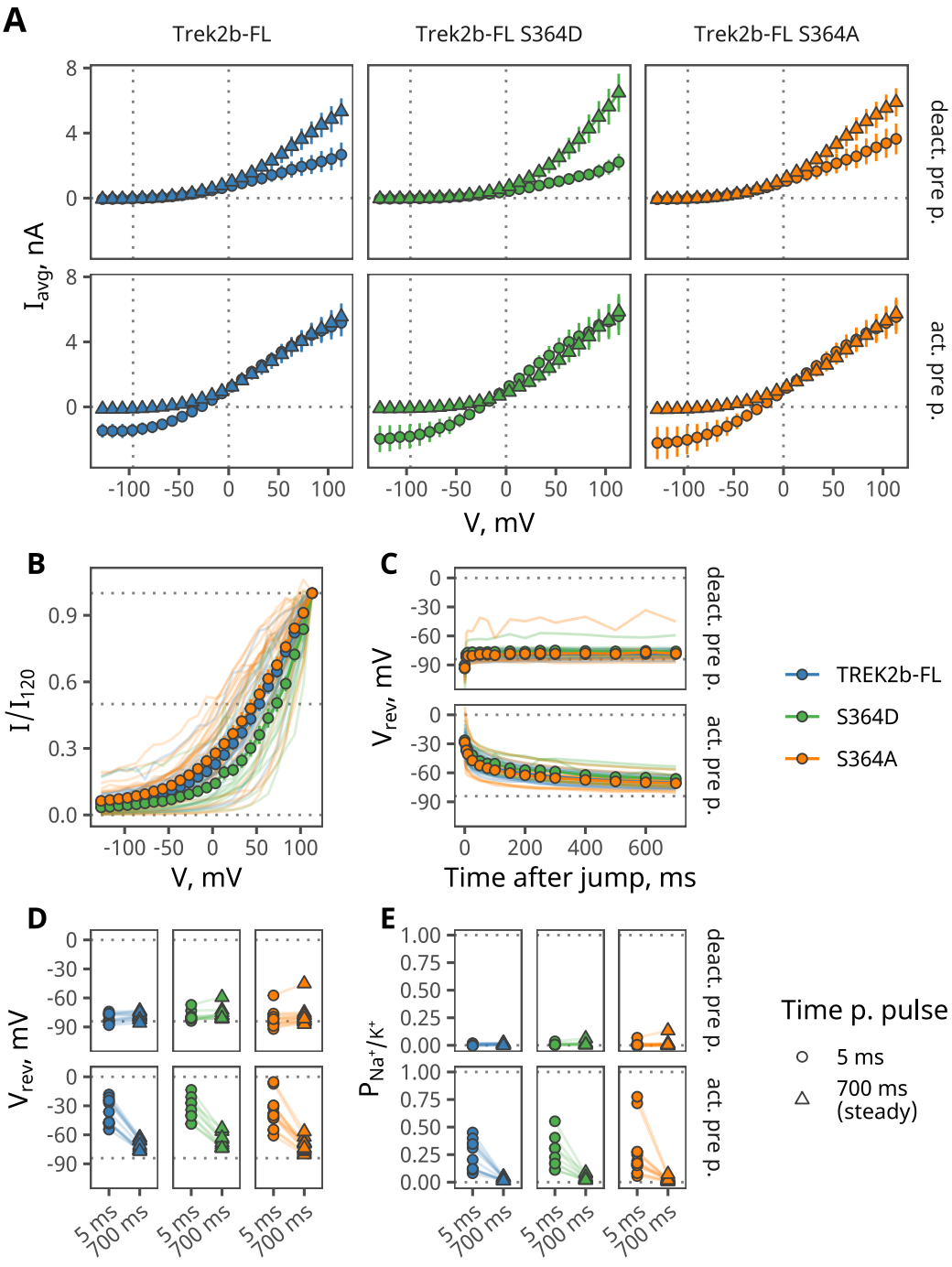


Figure 6.15: *Phosphorylation does not affect selectivity of TREK2* A: IsochronalIV-curves of TREK2 following a deactivating or activating pre-pulse. B: Normalised tail currents of the step-protocols. No saturation can be observed and threshold for activation varies. C: Time course of the V_{rev} change determined from isochronalIV-curves (see fig. 6.8B)s. D,E: V_{rev} and calculated permeability ratios based on them. E should be understood as a back-of-envelope calculation than a reliable quantification as we cannot be sure that all prerequisites of the equation used are correct in the recording conditions here (see eq. 6.1). n is > 9 for each construct.

dependent behaviour I therefore tested mutants of the TREK2 PKA phosphorylation site for a voltage-dependent selectivity change.

To this end phosphorylation-state mimicking mutations were introduced into the homologous site (S364) in TREK2. Excised patch experiments with voltage-step protocols probing deactivation and activation gating were then repeated with the Na^+ containing pipette solution. Additionally, voltage-ramps were recorded as before to monitor current levels following excision.

A summary of the analysis of dynamic selectivity behaviour is shown in fig. 6.15. As can be seen in fig. 6.15A none of the mutations appreciably changed the variable voltage-dependent gating and selectivity of TREK2 in this experiment. As previously, these currents showed variability in the kinetics of voltage-dependent gating as well as dynamic selectivity. The only detectable phenotypes were slight increases of the time-dependent activating current (fig. 6.15A) and activation threshold (fig. 6.15B) in the S364D mutant. Phosphorylation by PKA therefore does not seem to cause the variability of the voltage-gating behaviour of TREK2 in excised patches or control the change in selectivity.

A closer look at 'runup'

The excision of membranes from cells expressing TREK2 is followed by a spontaneous increase of currents that is often referred to as 'runup'. As the gating phenomenon that underlies runup is another possible source of the variability seen, the time course of runup was compared between all tested constructs (fig. 6.16).

As can be seen from the example trace shown in fig. 6.16A, little to no channel activity is present with an intact cell (cell-attached recording mode).

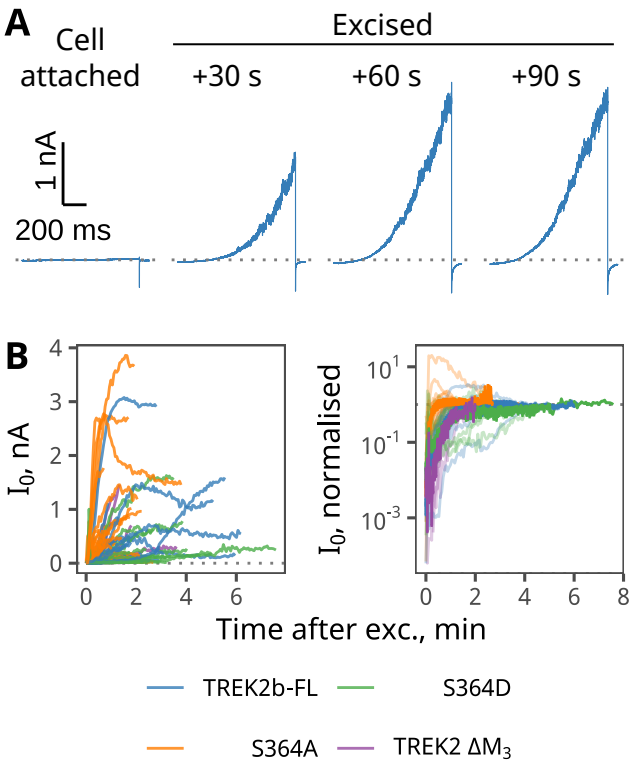


Figure 6.16: *Difference between intact cells and excised patches* A: example traces of ramp protocols recorded at different timepoint after excision B: Time course of amplitude at 0 mV extracted from consecutive ramps recorded while monitoring runup for all patches in the TREK2ΔM_3 and phosphorylation mutation dataset. C: Data of B normalised to their value at stabilisation, log scale. In many patches a rapid runup is also followed by a slower 'rundown'.

TREK2 currents of several nA amplitude develop over the course of 5 min to 10 min after excision. The extent and rate of runup was variable and no striking difference between the constructs could be seen fig. 6.16B and C.

6.4 Discussion

Here we found a considerable unexpected depolarising shift in reversal potentials of TREK2 currents in excised patches. Before discussing the data at hand it will be useful to introduce the pitfalls of interpreting such data.

6.4.1 Interpreting V_{rev} of small currents

Changes to the selectivity of K_{2P} channels have been reported to occur in many different contexts (Chen et al. 2014). Most of the situations in which

Na^+ currents through K_{2P} channels have been observed the P_o was low due to a loss of function mutation or variant, or presence of a strong inhibitory stimulus.

These small amplitude currents were used to determine the V_{rev} as an assessment of selectivity, often measured by TEVC in oocytes. This can be misleading for the following reason: If the contribution of the tested channel to the total membrane current is small, V_{rev} is determined by endogenous conductances or passive membrane leak. This can be the case even with apparently robust channel expression as shown in fig. 6.13. In this case, the open probability of the predominantly voltage-gated TREK2 is presumably too low at negative potentials to set the reversal potential in the presence of endogenous conductances. Here, repolarisation after activation of an endogenous Na^+ or Ca^{2+} current is mostly dependent on their deactivation although TREK2 is present at high density in the membrane.

However, the experiments in inside-out configuration conducted in this study are less confounded by these problems. In the same system and with comparable pipette sizes single-channel currents were recorded chapter 4. Interference of endogenous channels in this experiments was rare and limited to single-channels at a time. Also in cell-attached configuration, pending runup, little to no endogenous current is seen (fig. 6.16A). Passive membrane leak was likewise ruled out to contribute much to the measured currents (figs. 6.3 and 6.4C). In conclusion the robust excised patch currents seen should yield values of V_{rev} that accurately reflect the properties of the overexpressed channels.

Conceptually the observed effect is also different from the suggested dynamic selectivity of TWIK1 and TASK channels because it is occurring with *activation* by voltage, not in the presence of an *inhibitory* stimulus. This it-

self makes it less fragile to be confounded by other current contributions because a more robust, activated current underlies the measurement of the depolarised V_{rev} in question.

V_{rev} of isochronal IV-curves

Analysis of isochronal IV-curves of TREK2 in excised patches revealed a transient change in V_{rev} and therefore to its selectivity. The currents can be seen to change direction at fixed potentials (fig. 6.5). This is impossible without a change to the ion species carrying the current (see also eq. 1.6).

Non-selective permeability is TREK2 is a transient phenomenon, as can be seen from fig. 6.8B. Voltage-activated channels are mostly non-selective and return to K^+ selective behaviour during deactivation. TREK2b-FL shows selective behaviour in ramp-protocols and when pre-conditioned with a negative voltage. However, these measurement also show some variability and modestly depolarised values of V_{rev} can also be observed without previous voltage-activation. This suggests that K^+-selectivity at rest may also be imperfect.

Entry into this non-selective state appears to occur only with large depolarisations and this is why the V_{rev} of IV-curves determined from step-protocols with a deactivating pre-pulse or voltage-ramp protocols are not strongly affected. In this case the activated current is mostly sampled at potentials positive to the reversal potential and the change in selectivity may be overlooked. To measure this change the construction of instantaneous IV-curves following activation is therefore required.

Values for V_{rev} determined from isochronal IV-curves of activating currents were not reliable at the early phases of activation, presumably because current

amplitude was small relative to the simultaneously occuring capacitative transient. This resulted in artefactual values of V_{rev} smaller than the K^+ equilibrium potential in some cases (fig. 6.15C).

6.4.2 Transient selectivity changes during the gating cycle

The variability and seamless time-dependent transitions of V_{rev} can be best explained by a mixed population of non-selective and selective TREK2 channels present. These may open and close and also interconvert during the voltage-gating cycle with the result of a transient breakdown of selectivity at large depolarised potentials. The large inward tail current relaxations seen at negative potentials (fig. 6.9) are not only representing a decay of P_o (deactivation gating), but also a decay in driving force for the resulting macroscopic current as the selectivity of the resting channel is re-established. As can be seen in fig. 6.9, tail relaxations may occur without measurable prior activation. This either means that in some cases activation is too fast to be resolved by patch clamp, or that such tail-currents in the absence of a voltage-dependent activation represent the decay in driving force for the non-selective current as K^+ selectivity is restored.

Another argument in support of this interpretation comes from comparing the deactivation kinetics following a fixed pre-pulse with the deactivation kinetics at a fixed potential following a variable test-pulse (tail currents). Only in the latter case voltage-dependent rates can be observed (fig. 6.10C). This suggests that the channels opened by mild depolarisation close at a slower rate than channels opened by strong depolarisation and therefore may occupy different open states with distinct stability.

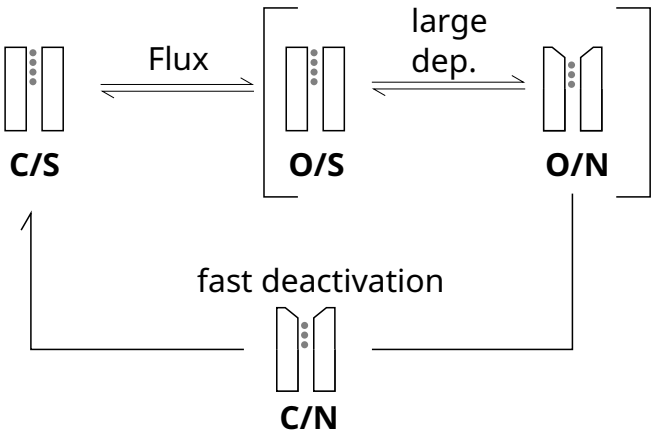


Figure 6.17: *Sketch of the observed voltage-gated relaxations* Activation of the channel by outward flux (Scheel et al. 2005) results in a mixture of selective and unselective channels (O/S and O/N). Larger depolarisations favour non-selective permeation. Closure from the non-selective state is faster than from the selective state and may occur through a different pathway.

This relationship between the rate of the tail relaxation does not hold if K^+ is the only cation species in the external solution (fig. 6.11). Speculatively, a non-selective, Na^+ bound state could be the fast deactivating more unstable state observed here.

TREK2 occupies different open states depending on mechanical stimulation as demonstrated by pharmacological, structural and electrophysiological methods (Dong et al. 2015; McClenaghan et al. 2016). Here there is some initial evidence that voltage-dependent gating may also involve states that are distinguishable by their differing selectivity and closing rate.

The deactivation behaviour agrees well with the idea of a channel population consisting of both selective and non-selective channels. The variability and complexity of the relaxations could reflect both the closing as well as the return to selectivity of this mixed population. This idea is summarised in the schematic shown in fig. 6.17.

Interestingly, activation-dependent dynamic selectivity has been observed in mutants of Shaker where it manifests on a per-channel basis with subconductances of differing selectivity (Zheng and Sigworth 1997). This gave the initial idea for the above interpretation. The variety of interconvertible modes and subconductance behaviours in TREK2 (chapter 4) would therefore be an

obvious place to start a more detailed investigation into the loss of selectivity of TREK2.

Dynamic selectivity requires a flexible SF

The V_{rev} of TREK2b-FL currents activated by depolarisation may assume values close to 0 mV. This corresponds to almost no preference between conducting K^+ vs other the ion as calculated by the GHK-Voltage equation (eq. 6.1). Inward currents through pre-activated TREK2 channels are prominent in the presence of external Li^+ and Na^+ and were only reduced in the $NMDG^+$ solution. However, the pipette solution used here also contained Mg^{2+} and Ca^{2+} to aid seal formation. It therefore seems more likely that the residual inward currents in the $NMDG^+$ solution are carried by these divalent ions than the large $NMDG^+$. Permeation of Li^+ and Na^+ generally requires permeation with an hydration shell that is at least partially intact (Hille 2001c). Permeation of hydrated ions at large rates is incompatible with the canonical SF structure of K^+channels.

Nevertheless, the tetrameric K^+channel architecture has been shown to support non-selective conduction and to accommodate ions like Na^+ with only minor changes to the selectivity filter structure. A combination of loss of the selective S1 and S2 K^+ binding sites in combination with maintenance of a high conduction rate has been proposed to underlie non-selective permeation through NaK channels (Liu and Lockless 2013). The potassium channel selectivity filter shows considerable flexibility and such rearrangements of the outer SF are compatible with the time-scale of the selectivity change observed in TREK2 ($\sim$500 ms). Mutants of NaK imitating the sequence of non-selective CNG channels (NaKCNG-N) lack only the S1 site and conduct

non-selective currents (Derebe et al. 2011a). Interestingly, the crystallographic data of TREK2 in the DOWN state showed reduced electron density in S1 and was modelled with only 3 K^+ bound (Dong et al. 2015). However, the resolution of the surrounding SF loop structure was insufficient to reliably establish the position of the residues forming the binding site. The reversible and fast (compared to dynamic selectivity in TWIK1) changes to selectivity in TREK2 suggest that the SF structure undergoes significant changes during voltage-dependent gating and must therefore exhibit a significant degree of structural plasticity.

6.4.3 Influence of the recording condition

Similar measurements in intact oocytes lacked the prominent inward currents seen during deactivation gating in excised patches. The strongly voltage-gated behaviour in combination with large endogenous Na^+ or Ca^{2+} currents made interpretation of the V_{rev} values extracted from these data difficult. Depending on the low P_o at negative potentials even overexpression of TREK2 may only have a minor influence on resting V_m or re-polarisation in the presence of other conductances (fig. 6.14B). Considering the endogenous currents as the cause for the depolarised membrane potentials observed, the data from this experiment is consistent with a high degree of K^+-selectivity for TREK2 in intact oocytes, as has been established many times in similar measurements (Bang et al. 2000; Staudacher et al. 2011; Simkin et al. 2008).

The biophysical properties of TREK2 in excised patches are often different from behaviour in intact cells and the variability between patches can be extreme (fig. 6.9). Recordings in the cell-attached configuration show almost no channel activity, whereas currents of several nA can be observed after

excision and completion of runup. This suggests that P_o of TREK2 in intact transfected HEK293 cells is extremely low whereas channel density in the membrane may be quite large. Currents of 10 nA amplitude at 120 mV membrane potential were easily reached. This corresponds to ∼1100 open channels assuming a driving force of 180 mV and an estimate of 52 pS for the conductance of TREK2b-FL.

TREK behaviour has previously been categorised into 2 distinguishable modes with high and low P_o (Bockenhauer et al. 2001; Sandoz et al. 2006). The high activity behaviour found here retains a voltage-gated behaviour, where previously observed high activity TREK-1 had uniform open probability in the physiological voltage range (Bockenhauer et al. 2001). The activation through runup therefore does not seem to be equivalent to this 'mode change' as voltage-dependent gating is preserved after completion of runup.

6.4.4 Possible physiological significance

TREK channels are well established as inhibitory conductances in DRG neurons (Mathie and Veale 2015). TREK2 expression in C-fiber nociceptors ensures a hyperpolarised resting V_m compared to knock-out models in these neurons (Acosta et al. 2014). The pain perception phenotype of TREK2 knock-out mice is also consistent with a inhibitory effect of TREK2 on DRG neuron firing rates (Pereira et al. 2014). Likewise, there is no evidence for a depolarising effect of TREK2 currents *in vivo* and we have little reason to assume that TREK2 produces a non-selective depolarising conductance based on the data from excised patches alone.

However, neither of the two forms of behaviour encountered in intact cells or excised patches are consistent with the expected behaviour of TREK as a

K^+ selective background conductance controlling V_m at rest. We therefore do not know whether or which of these two behaviours could be an artefact of the overexpression systems used.

TREK2 is expressed in wide range of tissues, with a specific composition of isoforms, ATI-variants and heterodimers with distinct behaviours present in different cell types (Gu et al. 2002; Staudacher et al. 2011; Lengyel et al. 2016; Blin et al. 2016). The context in which TREK2 is expressed is therefore expected to have profound effects on its gating and biophysical properties, including dynamic selectivity.

The data at hand do not allow us to conclude that transient Na^+ permeability of TREK2 occurs *in vivo*. TREK2 is expressed in the periphery (such as pancreas and kidney, Gu et al. 2002) and their role in these tissues is not yet well understood. It is therefore tempting to speculate that the ability of its structure to support non-selective permeation would have a role in these contexts. Isoform b studied here is expressed in these peripheral tissues, whereas isoform c is commonly expressed in neurons (Staudacher et al. 2011). To account for this differences study of a wider panel of TREK2 variants with regard to selectivity might be required.

In conjunction with further voltage-gated conductances, an ion channel with voltage switchable selectivity as encountered here would pose interesting possibilities for shaping AP waveform and frequency as well as resting V_m on an intermediate (0.5 s to 1 s) time scale. As the example of TWIK1 shows, the recovery kinetics of a selectivity change can be exploited in a regulatory mechanism to give rise to a 'molecular memory' (hysteresis) of several minutes (Chatelain et al. 2012; Feliciangeli et al. 2010).

6.4.5 Variability

A wide range of stimuli controls the P_o of TREK channels and not all of them can be sufficiently controlled in the experiments shown here. Therefore, several factors may account for the variability and difference in behaviour of TREK in cells and excised patches.

a. Phosphorylation

b. lipid signalling

c. mechanical factors

d. unknown intracellular soluble factors

In excised patches we expect TREK2 to become de-phosphorylated over time which would increase its activity. I speculated that differing levels of PKA activity in individual HEK293 cells might account for some of the variability.

However, experiments with phosphorylation mimicking mutants showed the same variable behaviour as the WT, and make it therefore unlikely that PKA phosphorylation contributes to this variability. Subtle effects on voltage-gating of the mutants are therefore difficult to ascertain for this dataset.

TREK2 is also regulated by PKC (Kang et al. 2006). The corresponding mutants were not tested here which leaves open whether PKC phosphorylation contributes to variability.

Additional mechanisms may be involved, as TREK channels are activated by both arachidonic acid and PIP_2 (Chemin et al. 2005). The content of the lipid second messengers also might change over the lifetime of a patch giving rise to runup. The mechanism of action and effect of PIP_2 on TREK channels is controversial and inhibition as well as activation has been observed, this is likely due to AA and PIP_2 binding and competing at multiple activatory

and inhibitory binding sites (Chemin et al. 2005). Assuming a dominating activating effect of PIP_2 we would expect that dropping PIP_2 content in an excised patch to cause rundown like for example in K_{ATP} channels (Proks et al. 2016), but the opposite is the case here.

Excised patches are complex systems with distinct mechanical properties. Interactions with cytoskeletal components are partially disrupted by excision, and adhesion of the lipid to the glass of the patch pipette causes stress and tension that may vary over the lifetime of the patch (Suchyna et al. 2009). Mechanosensitive K_{2P} channels such as TREK2 have a low threshold for activation by membrane tension and are partially activated by the adhesion tension in unpressurised patches (Brohawn et al. 2014a; Honoré et al. 2006). The runup of TREK currents has been attributed to the progressive loss of the cytoskeleton over the lifetime of the patch (Honoré et al. 2006). Intact cytoskeletal elements resist mechanical stimuli and may reduce local membrane tension, loss of this mechanoprotective structures over the lifetime of the patch increases the number of channels available for opening (Honoré et al. 2006). Similarly, intact cells have a large reserve of membrane area and membrane tension in a non-swollen cell should be low (Groulx et al. 2006), consistent with the low P_o assumed to underlie whole-cell currents. Therefore differences in membrane tension can well explain variability, runup and differences in behaviour of currents recorded from intact cells and excised patches.

Furthermore the measurements shown here were all conducted at room temperature. This additionally lowers the P_o of TREK at rest in whole cell configuration (Kang et al. 2005).

TREK, like any other ion channel, is expected to reside within complex assemblies comprised of scaffolding proteins and associated signalling ma-

chinery such as kinases, GPCRs and phosphatases. For example, TREK1 assembles on the AKAP150 scaffolding protein (Sandoz et al. 2006) which greatly increases P_o and has been proposed to cause loss of voltage-gating.

Speculatively, TREK channels are well situated to also be sensitive to other factors determined by cellular anatomy. Membrane surface structures such as villi, clathrin coated pits, synapses and dendrites as well as 'lipid rafts' in general may have distinct lipid compositions and mechanobiological properties that would be expected to have a profound effect on gating by lipid second-messengers and membrane tension.

These factors will not be faithfully reproduced in model overexpresssion systems and this may give rise to non-canonical behaviour. Finally the loss of a yet unknown soluble inhibiting intracellular factor of TREK2, protein or otherwise, could also be responsible for runup and variability.

6.4.6 Conclusions

The transient breakdown of selectivity in TREK2 is easily overlooked by either using high K^+_{ext} for biophysical characterisations or determining V_{rev} at rest alone. Here this phenomenon was revealed simply by recording a voltage-step protocol with an activating pre-pulse.

The significance of this phenomenon is yet uncertain, as dynamic selectivity was not observed in intact cells suggesting that its occurrence is dependent on intracellular and/or mechanical factors regulating TREK2. It is conceivable that TREK2 would have a dual role as an excitatory conductance upon sustained depolarisation.

Further work is required both to determine the context in which TREK2 becomes non-selective, as well as to characterise this dynamic selectivity in the

context of K^+channel SF structure and function. That the structure of TREK2 can support Na^+ permeation needs to be taken into account in the design and interpretation of further electrophysiological and even crystallographic experiments.

Chapter 7

General discussion

7.1 Summary

This project started with the ambition of contributing novel and quantitative insights into K_{2P} channel gating from single-channel recordings. To this end I built my own patch-clamp rig with single-channel recording capability. TASK3 had been chosen as a model channel to study a putative hydrophobic barrier in K_{2P} channels. However, because my results indicated no GoF at the TM2.6 site this particular project was not continued. Intriguingly, later research did find a modest gain of function in the same experiment (Ben Soussia et al. 2019).

Next, I collected single-channel data to help study the mechanism of action of the TREK opener BL1249 (Schewe et al. 2019). An increase to single-channel conductance was found that was associated with activation by BL1249 only and not other drugs that also activate the SF gate eg ML335. Although we cannot conclusively rule out other explanations, or the contribution of

additional mechanisms to this increase of conduction, an electrostatic effect of activation by BL1249 is in good agreement with the data.

The predicted K^+-dependence of the mechanism inspired a series of experiments in high concentrations of K^+_{int}. Here I observed an entirely novel property of the TREK—closure of the channel in the presence of high internal ionic strength. Furthermore, a concentration-conductance relation of TREK was recorded that demonstrates (as expected) hallmarks of a multi-ion permeation mechanism, a case in point against the erroneous description of K_{2P} channels as 'GHK-leaks'.

The observation of large transient inward currents in TREK2 caused me to investigate selectivity of these channels in the context of voltage-dependent gating. Here, another novel property of TREK emerged, a voltage-switchable dynamic ionic selectivity. While it was not possible to come to a full conclusion on the context and physiological relevance to this phenomenon during the course of this project, it raises the question of whether TREK2 can be non-selective channel in physiological conditions.

All these experiments face a particular challenge; to interpret gating and permeability effects that are likely to be caused by changes to SF occupancy. Such occupancy changes can be produced by changes in the electrostatics of the cavity (e.g. TM2.6 mutations and BL1249) or changes to the channels milieu (e.g. ionic strength, $[K^+]_{ext}$).

These channel properties are summarised by a hypothetical gating scheme in fig. 7.1. In the following sections I will discuss these findings as well as the challenges encountered during this project in the wider context of K^+ channel structure-function relationships.

7.2 K_{2P} channels in a general context

The function of K^+ channels can be conceptualised by the action of two structural elements, the SF and the inner helices (S2 in K_{ir}, S6 in K_v and M2 and 4 in K_{2P} channels). In some, but not all, K^+ channels the inner helices form an occlusion of the channel (called the activation gate AG, lower gate or helix bundle crossing in K_v, KcsA, K_{ir} and X-gate in TASK channels). In other K^+ channels the diameter of the channel cavity permit access to the SF at all times (BK, TREK channels, MthK).

In mechanosensitive K_{2P} channels the inner helices have been captured in two conformations, called UP and DOWN. Activation gate opening in KcsA can be incremental or gradual as demonstrated by a series of partially open states (Cuello et al. 2010b) but it is always symmetric. However, in mechanosensitive K_{2P} channels, both gradual (Lolicato et al. 2014) and asymmetric (Brohawn et al. 2014a) inner movements can be found.

In KcsA and K_v channels opening of the AG is coupled to inactivation of the SF (Cuello et al. 2010a), while other K^+ channels do not inactivate or show inverse coupling in which the resting AG/inner helix conformation is coupled to C-type inactivated filter states (Yan et al. 2016). Mechanosensitive K_{2P} as well as the related *Drosophila* K_{2P} channel KCNK0 likely gate by inverse coupling (Ben-Abu et al. 2009; McClenaghan et al. 2016).

C-type inactivation or other gating processes of the SF of K^+ channels are sensitive to mutations in the pore helix interface and extracellular pore entrance. This has lead to the idea of a 'molecular bowstring' of interactions in the back of the SF loop that determine stability of the conductive state as well as selectivity (Cheng et al. 2011). Beyond K^+ channels these principles

may even be conserved in distantly related channels with the same topology, such as the AMPA receptor (Poulsen et al. 2019).

A unique property that follows from the topology of K_{2P} channels is their 2-fold instead of 4-fold symmetry. Since the 'molecular bowstring' comprises both intra- and intersubunit interactions this could have consequences for the stabilisation of the SF. Indeed, this has been found to be the case by mimicking K_{2P} channel SFs in a K_v background (Chapman et al. 2001). However, this lack of symmetry as well as degenerate SF sequence have not been found to change the properties of ion coordination or to promote a abnormal SF conformations in known K_{2P} channel structures (Brohawn et al. 2012; Miller and Long 2012).

Accordingly, K_{2P} channels make use of the same principles and structural elements for their function as the tetrameric channels they evolved from. Except for a putative association of their asymmetric SF sequence with poor selectivity, their unique membrane topology does not seem to have obvious functional consequences.

K_{2P} channels are diverse

The sequence homology between different K_{2P} channels can be low and functional domains of K_{2P} channels, for example the C-terminus of TREK or the HRE of TASK are without known homologues. The crystal structure of TASK1 (Rödström et al. 2019) captured the channel in a closed state in which the pore is occluded by action of the X-gate/HRE.

This finding highlights the diversity within the K_{2P} channel family. As the range of behaviours, gating inputs and roles suggest these channels may have little in common with each other beyond their transmembrane helix topology.

Structures of further K_{2P} channel sub-subfamily members such as TALK and THIK may yet reveal further variations on the general theme of inner helix movement and SF gate that defines K^+ channel function. Major mechanistic changes such as direction of coupling of the AG movement to the SF have been shown to be conferred by point mutations in other K^+ channels (Labro et al. 2018). We should be careful to assume that apparently general structural or functional properties such as an occluding inner gate or inverse coupling is preserved for all K_{2P} channels or to over-interpret sequence similarities.

K_{2P} channels can be found in many roles

K_{2P} channels set the resting potential and influence firing rates and patterns in neurons (Brickley et al. 2007; Acosta et al. 2014), similar to M-current/KCNKQ type K_v channels (Brown and Passmore 2009). They can also be found as sensors of metabolic status in hormone secreting cells of the carotid body (Buckler 2015), similar to K_{ATP}/SUR channel complexes in pancreatic β-cells. Neuronal K_{2P} channels such as TRAAK are essential for propagation of APs in nodes of Ranvier (Brohawn et al. 2019) and non-exitable cells may can be enabled to fire APs by reconstituting the required voltage-dependent K^+ conductance through transfection of TASK3 or TREK1 (MacKenzie et al. 2015). This demonstrates that K_{2P} can fulfil the role of K_v channels which usually underlie the voltage-dependent K^+-currents of the AP. TRESK channels activate in the presence of $\left[Ca^{2+}\right]_{int}$ (Czirják et al. 2004) and may thus fulfil the role of a Ca^{2+} dependent K^+ channel.

Conclusions

There seems to be no major function commonly associated with K^+ channels that either cannot or is not fulfilled by K_{2P} channels in some context. K_{2P} channels may therefore not be as unique as previously thought.

Their unique topology is interesting and worth our attention but does not seem to be correlated with specific properties as far as can be determined. Therefore it is wrong to assign a general function to the whole family on this basis. Instead, K_{2P} channels appear to have evolved to fulfil an array of different roles by exploiting their diverse biophysical properties. Thus, contrary to common phrases that are used to describe this channel family, K_{2P} channels are not simple 'background' or 'leak' channels.

7.3 Gating, Permeation and Selectivity entwined

The permeant ion and the occupancy of the filter have been linked to stability of the conducting SF in many different K^+ channels (Schroeder and Hansen 2008; Baukrowitz and Yellen 1996; Matulef et al. 2016; Demo and Yellen 1992; Rauh et al. 2018). The SF serves as a principal gate in a growing list of K^+ channels (BK, TREK, MthK, TRESK Piechotta et al. 2011; Posson et al. 2015; Posson et al. 2012; Wilkens and Aldrich 2006; Lengyel et al. 2018). Thus the SF emerges as a site that is central to crucial aspects of K^+ channel function—gating and selective permeability.

Bound ions and SF stability

We can easily imagine why the stability of the SF structure will be dependent on the number and species of the ions bound within it. The orientation of

the SF backbone is constrained by maintaining the coordination of the bound K^+ and free to relax in its absence. Also, occupancy patterns of the SF in turn are sensitive to the concentrations of ions present on either side of the membrane (Ogielska and Aldrich 1999) and are likewise pivotal for selective permeation through the channel itself (Kopec et al. 2018). This interplay of conduction, SF-stability and gating can make it difficult to unambiguously interpret the effects of mutations or other interventions that are expected to affect occupancy. This was the case for TM2.6 mutations (chapter 3) and the mechanism by which BL1249 activates TREK channels (chapter 4).

Care must be taken not to assume all too simple or general correlations between occupancy patterns, number of binding sites and gating as well as selectivity behaviours. In the case of KcsA the putative strict dependence of C-type inactivation on occupancy of the S2 site (Devaraneni et al. 2013; Matulef et al. 2016) has been disproved (Li et al. 2017), likewise selective-permeation, which is associated with multi-ion occupancy (Derebe et al. 2011b; Kopec et al. 2018) has also been observed in channels with fewer than the usual 4 binding sites (by deletion of *inner* sites Heginbotham et al. 1994; Labro et al. 2012; Tilegenova et al. 2019).

7.3.1 Gating and conductance in practice

It is therefore clear that gating and permeation are interdependent due to the nature of the SF doubling as a gate. Therefore gating and permeation may be difficult to distinguish in a most electrophysiological recording settings. The equilibration of K^+ binding sites or changes in occupancy pattern must proceed at least as fast as permeation. Assuming a 10 pA unitary current ~62 ions pass the SF in 1 μs.

This timescale is therefore out of reach even for functional techniques with high temporal resolution such as single-channel recording. We do not expect to be able to directly observe gating events that are coupled to permeation events (Schroeder and Hansen 2009). Rather, such events will only be apparent in non-linear relationships of concentration and conductance (Läuger et al. 1980) as well as distorted openings and beta-distribution shapes of amplitude histograms (if gating is faster than time-resolution in general, see section 4.1.3).

Explicit analysis of such subresolution information will not be possible for all channels and likely remain a specialist technique. In practice estimates of conduction rates through single channels will in many cases be confounded by fast gating processes therefore blurring these two concepts.

MD simulations allow us to access conduction timescales, but long simulations that allow to fill the gap between electrophysiological and computational experiments are still too expensive to be routine. As the ongoing passionate controversy around permeation mechanisms demonstrates (Kopfer et al. 2014; Kratochvil et al. 2016; Tilegenova et al. 2019; Kopec et al. 2018), generation and interpretation of computational data without a means to directly validate the results can simply be a source of confusion. It may take many more years until the field converges on an agreed mechanistic understanding of the SF structure that was first visualised by Doyle et al. (1998) over 20 years ago.

7.4 A gating scheme of TREK

Drawing from the K_{2P} channel structure-function literature and the data collected here we can formulate a set of criteria and features that gating

models of TREK should fulfil. A cartoon model that presents my personal view and satisfies these constraints is shown in fig. 7.1.

1: Movement of the inner helices can be gradual (Lolicato et al. 2017) or asymmetric (Brohawn et al. 2014a)
2: Stimuli acting on the C-terminus are relayed to M4 helix movements (Bagriantsev et al. 2012).
3: Channels are activated by outward flux. This results in voltage-dependent gating. Filling of a closed depleted state (equivalent to recovery from inactivation in other K^+ channels) underlies this activation (Schewe et al. 2016).
4: Activating stimuli (such as AA override) the Flux mechanism. This may result in *IV*-curves of TREK currents with little apparent voltage-dependent gating ('leak modes', Schewe et al. 2016; Bockenhauer et al. 2001; Sandoz et al. 2006). From this and the previous point follows that activated 'leak mode' channels may not necessarily visit the depleted state that is prerequisite for voltage-dependent activation.
5: Rb^+ binding prevents entry into C-type inactivated SF states (Tilegenova et al. 2017), this too applies for the C-type inativation-related closed state of K_{2P} channels (Schewe et al. 2016).
6: Opening may occur regardless of the position of the inner helices, but is favoured in UP states (McClenaghan et al. 2016).
7: The channels do not inactivate and inner helix movements (UP, homologous to AG opening) are not coupled to SF collapse (Cohen and Schulten 2004; Ben-Abu et al. 2009)
8: Gating by membrane tension and heat is associated with inner-helix movements (McClenaghan et al. 2016).

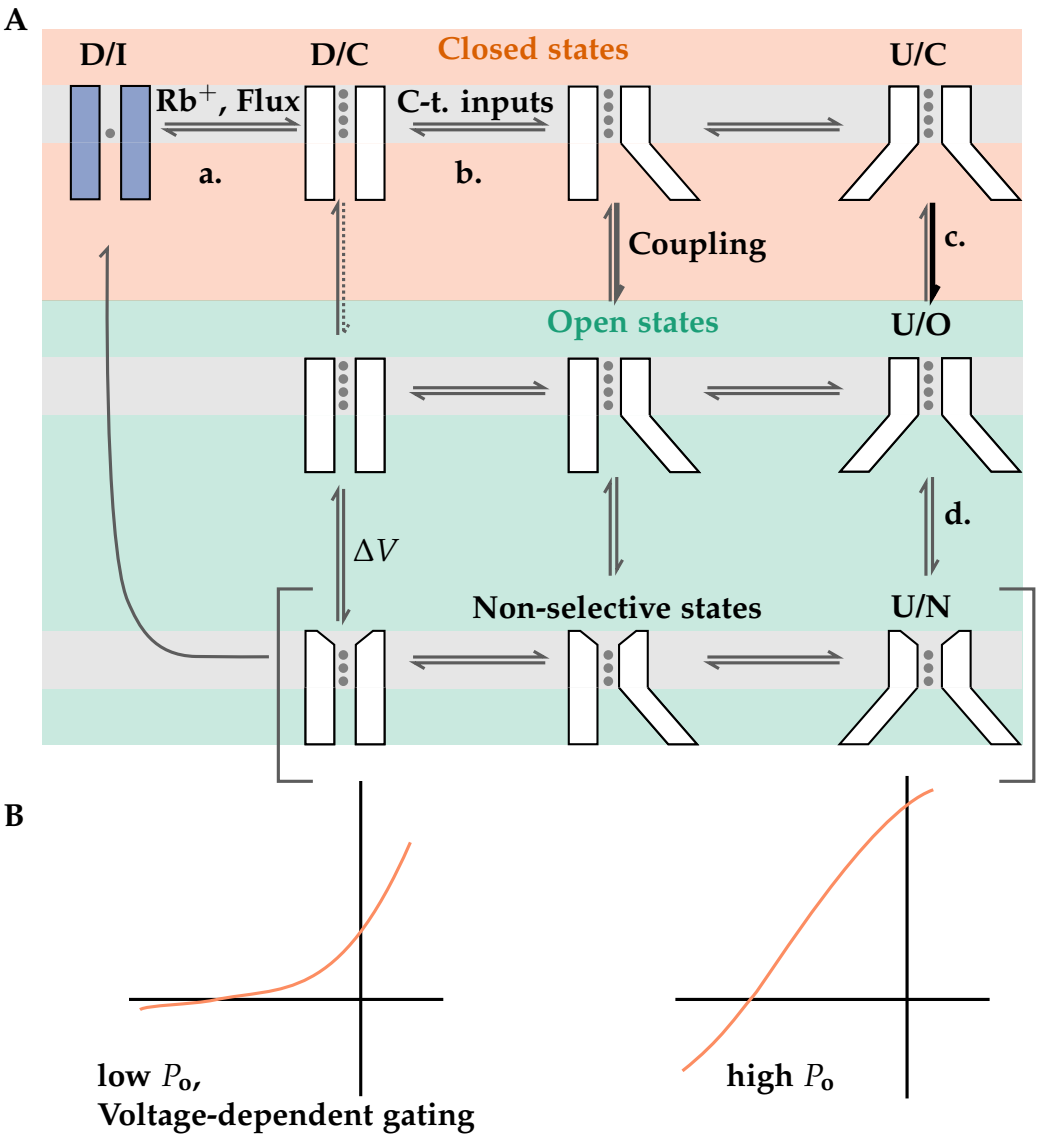


Figure 7.1: *A model of mechanogated K_{2P} channel gating* A: Cartoon model summarising the evidence for different states of mechanosensitive K_{2P} channels and how different stimuli may influence them. States are labelled with respect to the status of the AG (first letter) and the SF gate (last letter) as commonly done for KcsA (fig. 1.8). a. Flux or voltage dependent gating occurs from an inactivated depleted state. b. Other gating stimuli mediated via the C-terminus (stretch, heat, phosphorylation) lead to 'UP' movements of the inner helices (right half of the scheme). These conformational changes should be thought of as continuous gradual movements rather than structurally well defined conformations. c. These movements couple to opening of the SF gate, UP movements favour opening of the gate. If the SF is sufficiently stabilised it will not populate the depleted state and show no apparent flux gating ('leak mode'). d. Open states may become permeable to Na^+, speculatively by loss of an outer K^+ binding site. This state is quick to revert to a closed but voltage/flux gated state. It therefore may be an intermediate step towards losing further binding sites and reverting to the depleted filter state. B: Sketches of steady-state *IV*-curves of TREK2 gating dominantly by visiting the depleted state (voltage-dependent gating, left side of the scheme) as well as activated TREK2 ('leak mode', right half of the scheme).

9: Open channels are a heterogeneous population that includes transiently non-selective channels (chapter 6).

10: Non-selective permeation requires conformational flexibility in the outer SF and may be associated with a loss of binding at S1 (Derebe et al. 2011b; Shi et al. 2018)

11: Non-selective permeation or increased Na^+ permeability is related to inactivation and may occur during inactivation or en route from an inactivated state to a defunct state (Loboda et al. 2001)

7.5 Biophysical study of polymodal channels

All of the datasets collected from excised patches displayed a remarkable variability. The easiest explanation for this variability is that spontaneous gating (exemplified by the runup observed in the recordings) results in differences in the channel population under study. The measured properties may differ based on such events (state-dependence) and therefore vary with them.

7.5.1 Detailed investigations of polymodal gating

Due to apparent variability of TREK2 behaviour a rigorous quantitative analysis to dissect the underlying biophysical mechanisms (similar to the approaches used in BK or K_v channels) was not possible. The variability of TREK2 behaviour made it necessary to rely on within-experiment comparisons wherever possible. While this is a commendable strategy in general, some indispensable analyses such as comparing mutations cannot be done without comparing results pooled from separate patches and recordings. However,

the presence of variability in the data should not be brushed aside as 'bad quality data'. Presence of variability is evidence that we do not control the parameters of our experiments sufficiently. More so, we may not even clearly understand what those parameters are.

Many of the stimuli affecting P_o of TREK channels are not controlled when using HEK293 as a model system, such as membrane tension, and lipid content as well as other mechanical factors (see section 6.4.5). Not knowing what factors exactly affect the measurement, extracting mechanistic information from the data becomes difficult. One strategy to interpret and analyse the data more successfully would be to correlate the channel behaviour with measurements of P_o or simultaneous recordings of gating stimuli acting on the patch. With such additional measurements, we can use the state-dependence to our advantage, a strategy that has been used for example by McClenaghan et al. (2016) through measuring norfluoxetine block as an estimate for the status of the inner helices.

Dissecting gating of a polymodal channel will therefore require additional methods. Membrane stretch in an excised patch can be estimated by monitoring shape of the membrane with flourescence microscopy (Sokabe et al. 1991). When channels are reconstituted into artificial lipid bilayers, which is feasible for TREK channels (Berrier et al. 2013; Clausen et al. 2017), full control of the membrane lipid content can be achieved. This could be utilised to study lipid messenger regulated gating of these channels.

Another avenue to study is to use experimental conditions in which part of the response of the complex gating machinery is saturated or otherwise disabled. There is no way to quantitatively asses all transitions in a scheme as complex as fig. 7.1. Instead, single-channel recordings are commonly made in conditions in which only part of an assumed gating scheme is explored in

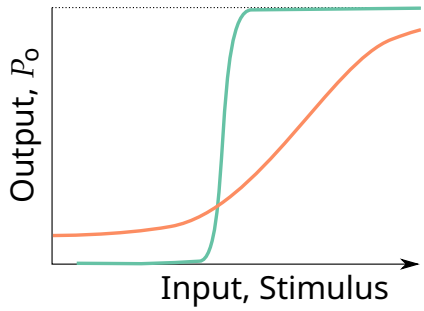


Figure 7.2: *Sketch of stimulus response curves* Sketch of the response (P_o) of a ligand gated channel (green) as well as a sensing or background channel with a more graded response (red).

order to estimate the rates of specific transitions (see Sivilotti and Colquhoun 2016, for a more in depths explanation). In the case of TREK channels several gain of function mutations are known that introduce a bias towards UP and DOWN conformations (McClenaghan et al. 2016; Bagriantsev et al. 2011).

Gating at the 'threshold' for activation

Beyond the particular difficulties in controlling all stimuli affecting TREK channels it is easy to imagine why polymodal channels pose challenges to biophysical characterisation. Common approaches and analysis techniques were developed with voltage- or ligand-gated channels in mind. The role of voltage-gated and ligand gated channels is to initiate the AP, which famously proceeds in an all-or-nothing fashion, therefore excessive spontaneous activity of these channels would contravene these roles.

Commonly gating is broken down into the action of a sensing domain coupled to a gate with a certain intrinsic open probability (Colquhoun 1998). Voltage- or ligand-gated channels mostly show tightly coupled sensing (or ligand binding) domains and little to no intrinsic activity in the absence of stimulus.

The more subtle and slow action of channels involved in setting V_m may not require such binary responses, a sketch of such response curves is shown

in fig. 7.2. In that case, multiple distinct sensing transitions may couple with low efficacy to a gate that also has some intrinsic open probability. This would mean that the channels are commonly exploring a wide range of the states depicted in fig. 7.1, with significant occupancy of intermediate and partially activated states. This would be similar to the behaviour of voltage gated channels at and around the threshold for activation, where such heterogeneity can also be seen (Chapman and VanDongen 2005).

This is the kind of behaviour the proposed role of mechanosensitive K_{2P} channels as signal integrators calls for. Although one should be careful with generalised evolutionary arguments, it does seem desirable that sensing ion-channels have shallow responses to their stimuli, *i.e.* that they are 'at threshold' over a wide range of stimuli. It also increases variability as we can expect small changes and noise of the gating stimuli to dramatically affect the experiment.

Such 'soft' gating by a multitude of stimuli will require more complex experimental designs to study and may still result in less detailed mechanistic insight than investigation of for example a glycine receptor α or K_v channel, in which stimuli can be more easily isolated.

The excised patch configuration that was chosen for most of the experiments shown here has considerable drawbacks for variability of a mechanosensitive current. Membrane tension as well as integrity of membrane associated cytoskeletal components change over the lifetime of the patch, which may stimulate TREKs. Excised patches provide easy access and control over intracellular solutions. However, the improved recording stability and preserved physiological cell architecture found in whole-cell recording may ultimately be a better approach.

Conclusions and final remarks

Overall, this work contributed to several different branches in the study of K_{2P} channel structure-function relationships and raised novel questions. For example, the recent discovery of the X-gate in TASK channels poses a new challenge to investigate the interplay of the X-gate to the SF and its precise role in gating. Likewise, the dynamic selectivity observed in TREK2 warrants further study to probe the possibility that under certain conditions TREK2 may even be an excitatory conductance.

The variability encountered posed a challenge to design and analyse the experiments but likewise spurred creativity in these aspects. I hope that updated and more elegant approaches to come will serve to provide us with a more quantitative functional description of TREK2 and other K_{2P} channels, which was the ambitious initial aim of this study.

Acknowledgements

> It takes courage to busy oneself continually with little objects, the examination of which requires the coldest patience and makes no demands on true talent.
>
> *(Georges-Louis Leclerc, Comte de Buffon)*

Firstly, I would like to thank Laura who has supported me with great love and patience through all that the completion of this undertaking has put me through.

Harvey Davis turned from collaborator to friend during the course of this project and has through countless conversations about patch-clamping over lunch helped to refine the experiments presented here.

Michael Puljung welcomed me into his journal club, the teaching and impulses received from these meetings with him as well as all other members of the group were instrumental in sharpening my arguments.

I would like to thank all members of the Tucker lab past and present: Prafulla Aryal, Michael Clausen, Conor McCleneghan, Ehsan Nematian and Manuel Arcangeletti for the practical training and hands-on support received as well as for the camaraderie and many discussions. Alexander Cloake and

Peter Proks deserve a special mention here for providing invaluable help with proof-reading the manuscript.

I am grateful to Vijay Renigunta, Günther Schlichthörl and Jürgen Daut for laying the foundation of my scientific education and electrophysiological apprenticeship and pushing me towards studying at this university.

Finally, I thank Stephen for his commitment to mentoring and supporting me for the last 5 years.

Bibliography

Acosta, C. et al. (2014). 'TREK2 Expressed Selectively in IB4-Binding C-Fiber Nociceptors Hyperpolarizes Their Membrane Potentials and Limits Spontaneous Pain'. In: *Journal of Neuroscience* 34.4, pp. 1494–1509.

Aller, M. I. (2005). 'Modifying the Subunit Composition of TASK Channels Alters the Modulation of a Leak Conductance in Cerebellar Granule Neurons'. In: *Journal of Neuroscience* 25.49, pp. 11455–11467.

Alloui, A. et al. (2006). 'TREK-1, a K+ channel involved in polymodal pain perception'. In: *The EMBO Journal* 25.11, pp. 2368–2376.

Alvarez, O. and R. Latorre (2017). 'The enduring legacy of the "constant-field equation" in membrane ion transport'. In: *The Journal of General Physiology* 149.10, pp. 911–920.

Armstrong, C. M. (1972). 'The Inner Quaternary Ammonium Ion Receptor in Potassium Channels of the Node of Ranvier'. In: *The Journal of General Physiology* 59.4, pp. 388–400.

Armstrong, C. M. and F. Bezanilla (1973). 'Currents Related to Movement of the Gating Particles of the Sodium Channels'. In: *Nature* 242.5398, pp. 459–461.

Aryal, P., M. S. Sansom and S. J. Tucker (2014a). 'Hydrophobic Gating in Ion Channels'. In: *Journal of Molecular Biology* 427.1, pp. 121–130.

Aryal, P. et al. (2014b). 'A hydrophobic barrier deep within the inner pore of the TWIK-1 K2P potassium channel'. In: *Nature Communications* 5.

Aryal, P. et al. (2017). 'Bilayer-Mediated Structural Transitions Control Mechanosensitivity of the TREK-2 K2P Channel'. In: *Structure* 25.5, 708–718.e2.

Ashmole, I. et al. (2009). 'The response of the tandem pore potassium channel TASK-3 (K2P9.1) to voltage: gating at the cytoplasmic mouth'. In: *The Journal of Physiology* 587.20, pp. 4769–4783.

Ashmole, I., P. Goodwin and P. Stanfield (2001). 'TASK-5, a novel member of the tandem pore K + channel family'. In: *Pflügers Archiv - European Journal of Physiology* 442.6, pp. 828–833.

Bagriantsev, S. N., K. A. Clark and D. L. Minor (2012). 'Metabolic and thermal stimuli control K(2P)2.1 (TREK-1) through modular sensory and gating domains'. In: *The EMBO journal* 31.15, pp. 3297–3308.

Bagriantsev, S. N. et al. (2011). 'Multiple modalities converge on a common gate to control K2P channel function: A common gate controls K2P function'. In: *The EMBO Journal* 30.17, pp. 3594–3606.

Bang, H., Y. Kim and D. Kim (2000). 'TREK-2, a New Member of the Mechanosensitive Tandem-pore K $^+$ Channel Family'. In: *Journal of Biological Chemistry* 275.23, pp. 17412–17419.

Barel, O. et al. (2008). 'Maternally Inherited Birk Barel Mental Retardation Dysmorphism Syndrome Caused by a Mutation in the Genomically Imprinted Potassium Channel KCNK9'. In: *The American Journal of Human Genetics* 83.2, pp. 193–199.

Barriere, H. et al. (2003). 'Role of TASK2 Potassium Channels Regarding Volume Regulation in Primary Cultures of Mouse Proximal Tubules'. In: *The Journal of General Physiology* 122.2, pp. 177–190.

Barry, P. H. and J. W. Lynch (1991). 'Liquid junction potentials and small cell effects in patch-clamp analysis'. In: *The Journal of Membrane Biology* 121.2, pp. 101–117.

Baukrowitz, T. and G. Yellen (1996). 'Use-dependent blockers and exit rate of the last ion from the multi-ion pore of a K+ channel'. In: *Science (New York, N.Y.)* 271.5249, pp. 653–656.

– (1995). 'Modulation of K+ current by frequency and external [K+]: a tale of two inactivation mechanisms'. In: *Neuron* 15.4, pp. 951–960.

Beckstein, O. and M. S. P. Sansom (2006). 'A hydrophobic gate in an ion channel: the closed state of the nicotinic acetylcholine receptor'. In: *Physical Biology* 3.2, pp. 147–159.

Beckstein, O., K. Tai and M. S. P. Sansom (2004). 'Not ions alone: barriers to ion permeation in nanopores and channels'. In: *Journal of the American Chemical Society* 126.45, pp. 14694–14695.

Ben Soussia, I. et al. (2019). 'Mutation of a single residue promotes gating of vertebrate and invertebrate two-pore domain potassium channels'. In: *Nature Communications* 10.1.

Ben-Abu, Y., Y. Zhou, N. Zilberberg and O. Yifrach (2009). 'Inverse coupling in leak and voltage-activated K+ channel gates underlies distinct roles in electrical signaling'. In: *Nature Structural & Molecular Biology* 16.1, pp. 71–79.

Bernèche, S. and B. Roux (2001). 'Energetics of ion conduction through the K+ channel'. In: *Nature* 414.6859, pp. 73–77.

Bernèche, S. and B. Roux (2005). 'A Gate in the Selectivity Filter of Potassium Channels'. In: *Structure* 13.4, pp. 591–600.

Berrier, C. et al. (2013). 'The Purified Mechanosensitive Channel TREK-1 Is Directly Sensitive to Membrane Tension'. In: *Journal of Biological Chemistry* 288.38, pp. 27307–27314.

Bezanilla, F. (2018). 'Gating currents'. In: *The Journal of General Physiology*, jgp.201812090.

Bichet, D., M. Grabe, Y. N. Jan and L. Y. Jan (2006). 'Electrostatic interactions in the channel cavity as an important determinant of potassium channel selectivity'. In: *Proceedings of the National Academy of Sciences* 103.39, pp. 14355–14360.

Bista, P. et al. (2015). 'Differential phospholipase C-dependent modulation of TASK and TREK two-pore domain K^+ channels in rat thalamocortical relay neurons: PLC-dependent modulation of thalamic activity'. In: *The Journal of Physiology* 593.1, pp. 127–144.

Bittner, S., T. Ruck, J. Fernández-Orth and S. G. Meuth (2014). 'TREK-King the Blood–Brain-Barrier'. In: *Journal of Neuroimmune Pharmacology* 9.3, pp. 293–301.

Blatz, A. L. (1984). 'Ion conductance and selectivity of single calcium-activated potassium channels in cultured rat muscle'. In: *The Journal of General Physiology* 84.1, pp. 1–23.

Blin, S. et al. (2014). 'Tandem Pore Domain Halothane-Inhibited K+ Channel Subunits THIK1 and THIK2 Assemble and Form Active Channels'. In: *The Journal of Biological Chemistry*.

Blin, S. et al. (2016). 'Mixing and matching TREK/TRAAK subunits generate heterodimeric K_{2P} channels with unique properties'. In: *Proceedings of the National Academy of Sciences* 113.15, pp. 4200–4205.

Blondeau, N. et al. (2007). 'Polyunsaturated Fatty Acids Are Cerebral Vasodilators via the TREK-1 Potassium Channel'. In: *Circulation Research* 101.2, pp. 176–184.

Bockenhauer, D., N. Zilberberg and S. A. Goldstein (2001). 'KCNK2: reversible conversion of a hippocampal potassium leak into a voltage-dependent channel'. In: *Nature Neuroscience* 4.5, pp. 486–491.

Bodnár, M., G. Schlichthörl and J. Daut (2015). 'The potassium current carried by TREK-1 channels in rat cardiac ventricular muscle'. In: *Pflügers Archiv - European Journal of Physiology* 467.5, pp. 1069–1079.

Bohnen, M. S. et al. (2017). 'Molecular Pathophysiology of Congenital Long QT Syndrome'. In: *Physiological Reviews* 97.1, pp. 89–134.

Borchers, H. W. (2018). *pracma: Practical Numerical Math Functions*. R package version 2.1.8.

Börjesson, S. I., T. Parkkari, S. Hammarström and F. Elinder (2010). 'Electrostatic Tuning of Cellular Excitability'. In: *Biophysical Journal* 98.3, pp. 396–403.

Boucherat, O. et al. (2015). 'Potassium channels in pulmonary arterial hypertension'. In: *European Respiratory Journal* 46.4, pp. 1167–1177.

Brelidze, T. I. and K. L. Magleby (2005). 'Probing the Geometry of the Inner Vestibule of BK Channels with Sugars'. In: *The Journal of General Physiology* 126.2, pp. 105–121.

Brelidze, T. I., X. Niu and K. L. Magleby (2003). 'A ring of eight conserved negatively charged amino acids doubles the conductance of BK channels and prevents inward rectification'. In: *Proceedings of the National Academy of Sciences* 100.15, pp. 9017–9022.

Brennecke, J. T. and B. L. de Groot (2018). 'Mechanism of Mechanosensitive Gating of the TREK-2 Potassium Channel'. In: *Biophysical Journal* 114.6, pp. 1336–1343.

Brickley, S. G. et al. (2007). 'TASK-3 Two-Pore Domain Potassium Channels Enable Sustained High-Frequency Firing in Cerebellar Granule Neurons'. In: *Journal of Neuroscience* 27.35, pp. 9329–9340.

Brohawn, S. G., E. B. Campbell and R. MacKinnon (2013). 'Domain-swapped chain connectivity and gated membrane access in a Fab-mediated crystal of the human TRAAK K+ channel'. In: *Proceedings of the National Academy of Sciences* 110.6, pp. 2129–2134.

Brohawn, S. G., J. del Marmol and R. MacKinnon (2012). 'Crystal Structure of the Human K2P TRAAK, a Lipid- and Mechano-Sensitive K+ Ion Channel'. In: *Science* 335.6067, pp. 436–441.

Brohawn, S. G., Z. Su and R. MacKinnon (2014a). 'Mechanosensitivity is mediated directly by the lipid membrane in TRAAK and TREK1 K+ channels'. In: *Proceedings of the National Academy of Sciences* 111.9, pp. 3614–3619.

Brohawn, S. G., E. B. Campbell and R. MacKinnon (2014b). 'Physical mechanism for gating and mechanosensitivity of the human TRAAK K+ channel'. In: *Nature* 516.7529, pp. 126–130.

Brohawn, S. G. et al. (2019). *The mechanosensitive ion channel TRAAK is localized to the mammalian node of Ranvier*. preprint. Neuroscience.

Brown, D. A. and G. M. Passmore (2009). 'Neural KCNQ (Kv7) channels: Neural KCNQ (Kv7) channels'. In: *British Journal of Pharmacology* 156.8, pp. 1185–1195.

Buckler, K. J. (2015). 'TASK channels in arterial chemoreceptors and their role in oxygen and acid sensing'. In: *Pflügers Archiv - European Journal of Physiology* 467.5, pp. 1013–1025.

Canul-Sánchez, J. A. et al. (2018). 'Different agonists induce distinct single-channel conductance states in TRPV1 channels'. In: *The Journal of General Physiology*, jgp.201812141.

Chakrapani, S., J. F. Cordero-Morales and E. Perozo (2007a). 'A Quantitative Description of KcsA Gating I: Macroscopic Currents'. In: *The Journal of General Physiology* 130.5, pp. 465–478.

– (2007b). 'A Quantitative Description of KcsA Gating II: Single-Channel Currents'. In: *The Journal of General Physiology* 130.5, pp. 479–496.

Chakrapani, S. et al. (2011). 'On the structural basis of modal gating behavior in K+ channels'. In: *Nature Structural & Molecular Biology* 18.1, pp. 67–74.

Chang, J.-M., P. Di Tommaso, J.-F. Taly and C. Notredame (2012). 'Accurate multiple sequence alignment of transmembrane proteins with PSI-Coffee'. In: *BMC Bioinformatics* 13 (Suppl 4), S1.

Chapman, M. L., H. S. Krovetz and A. M. VanDongen (2001). 'GYGD pore motifs in neighbouring potassium channel subunits interact to determine ion selectivity'. In: *The Journal of Physiology* 530 (Pt 1), pp. 21–33.

Chapman, M. L. and A. M. VanDongen (2005). 'K Channel Subconductance Levels Result from Heteromeric Pore Conformations'. In: *The Journal of General Physiology* 126.2, pp. 87–103.

Chapman, M. L., H. M. VanDongen and A. M. VanDongen (1997). 'Activation-Dependent Subconductance Levels in the drk1 K Channel Suggest a Subunit Basis for Ion Permeation and Gating'. In: *Biophysical Journal* 72.2, pp. 708–719.

Chatelain, F. C. et al. (2012). 'TWIK1, a unique background channel with variable ion selectivity'. In: *Proceedings of the National Academy of Sciences* 109.14, pp. 5499–5504.

Chatelain, F. C. et al. (2013). 'Silencing of the Tandem Pore Domain Halothane-inhibited K+ Channel 2 (THIK2) Relies on Combined Intracellular Retention and Low Intrinsic Activity at the Plasma Membrane'. In: *The Journal of biological chemistry* 288.49, pp. 35081–35092.

Chemin, J. (2003). 'Mechanisms underlying excitatory effects of group I metabotropic glutamate receptors via inhibition of 2P domain K+ channels'. In: *The EMBO Journal* 22.20, pp. 5403–5411.

Chemin, J. et al. (2005). 'A phospholipid sensor controls mechanogating of the K+ channel TREK-1'. In: *The EMBO Journal* 24.1, pp. 44–53.

Chen, H., F. C. Chatelain and F. Lesage (2014). 'Altered and dynamic ion selectivity of K+ channels in cell development and excitability'. In: *Trends in Pharmacological Sciences* 35.9, pp. 461–469.

Chen, T. Y. (1996). 'Nonequilibrium gating and voltage dependence of the ClC-0 Cl- channel'. In: *The Journal of General Physiology* 108.4, pp. 237–250.

Cheng, W. W. L. et al. (2011). 'Mechanism for selectivity-inactivation coupling in KcsA potassium channels'. In: *Proceedings of the National Academy of Sciences* 108.13, pp. 5272–5277.

Choe, H., H. Sackin and L. G. Palmer (2001). 'Gating properties of inward-rectifier potassium channels: effects of permeant ions'. In: *The Journal of Membrane Biology* 184.1, pp. 81–89.

Clausen, M. V. et al. (2017). 'Asymmetric mechanosensitivity in a eukaryotic ion channel'. In: *Proceedings of the National Academy of Sciences*, p. 201708990.

Cohen, A., Y. Ben-Abu, S. Hen and N. Zilberberg (2008). 'A Novel Mechanism for Human K2P2.1 Channel Gating: Facilitation of C-Type Gating by Protonation of extracellular Histidine Residues'. In: *Journal of Biological Chemistry* 283.28, pp. 19448–19455.

Cohen, J. and K. Schulten (2004). 'Mechanism of Anionic Conduction across ClC'. In: *Biophysical Journal* 86.2, pp. 836–845.

Colquhoun, D. (1998). 'Binding, gating, affinity and efficacy: The interpretation of structure-activity relationships for agonists and of the effects of mutating receptors'. In: *British Journal of Pharmacology* 125.5, pp. 923–947.

Cordero-Morales, J. F. et al. (2006). 'Molecular determinants of gating at the potassium-channel selectivity filter'. In: *Nature Structural & Molecular Biology* 13.4, pp. 311–318.

Cordero-Morales, J. F. et al. (2007). 'Molecular driving forces determining potassium channel slow inactivation'. In: *Nature Structural & Molecular Biology* 14.11, pp. 1062–1069.

Cuello, L. G., V. Jogini, D. M. Cortes and E. Perozo (2010a). 'Structural mechanism of C-type inactivation in K+ channels'. In: *Nature* 466.7303, pp. 203–208.

Cuello, L. G. et al. (2010b). 'Structural basis for the coupling between activation and inactivation gates in K+ channels'. In: *Nature* 466.7303, pp. 272–275.

Cuello, L. G., D. M. Cortes and E. Perozo (2017). 'The gating cycle of a K+ channel at atomic resolution'. In: *eLife* 6.

Cunningham, K. P. et al. (2019). 'Characterization and regulation of wild-type and mutant TASK-1 two pore domain potassium channels indicated in pulmonary arterial hypertension'. In: *The Journal of Physiology* 597.4, pp. 1087–1101.

Czirják, G., G. L. Petheő, A. Spät and P. Enyedi (2001). 'Inhibition of TASK-1 potassium channel by phospholipase C'. In: *American Journal of Physiology-Cell Physiology* 281.2, pp. C700–C708.

Czirják, G., Z. E. Tóth and P. Enyedi (2004). 'The Two-pore Domain K $^+$ Channel, TRESK, Is Activated by the Cytoplasmic Calcium Signal through Calcineurin'. In: *Journal of Biological Chemistry* 279.18, pp. 18550–18558.

Damdindorj, L. et al. (2014). 'A Comparative Analysis of Constitutive Promoters Located in Adeno-Associated Viral Vectors'. In: *PLoS ONE* 9.8, e106472.

Davies, L. A. et al. (2008). 'TASK channel deletion in mice causes primary hyperaldosteronism'. In: *Proceedings of the National Academy of Sciences* 105.6, pp. 2203–2208.

Decher, N. et al. (2011). 'Knock-Out of the Potassium Channel TASK-1 Leads to a Prolonged QT Interval and a Disturbed QRS Complex'. In: *Cellular Physiology and Biochemistry* 28.1, pp. 77–86.

Decher, N. et al. (2017). 'Sodium permeable and "hypersensitive" TREK-1 channels cause ventricular tachycardia'. In: *EMBO Molecular Medicine* 9.4, pp. 403–414.

Demo, S. and G. Yellen (1992). 'Ion effects on gating of the Ca(2+)-activated K+ channel correlate with occupancy of the pore'. In: *Biophysical Journal* 61.3, pp. 639–648.

Derebe, M. G. et al. (2011a). 'Structural studies of ion permeation and Ca2+ blockage of a bacterial channel mimicking the cyclic nucleotide-gated channel pore'. In: *Proceedings of the National Academy of Sciences* 108.2, pp. 592–597.

Derebe, M. G. et al. (2011b). 'Tuning the ion selectivity of tetrameric cation channels by changing the number of ion binding sites'. In: *Proceedings of the National Academy of Sciences* 108.2, pp. 598–602.

Derst, C. and A. Karschin (1998). 'Evolutionary link between prokaryotic and eukaryotic K+ channels'. In: *The Journal of Experimental Biology* 201 (Pt 20), pp. 2791–2799.

Devaraneni, P. K. et al. (2013). 'Semisynthetic K+ channels show that the constricted conformation of the selectivity filter is not the C-type inactivated state'. In: *Proceedings of the National Academy of Sciences* 110.39, pp. 15698–15703.

Diaz-Franulic, I. et al. (2015). 'Pore dimensions and the role of occupancy in unitary conductance of Shaker K channels'. In: *The Journal of General Physiology* 146.2, pp. 133–146.

Dibb, K. M. et al. (2003). 'Molecular Basis of Ion Selectivity, Block, and Rectification of the Inward Rectifier Kir3.1/Kir3.4 K^+ Channel'. In: *Journal of Biological Chemistry* 278.49, pp. 49537–49548.

Dong, X.-p. et al. (2009). 'Activating Mutations of the TRPML1 Channel Revealed by Proline-scanning Mutagenesis'. In: *Journal of Biological Chemistry* 284.46, pp. 32040–32052.

Dong, Y. Y. et al. (2015). 'K2P channel gating mechanisms revealed by structures of TREK-2 and a complex with Prozac'. In: *Science* 347.6227, pp. 1256–1259.

Doyle, D. A. et al. (1998). 'The structure of the potassium channel: molecular basis of K+ conduction and selectivity'. In: *Science* 280.5360, pp. 69–77.

Duprat, F. (1997). 'TASK, a human background K+ channel to sense external pH variations near physiological pH'. In: *The EMBO Journal* 16.17, pp. 5464–5471.

Eckert, M., B. Egenberger, F. Döring and E. Wischmeyer (2011). 'TREK-1 isoforms generated by alternative translation initiation display different susceptibility to the antidepressant fluoxetine'. In: *Neuropharmacology* 61.5, pp. 918–923.

Feliciangeli, S. et al. (2010). 'Potassium channel silencing by constitutive endocytosis and intracellular sequestration'. In: *The Journal of biological chemistry* 285.7, pp. 4798–4805.

Fitzhugh, R. (1983). 'Statistical properties of the asymmetric random telegraph signal, with applications to single-channel analysis'. In: *Mathematical Biosciences* 64.1, pp. 75–89.

Flaherty, D. P. et al. (2014). 'Potent and selective inhibitors of the TASK-1 potassium channel through chemical optimization of a bis-amide scaffold'. In: *Bioorganic & Medicinal Chemistry Letters* 24.16, pp. 3968–3973.

Fundamental Techniques in Cell Culture (2016).

Geng, Y., X. Wang and K. L. Magleby (2013). 'Lack of negative slope in I-V plots for BK channels at positive potentials in the absence of intracellular blockers'. In: *The Journal of General Physiology* 141.4, pp. 493–497.

Gnatenco, C., J. Han, A. K. Snyder and D. Kim (2002). 'Functional expression of TREK-2 K+ channel in cultured rat brain astrocytes'. In: *Brain Research* 931.1, pp. 56–67.

Goldman, D. E. (1943). 'Potential, impedance, and rectification in membranes'. In: *The Journal of General Physiology* 27.1, pp. 37–60.

Groulx, N., F. Boudreault, S. N. Orlov and R. Grygorczyk (2006). 'Membrane Reserves and Hypotonic Cell Swelling'. In: *Journal of Membrane Biology* 214.1, pp. 43–56.

Gu, W. et al. (2002). 'Expression pattern and functional characteristics of two novel splice variants of the two-pore-domain potassium channel TREK-2'. In: *The Journal of Physiology* 539 (Pt 3), pp. 657–668.

Guagliardo, N. A. et al. (2019). 'Adrenal Tissue-Specific Deletion of TASK Channels Causes Aldosterone-Driven Angiotensin II–Independent Hypertension'. In: *Hypertension* 73.2, pp. 407–414.

Gurney, A. et al. (2003). 'Two-Pore Domain K Channel, TASK-1, in Pulmonary Artery Smooth Muscle Cells'. In: *Circulation Research* 93.10, pp. 957–964.

Hamill, O. P. et al. (1981). 'Improved patch-clamp techniques for high-resolution current recording from cells and cell-free membrane patches'. In: *Pflügers Archiv - European Journal of Physiology* 391.2, pp. 85–100.

Hamilton, N. B. and D. Attwell (2010). 'Do astrocytes really exocytose neurotransmitters?' In: *Nature Reviews Neuroscience* 11.4, pp. 227–238.

Heer, F. T. et al. (2017). 'Mechanism of activation at the selectivity filter of the KcsA K+ channel'. In: *eLife* 6, e25844.

Heginbotham, L., M. LeMasurier, L. Kolmakova-Partensky and C. Miller (1999). 'Single streptomyces lividans K(+) channels: functional asymmetries and sidedness of proton activation'. In: *The Journal of General Physiology* 114.4, pp. 551–560.

Heginbotham, L., Z. Lu, T. Abramson and R. MacKinnon (1994). 'Mutations in the K+ channel signature sequence'. In: *Biophysical Journal* 66.4, pp. 1061–1067.

Heginbotham, L. and R. MacKinnon (1993). 'Conduction properties of the cloned Shaker K+ channel'. In: *Biophysical Journal* 65.5, pp. 2089–2096.

Heginbotham, L., L. Kolmakova-Partensky and C. Miller (1998). 'Functional Reconstitution of a Prokaryotic K^+ Channel'. In: *The Journal of General Physiology* 111.6, pp. 741–749.

Heurteaux, C. et al. (2006). 'Deletion of the background potassium channel TREK-1 results in a depression-resistant phenotype'. In: *Nature Neuroscience* 9.9, pp. 1134–1141.

Hille, B. (1973). 'Potassium Channels in Myelinated Nerve: Selective permeability to small cations'. In: *The Journal of General Physiology* 61.6, pp. 669–686.

Hille, B. (2001a). 'Classical Biophysics of the Squid Giant Axon'. In: *Ion channels of excitable membranes*. 3rd ed. Sunderland, Mass: Sinauer. ISBN: 0-87893-321-2.

– (2001b). 'Classical Mechanisms of Block'. In: *Ion channels of excitable membranes*. 3rd ed. Sunderland, Mass: Sinauer. ISBN: 0-87893-321-2.

– (2001c). 'Elementary Properties of Ions in Solution'. In: *Ion channels of excitable membranes*. 3rd ed. Sunderland, Mass: Sinauer. ISBN: 0-87893-321-2.

– (2001d). 'Elementary Properties of Pores'. In: *Ion channels of excitable membranes*. 3rd ed. Sunderland, Mass: Sinauer. ISBN: 0-87893-321-2.

– (2001e). 'Introduction'. In: *Ion Channels of Exciteable Membranes*. 3rd ed. Sinauer.

– (2001f). 'Selective Permeability: Independence'. In: *Ion channels of excitable membranes*. 3rd ed. Sunderland, Mass: Sinauer. ISBN: 0-87893-321-2.

– (2001g). 'Selective Permeability: Saturation and Binding'. In: *Ion channels of excitable membranes*. 3rd ed. Sunderland, Mass: Sinauer. ISBN: 0-87893-321-2.

– (2001h). 'The Superfamily of Voltage-gated Channels'. In: *Ion channels of excitable membranes*. 3rd ed. Sunderland, Mass: Sinauer. ISBN: 0-87893-321-2.

Hite, R. K., J. A. Butterwick and R. MacKinnon (2014). 'Phosphatidic acid modulation of Kv channel voltage sensor function'. In: *eLife* 3, e04366.

Hodgkin, A. L. and A. F. Huxley (1952). 'A quantitative description of membrane current and its application to conduction and excitation in nerve'. In: *The Journal of physiology* 117.4, pp. 500–544.

Hodgkin, A. L. and B. Katz (1949). 'The effect of sodium ions on the electrical activity of giant axon of the squid'. In: *The Journal of Physiology* 108.1, pp. 37–77.

Hodgkin, A. L. and R. D. Keynes (1955). 'The potassium permeability of a giant nerve fibre'. In: *The Journal of Physiology* 128.1, pp. 61–88.

Honore, E. (2002). 'An intracellular proton sensor commands lipid- and mechano-gating of the K+ channel TREK-1'. In: *The EMBO Journal* 21.12, pp. 2968–2976.

Honoré, E. et al. (2006). 'Desensitization of mechano-gated K2P channels'. In: *Proceedings of the National Academy of Sciences* 103.18, pp. 6859–6864.

Hoshi, T., W. N. Zagotta and R. W. Aldrich (1991). 'Two types of inactivation in Shaker K+ channels: effects of alterations in the carboxy-terminal region'. In: *Neuron* 7.4, pp. 547–556.

Hoshi, T. and C. M. Armstrong (2013). 'C-type inactivation of voltage-gated K^+ channels: Pore constriction or dilation?' In: *The Journal of General Physiology* 141.2, pp. 151–160.

Ishida, I. G., G. E. Rangel-Yescas, J. Carrasco-Zanini and L. D. Islas (2015). 'Voltage-dependent gating and gating charge measurements in the Kv1.2 potassium channel'. In: *The Journal of General Physiology* 145.4, pp. 345–358.

Ishihara, K. (2018). 'External K^+ dependence of strong inward rectifier K^+ channel conductance is caused not by K^+ but by competitive pore blockade by external Na^+'. In: *The Journal of General Physiology*, jgp.201711936.

Iwaki, Y. et al. (2019). 'Towards a TREK-1/2 (TWIK-Related K+ Channel 1 and 2) dual activator tool compound: Multi-dimensional optimization of BL-1249'. In: *Bioorganic & Medicinal Chemistry Letters* 29.13, pp. 1601–1604.

Jia, Z. et al. (2018). 'Hydrophobic gating in BK channels'. In: *Nature Communications* 9.1, p. 3408.

Jiang, Y. and R. MacKinnon (2000). 'The barium site in a potassium channel by x-ray crystallography'. In: *The Journal of General Physiology* 115.3, pp. 269–272.

Jiang, Y. et al. (2002). 'The open pore conformation of potassium channels'. In: *Nature* 417.6888, pp. 523–526.

Julio-Kalajzić, F. et al. (2018). 'K_{2P} TASK-2 and KCNQ1-KCNE3 K^+ channels are major players contributing to intestinal anion and fluid secretion: TASK-2 and KCNQ1-KCNE3 K^+ channels in intestinal anion secretion'. In: *The Journal of Physiology* 596.3, pp. 393–407.

Kang, D., C. Choe, E. Cavanaugh and D. Kim (2007). 'Properties of single two-pore domain TREK-2 channels expressed in mammalian cells: Two TREK-2 channel phenotypes'. In: *The Journal of Physiology* 583.1, pp. 57–69.

Kang, D., C. Choe and D. Kim (2005). 'Thermosensitivity of the two-pore domain K^+ channels TREK-2 and TRAAK: Thermosensitivity of TREK/TRAAK'. In: *The Journal of Physiology* 564.1, pp. 103–116.

Kang, D., J. Han and D. Kim (2006). 'Mechanism of inhibition of TREK-2 (K_{2P} 10.1) by the G_q-coupled M_3 muscarinic receptor'. In: *American Journal of Physiology-Cell Physiology* 291.4, pp. C649–C656.

Kang, D., J. O. Hogan and D. Kim (2014). 'THIK-1 (K2P13.1) is a small-conductance background K+ channel in rat trigeminal ganglion neurons'. In: *Pflügers Archiv - European Journal of Physiology* 466.7, pp. 1289–1300.

Kang, D. and D. Kim (2006). 'TREK-2 (K $_{2P}$ 10.1) and TRESK (K $_{2P}$ 18.1) are major background K $^{+}$ channels in dorsal root ganglion neurons'. In: *American Journal of Physiology-Cell Physiology* 291.1, pp. C138–C146.

Kennard, L. E. et al. (2005). 'Inhibition of the human two-pore domain potassium channel, TREK-1, by fluoxetine and its metabolite norfluoxetine'. In: *British Journal of Pharmacology* 144.6, pp. 821–829.

Kilisch, M. et al. (2015). 'The role of protein–protein interactions in the intracellular traffic of the potassium channels TASK-1 and TASK-3'. In: *Pflügers Archiv - European Journal of Physiology* 467.5, pp. 1105–1120.

Kim, D. (1992). 'A mechanosensitive K+ channel in heart cells. Activation by arachidonic acid'. In: *The Journal of General Physiology* 100.6, pp. 1021–1040.

Kim, Y., C. Gnatenco, H. Bang and D. Kim (2001). 'Localization of TREK-2 K + channel domains that regulate channel kinetics and sensitivity to pressure, fatty acids and pH i'. In: *Pflügers Archiv - European Journal of Physiology* 442.6, pp. 952–960.

Kiss, L., J. LoTurco and S. J. Korn (1999). 'Contribution of the Selectivity Filter to Inactivation in Potassium Channels'. In: *Biophysical Journal* 76.1, pp. 253–263.

Kisselbach, J. et al. (2014). 'Modulation of K $_{2P}$ 2.1 and K $_{2P}$ 10.1 K $^{+}$ channel sensitivity to carvedilol by alternative mRNA translation initiation: ATI regulates drug sensitivity of K $_{2P}$ channels'. In: *British Journal of Pharmacology* 171.23, pp. 5182–5194.

Klein, M. and E. R. Kandel (1980). 'Mechanism of calcium current modulation underlying presynaptic facilitation and behavioral sensitization in Aplysia'. In: *Proceedings of the National Academy of Sciences* 77.11, pp. 6912–6916.

Klesse, G., S. Rao, M. S. P. Sansom and S. J. Tucker (2019). 'CHAP: A Versatile Tool for the Structural and Functional Annotation of Ion Channel Pores'. In: *Journal of Molecular Biology* 431.17, pp. 3353–3365.

Kong, C. et al. (2012). 'Distinct gating mechanisms revealed by the structures of a multi-ligand gated K $^{+}$ channel'. In: *eLife* 1.

Kopec, W. et al. (2018). 'Direct knock-on of desolvated ions governs strict ion selectivity in K+ channels'. In: *Nature Chemistry* 10.8, pp. 813–820.

Kopfer, D. A. et al. (2014). 'Ion permeation in K+ channels occurs by direct Coulomb knock-on'. In: *Science* 346.6207, pp. 352–355.

Kratochvil, H. T. et al. (2016). 'Instantaneous ion configurations in the K^+ ion channel selectivity filter revealed by 2D IR spectroscopy'. In: *Science* 353.6303, pp. 1040–1044.

Kratochvil, H. T. et al. (2017). 'Probing the Effects of Gating on the Ion Occupancy of the K^+ Channel Selectivity Filter Using Two-Dimensional Infrared Spectroscopy'. In: *Journal of the American Chemical Society* 139.26, pp. 8837–8845.

Krieg, P. A. and D. A. Melton (1984). 'Functional messenger RNAs are produced by SP6 in vitro transcription of cloned cDNAs'. In: *Nucleic Acids Research* 12.18, pp. 7057–7070.

Labro, A. J., D. M. Cortes, C. Tilegenova and L. G. Cuello (2018). 'Inverted allosteric coupling between activation and inactivation gates in K^+ channels'. In: *Proceedings of the National Academy of Sciences* 115.21, pp. 5426–5431.

Labro, A. J. et al. (2012). 'The Role of the 2nd Threonine Within the TTVGYGD Sequence of Kv-Channels in C-Type Inactivation Gating, Ion Selectivity and Permeation'. In: *Biophysical Journal* 102.3, 13a.

Langan, P. S. et al. (2018). 'Anomalous X-ray diffraction studies of ion transport in K+ channels'. In: *Nature Communications* 9.1, p. 4540.

Läuger, P. (2009). 'Conformational Transitions of Ionic Channels'. In: *Single-channel recording*. 2nd ed. New York, NY: Springer. ISBN: 978-1-4419-1230-5.

Läuger, P., W. Stephan and E. Frehland (1980). 'Fluctuations of barrier structure in ionic channels'. In: *Biochimica et Biophysica Acta (BBA) - Biomembranes* 602.1, pp. 167–180.

Lei, Q. et al. (2014). 'Response of the human detrusor to stretch is regulated by TREK-1, a two-pore-domain (K2P) mechano-gated potassium channel'. In: *The Journal of Physiology* 592.14, pp. 3013–3030.

LeMasurier, M., L. Heginbotham and C. Miller (2001). 'KcsA: it's a potassium channel'. In: *The Journal of General Physiology* 118.3, pp. 303–314.

Lengyel, M., G. Czirják and P. Enyedi (2016). 'Formation of Functional Heterodimers by TREK-1 and TREK-2 Two-pore Domain Potassium Channel Subunits'. In: *Journal of Biological Chemistry* 291.26, pp. 13649–13661.

– (2018). 'TRESK background potassium channel is not gated at the helix bundle crossing near the cytoplasmic end of the pore'. In: *PLOS ONE* 13.5, e0197622.

Lesage, F. et al. (1996). 'TWIK-1, a ubiquitous human weakly inward rectifying K+ channel with a novel structure'. In: *The EMBO journal* 15.5, pp. 1004–1011.

Li, J. et al. (2017). 'Chemical substitutions in the selectivity filter of potassium channels do not rule out constricted-like conformations for C-type inactivation'. In: *Proceedings of the National Academy of Sciences* 114.42, pp. 11145–11150.

Limberg, S. H. et al. (2011). 'TASK-1 Channels May Modulate Action Potential Duration of Human Atrial Cardiomyocytes'. In: *Cellular Physiology and Biochemistry* 28.4, pp. 613–624.

Liu, S. and S. W. Lockless (2013). 'Equilibrium selectivity alone does not create K+-selective ion conduction in K+ channels'. In: *Nature Communications* 4, p. 2746.

Liu, Y. S., P. Sompornpisut and E. Perozo (2001). 'Structure of the KcsA channel intracellular gate in the open state'. In: *Nature Structural Biology* 8.10, pp. 883–887.

Loboda, A., A. Melishchuk and C. Armstrong (2001). 'Dilated and Defunct K Channels in the Absence of K+'. In: *Biophysical Journal* 80.6, pp. 2704–2714.

Lockless, S. W. (2015). 'Determinants of cation transport selectivity: Equilibrium binding and transport kinetics'. In: *The Journal of General Physiology* 146.1, pp. 3–13.

Lockless, S. W., M. Zhou and R. MacKinnon (2007). 'Structural and Thermodynamic Properties of Selective Ion Binding in a K+ Channel'. In: *PLoS Biology* 5.5, e121.

Lolicato, M. et al. (2014). 'Transmembrane Helix Straightening and Buckling Underlies Activation of Mechanosensitive and Thermosensitive K2P Channels'. In: *Neuron* 84.6, pp. 1198–1212.

Lolicato, M. et al. (2017). 'K2P2.1 (TREK-1)–activator complexes reveal a cryptic selectivity filter binding site'. In: *Nature* 547, p. 364.

Long, S. B. (2005). 'Crystal Structure of a Mammalian Voltage-Dependent Shaker Family K+ Channel'. In: *Science* 309.5736, pp. 897–903.

Lopatin, A. and C. Nichols (1996). '[K+] dependence of open-channel conductance in cloned inward rectifier potassium channels (IRK1, Kir2.1)'. In: *Biophysical Journal* 71.2, pp. 682–694.

Lopes, C. M. B. (2000). 'Proton Block and Voltage Gating Are Potassium-dependent in the Cardiac Leak Channel Kcnk3'. In: *Journal of Biological Chemistry* 275.22, pp. 16969–16978.

López-Barneo, J., T. Hoshi, S. H. Heinemann and R. W. Aldrich (1993). 'Effects of external cations and mutations in the pore region on C-type inactivation of Shaker potassium channels'. In: *Receptors & Channels* 1.1, pp. 61–71.

Loucif, A. J. C. et al. (2018). 'GI-530159, a novel, selective, mechanosensitive two-pore-domain potassium (K_{2P}) channel opener, reduces rat dorsal root ganglion neuron excitability: GI-

530159 activates TREK K $_{2P}$ channels'. In: *British Journal of Pharmacology* 175.12, pp. 2272–2283.

Lu, Z. and R. MacKinnon (1994). 'Electrostatic tuning of Mg2+ affinity in an inward-rectifier K+channel'. In: *Nature* 371.6494, pp. 243–246.

Ma, L., X. Zhang and H. Chen (2011a). 'TWIK-1 Two-Pore Domain Potassium Channels Change Ion Selectivity and Conduct Inward Leak Sodium Currents in Hypokalemia'. In: *Science Signaling* 4.176, ra37–ra37.

Ma, L., X. Zhang, M. Zhou and H. Chen (2012a). 'Acid-sensitive TWIK and TASK Two-pore Domain Potassium Channels Change Ion Selectivity and Become Permeable to Sodium in Extracellular Acidification'. In: *Journal of Biological Chemistry* 287.44, pp. 37145–37153.

Ma, L. et al. (2013). 'A Novel Channelopathy in Pulmonary Arterial Hypertension'. In: *New England Journal of Medicine* 369.4, pp. 351–361.

Ma, L., Y.-P. Xie, M. Zhou and H. Chen (2012b). 'Silent TWIK-1 Potassium Channels Conduct Monovalent Cation Currents'. In: *Biophysical Journal* 102.8, pp. L34–L36.

Ma, X.-Y. et al. (2011b). 'External Ba2+ Block of the Two-pore Domain Potassium Channel TREK-1 Defines Conformational Transition in Its Selectivity Filter'. In: *Journal of Biological Chemistry* 286.46, pp. 39813–39822.

MacKenzie, G., N. P. Franks and S. G. Brickley (2015). 'Two-pore domain potassium channels enable action potential generation in the absence of voltage-gated potassium channels'. In: *Pflügers Archiv - European Journal of Physiology* 467.5, pp. 989–999.

Madry, C. et al. (2018). 'Microglial Ramification, Surveillance, and Interleukin-1β Release Are Regulated by the Two-Pore Domain K + Channel THIK-1'. In: *Neuron* 97.2, 299–312.e6.

Maingret, F. (2000). 'TREK-1 is a heat-activated background K+ channel'. In: *The EMBO Journal* 19.11, pp. 2483–2491.

– (2001). 'The endocannabinoid anandamide is a direct and selective blocker of the background K+ channel TASK-1'. In: *The EMBO Journal* 20.1, pp. 47–54.

Maingret, F. et al. (1999). 'Mechano- or Acid Stimulation, Two Interactive Modes of Activation of the TREK-1 Potassium Channel'. In: *Journal of Biological Chemistry* 274.38, pp. 26691–26696.

Mathie, A. (2006). 'Neuronal two-pore-domain potassium channels and their regulation by G protein-coupled receptors'. In: *The Journal of Physiology* 578.2, pp. 377–385.

Mathie, A. and E. L. Veale (2015). 'Two-pore domain potassium channels: potential therapeutic targets for the treatment of pain'. In: *Pflügers Archiv - European Journal of Physiology* 467.5, pp. 931–943.

Matulef, K., A. W. Annen, J. C. Nix and F. I. Valiyaveetil (2016). 'Individual Ion Binding Sites in the K+ Channel Play Distinct Roles in C-type Inactivation and in Recovery from Inactivation'. In: *Structure* 24.5, pp. 750–761.

McClenaghan, C. (2015). 'Investigations into the Structure, Function and Pharmacology of TREK K2P Potassium Channels'. PhD thesis. University of Oxford.

McClenaghan, C. et al. (2016). 'Polymodal activation of the TREK-2 K2P channel produces structurally distinct open states'. In: *The Journal of General Physiology* 147.6, pp. 497–505.

Medhurst, A. D. et al. (2001). 'Distribution analysis of human two pore domain potassium channels in tissues of the central nervous system and periphery'. In: *Brain research. Molecular brain research* 86.1, pp. 101–114.

Melishchuk, A., A. Loboda and C. M. Armstrong (1998). 'Loss of Shaker K Channel Conductance in 0 K+ Solutions: Role of the Voltage Sensor'. In: *Biophysical Journal* 75.4, pp. 1828–1835.

Mi Hwang, E. et al. (2014). 'A disulphide-linked heterodimer of TWIK-1 and TREK-1 mediates passive conductance in astrocytes'. In: *Nature Communications* 5.1, p. 3227.

Millar, J. A. et al. (2000). 'A functional role for the two-pore domain potassium channel TASK-1 in cerebellar granule neurons'. In: *Proceedings of the National Academy of Sciences* 97.7, pp. 3614–3618.

Miller, A. N. and S. B. Long (2012). 'Crystal Structure of the Human Two-Pore Domain Potassium Channel K2P1'. In: *Science* 335.6067, pp. 432–436.

Miller, C. (1996). 'The long pore gets molecular'. In: *The Journal of General Physiology* 107.4, pp. 445–447.

– (1999). 'Ionic Hopping Defended'. In: *The Journal of General Physiology* 113.6, pp. 783–787.

Molina, A., A. G. Castellano and J. López-Barneo (1997). 'Pore mutations in Shaker K+ channels distinguish between the sites of tetraethylammonium blockade and C-type inactivation.' In: *The Journal of Physiology* 499.2, pp. 361–367.

Morais-Cabral, J. H., Y. Zhou and R. MacKinnon (2001). 'Energetic optimization of ion conduction rate by the K+ selectivity filter'. In: *Nature* 414.6859, pp. 37–42.

Moscoso, C. et al. (2012). 'K+ Conduction and Mg2+ Blockade in a Shaker Kv-Channel Single Point Mutant with an Unusually High Conductance'. In: *Biophysical Journal* 103.6, pp. 1198–1207.

Al-Moubarak, E., E. L. Veale and A. Mathie (2019). 'Pharmacologically reversible, loss of function mutations in the TM2 and TM4 inner pore helices of TREK-1 K2P channels'. In: *Scientific Reports* 9.1, p. 12394.

Nemetian-Ardestani, E. et al. (2019). *Selectivity Filter Instability Dominates the Low Intrinsic Activity of the TWIK-1 K2P K^+ Channel*. Preprint. BioArχive - Biophysics.

Nernst, W. (1888). 'Zur Kinetik der in Lösung befindlichen Körper'. In: *Zeitschrift für Physikalische Chemie* 2U.1, pp. 613–637.

Neyton, J. and C. Miller (1988a). 'Potassium blocks barium permeation through a calcium-activated potassium channel'. In: *The Journal of General Physiology* 92.5, pp. 549–567.

Neyton, J. and C. Miller (1988b). 'Discrete Ba2+ block as a probe of ion occupancy and pore structure in the high-conductance Ca2+ -activated K+ channel'. In: *The Journal of General Physiology* 92.5, pp. 569–586.

Ng, B. and P. H. Barry (1995). 'The measurement of ionic conductivities and mobilities of certain less common organic ions needed for junction potential corrections in electrophysiology'. In: *Journal of Neuroscience Methods* 56.1, pp. 37–41.

Niemeyer, M. I., L. P. Cid, L. F. Barros and F. V. Sepúlveda (2001). 'Modulation of the Two-pore Domain Acid-sensitive K^+ Channel TASK-2 (KCNK5) by Changes in Cell Volume'. In: *Journal of Biological Chemistry* 276.46, pp. 43166–43174.

Nimigean, C. M. and T. W. Allen (2011). 'Origins of ion selectivity in potassium channels from the perspective of channel block'. In: *The Journal of General Physiology* 137.5, pp. 405–413.

Nimigean, C. M., J. S. Chappie and C. Miller (2003). 'Electrostatic tuning of ion conductance in potassium channels'. In: *Biochemistry* 42.31, pp. 9263–9268.

Nimigean, C. M. and C. Miller (2002). 'Na^+ Block and Permeation in a K^+ Channel of Known Structure'. In: *The Journal of General Physiology* 120.3, pp. 323–335.

Niu, W. and F. Sachs (2003). 'Dynamic properties of stretch-activated K+ channels in adult rat atrial myocytes'. In: *Progress in Biophysics and Molecular Biology* 82.1, pp. 121–135.

Noceti, F. (1996). 'Effective gating charges per channel in voltage-dependent K+ and Ca2+ channels'. In: *The Journal of General Physiology* 108.3, pp. 143–155.

Noskov, S. Y., S. Bernèche and B. Roux (2004). 'Control of ion selectivity in potassium channels by electrostatic and dynamic properties of carbonyl ligands'. In: *Nature* 431.7010, pp. 830–834.

Nyquist, H. (1928). 'Certain Topics in Telegraph Transmission Theory'. In: *Transactions of the American Institute of Electrical Engineers* 47.2, pp. 617–644.

Ogielska, E. M. and R. W. Aldrich (1999). 'Functional consequences of a decreased potassium affinity in a potassium channel pore. Ion interactions and C-type inactivation'. In: *The Journal of general physiology* 113.2, pp. 347–358.

Öster, C. et al. (2019). 'The conduction pathway of potassium channels is water free under physiological conditions'. In: *Science Advances* 5.7, eaaw6756.

Ostmeyer, J. et al. (2013). 'Recovery from slow inactivation in K+ channels is controlled by water molecules'. In: *Nature* 501.7465, pp. 121–124.

Pang, D. S. J. et al. (2009). 'An unexpected role for TASK-3 potassium channels in network oscillations with implications for sleep mechanisms and anesthetic action'. In: *Proceedings of the National Academy of Sciences* 106.41, pp. 17546–17551.

Park, J. B., H. J. Kim, P. D. Ryu and E. Moczydlowski (2003). 'Effect of Phosphatidylserine on Unitary Conductance and Ba2+Block of the BK Ca2+–activated K+Channel: Re-examination of the Surface Charge Hypothesis'. In: *The Journal of General Physiology* 121.5, pp. 375–398.

Patel, A. J. (1998). 'A mammalian two pore domain mechano-gated S-like K+ channel'. In: *The EMBO Journal* 17.15, pp. 4283–4290.

Patel, A. J. et al. (1999). 'Inhalational anesthetics activate two-pore-domain background K+ channels'. In: *Nature Neuroscience* 2.5, pp. 422–426.

Patel, A. J. et al. (2000). 'TWIK-2, an Inactivating 2P Domain K^+ Channel'. In: *Journal of Biological Chemistry* 275.37, pp. 28722–28730.

Patil, N. et al. (1995). 'A potassium channel mutation in weaver mice implicates membrane excitability in granule cell differentiation'. In: *Nature Genetics* 11.2, pp. 126–129.

Pau, V. et al. (2017). 'Crystal structure of an inactivated mutant mammalian voltage-gated K+ channel'. In: *Nature Structural & Molecular Biology* 24.10, pp. 857–865.

Pereira, V. et al. (2014). 'Role of the TREK2 potassium channel in cold and warm thermosensation and in pain perception:' in: *Pain* 155.12, pp. 2534–2544.

Perozo, E., D. M. Cortes and L. G. Cuello (1999). 'Structural rearrangements underlying K+-channel activation gating'. In: *Science (New York, N.Y.)* 285.5424, pp. 73–78.

Perozo, E., R. MacKinnon, F. Bezanilla and E. Stefani (1993). 'Gating currents from a nonconducting mutant reveal open-closed conformations in Shaker K+ channels'. In: *Neuron* 11.2, pp. 353–358.

Perozo, E., D. M. Cortes and L. G. Cuello (1998). 'Three-dimensional architecture and gating mechanism of a K+ channel studied by EPR spectroscopy'. In: *Nature Structural Biology* 5.6, pp. 459–469.

Piechotta, P. L. et al. (2011). 'The pore structure and gating mechanism of K2P channels: K2P channel gating'. In: *The EMBO Journal* 30.17, pp. 3607–3619.

Plant, L. D. et al. (2012). 'SUMOylation Silences Heterodimeric TASK Potassium Channels Containing K2P1 Subunits in Cerebellar Granule Neurons'. In: *Science Signaling* 5.251, ra84–ra84.

Pless, S. A. et al. (2013). 'Hydrogen bonds as molecular timers for slow inactivation in voltage-gated potassium channels'. In: *eLife* 2, e01289.

Pope, L. et al. (2018). 'Protein and Chemical Determinants of BL-1249 Action and Selectivity for K_{2P} Channels'. In: *ACS Chemical Neuroscience* 9.12, pp. 3153–3165.

Posson, D. J., R. Rusinova, O. S. Andersen and C. M. Nimigean (2015). 'Calcium ions open a selectivity filter gate during activation of the MthK potassium channel'. In: *Nature Communications* 6, p. 8342.

Posson, D. J., A. N. Thompson, J. G. McCoy and C. M. Nimigean (2013). 'Molecular interactions involved in proton-dependent gating in KcsA potassium channels'. In: *The Journal of General Physiology* 142.6, pp. 613–624.

Posson, D. J., J. G. McCoy and C. M. Nimigean (2012). 'The voltage-dependent gate in MthK potassium channels is located at the selectivity filter'. In: *Nature Structural & Molecular Biology* 20.2, pp. 159–166.

Poulsen, M. H. et al. (2019). 'Gating modules of the AMPA receptor pore domain revealed by unnatural amino acid mutagenesis'. In: *Proceedings of the National Academy of Sciences* 116.27, pp. 13358–13367.

Priel, A. and S. D. Silberberg (2004). 'Mechanism of Ivermectin Facilitation of Human $P2X_4$ Receptor Channels'. In: *The Journal of General Physiology* 123.3, pp. 281–293.

Proks, P., J. F. Antcliff and F. M. Ashcroft (2003). 'The ligand-sensitive gate of a potassium channel lies close to the selectivity filter'. In: *EMBO reports* 4.1, pp. 70–75.

Proks, P., C. E. Capener, P. Jones and F. M. Ashcroft (2001). 'Mutations within the P-Loop of Kir6.2 Modulate the Intraburst Kinetics of the Atp-Sensitive Potassium Channel'. In: *The Journal of General Physiology* 118.4, pp. 341–353.

Proks, P. et al. (2016). 'Running out of time: the decline of channel activity and nucleotide activation in adenosine triphosphate-sensitive K-channels'. In: *Philosophical Transactions of the Royal Society B: Biological Sciences* 371.1700, p. 20150426.

Pusch, M., U. Ludewig, A. Rehfeldt and T. J. Jentsch (1995). 'Gating of the voltage-dependent chloride channel CIC-0 by the permeant anion'. In: *Nature* 373.6514, pp. 527–531.

Rajan, S. et al. (2000). 'TASK-3, a novel tandem pore domain acid-sensitive K+ channel. An extracellular histiding as pH sensor'. In: *The Journal of biological chemistry* 275.22, pp. 16650–16657.

Rajan, S. et al. (2001). 'THIK-1 and THIK-2, a novel subfamily of tandem pore domain K+ channels'. In: *The Journal of biological chemistry* 276.10, pp. 7302–7311.

Rajendra, Y. et al. (2012). 'Role of non-specific DNA in reducing coding DNA requirement for transient gene expression with CHO and HEK-293E cells'. In: *Biotechnology and Bioengineering* 109.9, pp. 2271–2278.

Ramírez, D. et al. (2017). 'Side Fenestrations Provide an "Anchor" for a Stable Binding of A1899 to the Pore of TASK-1 Potassium Channels'. In: *Molecular Pharmaceutics* 14.7, pp. 2197–2208.

Rao, S. et al. (2019). 'A heuristic derived from analysis of the ion channel structural proteome permits the rapid identification of hydrophobic gates'. In: *Proceedings of the National Academy of Sciences* 116.28, pp. 13989–13995.

Rauh, O. et al. (2018). 'Site-specific ion occupation in the selectivity filter causes voltage-dependent gating in a viral K+ channel'. In: *Scientific Reports* 8.1.

Rauh, O. et al. (2017). 'Extended beta distributions open the access to fast gating in bilayer experiments-assigning the voltage-dependent gating to the selectivity filter'. In: *FEBS Letters* 591.23, pp. 3850–3860.

Reeve, R. and J. R. Turner (2013). 'Pharmacodynamic Models: Parameterizing the Hill Equation, Michaelis-Menten, the Logistic Curve, and Relationships Among These Models'. In: *Journal of Biopharmaceutical Statistics* 23.3, pp. 648–661.

Renigunta, V., G. Schlichthörl and J. Daut (2015). 'Much more than a leak: structure and function of K2P-channels'. In: *Pflügers Archiv - European Journal of Physiology* 467.5, pp. 867–894.

Renigunta, V. et al. (2014). 'Breaking the silence: functional expression of the two-pore-domain potassium channel THIK-2'. In: *Pflügers Archiv - European Journal of Physiology* 466.9, pp. 1735–1745.

Reyes, R. et al. (1998). 'Cloning and Expression of a Novel pH-sensitive Two Pore Domain K $^{+}$ Channel from Human Kidney'. In: *Journal of Biological Chemistry* 273.47, pp. 30863–30869.

Rinné, S. et al. (2015). 'TASK-1 and TASK-3 may form heterodimers in human atrial cardiomyocytes'. In: *Journal of Molecular and Cellular Cardiology* 81, pp. 71–80.

Rinné, S. et al. (2019). 'The molecular basis for an allosteric inhibition of K+-flux gating in K2P channels'. In: *eLife* 8, e39476.

Rödström, K. E. J. et al. (2019). *A unique lower X-gate in TASK channels traps inhibitors within the vestibule*. Preprint. BioArχive - Molecular Biology.

Roth, R., D. Gillespie, W. Nonner and R. E. Eisenberg (2008). 'Bubbles, Gating, and Anesthetics in Ion Channels'. In: *Biophysical Journal* 94.11, pp. 4282–4298.

Roux, B. (1999). 'The Cavity and Pore Helices in the KcsA K+ Channel: Electrostatic Stabilization of Monovalent Cations'. In: *Science* 285.5424, pp. 100–102.

Royal, P. et al. (2019). 'Migraine-Associated TRESK Mutations Increase Neuronal Excitability through Alternative Translation Initiation and Inhibition of TREK'. In: *Neuron* 101.2, 232–245.e6.

Sandoz, G. et al. (2009). 'Extracellular acidification exerts opposite actions on TREK1 and TREK2 potassium channels via a single conserved histidine residue'. In: *Proceedings of the National Academy of Sciences* 106.34, pp. 14628–14633.

Sandoz, G. et al. (2006). 'AKAP150, a switch to convert mechano-, pH- and arachidonic acid-sensitive TREK K+ channels into open leak channels'. In: *The EMBO Journal* 25.24, pp. 5864–5872.

Santos, J. S., S. M. Grigoriev and M. Montal (2008). 'Molecular Template for a Voltage Sensor in a Novel K $^{+}$ Channel. III. Functional Reconstitution of a Sensorless Pore Module from a Prokaryotic Kv Channel'. In: *The Journal of General Physiology* 132.6, pp. 651–666.

Scheel, O., A. A. Zdebik, S. Lourdel and T. J. Jentsch (2005). 'Voltage-dependent electrogenic chloride/proton exchange by endosomal CLC proteins'. In: *Nature* 436.7049, pp. 424–427.

Schewe, M. et al. (2016). 'A Non-canonical Voltage-Sensing Mechanism Controls Gating in K2P K+ Channels'. In: *Cell* 164.5, pp. 937–949.

Schewe, M. et al. (2019). 'A pharmacological master key mechanism that unlocks the selectivity filter gate in K^+ channels'. In: *Science* 363.6429, pp. 875–880.

Schiekel, J. et al. (2012). 'The inhibition of the potassium channel TASK-1 in rat cardiac muscle by endothelin-1 is mediated by phospholipase C'. In: *Cardiovascular Research* 97.1, pp. 97–105.

Schroeder, I. (2015). 'How to resolve microsecond current fluctuations in single ion channels: The power of beta distributions'. In: *Channels* 9.5, pp. 262–280.

Schroeder, I. and U.-P. Hansen (2007). 'Saturation and Microsecond Gating of Current Indicate Depletion-induced Instability of the MaxiK Selectivity Filter'. In: *The Journal of General Physiology* 130.1, pp. 83–97.

– (2008). 'Tl^+-induced μs Gating of Current Indicates Instability of the MaxiK Selectivity Filter as Caused by Ion/Pore Interaction'. In: *The Journal of General Physiology* 131.4, pp. 365–378.

– (2009). 'Interference of Shot Noise of Open-Channel Current with Analysis of Fast Gating: Patchers do not (Yet) Have to Care'. In: *Journal of Membrane Biology* 229.3, pp. 153–163.

Schroeder, I., G. Thiel and U.-P. Hansen (2013). 'Ca^{2+} block and flickering both contribute to the negative slope of the IV curve in BK channels'. In: *The Journal of General Physiology* 141.4, pp. 499–505.

Sepulveda, F. V., L. Pablo Cid, J. Teulon and M. I. Niemeyer (2015). 'Molecular Aspects of Structure, Gating, and Physiology of pH-Sensitive Background K2P and Kir K+-Transport Channels'. In: *Physiological Reviews* 95.1, pp. 179–217.

Shi, C. et al. (2018). 'A single NaK channel conformation is not enough for non-selective ion conduction'. In: *Nature Communications* 9.1, p. 717.

Shi, N. et al. (2006). 'Atomic structure of a Na+- and K+-conducting channel'. In: *Nature* 440.7083, pp. 570–574.

Shi, N. et al. (2011). 'Crucial Points within the Pore as Determinants of K+ Channel Conductance and Gating'. In: *Journal of Molecular Biology* 411.1, pp. 27–35.

Silverå Ejneby, M. et al. (2018). 'Atom-by-atom tuning of the electrostatic potassium-channel modulator dehydroabietic acid'. In: *The Journal of General Physiology* 150.5, pp. 731–750.

Simkin, D., E. J. Cavanaugh and D. Kim (2008). 'Control of the single channel conductance of K_{2P} 10.1 (TREK-2) by the amino-terminus: role of alternative translation initiation: Control of unitary conductance of TREK-2'. In: *The Journal of Physiology* 586.23, pp. 5651–5663.

Sivilotti, L. and D. Colquhoun (2016). 'In praise of single channel kinetics'. In: *The Journal of General Physiology* 148.2, pp. 79–88.

Sokabe, M., F. Sachs and Z. Jing (1991). 'Quantitative video microscopy of patch clamped membranes stress, strain, capacitance, and stretch channel activation'. In: *Biophysical Journal* 59.3, pp. 722–728.

Starkus, J., T. Schlief, M. Rayner and S. Heinemann (1995). 'Unilateral exposure of Shaker B potassium channels to hyperosmolar solutions'. In: *Biophysical Journal* 69.3, pp. 860–872.

Starkus, J. G., L. Kuschel, M. D. Rayner and S. H. Heinemann (1997). 'Ion Conduction through C-Type Inactivated *Shaker* Channels'. In: *The Journal of General Physiology* 110.5, pp. 539–550.

Staudacher, K. et al. (2011). 'Alternative splicing determines mRNA translation initiation and function of human K_{2P} 10.1 K^+ channels: Translational regulation of K_{2P} 10.1 K^+ channels'. In: *The Journal of Physiology* 589.15, pp. 3709–3720.

Strange, K., T. Yamada and J. S. Denton (2019). 'A 30-year journey from volume-regulated anion currents to molecular structure of the LRRC8 channel'. In: *The Journal of General Physiology* 151.2, pp. 100–117.

Streit, A. K. et al. (2011). 'A Specific Two-pore Domain Potassium Channel Blocker Defines the Structure of the TASK-1 Open Pore'. In: *Journal of Biological Chemistry* 286.16, pp. 13977–13984.

Suchyna, T. M., V. S. Markin and F. Sachs (2009). 'Biophysics and Structure of the Patch and the Gigaseal'. In: *Biophysical Journal* 97.3, pp. 738–747.

Takeuchi, K., H. Takahashi, S. Kawano and I. Shimada (2007). 'Identification and characterization of the slowly exchanging pH-dependent conformational rearrangement in KcsA'. In: *The Journal of Biological Chemistry* 282.20, pp. 15179–15186.

Talley, E. M. and D. A. Bayliss (2002). 'Modulation of TASK-1 (Kcnk3) and TASK-3 (Kcnk9) Potassium Channels: Volatile Anesthetics and Neurotransmitters share a molecular Site of Action'. In: *Journal of Biological Chemistry* 277.20, pp. 17733–17742.

Talley, E. M., Q. Lei, J. E. Sirois and D. A. Bayliss (2000). 'TASK-1, a two-pore domain K+ channel, is modulated by multiple neurotransmitters in motoneurons'. In: *Neuron* 25.2, pp. 399–410.

Tertyshnikova, S. et al. (2005). 'BL-1249 [(5,6,7,8-tetrahydro-naphthalen-1-yl)-[2-(1H-tetrazol-5-yl)-phenyl]-amine]: a putative potassium channel opener with bladder-relaxant properties'. In: *The Journal of Pharmacology and Experimental Therapeutics* 313.1, pp. 250–259.

Thomas, D. et al. (2008). 'Alternative Translation Initiation in Rat Brain Yields K2P2.1 Potassium Channels Permeable to Sodium'. In: *Neuron* 58.6, pp. 859–870.

Thompson, A. N. et al. (2009). 'Mechanism of potassium-channel selectivity revealed by Na+ and Li+ binding sites within the KcsA pore'. In: *Nature Structural & Molecular Biology* 16.12, pp. 1317–1324.

Thomson, A. S. and B. S. Rothberg (2010). 'Voltage-dependent inactivation gating at the selectivity filter of the MthK K+ channel'. In: *The Journal of General Physiology* 136.5, pp. 569–579.

Tilegenova, C., D. M. Cortes and L. G. Cuello (2017). 'Hysteresis of KcsA potassium channel's activation– deactivation gating is caused by structural changes at the channel's selectivity filter'. In: *Proceedings of the National Academy of Sciences* 114.12, pp. 3234–3239.

Tilegenova, C. et al. (2019). 'Structure, function, and ion-binding properties of a K^+ channel stabilized in the 2,4-ion–bound configuration'. In: *Proceedings of the National Academy of Sciences* 116.34, pp. 16829–16834.

Trapani, J. G. and S. J. Korn (2003). 'Control of ion channel expression for patch clamp recordings using an inducible expression system in mammalian cell lines'. In: *BMC neuroscience* 4, p. 15.

Trapp, S., M. Isabel Aller, W. Wisden and A. V. Gourine (2008). 'A Role for TASK-1 (KCNK3) Channels in the Chemosensory Control of Breathing'. In: *Journal of Neuroscience* 28.35, pp. 8844–8850.

Veale, E. L., R. Buswell, C. E. Clarke and A. Mathie (2007a). 'Identification of a region in the TASK3 two pore domain potassium channel that is critical for its blockade by methanandamide: Methanandamide block of TASK3 channels'. In: *British Journal of Pharmacology* 152.5, pp. 778–786.

Veale, E. L. et al. (2007b). 'G q-Mediated Regulation of TASK3 Two-Pore Domain Potassium Channels: The Role of Protein Kinase C'. In: *Molecular Pharmacology* 71.6, pp. 1666–1675.

Veale, E. L. et al. (2014a). 'Influence of the N Terminus on the Biophysical Properties and Pharmacology of TREK1 Potassium Channels'. In: *Molecular Pharmacology* 85.5, pp. 671–681.

Veale, E. L. et al. (2014b). 'Recovery of Current through Mutated TASK3 Potassium Channels Underlying Birk Barel Syndrome'. In: *Molecular Pharmacology* 85.3, pp. 397–407.

Villarroel, A., N. Burnashev and B. Sakmann (1995). 'Dimensions of the narrow portion of a recombinant NMDA receptor channel'. In: *Biophysical Journal* 68.3, pp. 866–875.

Vivier, D. et al. (2017). 'Development of the First Two-Pore Domain Potassium Channel TWIK-Related K $^{+}$ Channel 1-Selective Agonist Possessing in Vivo Antinociceptive Activity'. In: *Journal of Medicinal Chemistry* 60.3, pp. 1076–1088.

Waterhouse, A. M. et al. (2009). 'Jalview Version 2–a multiple sequence alignment editor and analysis workbench'. In: *Bioinformatics* 25.9, pp. 1189–1191.

Weber, W.-M. (1999). 'Ion currents of Xenopus laevis oocytes: state of the art'. In: *Biochimica et Biophysica Acta (BBA) - Biomembranes* 1421.2, pp. 213–233.

Wilke, B. U. et al. (2014). 'Diacylglycerol mediates regulation of TASK potassium channels by Gq-coupled receptors'. In: *Nature Communications* 5, p. 5540.

Wilkens, C. M. and R. W. Aldrich (2006). 'State-independent Block of BK Channels by an Intracellular Quaternary Ammonium'. In: *The Journal of General Physiology* 128.3, pp. 347–364.

Woo, D. H. et al. (2012). 'TREK-1 and Best1 Channels Mediate Fast and Slow Glutamate Release in Astrocytes upon GPCR Activation'. In: *Cell* 151.1, pp. 25–40.

Woo, D. H. et al. (2018). 'Activation of Astrocytic μ-opioid Receptor Elicits Fast Glutamate Release Through TREK-1-Containing K2P Channel in Hippocampal Astrocytes'. In: *Frontiers in Cellular Neuroscience* 12.

Yan, J., Q. Li and R. W. Aldrich (2016). 'Closed state-coupled C-type inactivation in BK channels'. In: *Proceedings of the National Academy of Sciences* 113.25, pp. 6991–6996.

Yang, J., M. Yu, Y. N. Jan and L. Y. Jan (1997a). 'Stabilization of ion selectivity filter by pore loop ion pairs in an inwardly rectifying potassium channel'. In: *Proceedings of the National Academy of Sciences* 94.4, pp. 1568–1572.

Yang, Y., Y. Yan and F. J. Sigworth (1997b). 'How Does the W434F Mutation Block Current in *Shaker* Potassium Channels?' In: *The Journal of General Physiology* 109.6, pp. 779–789.

Ye, S., Y. Li and Y. Jiang (2010). 'Novel insights into K+ selectivity from high-resolution structures of an open K+ channel pore'. In: *Nature Structural & Molecular Biology* 17.8, pp. 1019–1023.

Yellen, G. (1984). 'Ionic permeation and blockade in Ca2+-activated K+ channels of bovine chromaffin cells'. In: *The Journal of General Physiology* 84.2, pp. 157–186.

Yellen, G. (2002). 'The voltage-gated potassium channels and their relatives'. In: *Nature* 419.6902, pp. 35–42.

Zanzouri, M. et al. (2006). 'Membrane Potential-regulated Transcription of the Resting K $^{+}$ Conductance TASK-3 via the Calcineurin Pathway'. In: *Journal of Biological Chemistry* 281.39, pp. 28910–28918.

Zheng, J. and F. J. Sigworth (1997). 'Selectivity Changes during Activation of Mutant *Shaker* Potassium Channels'. In: *The Journal of General Physiology* 110.2, pp. 101–117.

– (1998). 'Intermediate Conductances during Deactivation of Heteromultimeric *Shaker* Potassium Channels'. In: *The Journal of General Physiology* 112.4, pp. 457–474.

Zheng, W., E. O. Gracheva and S. N. Bagriantsev (2019). 'A hydrophobic gate in the inner pore helix is the major determinant of inactivation in mechanosensitive Piezo channels'. In: *eLife* 8, e44003.

Zhou, Y., J. H. Morais-Cabral, A. Kaufman and R. MacKinnon (2001). 'Chemistry of ion coordination and hydration revealed by a K+ channel-Fab complex at 2.0 A resolution'. In: *Nature* 414.6859, pp. 43–48.

Zhou, Y. and R. MacKinnon (2003). 'The Occupancy of Ions in the K+ Selectivity Filter: Charge Balance and Coupling of Ion Binding to a Protein Conformational Change Underlie High Conduction Rates'. In: *Journal of Molecular Biology* 333.5, pp. 965–975.

– (2004). 'Ion Binding Affinity in the Cavity of the KcsA Potassium Channel †'. In: *Biochemistry* 43.17, pp. 4978–4982.

Zilberberg, N., N. Ilan and S. A. Goldstein (2001). 'KCNKØ: opening and closing the 2-P-domain potassium leak channel entails "C-type" gating of the outer pore'. In: *Neuron* 32.4, pp. 635–648.

Zou, B. et al. (2010). 'ML365: Development of Bis-Amides as Selective Inhibitors of the KCNK3/TASK1 Two Pore Potassium Channel'. In: *Probe Reports from the NIH Molecular Libraries Program*. Bethesda (MD): National Center for Biotechnology Information (US).

Appendices

Publications

ION CHANNELS

A pharmacological master key mechanism that unlocks the selectivity filter gate in K^+ channels

Marcus Schewe[1]*†, Han Sun[2]*, Ümit Mert[1], Alexandra Mackenzie[3,4,5], Ashley C. W. Pike[3], Friederike Schulz[1], Cristina Constantin[6,7], Kirsty S. Vowinkel[8], Linus J. Conrad[4,5], Aytug K. Kiper[8], Wendy Gonzalez[9,10], Marianne Musinszki[1], Marie Tegtmeier[1], David C. Pryde[11]‡, Hassane Belabed[12], Marc Nazare[12], Bert L. de Groot[13], Niels Decher[8], Bernd Fakler[6,7], Elisabeth P. Carpenter[3,4], Stephen J. Tucker[4,5], Thomas Baukrowitz[1]†

Potassium (K^+) channels have been evolutionarily tuned for activation by diverse biological stimuli, and pharmacological activation is thought to target these specific gating mechanisms. Here we report a class of negatively charged activators (NCAs) that bypass the specific mechanisms but act as master keys to open K^+ channels gated at their selectivity filter (SF), including many two-pore domain K^+ (K_{2P}) channels, voltage-gated hERG (human ether-à-go-go–related gene) channels and calcium (Ca^{2+})–activated big-conductance potassium (BK)–type channels. Functional analysis, x-ray crystallography, and molecular dynamics simulations revealed that the NCAs bind to similar sites below the SF, increase pore and SF K^+ occupancy, and open the filter gate. These results uncover an unrecognized polypharmacology among K^+ channel activators and highlight a filter gating machinery that is conserved across different families of K^+ channels with implications for rational drug design.

Dampening cellular electrical activity by pharmacological activation of specific types of K^+ channels has therapeutic potential for the treatment of a variety of disease states, including epilepsy, arrhythmias, vascular constriction, and various pain conditions (*1*, *2*). Consequently, screening efforts have identified a number of agents that open different types of K^+ channels (*2*), presumably by targeting their respective channel-specific activation mechanisms.

Distinct structural mechanisms enable K^+ channels to respond to a plethora of physiological stimuli, including voltage, temperature, mechanical force, and various second messengers, such as adenosine triphosphate (ATP), Ca^{2+}, and H^+, as well as bioactive lipids such as phosphatidylinositol 4,5-bisphosphate (PIP_2) and arachidonic acid (*3*, *4*). However, despite this complexity, these activation pathways seem to converge on the two principal mechanisms known to gate K^+ channels open: dilation of the "lower" gate at the intracellular pore entrance used by inwardly rectifying (K_{ir}) (*5*) and voltage-gated (K_v) K^+ channels (*6*), and activation of the selectivity filter (SF) gate used by most two-pore domain K^+ (K_{2P}) channels (*4*, *7*, *8*) and Ca^{2+}-activated big-conductance K^+ (BK_{Ca}) channels (*9*, *10*). In voltage-gated hERG (human ether-à-go-go–related gene) channels, both mechanisms coexist, with voltage opening the lower gate but rapid inactivation occurring through closure of the SF gate (*11*, *12*). Here we identify a common mechanism for drug-induced channel opening that bypasses these physiological activation mechanisms in SF-gated K^+ channels.

For the mechanosensitive K_{2P} channels TREK-1 and TREK-2, the voltage-gated hERG channel, and the Ca^{2+}-activated BK_{Ca} channel, a series of small-molecule activators all harboring a negatively charged group (tetrazole or carboxylate) have been proposed to act as selective channel openers [i.e., BL-1249 for TREK-1/-2 (*13*); PD-118057 for hERG (*14*); and NS11021 for BK_{Ca} (*15*)]. However, application of these compounds to their respective "nontarget" channels revealed an unexpected polypharmacology: All three openers displayed equal efficiency in opening TREK-1 channels (Fig. 1A) and hERG channels (Fig. 1B), as well as BK_{Ca} channels (Fig. 1C), whose activation curve is strongly shifted to more negative voltages (fig. S1C). This suggests that these activators may not target channel-specific activation mechanisms and may instead share a common mechanism. In all cases, the compound-mediated effect was effectively antagonized by large quaternary ammonium ions (QA_L^+) such as tetra-pentylammonium (TPenA) or tetra-hexyl-ammonium (THexA) that are known to block K^+ channels at a site immediately below the inner entrance to the SF (*16*) (Fig. 1, A and B, and fig. S1C). Likewise, all these activators reduced the QA_L^+-mediated inhibition in these different K^+ channels (Fig. 1C and figs. S1, A and B, and S7, A and B). Furthermore, extended screening with BL-1249 also revealed potent activation of several other K_{2P} channels (TREK-2, TRAAK, TALK-1, TALK-2, THIK-1, and THIK-2; fig. S1D). Together, these data suggest that these negatively charged activators (NCAs) (BL-1249, PD-118057, and NS11021) act on a gating mechanism that is shared among these different classes of K^+ channels and that their action involves a site that overlaps with the conserved QA_L^+-binding site located below the SF.

A distinctive feature of all NCA-responsive K^+ channels is their gating by the SF, a mechanism that is intimately coupled to ion permeation (*17*, *18*). In K_{2P} channels, this coupling leads to pronounced activation by Rb^+, which displays an ion occupancy distinct to K^+ at the four SF K^+ binding sites (S1 to S4) that stabilizes the activated state of the SF gate (*17*). Interestingly, Rb^+ not only activated all NCA-responsive K_{2P} channels but also led to robust activation of BK_{Ca} and hERG channels (Fig. 1D). By contrast, Rb^+ failed to exert any activatory effect on K^+ channels gated at the helix-bundle crossing (i.e., K_{ir} and most K_v channels), as was observed for $K_v1.1$, $K_v1.5$, $K_v3.1$, and $K_{ir}1.1$ (Fig. 1D); consistent with this, these channels were also not activated by BL-1249 (fig. S2, A to E). Furthermore, cyclic nucleotide–gated channels that are also gated at the SF were not activated by BL-1249, indicating that the NCA mechanism may be specific to SF-gated K^+ channels (fig. S2F).

To gain further mechanistic insight into channel opening by the NCAs, we next investigated their binding by x-ray crystallography, cysteine-scanning mutagenesis, and atomistic molecular dynamics (MD) simulations. First, anomalous diffraction data were collected from TREK-2 channels cocrystallized with a brominated derivative of BL-1249 ($BL\text{-}1249^{Br}$) (Fig. 2A; fig. S3, A to C; and supplementary materials and methods). Although no discrete electron density was visible for BL-1249 itself, in anomalous difference maps, two bromine peaks were clearly visible per TREK-2 dimer (fig. S3, A and B) and the main-chain protein backbone showed excellent agreement with a previously crystallized high-resolution structure of TREK-2 [Protein Data Bank (PDB) 4XDJ] (*19*). Both bromine anomalous difference peaks were located at the entrance of the side fenestrations branching off the central pore cavity below the SF. Comparison with a structure

[1]Institute of Physiology, Christian-Albrechts University of Kiel, 24118 Kiel, Germany. [2]Leibniz-Forschungsinstitut für Molekulare Pharmakologie (FMP), Department of Structural Biology, 13125 Berlin, Germany. [3]Structural Genomics Consortium, University of Oxford, Oxford OX3 7DQ, UK. [4]OXION Initiative in Ion Channels and Disease, University of Oxford, Oxford OX1 3PN, UK. [5]Clarendon Laboratory, Department of Physics, University of Oxford, Oxford OX1 3PU, UK. [6]Institute of Physiology II, Albert-Ludwigs University of Freiburg, 79104 Freiburg, Germany. [7]Centers for Biological Signaling Studies CIBSS and BIOSS, 79104 Freiburg, Germany. [8]Institute of Physiology and Pathophysiology, Vegetative Physiology, Philipps-University of Marburg, 35037 Marburg, Germany. [9]Centro de Bioinformatica y Simulacion Molecular, Universidad de Talca, 3465548 Talca, Chile. [10]Millennium Nucleus of Ion Channels-Associated Diseases (MiNICAD), Universidad de Talca, 3465548 Talca, Chile. [11]Pfizer Worldwide Medicinal Chemistry, Neuroscience and Pain Research Unit, Portway Building, Granta Park, Great Abington, Cambridgeshire CB21 6GS, UK. [12]Leibniz-Forschungsinstitut für Molekulare Pharmakologie (FMP), Department of Medicinal Chemistry, 13125 Berlin, Germany. [13]Computational Biomolecular Dynamics Group, Max Planck Institute for Biophysical Chemistry, 37077 Göttingen, Germany.
*These authors contributed equally to this work.
†Corresponding author. Email: m.schewe@physiologie.uni-kiel.de (M.S.); t.baukrowitz@physiologie.uni-kiel.de (T.B.) ‡Present address: Curadev Pharma Ltd., Sandwich Kent, UK.

Downloaded from http://science.sciencemag.org/ on September 19, 2019

that included QA_L^+ (*16*) showed that these bromine positions reside within the spherical volume of THexA but outside that of the smaller tetra-ethyl-ammonium (TEA) ion. Consistent with this, BL-1249 activation of TREK-2 channels was antagonized by THexA but not by TEA (Fig. 2, B and C).

These structural data were complemented by cysteine-scanning mutagenesis of the pore-lining M2 and M4 helices of TREK-1. Six residues, including the highly conserved Pro^{183} (P183) and Leu^{304} (L304) (also investigated in TREK-2, fig. S3D), were identified where mutations markedly reduced the apparent affinity of BL-1249. These residues cluster around the bromine densities

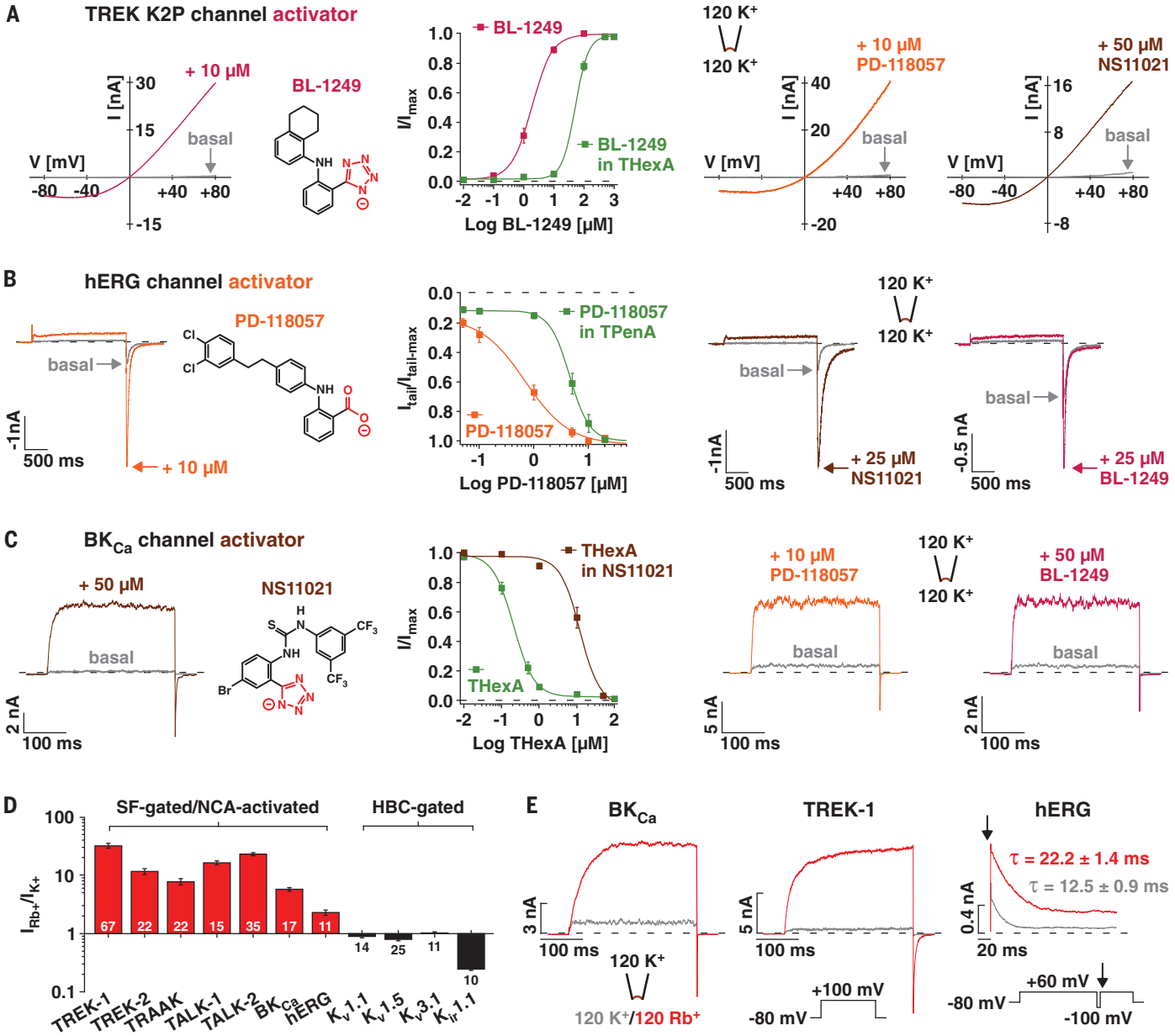


Fig. 1. NCAs open SF-gated K^+ channels via a similar site.
(**A**) Representative TREK-1 channel currents recorded in inside-out (i-o) patches evoked by voltage ramps in the absence (basal) and presence of the indicated compounds. BL-1249 (compound structure shown) dose-response curves represent currents at +40 mV and with or without 5 µM THexA that produced 77 ± 6% inhibition of basal currents ($n \geq 8$). I, current; V, voltage. (**B**) hERG channel currents (voltage steps from −80 to +60 mV) in i-o patches with or without the indicated compounds; arrows indicate peak tail current amplitudes at −100 mV. PD-118057 (compound structure shown) dose-response curves represent normalized tail currents with or without 1 µM TPenA that produced 91 ± 1% inhibition of basal currents ($n \geq 6$). (**C**) BK_{Ca} channel currents [voltage steps from a holding potential of −80 to +100 mV (zero Ca^{2+})] in i-o patches with or without the indicated compounds. THexA inhibition represents currents at +100 mV and with or without 50 µM NS11021 (compound structure shown; $n \geq 11$). (**D**) Rb^+ effects on different K^+ channels measured in i-o patches. Bars ± SEM represent fold change of outward currents upon exchange of intracellular K^+ by Rb^+ for K_{2P} and BK_{Ca} channels (+100 mV); for hERG, $K_v1.1$, $K_v1.5$, and $K_v3.1$ channels (+60 mV); and for $K_{ir}1.1$ channels (+40 mV). The channels are grouped as either SF-gated and NCA-activated or helix-bundle crossing (HBC)–gated. (**E**) Representative traces of Rb^+ activation for BK_{Ca}, TREK-1, and hERG channels using the indicated protocols [arrow indicates the starting point of hERG inactivation after inactivation recovery (at −100 mV)]. Time constant (τ) values from monoexponential fits to inactivation time course ($n \geq 12$). For (A) to (C), errors bars indicate SEM.

Downloaded from http://science.sciencemag.org/ on September 19, 2019

detected in the TREK-2 cocrystal with BL-1249^{Br} (Fig. 2D and fig. S3, C and D). A role for L304 in this presumed binding site was further supported by cysteine-modification protection experiments in which the time course of irreversible pore blockade induced by application of the cysteine-modifying agent MTS-TBAO [8-(tributylammonium)octyl methanethiosulfonate] (*20*) to TREK-1 L304C (Leu^{304}→Cys) channels was markedly slowed by the presence of BL-1249 (Fig. 2, E and F). This effect was specific for BL-1249, as two further channel activators with distinct binding sites [2-APB at the C terminus (*21*) and ML335 behind the SF (*22*)] both failed to slow this rate (Fig. 2, E and F). Furthermore, TREK-1 activation with 2-APB or ML335 was not antagonized by QA_L^+ inhibition, and mutations at the BL-1249 site did not affect 2-APB activation (fig. S4, A, B, and E).

In addition, we performed MD simulations to examine the orientation of BL-1249^{Br} within its proposed binding site (Fig. 2G). The favored binding pose oriented the negatively charged tetrazole group of BL-1249 toward the S6 "cavity binding site" for K^+ just below the SF. The remainder of the BL-1249 molecule engaged with residues in M2 and M4 consistent with our scanning mutagenesis data (Fig. 2D and fig. S3D). Moreover, the bromine atom in these simulations was found to be within 3 to 4 Å of the bromine densities determined by crystallography (fig. S3E). Together, these data indicate that BL-1249 binds to a site below the SF and reveal a critical role of the negative charge of the acidic tetrazole ring (pK_a around 5, where K_a is the dissociation constant), implying a pH-dependent compound efficacy. Indeed, when tested with the K_{2P} channel TALK-2 [exhibiting little intrinsic intracellular pH (pH_i) sensitivity], BL-1249 potency dropped strongly with a lowering of the solution pH_i to 5, whereas control experiments with 2-APB lacked this pH dependence (Fig. 3F).

We have recently used atomistic MD simulations and a double-bilayer setup to study ion permeation in the TRAAK K_{2P} channel (*17*). Therefore, we carried out simulations of ion permeation in

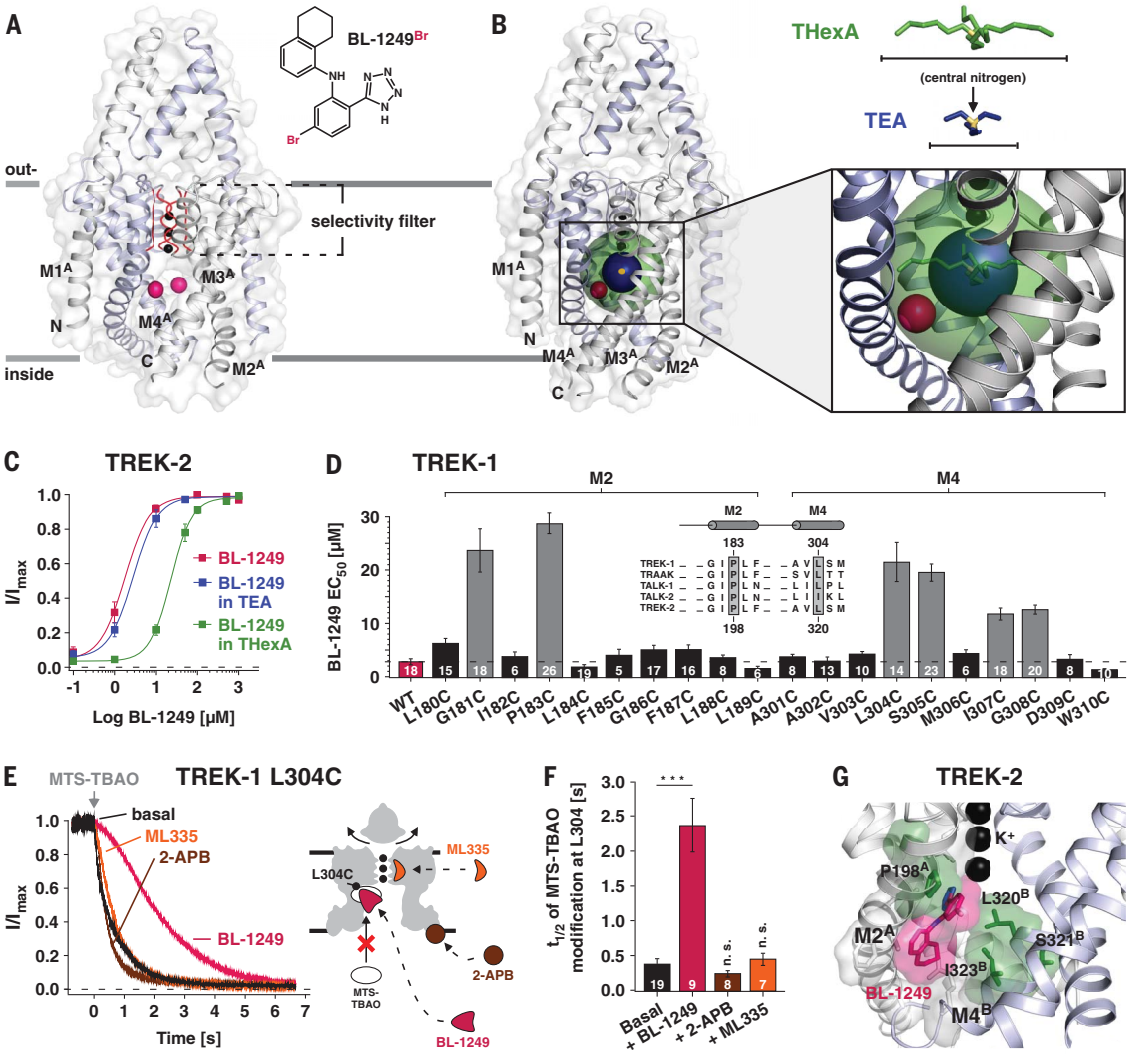


Fig. 2. Identification of the BL-1249 binding site in TREK K_{2P} channels. (**A**) The structure depicts TREK-2 (PDB 4XDJ), with pink spheres representing the positions of Br atoms in a brominated BL-1249 derivate (BL-1249Br) obtained by cocrystallization of TREK-2 and BL-1249Br (see also fig. S3). With this medium-resolution data, only the Br atoms were identified, because they gave peaks in anomalous difference maps. N, N terminus; C, C terminus. (**B**) The same structure also showing spherical representations of THexA (green) and TEA (dark blue) with their central nitrogen atoms (yellow). Their positions are based on the crystal structures of KcsA with QA^+s (*16*). Note that the Br atoms [pink spheres in (A)] are within the sphere of THexA but not of TEA. (**C**) BL-1249 dose-response curves for TREK-2 with or without 100 mM TEA ($n \geq 12$) or 5 μM THexA ($n \geq 13$) (TEA and THexA produce 74 ± 3 and 83 ± 2% basal current inhibition, respectively). Error bars indicate SEM. (**D**) Scanning mutagenesis of M2 and M4 helices showing BL-1249 median effective concentration (EC_{50}) values ± SEM determined at +40 mV; the inset shows a K_{2P} channel alignment for channels strongly activated by BL-1249 (see also fig. S1D) with residues homologous to TREK-1 P183 and L304 highlighted. (**E**) Time courses of 10 μM MTS-TBAO cysteine modification of L304C in TREK-1 before and after maximal activation by BL-1249 (50 μM), ML335 (50 μM), and 2-APB (1 mM) (left panel). The graphic depicts TREK-1 with predicted drug binding sites relative to the position of residue L304C. (**F**) Time values ± SEM for half-maximal MTS-TBAO modification inhibition ($t_{1/2}$) in the presence of different agonists. ***$P \leq 0.001$; n.s., not significant. (**G**) Representation of favored binding pose of BL-1249 (pink) in TREK-2 along with the location of the TREK-1 corresponding mutations (green) that reduce BL-1249 activation. For (A) and (G), the A and B superscripts indicate the subunit of the TREK-2 dimer. Single-letter abbreviations for amino acid residues are as follows: A, Ala; C, Cys; D, Asp; E, Glu; F, Phe; G, Gly; H, His; I, Ile; K, Lys; L, Leu; M, Met; N, Asn; P, Pro; Q, Gln; R, Arg; S, Ser; T, Thr; V, Val; W, Trp; and Y, Tyr.

Downloaded from http://science.sciencemag.org/ on September 19, 2019

TRAAK with BL-1249 modeled into the equivalent site in the TRAAK channel structure (PDB 4I9W) (Fig. 3A). This indicated several changes induced by BL-1249: (i) K^+ occupancy at the S6 site located adjacent to the negatively charged tetrazole group of BL-1249 increased ~16-fold (Fig. 3, A and B), (ii) K^+ occupancy of the S1 and S4 sites increased (Fig. 3B), and (iii) the rate of K^+ permeation increased by 1.6-fold (24 ± 2 ions/μs compared to 15 ± 2 ions/μs without BL-1249; Fig. 3C).

The effect of BL-1249 on ion permeation was further investigated with single-channel recordings of TREK-2 expressed in human embryonic kidney (HEK) 293 cells. Besides an increase in open probability, an increase in the measured single-channel amplitude was also observed in both the inward (from −29.3 ± 1.5 to −34.1 ± 1.9 pA at −100 mV; n = 7) and outward (from 17.7 ± 1.3 to 21.7 ± 1.4 pA at +100 mV; n = 7) directions in response to BL-1249 (Fig. 3, D and E). This result is consistent with the observed increase in SF ion occupancy at S1 and S4 that is expected to enhance ion permeation via a direct knock-on effect for ions entering the SF from either side (*23*). A similar increase in unitary conductance was also observed for TREK-1 channels recorded in patches from *Xenopus* oocytes (fig. S4, A to C). Notably, increases in single-channel conductance have not been observed upon activation of TREK-1, TREK-2, or TRAAK K_{2P} channels by other physiological stimuli (*24*, *25*).

Collectively, these results indicate that BL-1249 increases ion permeation and channel-open probability by influencing K^+ occupancy at sites below and within the SF. In line with this notion, mutations in the SF that change filter ion occupancy at the S1 and S4 sites (*17*, *26*) and induce the activated "leak mode" in K_{2P} channels (*17*) also render them insensitive to BL-1249 (and various other activators discussed below; fig. S6, A to D).

The negatively charged moiety identified within BL-1249, PD-118057, and NS11021 is also found in a series of known activators of TREK-1 and TREK-2 K_{2P} channels [ML67-33 (*27*), tetrazole; DCPIB (*28*), carboxylate], hERG channels [PD-307243 (*29*), carboxylate; NS3623 (*30*), tetrazole], and BK_{Ca} channels [GoSlo-SR-5-6 (*31*), sulphonate], and its requirement for channel activation has been demonstrated for ML67-33 and GoSlo-SR-5-6 (*27*, *31*). Indeed, these compounds also share all the hallmark features of BL-1249 action, including polypharmacology [i.e., mutual activation of K_{2P}, BK_{Ca}, and hERG channels (Fig. 4, C and D), sensitivity to QA_L^+ (Fig. 4A; fig. S7, A to C; and tables S2 and S3] and mutations that reduce BL-1249 activation in TREK-1 (fig. S4, C and D). In addition, MD simulations of their interaction with structures of the TREK-2, BK_{Ca}, and hERG channel pores identified similar stable binding poses below the SF with orientation of the negative moiety toward the cavity and a concomitant increase in K^+ occupancy at cavity and SF ion binding sites (Fig. 4, C and D, and figs. S7D and S8, A to C). Notably, this assumed NCA binding site overlaps with the "promiscuous inhibitor binding site" in the hERG channel, which underlies drug-induced long QT syndrome (*12*, *32*). This site is thought to accommodate many hydrophobic molecules (e.g., terfenadine), and consistent with this, we found that activation by PD-118057 strongly reduced inhibition by terfenadine (Fig. 4B).

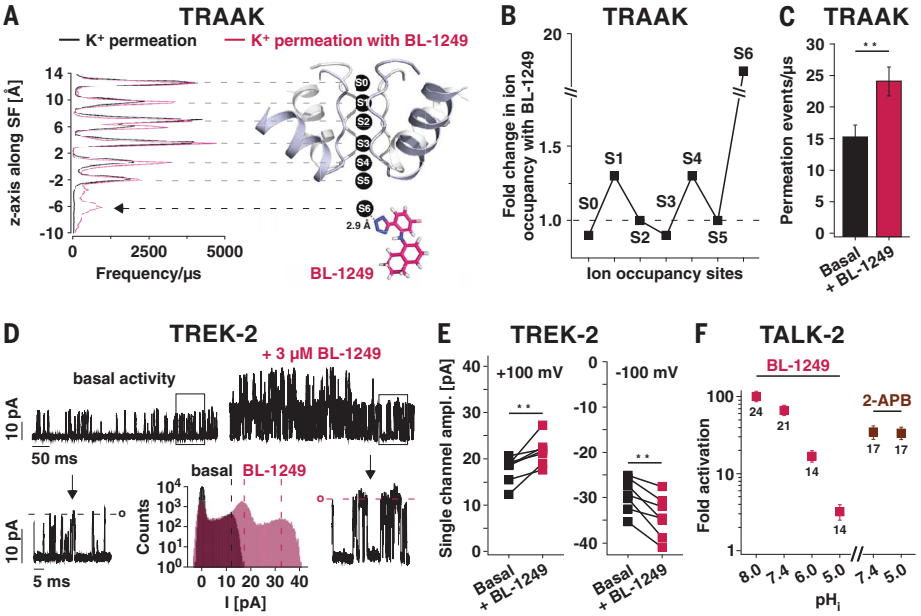


Fig. 3. Effects of BL-1249 on pore K^+ occupancy and permeation. (**A**) Ion occupancy (frequency/μs) of K^+ binding sites (S0 to S6) obtained from permeation MD simulations of TRAAK in the presence or absence of BL-1249, with BL-1249 adopting the identical position in TREK-2 (see Fig. 2G), that is, the negatively charged tetrazole ring (blue) in close proximity to the S6 K^+ ion. Coordinates were saved every 40 ps. The black arrow points to the increase in S6 K^+ occupancy. (**B**) Fold change in ion occupancy for the S0 to S6 sites. (**C**) MD simulations of K^+ permeation in TRAAK. Bars represent permeation events/μs from independent 200-ns MD simulations without (n = 50) and with BL-1249 (n = 30). $^{**}P \leq 0.01$. (**D**) Single-channel TREK-2 currents recorded at +80 mV from i-o patches before (basal) and after addition of 3 μM BL-1249, with arrows pointing to expanded scales of framed sections. The lower-middle panel depicts current amplitude histograms with or without 3 μM BL-1249 from i-o patches with ≤2 active channels (the right-hand peak represents the amplitude of two BL-1249–activated channels). Dotted lines indicate the single-channel amplitude maxima with or without BL-1249. (**E**) Paired single-channel current amplitudes before and after addition of 3 μM BL-1249 (n = 7). $^{**}P \leq 0.01$. (**F**) Fold activation of TALK-2 currents in i-o patches with 50 μM BL-1249 or 1 mM 2-APB applied at the indicated pH_i values. Error bars indicate SEM.

The molecular features of the NCA compounds define a common pharmacophore that, besides the negatively charged group, comprises both aromatic and hydrophobic moieties (Fig. 4E). As a control, we tested tetrazole-containing compounds that do not fit this common pharmacophore on TREK-1, BK_{Ca}, and hERG channels and found that they were unable to promote channel activation (fig. S9, A to C).

Our results uncover a class of K^+ channel openers, the NCAs, that act as a universal master key to unlock the SF gate. Mechanistically, these NCAs bind below the SF, where their negative charge promotes K^+ binding to the pore cavity, and thereby also alter the ion occupancy in the SF in a way that is known to promote activation of the filter gate (*17*). We hypothesize that, in particular, the increase at the S1 and S4 sites is responsible for activating the SF gate because all NCA-responsive channels are also activated by Rb^+ permeation, which is thought to increase ion occupancy at these sites, whereas mutations known to reduce S1 and S4 ion occupancy in K_{2P} channels abolish NCA activation. Furthermore, a loss of K^+ binding to the S1 site has been implicated in SF inactivation in K_v channels (*33*), hERG channels (*32*), and TREK-2 K_{2P} channels (*19*). However, at this time, we cannot exclude the possibility that nonelectrostatic interactions of the NCAs with their respective binding sites also contribute to the stabilization of the active SF state because these sites involve gating-sensitive regions [i.e., the TM4 (*8*, *19*) and S6 segments (*6*, *34*)]. In any case, our results support the view that many K_{2P} channels, as well as BK_{Ca} channels, adopt a low-activity (i.e., inactivated) state of their SF at rest and that the various physiological stimuli induce structural changes that drive the SF into an active (open) state. The NCAs appear to operate by means of bypassing these activation mechanisms to directly stabilize the SF in its active state.

Downloaded from http://science.sciencemag.org/ on September 19, 2019

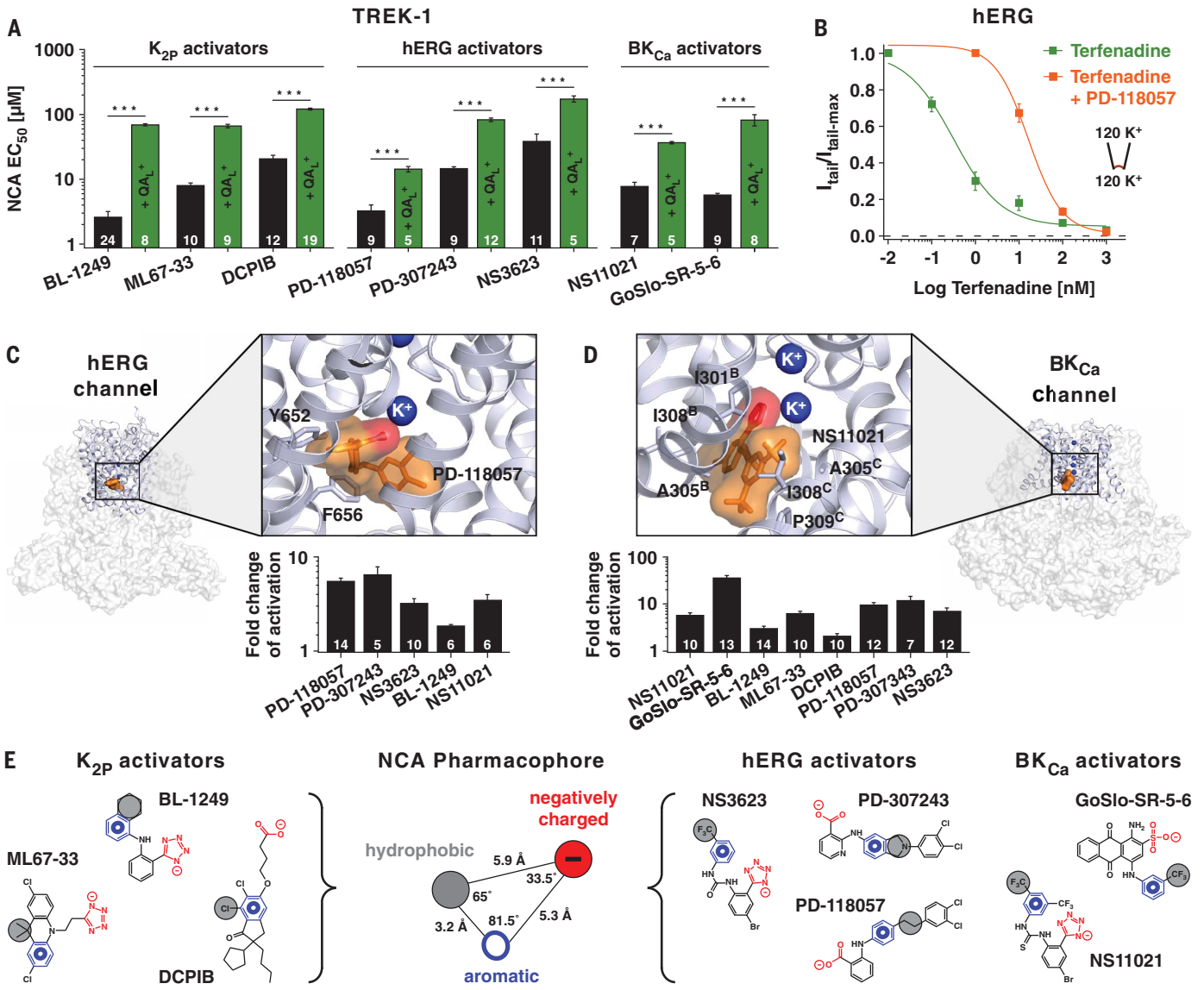


Fig. 4. NCA binding sites and common pharmacophores. (**A**) EC_{50} values (at +40 mV) for TREK-1 activation with compounds described as activators of either K_{2P}, hERG, or BK_{Ca} channels. Competitive antagonism is seen in the presence of QA_L^+ (either THexA or TPenA, which produce ~70 to 80% inhibition of respective basal K^+ currents). ***$P \leq 0.001$; error bars indicate SEM. (**B**) Terfenadine inhibition of hERG channels with or without 10 μM PD-118057. Error bars indicate SEM. (**C**) Structure of the hERG channel (PDB 5VA1) with the pore region expanded. This region was used for molecular docking and MD simulations to obtain the favored binding pose of PD-118057 (orange). Terfenadine-interacting residues are highlighted. The carboxylate group (red) interacts with a K^+ ion below the SF (see also fig. S7D); the bar chart below represents the fold activation of hERG tail currents at −100 mV with 10 μM of the indicated compounds. Error bars indicate SEM. (**D**) Same as in (C) but for the BK_{Ca} channel (PDB 5TJI), showing the favored binding pose of NS11021 (orange) where the tetrazole group (red) interacts with a K^+ ion below the SF and the residues in proximity to NS11021 highlighted. The bar chart below shows the fold activation of BK_{Ca} at +100 mV with 10 μM of the indicated compounds (at zero Ca^{2+}). Error bars indicate SEM; the B and C superscripts indicate the subunit of the tetramer. (**E**) Representation of the K_{2P} hERG, and BK_{Ca} activators used to generate a common NCA pharmacophore consisting of aromatic (blue), hydrophobic (gray), and acidic (red) moieties, with distances and angles as shown.

In addition, our findings have important implications for the development of drugs that target K^+ channels, because they reveal the binding sites and the mechanism of action for many established activators in various K^+ channels. Our findings have also identified the first activators for several K_{2P} channels (e.g., TALK-1/-2 and THIK-1/-2). Notably, the NCA binding site overlaps with the promiscuous inhibitor site in hERG, and thus, targeting this NCA site might represent a promising approach to circumvent the drug-induced long QT syndrome, which is, as of now, a serious burden in drug development (*12*). However, the identified polypharmacology also represents a challenge for the development of any NCA-based compound into a highly subtype-specific K^+ channel agonist. Nevertheless, structural differences between K_{2P}, hERG, and BK_{Ca} channels may still permit a rational drug design that reduces this promiscuity. However, in some acute situations such as ischemic stroke or status epilepticus, exploiting the polypharmacology of NCAs to promote simultaneous opening of multiple neuroprotective K^+ channels (e.g., BK_{Ca}, TREK-1, TREK-2, TRAAK, THIK-1, and THIK-2) may even be beneficial.

REFERENCES AND NOTES

1. S. I. V. Judge, P. J. Smith, P. E. Stewart, C. T. Bever Jr., *Recent Pat. CNS Drug Discov.* **2**, 200–228 (2007).

Downloaded from http://science.sciencemag.org/ on September 19, 2019

2. V. K. Vyas, P. Parikh, J. Ramani, M. Ghate, *Curr. Med. Chem.* 10.2174/0929867325666180430152023 (2018).
3. S. Hou, S. H. Heinemann, T. Hoshi, *Physiology* **24**, 26–35 (2009).
4. M. I. Niemeyer, L. P. Cid, W. González, F. V. Sepúlveda, *Mol. Pharmacol.* **90**, 309–317 (2016).
5. F. V. Sepúlveda, L. Pablo Cid, J. Teulon, M. I. Niemeyer, *Physiol. Rev.* **95**, 179–217 (2015).
6. G. Yellen, *Nature* **419**, 35–42 (2002).
7. P. L. Piechotta *et al*., *EMBO J.* **30**, 3607–3619 (2011).
8. S. N. Bagriantsev, R. Peyronnet, K. A. Clark, E. Honoré, D. L. Minor Jr., *EMBO J.* **30**, 3594–3606 (2011).
9. C. M. Wilkens, R. W. Aldrich, *J. Gen. Physiol.* **128**, 347–364 (2006).
10. Y. Zhou, X.-M. Xia, C. J. Lingle, *Proc. Natl. Acad. Sci. U.S.A.* **108**, 12161–12166 (2011).
11. P. L. Smith, T. Baukrowitz, G. Yellen, *Nature* **379**, 833–836 (1996).
12. J. I. Vandenberg, E. Perozo, T. W. Allen, *Trends Pharmacol. Sci.* **38**, 899–907 (2017).
13. L. Pope *et al*., *ACS Chem. Neurosci.* **9**, 3153–3165 (2018).
14. J. Zhou *et al*., *Mol. Pharmacol.* **68**, 876–884 (2005).
15. B. H. Bentzen *et al*., *Mol. Pharmacol.* **72**, 1033–1044 (2007).
16. M. J. Lenaeus, D. Burdette, T. Wagner, P. J. Focia, A. Gross, *Biochemistry* **53**, 5365–5373 (2014).
17. M. Schewe *et al*., *Cell* **164**, 937–949 (2016).
18. J. G. McCoy, C. M. Nimigean, *Biochim. Biophys. Acta* **1818**, 272–285 (2012).
19. Y. Y. Dong *et al*., *Science* **347**, 1256–1259 (2015).
20. M. Rapedius *et al*., *Channels* **6**, 473–478 (2012).
21. R.-G. Zhuo *et al*., *Front. Cell. Neurosci.* **10**, 127 (2016).
22. M. Lolicato *et al*., *Nature* **547**, 364–368 (2017).
23. W. Kopec *et al*., *Nat. Chem.* **10**, 813–820 (2018).
24. M. V. Clausen, V. Jarerattanachat, E. P. Carpenter, M. S. P. Sansom, S. J. Tucker, *Proc. Natl. Acad. Sci. U.S.A.* **114**, E8343–E8351 (2017).
25. D. Kang, C. Choe, D. Kim, *J. Physiol.* **564**, 103–116 (2005).
26. M. Zhou, R. MacKinnon, *J. Mol. Biol.* **338**, 839–846 (2004).
27. S. N. Bagriantsev *et al*., *ACS Chem. Biol.* **8**, 1841–1851 (2013).
28. L. Minieri *et al*., *Br. J. Pharmacol.* **168**, 1240–1254 (2013).
29. E. Gordon *et al*., *Mol. Pharmacol.* **73**, 639–651 (2008).
30. R. S. Hansen *et al*., *Mol. Pharmacol.* **70**, 1319–1329 (2006).
31. S. Roy *et al*., *ChemMedChem* **7**, 1763–1769 (2012).
32. W. Wang, R. MacKinnon, *Cell* **169**, 422–430.e10 (2017).
33. V. Pau, Y. Zhou, Y. Ramu, Y. Xu, Z. Lu, *Nat. Struct. Mol. Biol.* **24**, 857–865 (2017).
34. H. Yang, G. Zhang, J. Cui, *Front. Physiol.* **6**, 29 (2015).

ACKNOWLEDGMENTS

We thank F. Lesage for the THIK-1 and THIK-2 K_{2P} channel clones; M. A. Hollywood for providing the BK_{Ca} activator GoSlo-SR-5-6; and J. Kusch for initially testing the BL-1249 effect on CNGA1 channels. We thank all members of our respective laboratories for technical support and comments on the manuscript. We thank Diamond Light Source Ltd. and its staff for access to the macromolecular crystallography beamlines. We also acknowledge the North-German Supercomputing Alliance (HLRN) for providing High Performance Computing (HPC) resources that have contributed to the research results reported in this paper. **Funding:** T.B. and B.L.d.G. were supported by the DFG; B.F. was supported by the DFG (SFB746, TRR 152, and EXC 294 and 2189); S.J.T. and E.P.C were supported by a BBSRC Industrial Partnership Award (BB/N009274/1); and L.J.C. was supported by a Wellcome Trust (OXION) Ph.D. studentship. A.M. was funded by the EPSRC Life Sciences Interface Doctoral Training Centre. A.C.W.P. and E.P.C. are members of the SGC (charity reference no. 1097737) funded by AbbVie, Bayer Pharma AG, Boehringer Ingelheim, the Canada Foundation for Innovation, Genome Canada, Janssen, Merck KGaA, MSD, Novartis, the Ontario Ministry of Economic Development and Innovation, Pfizer, São Paulo Research Foundation-FAPESP, and Takeda, as well as the Innovative Medicines Initiative Joint Undertaking ULTRA-DD grant 115766 and the Wellcome Trust 106169/Z/14/Z. D.C.P. was an employee of Pfizer at the time of the research. **Author contributions:** M.S. and T.B. conceived the study and designed the electrophysiological experiments. M.S., Ü.M., F.S., and M.T. performed all inside-out patch-clamp experiments in *Xenopus* oocytes. M.S. and T.B. analyzed the data. M.M. designed K^+ channel mutations. C.C. performed whole-cell recordings in CHO cells and analyzed the data together with B.F. Single-channel recordings in *Xenopus* oocytes were carried out and analyzed by K.S.V. and A.K.K., supervised by N.D. Single-channel recordings in HEK293 cells were performed and analyzed by L.J.C., supervised by S.J.T. A.M. purified TREK-2 and cocrystallized TREK-2 with BL-1249^{Br}. A.M. and A.C.W.P. obtained and analyzed the x-ray data, supervised by E.P.C. and S.J.T. D.C.P. synthesized the brominated BL-1249. H.B. synthesized ML67-33, supervised by M.N. H.S. designed, performed, and analyzed all molecular dockings and MD simulations with critical comments of B.L.d.G. W.G. calculated and analyzed the NCA pharmacophore together with M.S. and N.D. M.S. and M.M. prepared and edited all figures. T.B., M.S., B.F., E.P.C., and S.J.T. contributed to the writing and editing of the manuscript and approved the manuscript. **Competing interests:** The authors declare no competing interests. **Data and materials availability:** All data are available in the main text or the supplementary materials. Requests for materials should be addressed to the corresponding authors.

SUPPLEMENTARY MATERIALS

www.sciencemag.org/content/363/6429/875/suppl/DC1
Materials and Methods
Figs. S1 to S9
Tables S1 to S3
References (*35*–*67*)

9 August 2018; accepted 28 January 2019
10.1126/science.aav0569

Downloaded from http://science.sciencemag.org/ on September 19, 2019

Science

A pharmacological master key mechanism that unlocks the selectivity filter gate in K^+ channels

Marcus Schewe, Han Sun, Ümit Mert, Alexandra Mackenzie, Ashley C. W. Pike, Friederike Schulz, Cristina Constantin, Kirsty S. Vowinkel, Linus J. Conrad, Aytug K. Kiper, Wendy Gonzalez, Marianne Musinszki, Marie Tegtmeier, David C. Pryde, Hassane Belabed, Marc Nazare, Bert L. de Groot, Niels Decher, Bernd Fakler, Elisabeth P. Carpenter, Stephen J. Tucker and Thomas Baukrowitz

Science **363** (6429), 875-880.
DOI: 10.1126/science.aav0569

A key to potassium channel activation

Using drugs to activate potassium channels has the potential to treat conditions like epilepsy, heart arrhythmias, and pain. Schewe *et al.* report a class of negatively charged activators (NCAs) with a defined pharmacore that use a similar mechanism to activate many types of potassium channels. X-ray crystallography, functional analysis, and molecular dynamics simulations showed that the NCAs bind below the selectivity filter to open the filter gate and activate the channels. Targeting this NCA site might be exploited in rational drug design.

Science, this issue p. 875

ARTICLE TOOLS http://science.sciencemag.org/content/363/6429/875

SUPPLEMENTARY MATERIALS http://science.sciencemag.org/content/suppl/2019/02/20/363.6429.875.DC1

REFERENCES This article cites 64 articles, 15 of which you can access for free
http://science.sciencemag.org/content/363/6429/875#BIBL

PERMISSIONS http://www.sciencemag.org/help/reprints-and-permissions

Use of this article is subject to the Terms of Service

Science (print ISSN 0036-8075; online ISSN 1095-9203) is published by the American Association for the Advancement of Science, 1200 New York Avenue NW, Washington, DC 20005. The title *Science* is a registered trademark of AAAS.

Copyright © 2019 The Authors, some rights reserved; exclusive licensee American Association for the Advancement of Science. No claim to original U.S. Government Works

Downloaded from http://science.sciencemag.org/ on September 19, 2019

bioRxiv preprint first posted online Jul. 19, 2019; doi: http://dx.doi.org/10.1101/706168. The copyright holder for this preprint (which was not peer-reviewed) is the author/funder, who has granted bioRxiv a license to display the preprint in perpetuity. It is made available under a CC-BY-ND 4.0 International license.

A unique lower X-gate in TASK channels traps inhibitors within the vestibule

Authors

Karin E. J. Rödström[1,#], Aytuğ K. Kiper[2,#], Wei Zhang[1, 5,ϕ], Susanne Rinné[2,ϕ], Ashley C. W. Pike[1,ϕ], Matthias Goldstein[2], Linus Conrad[3], Martina Delbeck[4], Michael Hahn[4], Heinrich Meier[4], Magdalena Platzk[4], Andrew Quigley[1,6], David Speedman[1], Leela Shrestha[1], Shubhashish M.M. Mukhopadhyay[1], Nicola A. Burgess-Brown[1], Stephen J. Tucker[3], Thomas Mueller[4], Niels Decher[2,§,*], Elisabeth P. Carpenter[1,§,*].

[1] Structural Genomics Consortium, University of Oxford, Oxford, OX3 7DQ, UK.

[2] Institute for Physiology and Pathophysiology, Vegetative Physiology, University of Marburg, Marburg, Germany.

[3] Department of Physics, University of Oxford, OX1 3QT, UK.

[4] Bayer AG, Research & Development, Pharmaceuticals, Wuppertal, Germany.

[5] Present address: CAS Key Laboratory of Pathogenic Microbiology and Immunology, Institute of Microbiology, Chinese Academy of Sciences, Beijing 100101, China.

[6] Present address: Membrane Protein Laboratory, Research Complex at Harwell, Harwell, UK.

[#] These authors contributed equally to this work.

[ϕ] These authors contributed equally to this work.

[§] These authors jointly supervised this work.

[*]e-mail: decher@staff.uni-marburg.de, liz.carpenter@sgc.ox.ac.uk

bioRxiv preprint first posted online Jul. 19, 2019; doi: http://dx.doi.org/10.1101/706168. The copyright holder for this preprint (which was not peer-reviewed) is the author/funder, who has granted bioRxiv a license to display the preprint in perpetuity. It is made available under a CC-BY-ND 4.0 International license.

TASK channels are unusual members of the two-pore domain potassium (K_{2P}) channel family, with unique and unexplained physiological and pharmacological characteristics. TASKs are found in neurons[1,2], cardiomyocytes[3-5] and vascular smooth muscle cells[6] where they are involved in regulation of heart rate[7], pulmonary artery tone[6,8], sleep/wake cycles[9] and responses to volatile anaesthetics[9-12]. K_{2P} channels regulate the resting membrane potential, providing background K^+ currents controlled by numerous physiological stimuli[13,14]. Unlike other K_{2P} channels, TASK channels have the capacity to bind inhibitors with high affinity, exceptional selectivity and very slow compound washout rates. These characteristics make the TASK channels some of the the most easily druggable potassium channels, and indeed TASK-1 inhibitors are currently in clinical trials for obstructive sleep apnea (OSA) and atrial fibrillation (Afib)[15] (The DOCTOS and SANDMAN Trials). Generally, potassium channels have an intramembrane vestibule with a selectivity filter above and a gate with four parallel helices below. However, K_{2P} channels studied to date all lack a lower gate. Here we present the structure of TASK-1, revealing a unique lower gate created by interaction of the two crossed C-terminal M4 transmembrane helices at the vestibule entrance, which we designate as an "X-gate". This structure is formed by six residues ($V^{243}LRFMT^{248}$) that are essential for responses to volatile anaesthetics[11], neuro-transmitters[16] and G-protein coupled receptors[16]. Interestingly, mutations within the X-gate and surrounding regions drastically affect both open probability and activation by anaesthetics. Structures of TASK-1 with two novel, high-affinity blockers, shows both inhibitors bound below the selectivity filter, trapped in the vestibule by the X-gate, thus explaining their exceptionally low wash-out rates. Thus, the presence of the X-gate in TASK channels explains many aspects of their unusual physiological and pharmacological behaviour, which is invaluable for future development and optimization of TASK modulators for treatment of heart, lung and sleep disorders.

bioRxiv preprint first posted online Jul. 19, 2019; doi: http://dx.doi.org/10.1101/706168. The copyright holder for this preprint (which was not peer-reviewed) is the author/funder, who has granted bioRxiv a license to display the preprint in perpetuity. It is made available under a CC-BY-ND 4.0 International license.

To understand the molecular basis of the unusual properties of TASK channels we solved the structure of human TWIK-related acid-sensitive potassium channel 1 (TASK-1, K_{2P}3.1) by X-ray crystallography. We used a C-terminally truncated construct (Met1 to Glu259) for the structural studies, which had similar properties to the full-length channel, in particular its response to the pore-blockers A1899 and ML365, and its activation by pH (Extended Data Fig. 1). We grew crystals using the HiLiDe method[17] and determined the structure by molecular replacement using X-ray data to 3.0 Å resolution (Methods, Extended Data Table 1, Fig. 1, Extended Data Fig. 2a-f). TASK-1 forms a domain-swapped homodimer (Fig. 1a), with a pseudo-tetrameric selectivity filter, four transmembrane helices (M1-M4) and an extracellular cap, similar to previously solved structures of other K_{2P} channels[18-22] (Fig. 1b). The selectivity filter resembles that of other K_{2P} channels, with binding sites for four K^+ ions. TASK-1 is inactivated by extracellular acidic pHs[23] (Extended Data Fig. 1c) and His98, near the top of the selectivity filter, is thought to be the extracellular pH sensor[24]. Crystals were grown at pH 8.5 and the structure shows His98 forming a hydrogen bond to a water molecule behind the selectivity filter (Extended Data Fig. 2c). His98 is positioned below the sidechains of Gln77 and Gln209, which interact with each other, so that in this conformation it cannot access the extracellular space. It has been proposed that protonation of His98 could lead to reorientation of the sidechain into the extracellular space[25], which would also require disruption of the Gln77-Gln209 interaction.

One unusual feature of the TASK and THIK channels is the absence of the intermolecular disulphide bond at the apex of the external cap domain (Extended Data Fig. 3b). However, we found that in TASK-1 the domain-swapped cap structure is preserved without this disulphide bond (Extended Data Fig. 2e-h), as previously predicted[26]. Therefore, this feature does not explain the differences in TASK-1 properties. The relative positions of the M2-M4 helices determine whether stretch-activated K_{2P} channels are in a more active “up” state with raised helices and closed fenestrations, or a lower activity “down” state with open fenestrations[20,21]. Overall the TASK-1 structure adopts a “down”–like state, with some adjustment of the M2 position and open fenestrations connecting the small central vestibule to the lipid bilayer (Fig. 1b-d).

Surprisingly, we found that at the distal end of M4 there was an unexpected conformational rearrangement, causing the M4 helices to lie across the entrance of the vestibule, forming a closed gate which we have designated as an “X-gate” (Fig. 1c-h). This conformational change is caused by bends in M4 at residues Leu241 and Asn250, on either

bioRxiv preprint first posted online Jul. 19, 2019; doi: http://dx.doi.org/10.1101/706168. The copyright holder for this preprint (which was not peer-reviewed) is the author/funder, who has granted bioRxiv a license to display the preprint in perpetuity. It is made available under a CC-BY-ND 4.0 International license.

side of a six residue sequence ($V^{243}LRFMT^{248}$) which forms the X-gate. This leaves a gap of 2-3 Å between the M4 helices, in contrast to TREK-2 which has a gap of at least 7.5 Å (Fig. 1e,f). The X-gate adopts an unusual extended two-turn helical structure, lacking the hydrogen bonding patterns seen in α or 3_{10} helices (Extended Data Fig. 2i). The interface is lined by the hydrophobic sidechains of Leu244, Met247 and the methyl group of Thr248 (Fig. 1g,h), which block the ion conduction pathway. Interestingly, this region is essential for TASK-1 responses to volatile anaesthetics[9-12], neurotransmitters[16], drugs[27] and G-protein coupled receptors[16] (potentially through diacylglycerol[28] or PIP_2 interactions[29]). Sequence alignments suggest TASK-3 and TASK-5 may also form similar structures (Extended Data Fig. 3). The presence of the X-gate in the TASK subfamily is an exception to the paradigm that K_{2P} channels lack a lower gate[30]. Surprisingly, the structure of the dimeric X-gate is unrelated to the 'helix bundle crossing' gates found in tetrameric K^+ channels, which have four parallel helices forming a funnel shape.

To determine whether the X-gate explains the unusual properties of TASK channels, we performed alanine scanning mutagenesis across the distal M4 helix (Thr230-Thr248), and assessed channel activity and surface expression of the mutants. We predicted that disruption of the X-gate would increase the very low TASK-1 basal channel activity[7,30,31]. Strikingly, mutation of any residue within the X-gate (except Val243), led to increased currents (Fig. 2a), which were not caused by increased surface expression, as we observed similar or reduced surface expression (Extended Data Fig. 4a). The centre of the X-gate is formed by Leu244, which is packed between residues on M2, M4 and M4' (Fig. 1h,2b) and the Val244A mutation resulted in the largest current increase (Fig. 2a). Inside out single channel recordings of Leu244Ala confirmed a direct effect on channel gating with a 6-fold increase in channel open probability from 0.7 to 4.0% (Fig. 2c,d) and increased channel open times (Fig. 2e). Mutation of the equivalent residue in TASK-3 (Leu244Ala) also resulted in increased channel activity (Fig. 2f). The X-gate is also important for activation by volatile anaesthetics such as halothane and sevoflurane[**9-12**], and was originally called the "halothane response element". Here we confirm that sevoflurane, a modern and widely used anaesthetic, also activates TASK-1 and that mutations in the X-gate reduces this activation (Fig. 2g,h), indicating a role for the X-gate in responses to volatile anaesthetics.

Next we investigated residues surrounding the X-gate, which may be important for its formation and stability. The X-gate is preceded by a hinge point in M4 around Leu241-Val242, where the helix axis is bent by ~40° (Fig. 3a). After the bend the X-gate itself adopts an

bioRxiv preprint first posted online Jul. 19, 2019; doi: http://dx.doi.org/10.1101/706168. The copyright holder for this preprint (which was not peer-reviewed) is the author/funder, who has granted bioRxiv a license to display the preprint in perpetuity. It is made available under a CC-BY-ND 4.0 International license.

expanded helical conformation (Extended Data Fig. 2i). The side chain of Leu241 inserts into a hydrophobic pocket, pulling it away from the helix axis and stabilizing the bend in M4. This exposes the Leu241 carbonyl so that it can hydrogen bond with the Arg245 sidechain (Fig. 3a). Mutation of either Leu241 or Arg245 to Ala increased channel activity by 5-7 fold (Fig. 2a), confirming the importance of these interactions in X-gate stability. Furthermore, a hydrogen bond between the carbonyl oxygen of Ala237 on M4 and Asn133 on M2 also disrupts the M4 α helix, stabilizing the bend, and mutation of Asn133 increased channel activity (Fig. 3b).

Following the X-gate, a second bend in M4 at residue Asn250 allows the distal end of M4 to adopt an α-helical structure which forms extensive interactions with the opposite side of the vestibule, a region we have named the "latch" (Fig. 3a). This consists of an extensive network of salt bridges and hydrogen bonds linking M4 to M1 and M2' (Fig. 3a). Mutation of several residues across the proximal M1, distal M2' and distal M4 regions gave increased channel activity, consistent with the latch region playing an important role in stabilizing the X-gate (Fig. 3b). In particular, Arg7 and Arg131' appear to be important for the integrity of the latch, since mutations to acidic residues causes a 5 – 10 fold increase in currents (Fig. 3c). The reduced levels of surface expression for these mutants indicates their increased currents are likely due to direct effects on channel gating, not increased surface expression (Extended data Fig. 4b).

Lipids are also important regulators of K_{2P} channels and the structures reveal binding sites for lipids, including the cholesterol analogue cholesteryl hemisuccinate (CHS) (Extended Data Fig. 2d). CHS (added during TASK-1 purification) extends along the X-gate, interacting with M1, M4 and M2' (Fig. 3a). Phe246 in the X-gate lies next to the CHS molecule (Fig. 3a), and the Phe246Ala mutation produces a 4-fold increase in current (Fig. 2a). Therefore, cholesterol may also help to stabilize the X-gate in a closed conformation.

Unlike many other K_{2P} channels that exhibit very poor pharmacology, several high affinity and highly selective inhibitors exist for TASK-1 and TASK-3 channels. Furthermore, these blockers exhibit exceptionally low wash-out rates after removal of the inhibitor. Together, these characteristics make TASK inhibitors interesting pharmacological tools to investigate the physiological and pharmacological function of TASK channels. Therefore, we performed an ultra-high throughput screen (uHTS) on TASK-1, which identified two highly potent and selective inhibitors of TASK-1, BAY 1000493 and BAY 2341237 (Fig. 4a,b), with EC_{50} values of 9.5 and 7.6 nM. Crystal structures of complexes of TASK-1 with these inhibitors showed that they both bind within the inner vestibule, directly below the selectivity filter (Fig

bioRxiv preprint first posted online Jul. 19, 2019; doi: http://dx.doi.org/10.1101/706168. The copyright holder for this preprint (which was not peer-reviewed) is the author/funder, who has granted bioRxiv a license to display the preprint in perpetuity. It is made available under a CC-BY-ND 4.0 International license.

4c-g, Extended Data Fig. 5). In both cases, a single molecule binds across the 2-fold axis of the dimer, with one molecule bound per dimer. The electron density for BAY 1000493 shows a superposition of two copies of the inhibitor, with 50% occupancy for each orientation (Extended Data Fig. 5a,d), as expected. This arrangement was confirmed using anomalous difference maps with data collected at the Br absorption edge (Extended Data Fig. 5a). In contrast, BAY 2341237 only binds in one orientation, with 100% occupancy, due to small differences in the two chains of the dimer (Fig. 4d,f,g, Extended Data Fig. 5b,e).

Both inhibitors bind to the closed conformation of TASK-1, below the selectivity filter, without perturbing the X-gate structure. They fit precisely to the surface at the top of the vestibule, with Leu122 projecting into the vestibule below the compounds, holding them in place (Fig. 4e-g). Consistent with these observations, we found that mutation of residues lining the inhibitor binding site (Thr93Cys, Ile118Ala, Leu122Ala, Thr199Cys and Leu239Ala) drastically reduced inhibition by BAY 1000493 (Fig. 4h). Leu122 is important for binding of other TASK-1 pore blockers[27,32] and it occupies a key position below the binding site for our inhibitors (Fig. 4g). When we recorded full dose-response curves with TASK-1 and a Leu122Ala mutant, we found a >100-fold decrease in EC_{50} values for both inhibitors with the mutation (Fig 4i). In addition, we found that BAY 1000493 is highly selective for TASK-1 and TASK-3, when compared to a wide range of other ion channels (Extended Data Fig. 6a,b, Extended Data Table 2).

Our structures show that both compounds bind at the top of the vestibule, trapped but not in direct contact with the X-gate. Leu244 is central to the X-gate structure, but is not part of the inhibitor binding site and a Leu244Ala mutation did not alter inhibition by BAY 1000493 (Fig. 4h). However, TASK channels have another critical feature, their ability to retain bound compounds for long periods during washout experiments. BAY 1000493 shows very slow washout rates from TASK-1 (Fig. 4j, Extended Data Fig. 6c), unlike a larger TASK inhibitor, A1899, which has an IC_{50} value of 35 nM and washes off significantly faster[27] (Extended Data Fig. 6d-f). When the Leu244Ala mutation is introduced at the X-gate or the Arg131Asp mutation at the latch, we observed a significant increases in the BAY 1000493 washout rate (Fig. 4j,k, Extended Data Fig. 6c). Conversely, a mutation near the latch (Thr134Cys), that has relatively little effect on X-gate function (Fig. 3b), also has less effect on washout rates (Fig., 4j, Extended Data Fig. 6c). This suggests that disruption of the X-gate or the latch may stabilise the open state of the channel, thereby allowing BAY 1000493 to dissociate more easily from this site.

bioRxiv preprint first posted online Jul. 19, 2019; doi: http://dx.doi.org/10.1101/706168. The copyright holder for this preprint (which was not peer-reviewed) is the author/funder, who has granted bioRxiv a license to display the preprint in perpetuity. It is made available under a CC-BY-ND 4.0 International license.

The X-gate must be capable of opening wide enough to allow inhibitors to enter, as well as hydrated K^+ ions. Therefore, it is likely that X-gate opening requires a significant conformational change, not simply small adjustments in sidechain positions or helix orientation. We speculate that this could involve opening of the latch, relaxation of the X-gate extended helix into an α-helical conformation and straightening of M4 (Extended Data Fig. 7), giving a conformation similar to other K_{2P} structures[18-22]. This would also allow the M1-M4 helices to adopt a more "up"-like conformation, without fenestrations, consistent with the proposed higher activity state of other K_{2P}s (Extended Data Fig. 7).

Loss of function (LoF) missense variants in TASK channels are associated with two genetic diseases. Mutations in TASK-1 cause autosomal dominant primary pulmonary hypertension Type 4[33] (PPH4: OMIM: 615344), a serious condition that is often fatal in mid-life[33], whilst mutations in TASK-3 are linked to the developmental disorder Birk-Barel syndrome[34]. These mutations are distributed throughout the structure (see Extended Data Fig. 8a-g, Supplementary Discussion). However, one PPH4-associated TASK-1 mutation, Thr8Lys on M1, is located within the X-gate latch and causes ~2-fold decreased currents (Fig. 3a, Extended Data Fig 8c). Furthermore, two Birk-Barel syndrome associated mutations in TASK-3 (Gly236Arg[34] and Ala237Asp[35]) preceded the hinge on M4. Gly236Arg places a large positively charged residue within the vestibule, near the ion conduction pathway and the X-gate, whereas Ala237Asp places a charged residue adjacent to the hinge (Extended Data Fig. 8h). These mutations emphasize the significance of these regions in TASK channel function.

In conclusion, we have shown that the TASKs channels are highly unusual members of the K_{2P} channel family in that they have the ability to form a cytoplasmic X-gate, which may contribute to the low open probability of TASK-1. We have also shown that two nanomolar affinity inhibitors bind in the closed vestibule, trapped by the X-gate. Their precise fit to the top surface of the vestibule, combined with the trapping effect of the X-gate may explain the exceptionally high affinity and selectivity observed with these pore blockers. In addition, the presence of the X-gate may also explain the very low wash-out rates of these inhibitors. Compound trapping within the inner cavity has been proposed previously for many ion channels[36-39]. TASK-1 inhibitor binding requires opening of the X-gate, allowing compounds to enter and bind to the high affinity site below the selectivity filter. Since the X-gate is closed most of the time and there is little space for the compound to dissociate, they will remain bound, trapped by the X-gate, resulting in an increased apparent affinity and reduced washout rate. However, whether the open state of TASK-1 involves any change in the conformation of the

bioRxiv preprint first posted online Jul. 19, 2019; doi: http://dx.doi.org/10.1101/706168. The copyright holder for this preprint (which was not peer-reviewed) is the author/funder, who has granted bioRxiv a license to display the preprint in perpetuity. It is made available under a CC-BY-ND 4.0 International license.

compound binding site, or whether these compounds can stabilize the X-gate in its closed conformation, remains to be seen.

The X-gate is clearly important for the control of TASK channel activity and may contribute to their regulation by neurotransmitters[16], intracellular signalling pathways[16,28,29], volatile anaesthetics[9-12] and small molecules[27]. However, given the polymodal nature of K_{2P} channel regulation and the known role of the selectivity filter in K_{2P} channel gating, the X-gate is unlikely to be the only route for TASK channel regulation. For example, their physiologically relevant regulation by extracellular pH involves His98, which is extracellular, located next to the selectivity filter. Further studies are needed to determine if these two gating mechanisms are coupled.

This study also provides insight into the mechanism of TASK-1 inhibitors that are already in clinical trials as potential treatments for obstructive sleep apnea and atrial fibrillation. The unique environment of the inhibitor binding site within the vestibule, created by the X-gate, has significant implications for interpretation of pharmacokinetic properties of TASK inhibitors. In particular, questions of bioavailability, metabolism and half-life should be interpreted in the light of the discovery of the X-gate. Once a blocker becomes sequestered within this vestibule, it is likely to remain bound and ‘active’ for much longer than anticipated by studying its pharmacokinetic properties. Such factors should be carefully evaluated during drug development and trials. Overall, this work provides critical understanding of the gating mechanism in TASK channels and the action of clinically-relevant inhibitors, processes that are of uppermost importance for their use as targets for efficient and safe treatment of disease.

bioRxiv preprint first posted online Jul. 19, 2019; doi: http://dx.doi.org/10.1101/706168. The copyright holder for this preprint (which was not peer-reviewed) is the author/funder, who has granted bioRxiv a license to display the preprint in perpetuity. It is made available under a CC-BY-ND 4.0 International license.

Methods

Cloning and expression of TASK-1$^{Met1\text{-}Glu259}$ for structural studies

The human *KCNK3* gene (Genbank ID 4504849), which encoded the TASK-1 protein, was obtained from Origene. The TASK-1 construct, residues Met1 to Glu259, was subcloned in the SGC vector pFB-CT10HF-LIC, with a C terminal TEV site followed by decahistidine and FLAG tags. Baculovirus was generated with the Bac-to-bac system and passaged twice before it was used for infecting Sf9 cells at a density of 2 x 10^6 cells/mL and a ratio of 5 mL virus per litre cells. Infected cells were harvested after 72 h by centrifugation, frozen in liquid nitrogen and stored at -80°C.

Purification of TASK-1

Cells were broken with an EmulsiFlex-C3 or C5 high-pressure homogenizer (Avestin Inc.) in 40 ml breaking buffer (50 mM HEPES pH 7.5, 200 mM KCl, 5% v/v glycerol) per initial litre culture volume. Protein was solubilized by addition of 1% w/v n-decyl-β-D-maltopyranoside (DM) (Anatrace) and 0.1% w/v cholesteryl hemisuccinate (CHS) Tris salt (Sigma-Aldrich) and rotated at 4°C for 1 h. Cell debris was pelleted at 35,000 g, 1 h, 4°C, 5 mM imidazole pH 8.0 was added, and protein was incubated with Talon (Clontech), 0.5 ml resin per litre cell culture for 1 h at 4°C. Resin was collected and washed with 30 CV wash buffer (50 mM HEPES pH 7.5, 200 mM KCl, 5% v/v glycerol, 20 mM imidazole pH 8.0, 0.24% w/v DM, 0.024% w/v CHS), and eluted with elution buffer (50 mM HEPES pH 7.5, 200 mM KCl, 5% v/v glycerol, 250 mM imidazole pH 8.0, 0.24% w/v DM, 0.024% w/v CHS). The protein was exchanged into desalting buffer (50 mM HEPES pH 7.5, 200 mM KCl, 5% v/v glycerol, 0.24% w/v DM, 0.024% w/v CHS) by passing over PD10 columns and purification tags were cleaved by addition of a 1:3 w:w ratio of 6x His-tagged TEV protease and deglycosylated with a 1:10 w:w ratio of 6x His-tagged PNGaseF, for 12-16 h at 4°C. Enzymes were removed by addition of 0.1 ml Talon resin per litre initial cell culture and 7.5 mM imidazole pH 8.0. The protein was concentrated to 500 µl and subjected to size exclusion chromatography on a Superose 6 Increase 10/300 GL column (GE Healthcare) in gel filtration buffer (20 mM HEPES pH 7.5, 200 mM KCl, 0.12% w/v DM, 0.012% w/v CHS). Fractions containing the highest concentration of TASK-1 were pooled and concentrated to 12-30 mg/ml ml with a 50 kDa molecular weight cut off spin concentrator (GE Healthcare).

bioRxiv preprint first posted online Jul. 19, 2019; doi: http://dx.doi.org/10.1101/706168. The copyright holder for this preprint (which was not peer-reviewed) is the author/funder, who has granted bioRxiv a license to display the preprint in perpetuity. It is made available under a CC-BY-ND 4.0 International license.

Crystallisation, X-ray data collection and data processing

Crystallization trials were performed in 96-well sitting drop vapour diffusion plates using a Mosquito crystallization robot (TTP Labtech) at 8 - 12 mg/ml with 150 nl drops and 2:1, 1:1 and 1:2 protein:reservoir ratios. Initial crystals were obtained at 20°C in an in-house version of MemGold HT-96, condition D7 (0.1 M TRIS pH 8.5, 0.1 mM KCl and 39% v/v polyethylene glycol (PEG) 400). Crystals were further optimized by addition of 3% w/v sucrose to the precipitant solution and by using the HiLiDe method[17]. Briefly, 1,2-dioleoyl-sn-glycero-3-phosphocholine (DOPC) (Avanti Polar Lipids, Inc.) in chloroform was dried down in a round-bottomed glass vial, 1.5 µg lipid per µl protein. Protein at 5.7-6.2 mg/ml was added along with 15 µg/µl DM and 1.5 µg/µl CHS, incubated slowly shaking at 4°C for 16-24 h and centrifuged at 15,000 g, 2 h, 4°C. Crystallization was carried out in 24-well hanging drop plates with 2 µl drops and a 2:1 protein:reservoir ratio at 20°C. Crystals grew over 1-8 weeks in 0.1 M TRIS pH 8.5, 0.05 M KCl, 32% PEG 400 and 3% w/v sucrose and were harvested at 6°C directly from the drop and vitrified.

Data collection was carried out at Diamond Light Source Ltd. (DLS) using the microfocus beamline I24. The final dataset was assembled from a series of 40° wedges collected from two crystals, using a 9x6 µm microbeam.

Crystals of complexes of TASK-1 with inhibitors were also grown using the HiLiDe method. Each inhibitor, dissolved in 100% DMSO at 130 mM, was added to the HiLiDe setup to a final concentration of 1.3 mM. Crystals grew in 0.1 M TRIS pH 8.5, 0.05 M KCl, and 3% w/v sucrose with 24% PEG 400 for BAY 1000493 and 31% PEG 400 for BAY 2341237 over 1 - 12 weeks and were harvested at 6°C. Data were collected at the DLS on beamline I24 at a wavelength of 0.9686 Å, with 0.1 s exposures, a beam size of 20x20 µm and 0.2° oscillations. A full dataset for the BAY 1000493 complex was assembled from several 40° wedges from one crystal whereas the BAY 2341237 dataset was collected as a single wedge, both with a 20x20 µm beam. Anomalous data for BAY 1000493 were collected at the bromine edge, (λ = 0.9116 Å) in four 360° passes.

Model building and refinement for structures

Data were processed as individual wedges in XDS[40] and scaled together in XSCALE[40]. The data were merged in AIMLESS[41,42] (Extended Data Table 1). Due to the anisotropy of the data, an anisotropic cut-off was applied using the STARANISO server[43]. The structure was solved using molecular replacement with Phaser, using a truncated model of TREK-2[21] (PDB

bioRxiv preprint first posted online Jul. 19, 2019; doi: http://dx.doi.org/10.1101/706168. The copyright holder for this preprint (which was not peer-reviewed) is the author/funder, who has granted bioRxiv a license to display the preprint in perpetuity. It is made available under a CC-BY-ND 4.0 International license.

ID: 4BW5) with separate search models consisting of the TM domain and the cap. Two copies of the TASK-1 dimer were located in the asymmetric unit. An initial TASK-1 model was built using a density modified prime-and-switch map calculated using *phenix.autobuild*[44] as a guide and was improved by several rounds of manual model building and refinement in COOT[45]. Refinement was carried out in BUSTER version 2.10.3[46], using all data to 3.0 Å in the highest resolved direction, with NCS restraints and one TLS group per chain. Four potassium ions per homodimer were modelled and distances from the oxygen atoms in the filter were restrained to 2.8 Å. The final model for the native structure comprised residues Met1 to Asp257 in chains A and C, and Met1 to Leu261 in chains B and D. In the AB dimer, residues 149 to 151 are disordered and were not modelled. The selectivity filter of TASK-1 consists of residues $T^{93}IGY^{96}$ and $T^{199}IGF^{202}$ from each subunit, and they adopt the expected conformation seen in other K2P structures[18-22]. The carbonyl oxygens of these residues, as well as the sidechain oxygens of Thr93 and Thr199, coordinate four K^+ ions in sites S1-S4 (Fig. 1c,d, Extended Data Fig. 2a-d). However, there is weaker density for the S2 K^+ ion and it refines to have a higher B factor in all structures, compared to the three other K^+ ions. Omitting this K^+ ion altogether resulted in a positive Fo-Fc peak, so it was included in the model, with 100% occupancy and a higher B factor.

The structure contains a well-defined CHS molecule packed against the X-gate. It lies in an extensive, largely hydrophobic groove formed by residues Arg3, Arg7, Pro119, Val123, Val243, Phe246 and Met249. The two arginine residues are adjacent to the hemisuccinate moiety whereas the hydrophobic residues are adjacent to the cholesterol unit.

Data for the ligand complexes were processed in the same way as the native complex (Extended Data Table 1) to 2.9 Å and 3.1 Å for BAY 1000493 and BAY 2341237, respectively. After one round of refinement in BUSTER version 2.10.3[46], positive difference density was apparent in the vestibule. For BAY 1000493, an anomalous difference map was calculated in PHENIX[44], revealing two Br peaks per dimer. Since BAY 1000493 binds across the dimer axis below the selectivity filter, only one copy of the inhibitor is bound per TASK-1 dimer. In the case of BAY 1000493, the dimer is symmetrical, and the inhibitor binds in either orientation with a 50% probability, so the density in the pore is the average of the two possible orientations throughtout the crystal. However, each dimer has one molecule of BAY 1000493 bound and it only binds in one position, with the same interactions regardless of the orientation. In contrast, The Fo-Fc difference density map calculated with BAY 2341237 omitted from the structure, revealed a single conformation for the compound, which was modelled with 100% occupancy.

bioRxiv preprint first posted online Jul. 19, 2019; doi: http://dx.doi.org/10.1101/706168. The copyright holder for this preprint (which was not peer-reviewed) is the author/funder, who has granted bioRxiv a license to display the preprint in perpetuity. It is made available under a CC-BY-ND 4.0 International license.

This is the result of BAY 2341237 inducing some small degree of asymmetry into the dimer, resulting in the dimer/inhibitor complex packing in only one orientation in the crystal. The final models were refined against the anisotropically truncated STARANISO[43] data.

Two-electrode voltage-clamp measurements

X. laevis oocytes were obtained and the TEVC measurements were recorded as described previously[27]. Briefly, collected oocytes were stored at 18 °C in ND96 solution (in mM: NaCl 96, KCl 2, $CaCl_2$ 1.8, $MgCl_2$ 1, HEPES 5 and pH 7.5) supplemented with 50 mg/l gentamycin, 274 mg/l sodium pyruvate and 88 mg/l theophylline. Oocytes were injected with 5 ng of TASK-1 cRNA and incubated for 48 h at 18 °C. ND96 was used as recording solution. Oocytes were held at -80 mV and voltage was ramped from -120 to +45 mV within 3.5 s, using a sweep time interval of 4 s. Block was analysed with voltage steps from a holding potential of -80 mV. A first test pulse to 0 mV of 1 s duration was followed by a repolarising step to -80 mV for 1 s, directly followed by another 1 s test pulse to +40 mV. The sweep time interval was 10 s. All inhibitors were dissolved in DMSO, aliquoted, stored at -20 °C or room temperature and added to the external solution (ND96) just before the recordings. The EC_{50} was determined from Hill plots using four concentrations for each construct. Final DMSO concentration of 0.1 % was not exceed.

For measurements of the TASK-1$^{Met1\text{-}Glu259}$ currents shown in the Extended Data Fig. 1 oocytes were injected with 1 ng of Task-1 RNA and two electrode voltage clamp experiments performed with a Warner oocyte-clamp (OC-725-C). Data were digitalised with an Digidata1400A interface (Molecular Devices). Voltage-ramp protocols were used to measure IV-responses. The ramps lasted for 0.5 s with ranges of -120 mV to 50 mV. In each experimental condition 10 ramps were recorded with the last 5 sweeps of such a series averaged and used for analysis. Voltage-clamp recordings were performed in ND96 solution adjusted to the desired pH at room temperature with NaOH. For experiments at pH 5.5, HEPES was exchanged for MES.

Chemiluminescence assay in *X. laevis* oocytes

Surface expression of TASK-1 channel constructs was studied as previously described[47]. Briefly, *X. laevis* oocytes were injected with cRNA of HA-tagged channels. After 48h, oocytes were incubated in ND96 plus 1 % BSA on ice for 30 min to reduce unspecific antibody binding. Subsequently, the oocytes were incubated with primary antibody (rat anti-HA (Roche), 1:100) for 1 h, and after extensive washing they were incubated with secondary

bioRxiv preprint first posted online Jul. 19, 2019; doi: http://dx.doi.org/10.1101/706168. The copyright holder for this preprint (which was not peer-reviewed) is the author/funder, who has granted bioRxiv a license to display the preprint in perpetuity. It is made available under a CC-BY-ND 4.0 International license.

antibody (goat anti-rat-IgG, HRP-coupled (Dianova), 1:500) for 1 h. After oocytes were individually placed into a vial with 20 µl of luminescence substrate (SuperSignal Femto (Thermo Scientific)), light emission was detected with a GloMax luminometer (Promega).

Single channel measurements

Inside-out single channel patch clamp recordings of *Xenopus* oocytes were performed similar as previously described[31]. Briefly, all experiments were conducted at room temperature with a bath solution containing in mM: KCl 140, HEPES 5, EGTA 1 and pH 7.4. Single channel current recordings were executed with an Axopatch 200B amplifier (Axon Instruments), a Digidata 1550B A/D converter (Axon Instruments) and pClamp10 software (Axon Instruments). The sampling rate was 15 kHz with the analog filter set to 2 kHz. Voltage pulses were applied from 0 mV (holding potential) to +140 mV and/or -140 mV for 1 s with an interpulse interval of 8 s. Data were analysed with ClampFit10 and Origin 2016 (OriginLab Corporation).

Quantification and statistical analysis

Quantification and the statistical analysis of the data were executed as previously described[48]. Briefly, normality and variance of every dataset was tested. A paired or unpaired Student´s t-test was used to probe the significance but for not normally distributed data, a non-parametric Mann-Whitney U-test and a Wilcoxon signed-rank test for paired analyses was used, respectively. In case of different variances, significance was probed with Welch's t-test and for not normally distributed data with Mood's median test. All data are presented as mean ± s.e.m. and all experiments were repeated from N = 2 - 5 different batches (biological replicates). The number of experiments (n) as technical replicates are indicated in the subpanels of the Figures. Significances are indicated with *, $P < 0.05$; **, $P < 0.01$; ***, $P < 0.001$ in the Figures.

Synthesis of TASK-1 inhibitors BAY 1000493 and BAY 2341237

The synthesis of BAY 1000493 and BAY 2341237 are described in patent number WO2017097792A1 and in the supplementary methods file.

bioRxiv preprint first posted online Jul. 19, 2019; doi: http://dx.doi.org/10.1101/706168. The copyright holder for this preprint (which was not peer-reviewed) is the author/funder, who has granted bioRxiv a license to display the preprint in perpetuity. It is made available under a CC-BY-ND 4.0 International license.

References

1 Bayliss, D. A. *et al.* TASK-1 is a highly modulated pH-sensitive 'leak' K^+ channel expressed in brainstem respiratory neurons. *Respir. Physiol.* **129**, 159-174 (2001).

2 Karschin, C. *et al.* Expression pattern in brain of TASK-1, TASK-3, and a tandem pore domain K(+) channel subunit, TASK-5, associated with the central auditory nervous system. *Mol. Cell Neurosci.* **18**, 632-648 (2001).

3 Jones, S. A. *et al.* Expression of TASK-1, a pH-sensitive twin-pore domain K^+ channel, in rat myocytes. *Am. J. Physiol. Heart Circ. Physiol.* **283**, H181-185 (2002).

4 Donner, B. C. *et al.* Functional role of TASK-1 in the heart: studies in TASK-1-deficient mice show prolonged cardiac repolarization and reduced heart rate variability. *Basic Res. Cardiol.* **106**, 75-87 (2011).

5 Decher, N. *et al.* Knock-out of the potassium channel TASK-1 leads to a prolonged QT interval and a disturbed QRS complex. *Cell Physiol. Biochem.* **28**, 77-86 (2011).

6 Olschewski, A. *et al.* Impact of TASK-1 in human pulmonary artery smooth muscle cells. *Circ. Res.* **98**, 1072-1080 (2006).

7 Putzke, C. *et al.* The acid-sensitive potassium channel TASK-1 in rat cardiac muscle. *Cardiovasc. Res.* **75**, 59-68 (2007).

8 Gurney, A. M. *et al.* Two-pore domain K channel, TASK-1, in pulmonary artery smooth muscle cells. *Circ. Res.* **93**, 957-964 (2003).

9 Steinberg, E. A. *et al.* The role of K_{2P} channels in anaesthesia and sleep. *Pflugers Arch.* **467**, 907-916 (2015).

10 Putzke, C. *et al.* Differential effects of volatile and intravenous anesthetics on the activity of human TASK-1. *Am. J. Physiol. Cell Physiol.* **293**, C1319-1326 (2007).

11 Patel, A. J. *et al.* Inhalational anesthetics activate two-pore-domain background K^+ channels. *Nat. Neurosci.* **2**, 422-426 (1999).

12 Sirois, J. E. *et al.* The TASK-1 two-pore domain K^+ channel is a molecular substrate for neuronal effects of inhalation anesthetics. *J. Neurosci.* **20**, 6347-6354 (2000).

13 Enyedi, P. & Czirjak, G. Molecular background of leak K+ currents: two-pore domain potassium channels. *Physiol. Rev.* **90**, 559-605 (2010).

bioRxiv preprint first posted online Jul. 19, 2019; doi: http://dx.doi.org/10.1101/706168. The copyright holder for this preprint (which was not peer-reviewed) is the author/funder, who has granted bioRxiv a license to display the preprint in perpetuity. It is made available under a CC-BY-ND 4.0 International license.

14 Renigunta, V. *et al.* Much more than a leak: structure and function of K_{2P}-channels. *Pflugers Arch.* **467**, 867-894 (2015).

15 Kiper, A. K. *et al.* Kv1.5 blockers preferentially inhibit TASK-1 channels: TASK-1 as a target against atrial fibrillation and obstructive sleep apnea? *Pflugers Arch.* **467**, 1081-1090 (2015).

16 Talley, E. M. & Bayliss, D. A. Modulation of TASK-1 (Kcnk3) and TASK-3 (Kcnk9) potassium channels: volatile anesthetics and neurotransmitters share a molecular site of action. *J. Biol. Chem.* **277**, 17733-17742 (2002).

17 Sitsel, O. *et al.* Crystallization of P-type ATPases by the High Lipid-Detergent (HiLiDe) Method. *Methods Mol. Biol.* **1377**, 413-420 (2016).

18 Miller, A. N. & Long, S. B. Crystal structure of the human two-pore domain potassium channel K2P1. *Science* **335**, 432-436 (2012).

19 Brohawn, S. G. *et al.* Crystal structure of the human K2P TRAAK, a lipid- and mechano-sensitive K^+ ion channel. *Science* **335**, 436-441 (2012).

20 Brohawn, S. G. *et al.* Domain-swapped chain connectivity and gated membrane access in a F_{ab}-mediated crystal of the human TRAAK K+ channel. *Proc. Natl Acad. Sci. U S A* **110**, 2129-2134 (2013).

21 Dong, Y. Y. *et al.* K2P channel gating mechanisms revealed by structures of TREK-2 and a complex with Prozac. *Science* **347**, 1256-1259 (2015).

22 Lolicato, M. *et al.* K2P2.1 (TREK-1)-activator complexes reveal a cryptic selectivity filter binding site. *Nature* **547**, 364-368 (2017).

23 Duprat, F. *et al.* TASK, a human background K^+ channel to sense external pH variations near physiological pH. *EMBO J.* **16**, 5464-5471 (1997).

24 Morton, M. J. *et al.* Determinants of pH sensing in the two-pore domain K^+ channels TASK-1 and -2. *Pflugers Arch.* **445**, 577-583 (2003).

25 Stansfeld, P. J. *et al.* Insight into the mechanism of inactivation and pH sensitivity in potassium channels from molecular dynamics simulations. *Biochem.* **47**, 7414-7422 (2008).

26 Goldstein, M. *et al.* Functional mutagenesis screens reveal the 'cap structure' formation in disulfide-bridge free TASK channels. *Scientific Reports* **6**, 19492 (2016).

bioRxiv preprint first posted online Jul. 19, 2019; doi: http://dx.doi.org/10.1101/706168. The copyright holder for this preprint (which was not peer-reviewed) is the author/funder, who has granted bioRxiv a license to display the preprint in perpetuity. It is made available under a CC-BY-ND 4.0 International license.

27 Streit, A. K. *et al.* A specific two-pore domain potassium channel blocker defines the structure of the TASK-1 open pore. *J. Biol. Chem.* **286**, 13977-13984 (2011).

28 Wilke, B. U. *et al.* Diacylglycerol mediates regulation of TASK potassium channels by Gq-coupled receptors. *Nat. Commun.* **5**, 5540 (2014).

29 Lopes, C. M. *et al.* PIP2 hydrolysis underlies agonist-induced inhibition and regulates voltage gating of two-pore domain K^+ channels. *J. Physiol.* **564**, 117-129 (2005).

30 Piechotta, P. L. *et al.* The pore structure and gating mechanism of K2P channels. *EMBO J.* **30**, 3607-3619 (2011).

31 Rinne, S. *et al.* TASK-1 and TASK-3 may form heterodimers in human atrial cardiomyocytes. *J. Mol. Cell Cardiol.* **81**, 71-80 (2015).

32 Chokshi, R. H. *et al.* Breathing Stimulant Compounds Inhibit TASK-3 Potassium Channel Function Likely by Binding at a Common Site in the Channel Pore. *Mol. Pharmacol.* **88**, 926-934 (2015).

33 Ma, L. *et al.* A novel channelopathy in pulmonary arterial hypertension. *N. Engl. J. Med.* **369**, 351-361 (2013).

34 Barel, O. *et al.* Maternally inherited Birk Barel mental retardation dysmorphism syndrome caused by a mutation in the genomically imprinted potassium channel KCNK9. *Am. J. Hum. Genet.* **83**, 193-199 (2008).

35 Sediva, M. *et al.* Novel variant in the KCNK9 gene in a girl with Birk Barel syndrome. *Eur. J. Med. Genet.* (2019).

36 Armstrong, C. M. Interaction of tetraethylammonium ion derivatives with the potassium channels of giant axons. *J. Gen. Physiol.* **58**, 413-437 (1971).

37 Bolshakov, K. V. *et al.* Determinants of trapping block of N-methyl-d-aspartate receptor channels. *J. Neurochem.* **87**, 56-65 (2003).

38 Linder, T. *et al.* Structural insights into trapping and dissociation of small molecules in K^+ channels. *J. Chem. Inf. Model.* **54**, 3218-3228 (2014).

39 Linder, T. *et al.* Drug trapping in hERG K^+ channels: (not) a matter of drug size? *Medchemcomm.* **7**, 512-518 (2016).

40 Kabsch, W. Xds. *Acta Crystallogr. D* **66**, 125-132 (2010).

41 Evans, P. Scaling and assessment of data quality. *Acta Crystallogr. D* **62**, 72-82 (2006).

bioRxiv preprint first posted online Jul. 19, 2019; doi: http://dx.doi.org/10.1101/706168. The copyright holder for this preprint (which was not peer-reviewed) is the author/funder, who has granted bioRxiv a license to display the preprint in perpetuity. It is made available under a CC-BY-ND 4.0 International license.

42 Winn, M. D. *et al.* Overview of the CCP4 suite and current developments. *Acta Crystallogr. D.* **67**, 235-242 (2011).

43 Tickle, I. J. *et al.* STARANISO (http://staraniso.globalphasing.org/cgi-bin/staraniso.cgi). *Cambridge, United Kingdom: Global Phasing Ltd.* (2018).

44 Adams, P. D. *et al.* PHENIX: a comprehensive Python-based system for macromolecular structure solution. *Acta Crystallogr. D.* **66**, 213-221 (2010).

45 Emsley, P. *et al.* Features and development of Coot. *Acta Crystallogr. D* **66**, 486-501 (2010).

46 BUSTER version 2.10.0 (Global Phasing Ltd, Cambridge, UK, 2011).

47 Zuzarte, M. *et al.* Intracellular traffic of the K+ channels TASK-1 and TASK-3: role of N- and C-terminal sorting signals and interaction with 14-3-3 proteins. *J. Physiol.* **587**, 929-952 (2009).

48 Rinne, S. *et al.* The molecular basis for an allosteric inhibition of K^+-flux gating in K2P channels. *Elife* **8** (2019).

49 Klesse, G. *et al.* CHAP: a versatile tool for the structural and functional annotation of ion channel pores. *bioRxiv*, 527275 (2019).

Acknowledgements

K.E.J.R. and D.S. are supported by B.B.S.R.C grant no BB/N009274/1. K.E.J.R., A.C.W.P., D.S., S.M.M.M., N.B.-B., E.P.C. are members of the SGC, a registered charity (number 1097737) that receives funds from AbbVie, Bayer Pharma AG, Boehringer Ingelheim, the Canada Foundation for Innovation, Genome Canada, Janssen, Merck KGaA, Merck & Co., Novartis, the Ontario Ministry of Economic Development and Innovation, Pfizer, São Paulo Research Foundation-FAPESP and Takeda, as well as the Innovative Medicines Initiative Joint Undertaking ULTRA-DD grant 115766 and the Wellcome Trust (106169/Z/14/Z). L.C. is supported by the Wellcome Trust (OXION grant No: WT084655MA). N.D. is supported by Deutsche Forschungsgemeinschaft (DFG) grant DE1482-4/1.

We thank Diamond Light Source Ltd for access to the macromolecular crystallography beamlines and we thank the Diamond Light Source staff for their help with data collection. We thank all members of the SGC Biotech team, including Shayla Venkaya, Claire Strain-Damerell; Kasia Kupinska, Dong Wang and Katie Ellis. We thank all members of the SGC IMP1 group, including Yin Yao Dong. We thank David Eberhardt for help with the

bioRxiv preprint first posted online Jul. 19, 2019; doi: http://dx.doi.org/10.1101/706168. The copyright holder for this preprint (which was not peer-reviewed) is the author/funder, who has granted bioRxiv a license to display the preprint in perpetuity. It is made available under a CC-BY-ND 4.0 International license.

electrophysiology experiments. We are grateful to Rod Chalk, Tiago Moreira, Georgina Berridge and Octawia Borkowska for help with mass spectrometry and Brian Marsden and David Damerell, James Bray, James Crowe and Chris Sluman for bioinformatics support. We thank Frank von Delft, Tobias Krojer and Beth MacLean for assistance with crystallography infrastructure. We thank Oxana Nowak for technical assistance. We thank Thomas Baukrowitz (Christian Albrechts University of Kiel, Kiel, Germany) for critical reading of the manuscript.

Author Contributions

The project was conceived and managed by E.P.C., N.D. and T.M.. K.E.J.R., obtained crystals that diffracted to beyond 4 Å resolution, collected data and solved the structure of TASK-1 and the complexes with drug molecules, assisted by D.S., and supervised by A.C.W.P. and E.P.C.. W.Z. was involved in optimization of the constructs, protein purification and production of initial crystals, supervised by A.Q. and E.P.C.. A.K.K. performed voltage clamp recordings, pharmacological experiments and single channel recordings and S.R. performed voltage clamp recordings, introduced all TASK-1 mutants and performed ELISA surface expression assays, M.G. performed all experiments with sevoflurane, all experiments were supervised by N.D.. Initial constructs for structural biology were screened for expression by L.S. and large scale insect cell expressions were produced by S.M.M.M., supervised by N.B.B.. Initial tests of the relative activities of TASK-1 and the crystal construct were performed by L.J.C., supervised by S.J.T.. The TASK-1 inhibitors were designed and produced by M.D., M.H., H.M and T.M., supervised by T.M.. Data were analyzed and the paper was written by K.E.J.R., A.C.W.P., A.K.K., S.R., L.C., S.J.T., T.M., N.D. and E.P.C..

Author Information

M.D. M.H., H.M., T.M., are inventors on patent no. WO2017097792A1, Priority date 10 December, 2018, entitled “2-phenyl-3-(piperazinomethyl)imidazo[1,2-a]pyridine derivatives as blockers of TASK-1 and TASK-3 channels, for the treatment of sleep-related breathing disorders”. The other authors declare no competing interests. They were not involved in the development of the compounds described in this patent and will not benefit from the patent.

Correspondence and requests for materials should be addressed to N.D. (decher@staff.uni-marburg.de) and E.P.C. (liz.carpenter@sgc.ox.ac.uk).

bioRxiv preprint first posted online Jul. 19, 2019; doi: http://dx.doi.org/10.1101/706168. The copyright holder for this preprint (which was not peer-reviewed) is the author/funder, who has granted bioRxiv a license to display the preprint in perpetuity. It is made available under a CC-BY-ND 4.0 International license.

Figures

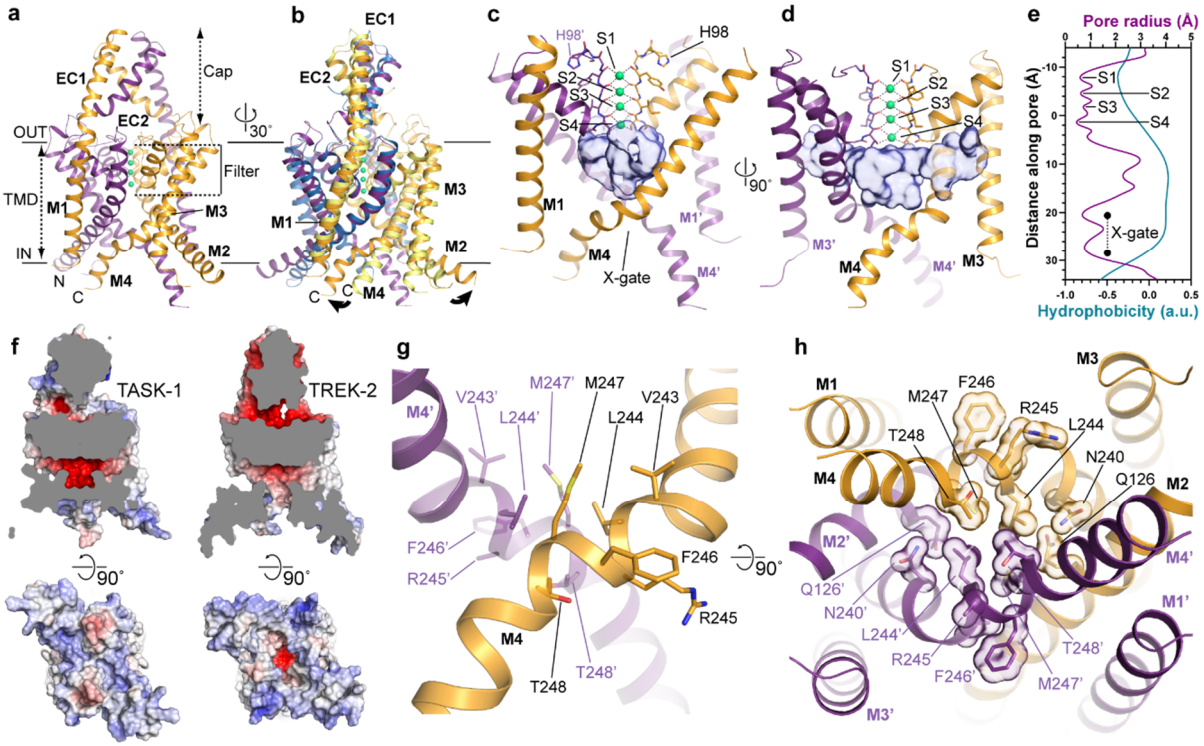


Fig. 1. **The structure of TASK-1 reveals a unique crossed helix X-gate. a,** Cartoon of the TASK-1 structure, with chain A (gold), B (purple) and potassium ions (green), viewed from the membrane plane. **b,** Superposition of the TASK-1 and TREK-2 (yellow and blue) "down" state (PDB: 4XDJ) structures. The TASK-1 structure with the X-gate enclosing the vestibule and fenestrations (depicted with semi-transparent surfaces), **c,** viewed from the membrane plane and **d,** rotated 90°. **e,** Radius and hydrophobicity of the TASK-1 pore (CHAP[49]). **f,** Electrostatic surfaces of TASK-1 and TREK-2 (PDB: 4XDJ) shown as a cross section perpendicular to membrane and seen from below. The X-gate viewed from **g,** the plane of the membrane and **h,** below the membrane.

bioRxiv preprint first posted online Jul. 19, 2019; doi: http://dx.doi.org/10.1101/706168. The copyright holder for this preprint (which was not peer-reviewed) is the author/funder, who has granted bioRxiv a license to display the preprint in perpetuity. It is made available under a CC-BY-ND 4.0 International license.

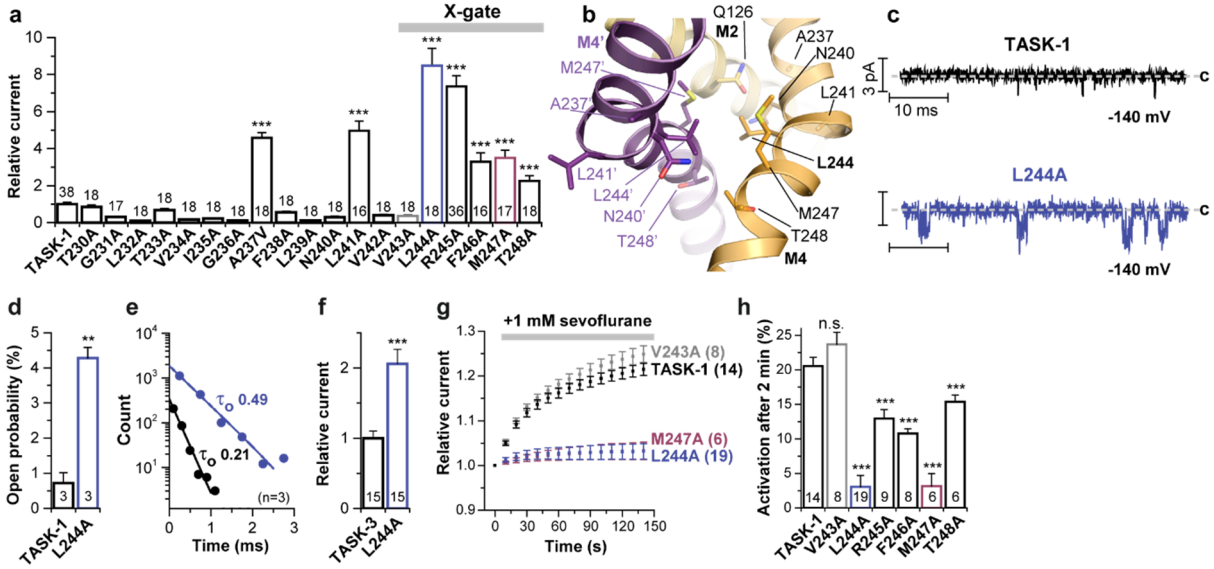


Fig. 2. **Mutation of X-gate residues results in an increase in ion conduction and loss of anaesthetic activation. a,** Relative current amplitudes of wild-type and mutated TASK-1. **b,** The X-gate viewed from the membrane plane, rotated 90^{o} relative to Fig. 1g showing Leu244 and surrounding residues. **c,** Representative inside-out single channel recordings of TASK-1 wild-type and Leu244Ala. Analysis of **d,** the open probability and **e,** the mean open times. **f,** Relative current amplitudes of wild-type TASK-3 and Leu244Ala. **g,** Application of 1 mM sevoflurane to wild-type and mutated TASK-1 and **h,** analysis 2 minutes after application. All two-electrode voltage-clamp recordings and single channel measurements in Fig. 2-4 were performed in *X. laevis* oocytes. The number of experiments performed are illustrated in the respective graphs. Panels **a,d,f,g,h** data are presented as mean ± s.e.m..

bioRxiv preprint first posted online Jul. 19, 2019; doi: http://dx.doi.org/10.1101/706168. The copyright holder for this preprint (which was not peer-reviewed) is the author/funder, who has granted bioRxiv a license to display the preprint in perpetuity. It is made available under a CC-BY-ND 4.0 International license.

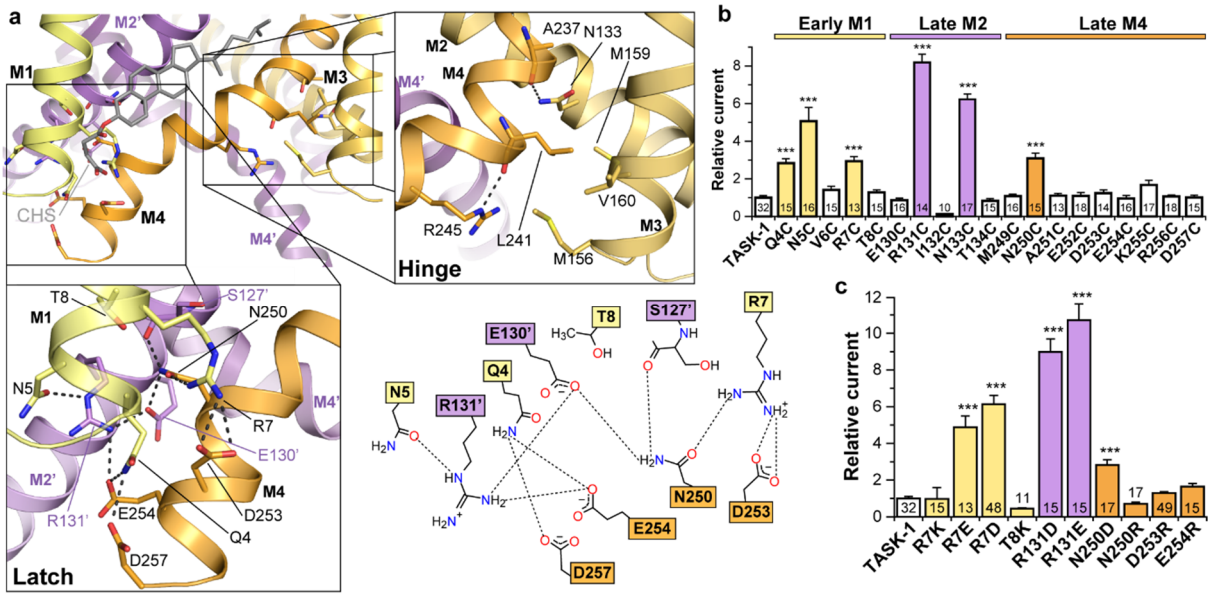


Fig. 3. **The X-gate environment includes a hinge and a latch on either side of the vestibule which are required for X-gate integrity. a,** The X-gate in TASK-1, with the cholesteryl hemisuccinate (CHS) binding site. The hinge is shown on the right and the latch region below. **b,** Relative current amplitudes of wild-type and mutated TASK-1. **c,** Relative current amplitudes for mutated residues in the latch. **b, c**, Data are presented as mean ± s.e.m..

bioRxiv preprint first posted online Jul. 19, 2019; doi: http://dx.doi.org/10.1101/706168. The copyright holder for this preprint (which was not peer-reviewed) is the author/funder, who has granted bioRxiv a license to display the preprint in perpetuity. It is made available under a CC-BY-ND 4.0 International license.

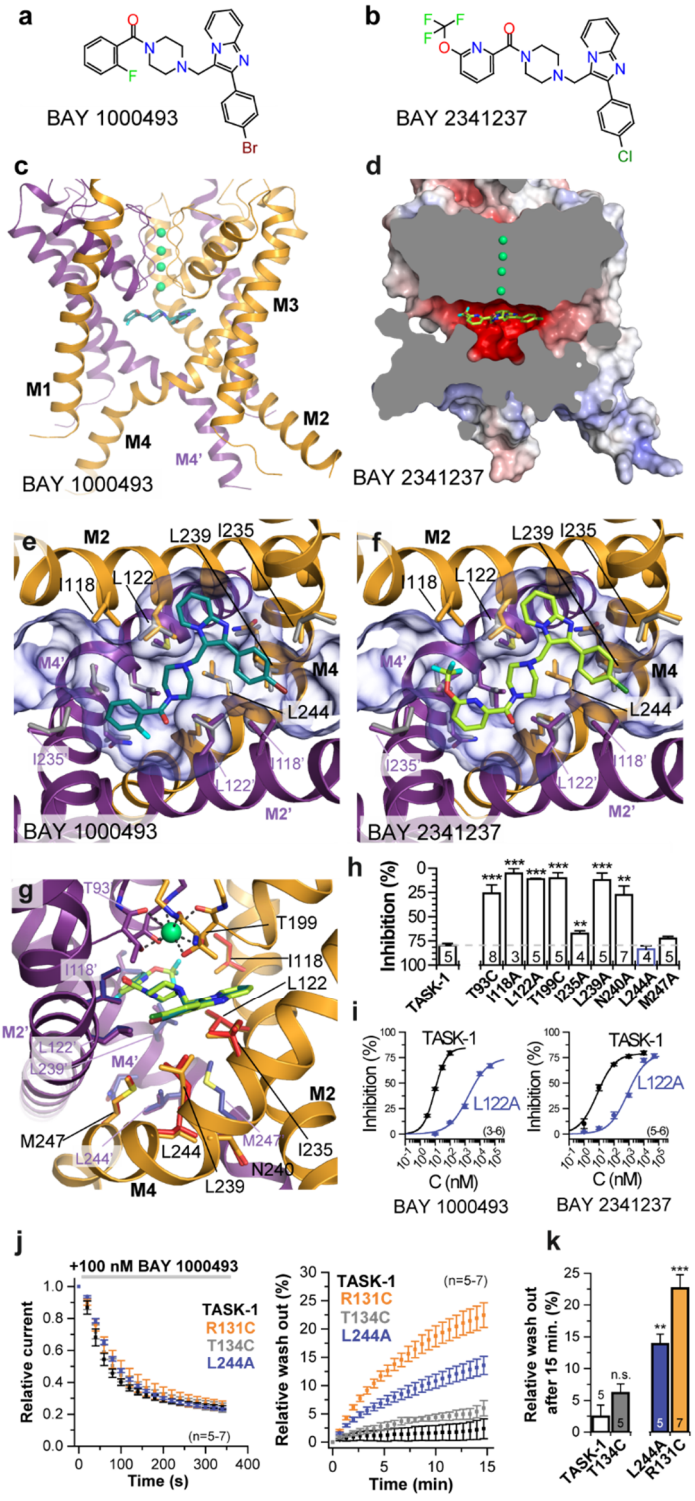


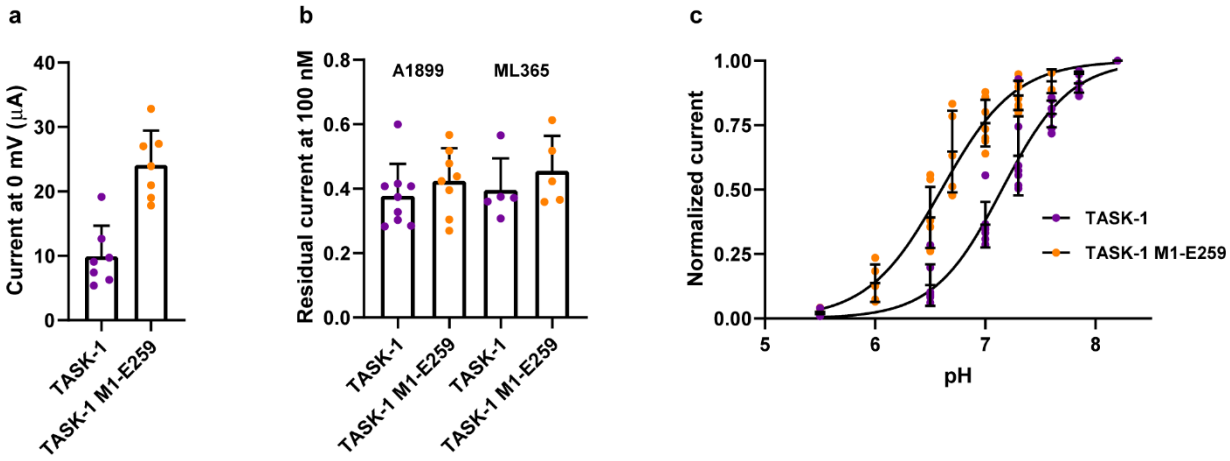
Fig. 4. **Structures of complexes with two highly potent inhibitors show binding in the vestibule, trapped by the X-gate.** Chemical structures of **a,** BAY 1000493 ((4-{[2-(4-bromophenyl)imidazo[1,2-a]pyridin-3-yl]methyl}vpiperazin-1-yl)(2-fluorophenyl)methanone) and **b,** BAY 2341237 (4-{[2-(4-chlorophenyl)imidazo[1,2-a]pyridin-3-yl]methyl} piperazin-1-yl)[6-(trifluoromethoxy) pyridin-2-yl]methanone. **c,** Structure of the TASK-1/BAY 1000493 (teal) complex (M2' excluded). For simplicity, only

bioRxiv preprint first posted online Jul. 19, 2019; doi: http://dx.doi.org/10.1101/706168. The copyright holder for this preprint (which was not peer-reviewed) is the author/funder, who has granted bioRxiv a license to display the preprint in perpetuity. It is made available under a CC-BY-ND 4.0 International license.

one orientation of BAY 1000493 is shown, although it binds to the dimer equally well in either orientation (see Extended Data Fig. 6a). **d,** Cross section of an electrostatic surface of the TASK-1/BAY 2341237 (green) complex. **e,** The BAY 1000493 and **f,** BAY 2341237 binding sites below the selectivity filter, looking towards the X-gate and **g,** superposition of the two complexes seen from the membrane plane with sidechains from the BAY 2341237 complex in red and blue. **h,** Percentage of inhibition of wild-type and mutated TASK-1 by 100 nM BAY 1000493. **i,** Dose-response curves for BAY 1000493 and BAY 2341237 for wild-type TASK-1 and Leu122Ala. **j,** Analysis of relative current amplitudes over time while washing BAY 1000493 in and out. **k,** Analysis of the relative wash-out. Data in **h,i,j,k**, are presented as mean ± s.e.m..

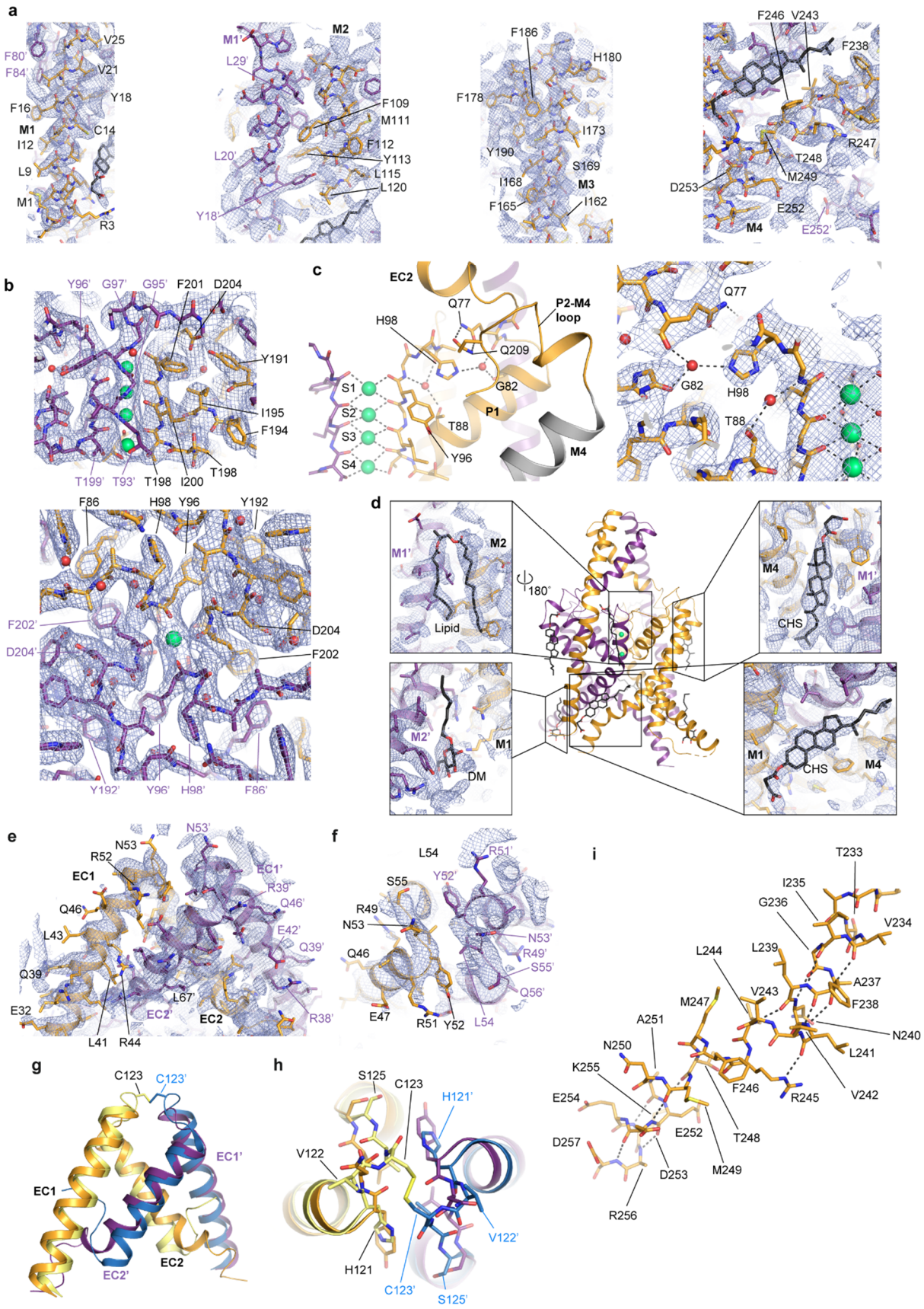
bioRxiv preprint first posted online Jul. 19, 2019; doi: http://dx.doi.org/10.1101/706168. The copyright holder for this preprint (which was not peer-reviewed) is the author/funder, who has granted bioRxiv a license to display the preprint in perpetuity. It is made available under a CC-BY-ND 4.0 International license.

Extended Data Figures



Extended Data Fig. 1. The crystallisation construct TASK-1$^{M1\text{-}E259}$ has similar channel properties to WT protein. a, Whole-cell TASK-1 wild-type and TASK-1$^{M1\text{-}E259}$ currents recorded after expression in *Xenopus* oocytes showing that the crystallisation construct is functionally active. **b,** The truncated crystallisation construct TASK-1$^{M1\text{-}E259}$ retains normal inhibition by the pore-blockers A1899 and ML365. **c,** The crystallisation construct retains sensitivity to changes in extracellular pH. The small change in half maximal activation from pH 7.2 to pH 6.4 suggests the truncated cytoplasmic region may influence this process. But overall, the truncated construct exhibits a similar pharmacology and regulation to the wild-type channel. Data are presented as mean ± s.e.m. and shown as individual points.

bioRxiv preprint first posted online Jul. 19, 2019; doi: http://dx.doi.org/10.1101/706168. The copyright holder for this preprint (which was not peer-reviewed) is the author/funder, who has granted bioRxiv a license to display the preprint in perpetuity. It is made available under a CC-BY-ND 4.0 International license.

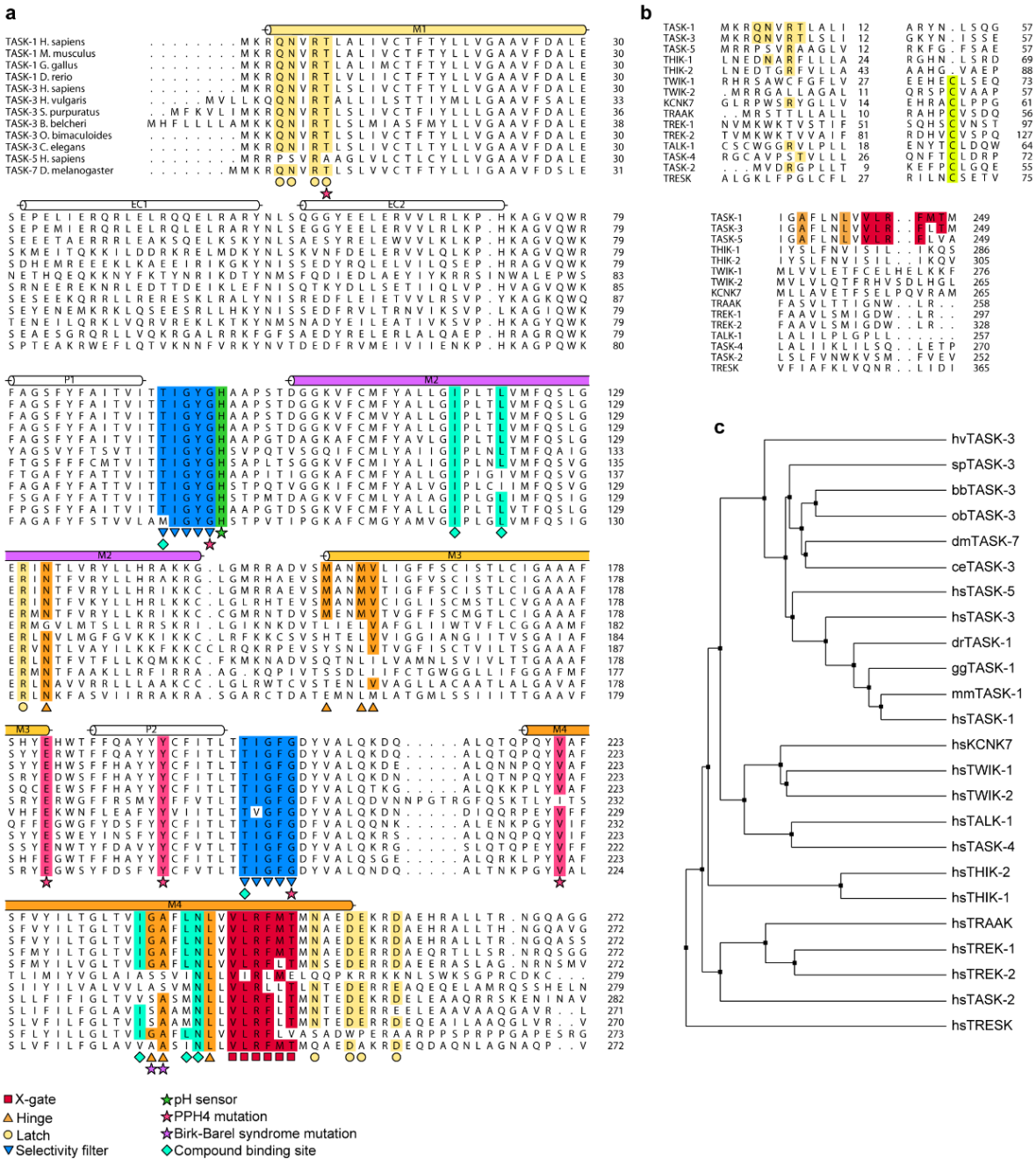


Extended Data Fig. 2. The structure of TASK-1 at 3.1 Å resolution indicates that the cap in TASK-1 forms the classic cap domain structure without an intramolecular disulphide

bioRxiv preprint first posted online Jul. 19, 2019; doi: http://dx.doi.org/10.1101/706168. The copyright holder for this preprint (which was not peer-reviewed) is the author/funder, who has granted bioRxiv a license to display the preprint in perpetuity. It is made available under a CC-BY-ND 4.0 International license.

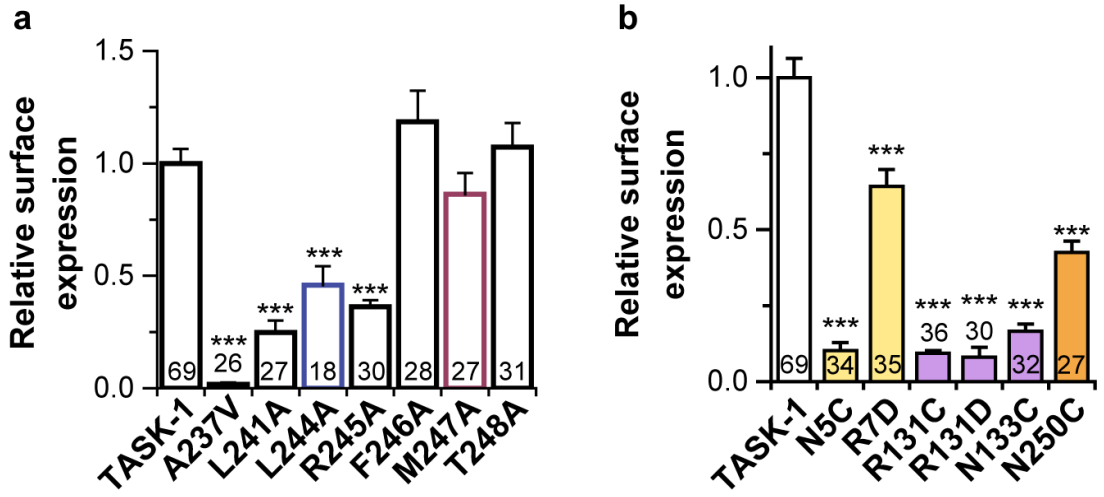
bond. a, Final BUSTER 2Fo-Fc electron density maps contoured at 1.0σ, showing the M1-M4 helices. **b,** The selectivity filter with 2Fo-Fc maps shown from the plane of the membrane and from above the membrane. **c,** The pH sensor residue, His98, the surrounding residues and the pore, with the K^+ ions shown in green, shown both without the map (left) and with the 2Fo-Fc map shown in blue (right). **d,** Cartoon representation of the TASK-1 structure, with lipids, detergents and CHS shown as ball and stick, with zoomed views of the binding sites. **e,** 2Fo-Fc electron density maps of the TASK-1 cap and **f,** view of the cap apex. **g,** superposition of the TASK-1 cap (gold and purple) and TREK-2 (PDB: 4XDJ) cap (yellow and blue), illustrating lack of disulphide bond in TASK-1 and **h,** view of the aligned cap apices. **i**, The M4 helix residues 233-257 represented as sticks, with the main chain hydrogen bonding pattern shown as dashed lines.

bioRxiv preprint first posted online Jul. 19, 2019; doi: http://dx.doi.org/10.1101/706168. The copyright holder for this preprint (which was not peer-reviewed) is the author/funder, who has granted bioRxiv a license to display the preprint in perpetuity. It is made available under a CC-BY-ND 4.0 International license.



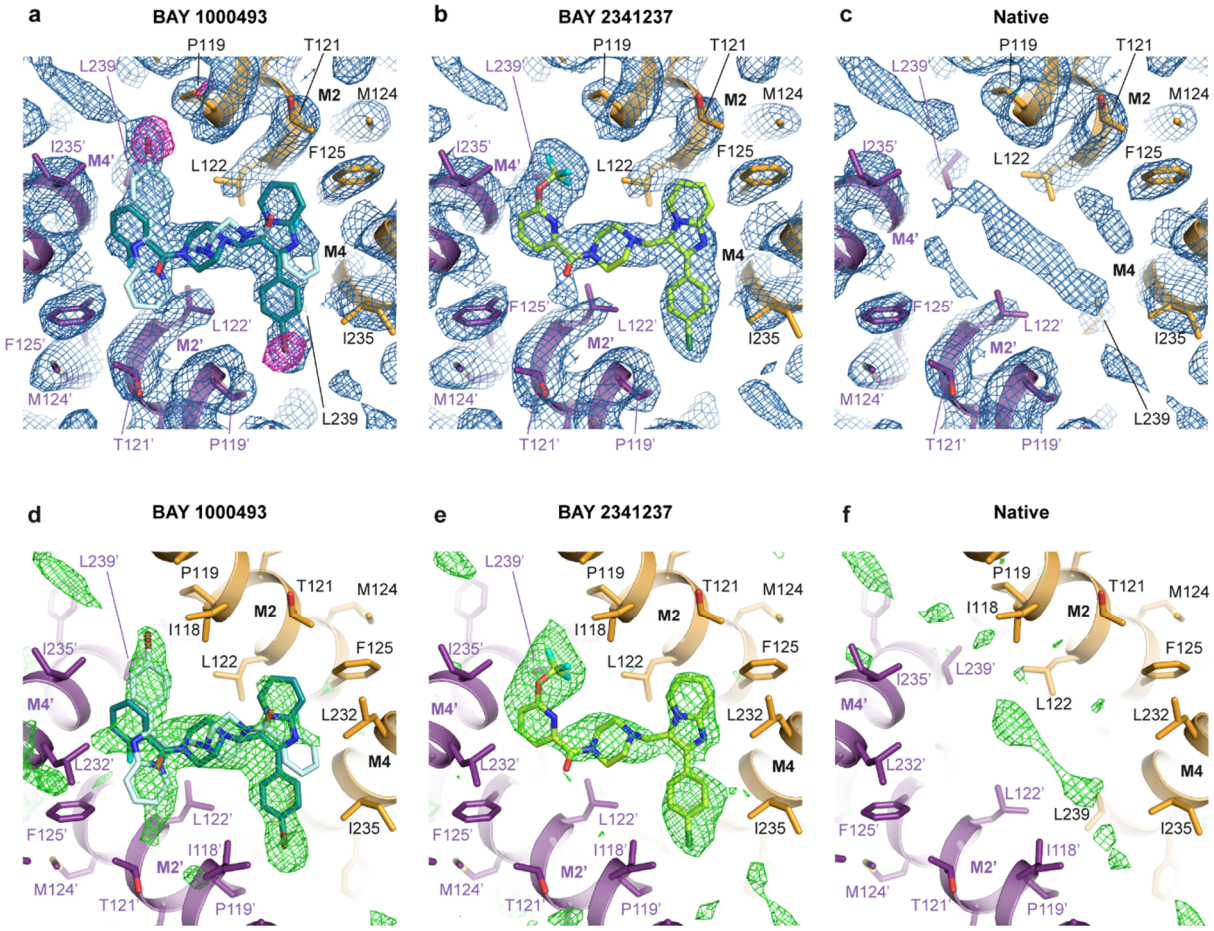
Extended Data Fig. 3. Alignment and phylogenetic trees for the TASKs and K_{2P} channels reveal conservation of X-gate residues in TASK-1, 3 and 5, and a lack of an X-gate in other K_{2P} channels. a, Sequence alignment of TASK channels from different species. **b,** Alignment of the human K_{2P} proximal M1, cap and distal M4 regions. The cysteine residue in the cap apex is highlighted in yellow and the X-gate residues in red. **c,** Phylogenetic tree of the human K_{2P}s and the TASK channels in **a**. The TASK-1, -3 and -5 channels are highly conserved, whereas the K_{2P} channels that were originally designated at TASK-2 and TASK-4/TALK-2 have much lower homology and belong in the subfamily of TALK channels.

bioRxiv preprint first posted online Jul. 19, 2019; doi: http://dx.doi.org/10.1101/706168. The copyright holder for this preprint (which was not peer-reviewed) is the author/funder, who has granted bioRxiv a license to display the preprint in perpetuity. It is made available under a CC-BY-ND 4.0 International license.



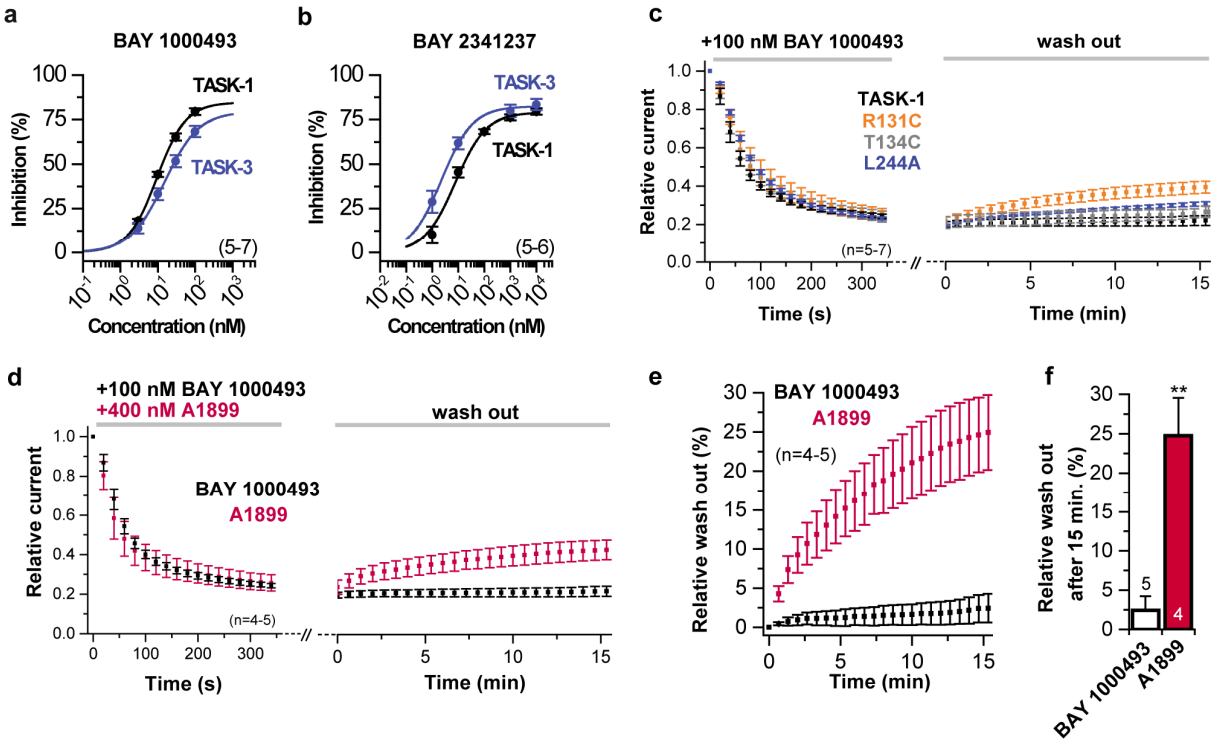
Extended Data Fig. 4. Relative surface expression levels for TASK-1 mutants. a, Relative surface expression of wild-type TASK-1 and TASK-1 channels with mutations in the X-gate. **b,** Relative surface expression of wild-type TASK-1 and TASK-1 mutations in the latch region. All data were recorded in *X. laevis* oocytes. Numbers on plots indicate the number of repeats per data point. Data are presented as mean ± s.e.m..

bioRxiv preprint first posted online Jul. 19, 2019; doi: http://dx.doi.org/10.1101/706168. The copyright holder for this preprint (which was not peer-reviewed) is the author/funder, who has granted bioRxiv a license to display the preprint in perpetuity. It is made available under a CC-BY-ND 4.0 International license.



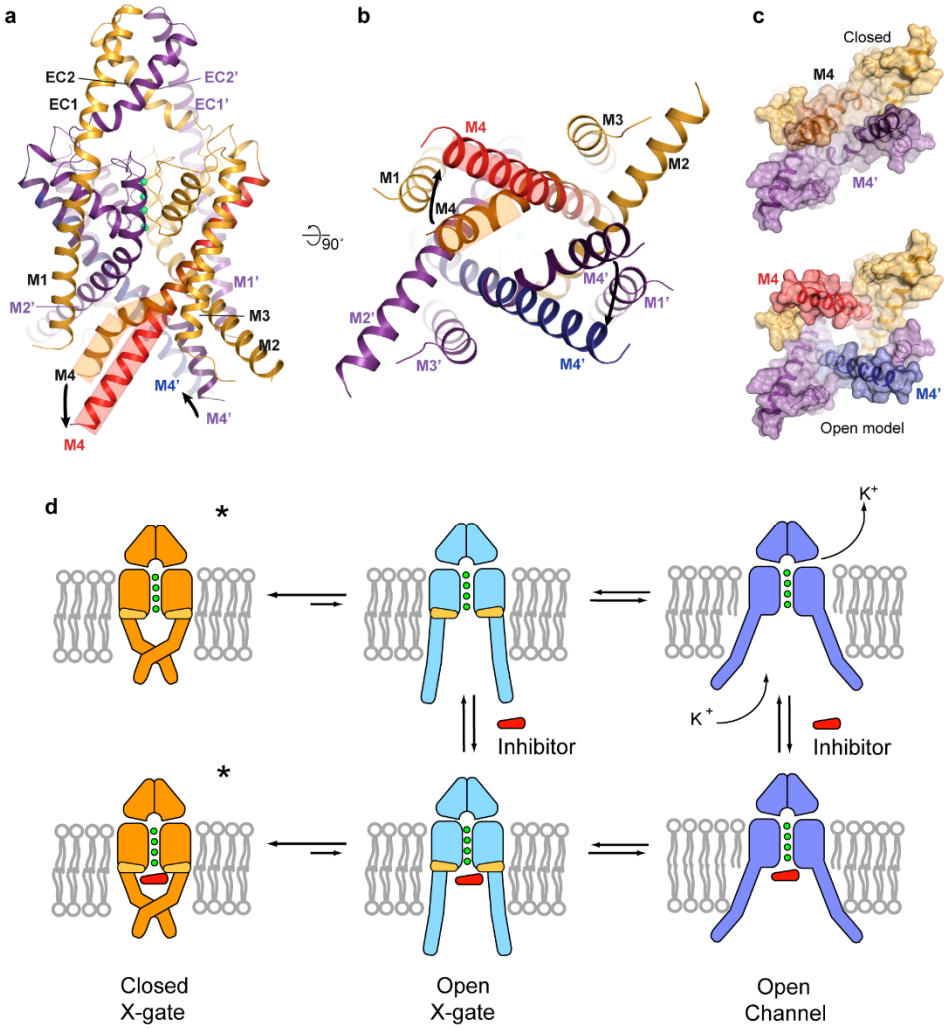
Extended Data Fig. 5. Structures, electron density maps and bromine anomalous data for TASK-1 in complex with BAY 1000493 or BAY 2341237. a, The TASK-1/BAY 1000493 complex structure, shown from the selectivity filter, looking towards the vestibule, with the 2Fo-Fc map shown in blue and the anomalous difference map at 3.3 Å collected at the Br edge shown in magenta. The two 50% occupancy BAY 1000493 molecules are shown with carbons coloured teal or light blue, oxygens in red, nitrogens in dark blue, fluorines in cyan and bromines in maroon. **b,** The TASK-1/BAY 2341237 complex structure, shown as for a, with the 2Fo-Fc map shown in blue. The single 100% occupancy BAY 1000493 molecule is shown with carbons coloured green, oxygens in red, nitrogens in dark blue, fluorines in cyan and chlorines in dark green. **c,** The TASK-1 native structure, shown as for a, with the 2Fo-Fc map shown in blue. There is some residual density below the selectivity filter, as is seen in many K2P structures. This type of density is sometimes interpreted as lipid aliphatic chains, but in this instance the correct interpretation was unclear, so we did not model anything into this density. **d, e,** and **f,** represent the same structures as in **a, b** and **c**, with the positive Fo-Fc difference density from omit maps calculated with the inhibitors excluded shown in green. 2Fo-Fc and Fo-Fc maps are contoured at 1.0σ and 2.5σ respectively. The anomalous difference map in **a,** is contoured at 3.5σ.

bioRxiv preprint first posted online Jul. 19, 2019; doi: http://dx.doi.org/10.1101/706168. The copyright holder for this preprint (which was not peer-reviewed) is the author/funder, who has granted bioRxiv a license to display the preprint in perpetuity. It is made available under a CC-BY-ND 4.0 International license.



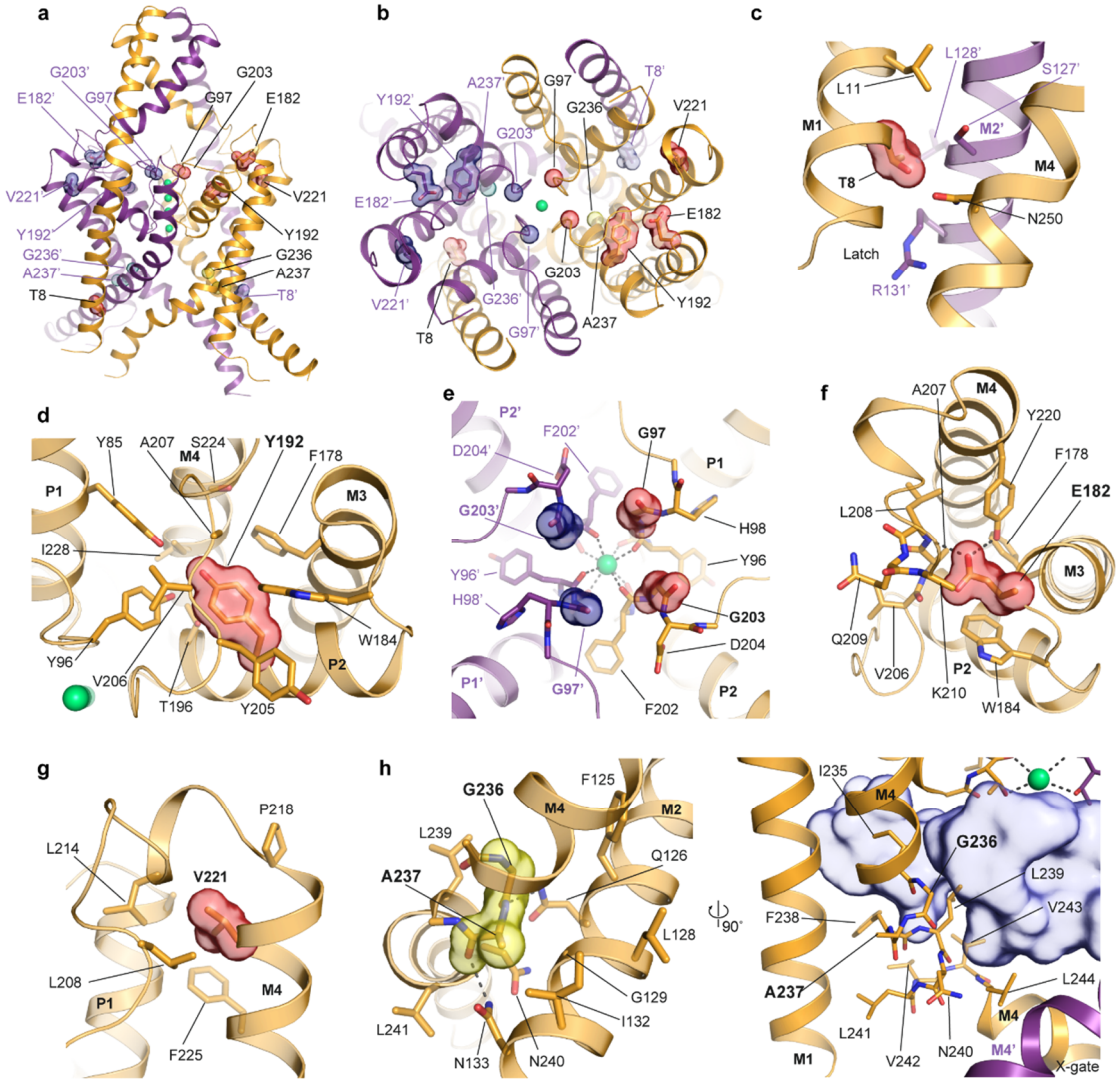
Extended Data Fig. 6. Effects of BAY 1000493 and BAT 2341237 on TASK-1 and TASK-3, and inhibitor washout data for BAY 1000493 and A1899 inhibitor. a, Dose response curves for BAY 1000493 on TASK-1 and TASK-3. **b,** Dose response curves for BAY 2341237 on TASK-1 and TASK-3. **c,** Washout of BAY 1000493 from TASK-1 and TASK-1 mutants. **d,** Washout of BAY 1000493 compared to A1899. **e,** relative washout rates for BAY 1000493 and A1899. **f,** Analysis of the washout rates for the compounds shown in **c**. Data are presented as mean ± s.e.m..

bioRxiv preprint first posted online Jul. 19, 2019; doi: http://dx.doi.org/10.1101/706168. The copyright holder for this preprint (which was not peer-reviewed) is the author/funder, who has granted bioRxiv a license to display the preprint in perpetuity. It is made available under a CC-BY-ND 4.0 International license.



Extended Data Fig. 7. Model of the conformation that TASK-1 could adopt with a straight, continuous M4 helix and a gating scheme for TASK-1. a,b Model of TASK-1 with M4 adopting a straight α-helical conformation (in red and blue) aligned with the TASK-1 structure shown from **a**, the side and **b,** below the membrane. **c,** The TASK-1 structure and open model viewed from below the membrane. **d,** A schematic model for TASK-1 activation, with the X-gate closed state shown in orange, the X-gate open state shown in blue and the open channel state shown in mauve. Stars indicate the conformations for which we have structures. The exact nature of the open X-gate and open channel conformations are not yet known.

bioRxiv preprint first posted online Jul. 19, 2019; doi: http://dx.doi.org/10.1101/706168. The copyright holder for this preprint (which was not peer-reviewed) is the author/funder, who has granted bioRxiv a license to display the preprint in perpetuity. It is made available under a CC-BY-ND 4.0 International license.



Extended Data Fig. 8. TASK-1 mutations associated with PPH4 – structure and location of mutations. Location of mutations in TASK-1 and TASK-3 mapped onto the TASK-1 structure shown from **a,** the membrane plane and **b,** from the extracellular side. Close-up views of **c** Thr8Lys in the latch region on M1, **d,** Tyr192Cys, **e,** Gly97Arg and Gly203Asp in the pore loops, **f,** Glu182Lys, and **g,**Val221Leu . **h,** the TASK-3 Birk-Barel syndrome mutations Gly236Arg and Ala237Asp in M4 (highlighted in yellow in the panel to the left), shown from the membrane plane and rotated 90° with the vestibule shown in blue in the panel to the right.

bioRxiv preprint first posted online Jul. 19, 2019; doi: http://dx.doi.org/10.1101/706168. The copyright holder for this preprint (which was not peer-reviewed) is the author/funder, who has granted bioRxiv a license to display the preprint in perpetuity. It is made available under a CC-BY-ND 4.0 International license.

Extended Data Tables

Extended Data Table 1 | X-ray crystallography data, refinement and model statistics.

	TASK-1		TASK-1 BAY 1000493		TASK-1 BAY 1000493 Br edge data		TASK-1 BAY 2341237	
PDB Code	6RV2		6RV3				6RV4	
Data Collection								
Beamline	I24		I24		I24		I24	
Wavelength [Å]	0.9686		0.9686		0.9116		0.9686	
Space group	$P22_12_1$		$P22_12_1$		$P22_12_1$		$P22_12_1$	
Crystallisation conditions	0.1 M TRIS pH 8.5, 0.05 M KCl, 32% v/v PEG400, 3% w/v/ sucrose		0.1 M TRIS pH 8.5, 0.05 M KCl, 24% v/v PEG 400, 3% w/v/ sucrose		0.1 M TRIS pH 8.5, 0.05 M KCl, 24% v/v PEG 400, 3% w/v/ sucrose		0.1 M TRIS pH 8.5, 0.05 M KCl, 31% v/v PEG 400, 3% w/v/ sucrose	
Cell dimensions *a*, *b*, *c* (Å) α, β, γ (°)	45.14, 204.79, 238.34 90, 90, 90		45.07, 204.50, 239.32 90, 90, 90		45.03, 201.91, 238.91 90, 90, 90		45.10, 201.33, 238.57 90, 90, 90	
Processing	AIMLESS	STARANISO	AIMLESS	STARANISO	AIMLESS	STARANISO	AIMLESS	STARANISO
Resolution [Å][1]	47.67-3.00 (3.11-3.00)[1]	47.67-3.00 (3.12-3.00)[1]	44.29-2.90 (3.00-2.90)[1]	44.29-2.90 (3.01-2.90)[1]	44.67-3.30 (3.46-3.30)[1]	44.67-3.30 (3.37-3.30)[1]	44.01-3.10 (3.23-3.10)[1]	43.12-3.10 (3.23-3.10)[1]
Resolution limits [Å][2,3]	3.00, 3.97, 3.38 (3.00, 3.47, 3.09)[3]		2.90, 3.77, 3.27 (2.90, 3.49, 3.09)[3]		3.30, 3.65, 3.44 (3.30, 3.45, 3.30)[3]		3.10, 3.82, 3.70 (3.10, 3.57, 3.47)[3]	
Nominal Resolution [Å][4]	3.31		3.08		3.30		3.35	
$CC_{1/2}$	0.989 (0.346)[1]	0.993 (0.697)[1]	0.991 (0.467)[1]	0.998 (0.795)[1]	0.997 (0.810)[1]	0.999 (0.741)[1]	0.989 (0.542)[1]	0.998 (0.792)[1]
R_{meas}	0.285 (2.177)[1]	0.239 (1.124)[1]	0.258 (1.969)[1]	0.194 (0.860)[1]	0.523 (2.783)[1]	0.500 (3.052)[1]	0.276 (1.519)[1]	0.219 (0.702)[1]
R_{pim}	0.124 (0.947)[1]	0.103 (0.464)[1]	0.126 (0.958)[1]	0.094 (0.421)[1]	0.089 (0.468)[1]	0.085 (0.517)[1]	0.143 (0.774)[1]	0.113 (0.348)[1]
I / σI	4.4 (1.0)[1]	5.6 (1.9)[1]	6.0 (1.3)[1]	7.2 (2.5)[1]	10.0 (2.3)[1]	10.2 (2.0)[1]	5.6 (1.3)[1]	6.6 (2.7)[1]
Completeness [%][5]	99.7 (99.8)[1]	79.7 (37.2)[1,5]	99.3 (97.7)[1]	80.0 (40.0)[1,5]	100.0 (100.0)[1]	98.0 (85.0)[1,5]	99.7 (99.7)[1]	80.9 (34.8)[1,5]
Redundancy	5.1 (5.3)[1]	5.3 (5.7)[1]	3.9 (3.9)[1]	3.9 (3.8)[1]	34.3 (35.2)[1]	34.3 (34.5)[1]	3.5 (3.6)[1]	3.5 (3.7)[1]
No. reflections / unique	231490 / 45475	193749 / 36417	196329 / 50143	157963 / 40478	1169177 / 34128	1145529 / 33435	143532 / 40728	117488 / 33101
Anomalous completeness [%]					99.9 (99.9)[1]	98.4 (88.6)[1]		
Anomalous redundancy					17.3 (17.5)[1]	18.5 (17.8)[1]		
Refinement								
Resolution (Å)	47.0 – 3.0		42.5 – 2.9				41.2 – 3.1	
R_{work} / R_{free}	25.42 / 25.70		23.54 / 24.21				25.08 / 25.60	
No. atoms								
Protein	8006		8070				7985	
Other	457		570				405	
B-factors (Å^2)								
Protein	66.13		47.86				48.58	
Other	78.09		61.83				53.41	
R.m.s. deviations								
Bond lengths (Å)	0.008		0.008				0.008	
Bond angles (°)	0.904		0.915				0.896	
Ramachandran statistics								
Favoured	97.74%		97.56%				97.54%	
Allowed	2.26%		2.44%				2.46%	
Outliers	0%		0%				0%	

[1] Values in parentheses are statistics for highest resolution shell
[2] Anisotropic resolution limits along each of the three principal directions as defined by AIMLESS based on Mn (I/sd(I)) > 1.5
[3] Values in parentheses are resolution limits in each direction based on half dataset correlation > 0.3 ($CC_{1/2}$).
[4] Nominal resolution is defined based on overall Mn (I/sd(I)) > 1.5 as estimated by AIMLESS.
[5] Spherical completeness of anisotropically truncated data in STARANISO.

bioRxiv preprint first posted online Jul. 19, 2019; doi: http://dx.doi.org/10.1101/706168. The copyright holder for this preprint (which was not peer-reviewed) is the author/funder, who has granted bioRxiv a license to display the preprint in perpetuity. It is made available under a CC-BY-ND 4.0 International license.

Extended Data Table 2 | Effects of BAY1000493 on a range of ion channels.

Voltage sensitive dye measurements (FLIPR membrane potential assay)[1]	
TRESK	>30 uM
TWIK2	>30 uM
EAG1	>30 uM
$K_{ir}3.1/3.4$	>30 µM
Kv7.1	>10 µM
$K_{ca}3.1$	>30 µM
Calcium sensitive dye measurements (FLIPR Tetra System)[2]	
$Ca_v3.2$	>30 µM
TRPC5	>30 µM
TRPC6	>30 µM
TRPA1	>30 µM
TRPV4	>30 µM
Extended Cardiac Safety Profiler Panel (Eurofins)[3]	
hERG	2.4 uM
$Na_v1.5$	>30 µM
$Ca_v1.2$	>30 µM
$K_v1.1$	29 µM
$K_v1.3$	17 µM
$K_v1.5$	19 µM
$K_v4.3$	>10 µM
KCNQ1	>30 µM
HCN4	>30 µM

[1.] As described here: https://www.moleculardevices.com/sites/default/files/en/assets/data-sheets/reagents/flipr-membrane-potential-assay-kits.pdf

[2.] As described here: https://www.moleculardevices.com/sites/default/files/en/assets/data-sheets/reagents/calcium-assays-for-the-flipr-tetra-system.pdf

[3.] As described here: https://www.eurofinsdiscoveryservices.com/cms/cms-content/services/in-vitro-assays/ion-channels/cardiacprofiler/